UNIVERSITÀ DEGLI STUDI DI NAPOLI FEDERICO II

DOTTORATO IN INGEGNERIA INDUSTRIALE – XXXII CICLO

Settore Scientifico Disciplinare: ING-IND/05
Impianti e Sistemi Aerospaziali

PLANNING GUIDANCE AND NAVIGATION FOR AUTONOMOUS DISTRIBUTED AEROSPACE PLATFORMS

Flavia Causa

Relatori

Prof. Michele Grassi
Prof. Giancarmine Fasano
Prof. Alfredo Renga

Coordinatore

Prof. Michele Grassi

Keywords

UAV Swarms, Cooperation, Formation, Cooperative Navigation, GNSS Challenging environment, Planning, Differential GNSS, Carrier Phase, Integer Ambiguity Resolution, Large Baselines, Single Frequency.

Abstract

Many current and future aerial and space missions are based on the paradigm of distributing the tasks among several platforms to overcome the limits of the single vehicle. This thesis tackles navigation planning and guidance of both distributed spacecraft and cooperative UAVs.

Cooperation among UAV platforms improves reliability and reconfigurability of the formation and allows to accomplish the mission in a reduced time. Not only does cooperation enhance reliability and overall mission time, but it enables mission and performance that would not be achievable in a single vehicle configuration. In this thesis the advantage of using cooperation to improve navigation performance is analysed, highlighting the potential of cooperative formations with respect to the single platform and the benefits related to having more than one platform to perform the mission. Specifically, two scenarios are taken into account. Navigation performance with cooperation among platforms is analysed either under GNSS nominal or non-nominal coverage. The latter can be also referred as GNSS challenging condition.

In case of non-nominal GNSS coverage, the flight of UAV in the GNSS challenging area can be enabled only using one or more cooperative platforms, whose absolute position along with relative measurement is shared with the formation and used to improve the navigation performance of the vehicle under non-nominal GNSS coverage. A cooperative navigation filter is developed for this purpose and planning and guidance technique are developed for the cooperative platforms in order to guarantee satisfactory navigation performance for the vehicle in the GNSS challenging area. In addition, due to the heterogenous nature of the GNSS coverage in an urban scenario a task assignment and path planning technique has been developed for a swarm of UAV operating in a urban scenario, exploiting cooperation in the GNSS challenging areas, and allowing UAVs to act independently under nominal coverage, in order to optimize the available resources.

When under nominal GNSS coverage, all the UAVs of the formation show satisfactory positioning performance, that could be improved by using differential or carrier phase differential GNSS. Nevertheless, integration of low cost IMUs, GNSS and magnetometers allows real time stabilization and flight control but may not be

suitable for applications requiring fine sensor pointing. In these scenarios, cooperation is used to improve attitude accuracy using as additional measurement an Inertial- and Magnetometer- independent measurement, that is related to carrier phase differential GNSS and visual measurements. This concept extends the paradigm of multi-antenna GNSS attitude estimation to a distributed aircraft scenario. The independent measurement allows to have a fine pointing that is compliant with the requirements of mapping mission. The enhancement of attitude accuracy produces also improved performance in positioning estimation.

As regards space, many space missions will rely on distributed platform, to optimize the reconfigurability, maintainability and performance of the systems. Satellite formation flying requires the knowledge of the relative navigation between the platforms in real time, with very high accuracy. This thesis uses GNSS relative navigation based on carrier phase double differences to estimate with high precision the 3D components of the distance of two Low Earth Orbit spacecraft with large baseline. In case of large baseline, the ionosphere delay could dramatically affect the correct estimation of carrier phase double difference ambiguity. In this thesis a new model for real time estimation of the ionospheric delay is proposed, which accounts for the spatial difference of the ionosphere. This model is tested in an EKF that uses real flight data coming from the Gravity Recovery And Climate Experiment mission, and its performance is compared with the classic model for ionosphere estimation.

Table of Contents

List of Figures

List of Tables

Acknowledgements

Pozzuoli 15/2/2019

Pochi giorni fa, quando ho compilato il modulo per l’esame finale mi sono resa conto che tutto questo è realmente finito. Un senso di nostalgia mi ha travolto e un grande punto interrogativo su cosa farò da grande è qui davanti a me.

Scrivere i ringraziamenti per il mio dottorato significa premere il tasto rewind sul registratore e scorrere lentamente questi tre anni, che sono stati tra i più significativi della mia vita. Anni di consapevolezza e di paura. Anni di “Basta! Non valgo niente!”, anni di “Che bello! Ho vinto un altro premio!”. Anni di lotta e di tregua. Anni per comprendere me stessa, anni per superare i miei limiti.

Questi tre anni sono passati via come un lampo. Ma questo fulmine, potente e rumoroso, ha lasciato una scintilla che mi ha reso diversa e che illuminerà per sempre la mia vita. Mi ha insegnato che a volte la soluzione giusta è quella che non ti aspettavi. Mi ha insegnato a dare luce e scoprirmi capace anche alle cose che ritenevo noiose e meno importanti.

E anche se un fulmine non cade mai due volte nello stesso posto, io continuerò a tornare dove risiede la mia passione, ad inseguire i miei sogni, anche se non sono state poche le volte in cui ho pensato di aver perso la direzione giusta. Me l’hanno sempre detto che l’heading è un grosso guaio.

Ma io da brava navigatrice, ho imparato la lezione. Una IMU come me non avrebbe mai potuto farcela senza usare un po' di sensor fusion.

E fortunatamente io ho avuto i migliori magnetometri possibili. Giancarmine, Michele ed Alfredo, più che tutor sono stati dei maestri di vita, capaci di dispensare consigli utili, anche al di là delle competenze ingegneristiche. Grazie per avermi supportato e sopportato per quelli che sono stati per voi tre lunghissimi anni. Grazie per non aver mai smesso di credere in me, anche quando io non ci credevo neanche un po’. E’ risaputo che sono una rompiballe, con una grossa bias instability, ma il vostro aiuto a 10 Hz mi ha consentito di non divergere, indicandomi sempre la direzione giusta.

Senza GPS una IMU potrebbe essere dovunque, ma non ritrovarsi mai. Fortunatamente, la mia famiglia mi ha inizializzato con la giusta posizione e ha continuato ad esserci sempre durante il mio volo. Grazie a mamma che mi ha insegnato l'equilibrio tra la consapevolezza e l'umiltà. Mi ha insegnato a non arrendersi mai e a non dare mai niente per scontato. Mi ha insegnato a superare i miei limiti, senza sentirsi mai arrivati. Mi ha insegnato a credere in me, ma a mettermi sempre in discussione. E sebbene sia risaputo che la passione per i numeri l'abbia presa da lei, il vero ingegno risiede in Papà. Grazie per avermi trasferito la passione per il volo e l'intuito per trovare sempre la soluzione giusta guardando oltre il convenzionale.

Grazie ai miei fratelli, per tutte le volte che abbiamo litigato e per tutte le volte che ci siamo capiti con uno sguardo. Per tutte le volte che abbiamo lottato insieme, per tutte le volte che siamo scoppiati a ridere per nulla, per tutti i "piezzi" incontrati lungo la via. Grazie ad Erika che mi ha ricordato quanto valessi nei momenti più bui, e a Simone, da cui ho preso la forza per difendere le mie idee e combattere per i miei obiettivi. Grazie poi a Zizia che, nonostante gli anni passino, riesce sempre con un abbraccio a riportarmi il sorriso.

Un doveroso ringraziamento va ai miei zii, sempre al passo con i tempi, dispensatori di consigli e talvolta dei grandi rompiballe (dovevo pur aver preso da qualcuno!). Grazie per vedere in me sempre qualcosa di speciale, grazie per riportarmi sempre con i piedi per terra.

Grazie a chi ha creduto in me fin dalla culla, grazie a chi ha visto in me quel pizzico di follia in più, a chi ha sempre combattuto con me da sempre. Grazie a chi c'è sempre stato e c'è ancora, oltre il reale, oltre la tridimensionalità del tempo. Grazie ai miei nonni per aver sorriso ad ogni traguardo raggiunto, per aver festeggiato ad ogni piccolo passo, per avere dato un senso ad ogni mio piccolo sacrificio, per avermi fatto credere un po' migliore di quello che sono. Da sempre e per sempre, ovunque io sia, ovunque voi siate.

E quando il gioco si fa duro, le misure cooperative entrano in campo. Un concetto semplice, ma efficace. Qualcuno una volta ha detto che le leggi della somma non si applicano alle persone, e 1+1 non fa mai 2, ma sempre di più. Il vostro supporto in questi anni ha fatto sempre almeno 3 per me. Grazie Daniela, Roberto e Salvatore per aver condiviso con me la stanza, i voli, gli assemblaggi, le deadline e le mie chiacchere e preoccupazioni infinite. Grazie per le nostre merende pomeridiane, le nostre canzoni e grazie un po' di meno per le squisite gomme alla fragola.

E anche se tutto sembra essere perfetto, la soluzione è sempre migliore se aggiungi il vecchio schema cooperativo. Quello in cui devi preprocessare i dati e stimare con grande accuratezza le tre componenti della distanza con i tuoi compagni. Grazie a chi se ne è andato, a chi è ritornato a chi c'è sempre stato. Grazie Salvio, Livio, Alberto e Fabio per avermi messo in dubbio, per avermi fatto dimenticare i problemi, per aver sempre creduto in me. Grazie per ritornare sempre insieme a me, a come eravamo ieri anche se non ci vediamo da mesi.

Ultima ma sicuramente non meno importante è la normalizzazione della matrice di rotazione. Una formula semplice, ma necessaria. Provateci voi a far funzionare un filtro senza! Non importa quali misure usi, quella formula raramente scritta sui libri è l'unica cosa che assicura la convergenza della soluzione. Marco, sei tu la mia formula di normalizzazione, il mio punto fisso, la condizione che separa la realtà dalla follia. Siamo io e te che restiamo li, nonostante i cambiamenti, nonostante tutte le altre misure vadano e vengano ad un rate imprecisato. Solo tu corri con me a 100 Hz e mi tieni la mano impedendo alla soluzione di impazzire.

E' strano vedere i passati tre anni schematizzati in queste due pagine, come avrei fatto in un paper, come un filtro di navigazione, che pochi di voi capiranno veramente. Ma forse per le persone come me è più facile scrivere formule che parole, è più facile fotografarvi così che dichiarare a voce alta quanto ciascuno di voi sia importante per me.

Ma una cosa è certa: non smetterò mai di essere grata ad ognuno di voi per aver scelto di accompagnarmi in questo confuso ma bellissimo filtro di Kalman che è la mia vita.

Chapter 1: Introduction

The concept of distributed mission has been widely applied in the Aerospace scientific community, both for space [1, 2] and aerial platforms [3]. Distributing tasks among the platforms reduces the costs, increases the system flexibility and reactivity to failures and enables missions that were too complex to be carried out by a monolithic platform. As a consequence, most of the next generation of space mission and systems will rely on co-flying, distributed architectures.

As far as the aerial platforms are concerned, the miniaturization and the autonomy introduced by the UAVs created a revolution in many industries and in our daily life [4]. Cooperation among UAVs increases their potential, extending the autonomy and the reliability of the system, and overcomes the limits imposed by the single vehicle configuration. Most of the missions the UAVs are demanded to perform includes fast deployment and fast response that can be guaranteed by using a system of several elements that behaves in a coordinated bio-inspired way.

This thesis discusses approaches and advantages of cooperative navigation for both UAV and space platforms. Section 1.1 and 1.2 detail the objectives and the main motivations of this thesis, both for UAV (section 1.1) and space vehicles (section 1.2). Finally, section 1.3 includes an outline of the remaining chapters.

1.1 COOPERATION OF UAV PLATFORMS

Recently, the scientific research of the UAS community is driven by an increasing interest in integrating the UAVs in daily life applications. Applications such as small packet delivery, urban surveillance, infrastructure inspection, and three-dimensional mapping can be speeded-up by the usage of autonomous aerial vehicles. Nevertheless, several missions (e.g. long autonomy missions, delivery of multiple goods) often requires very expensive vehicles, that can embark a huge payload. A common solution to this problem is distributing the mission tasks among a swarm of cooperative UAVs.

Distributed or cooperative missions offer several advantages and enable an increased precision in vehicles localization, by cooperative navigation. Cooperative or networked navigation is a term used to describe those techniques whereby a community of users exploits shared measurements and information exchange to the navigation advantage [5, 6]. Cooperative navigation can be used to enhance the performance of all the members of the swarm [5] or it can be used to serve few element more in needing of a navigation performance improvement.

The latter approach is often used in the case a non-homogeneous required navigation performance exists among the UAVs that compose the formation or in the case the UAVs experience a spatial difference in sensors availability. As an example, cooperative navigation has been widely used in applications where the UAVs are demanded to fly within an area with non-nominal GNSS coverage, usually named GNSS challenging areas, by exploiting the information coming by other vehicles with nominal navigation performances [7–9]. Whereas, in the case the UAV formation stands upon homogenous coverage, it could be required to improve navigation accuracy of few members of the swarm. As an example, some UAVs could be required to have attitude accuracy higher to the one suitable for real time stabilization and flight control, for fine sensor pointing applications, such as direct georeferencing [10] and LiDAR-based 3D mapping [11]. To this aim [12] proposed a cooperative navigation strategy for improving the pointing accuracy of one of the UAV of the formation demanded to 3d mapping mission.

Following these approaches, this thesis uses cooperative navigation as a mean to guarantee highest navigation accuracy both under nominal GNSS coverage and in GNSS challenging scenarios. Navigation results are demonstrated with simulated and experimental data.

1.1.1 Navigation under non nominal GNSS coverage

Similarly to [7–9], navigation in GNSS challenging scenarios has been carried out in this thesis supporting the flight of the UAV under non nominal GNSS coverage, termed son, by complementing the available GNSS measurements with relative sensing and absolute positioning information shared by several cooperative platforms, termed fathers. The position of the cooperative platforms should be carefully selected in order to ensure them to be always in line of sight with the son and always outside the challenging area.

This thesis designs a cooperative navigation filter that supports flight in GNSS challenging environment by using several relative sensing instruments (RF-ranging, camera) that could be alternatively chosen to support the flight of the son UAVs. It is intuitive that the performance of the cooperative navigation depends on

- the geometry of the current GNSS satellites seen by the son UAV,
- the adopted relative sensor
- the relative formation of the cooperative vehicles.

The concept of Generalized dilution of precision (geDOP) has been introduced in this thesis to predict the performance of the cooperative filter, based on the aforementioned parameters. geDOP appears to be a powerful instrument, also used to design the formation geometries that maximizes the cooperative navigation advantage.

With the aim of maximizing the cooperative navigation advantages, this thesis tackles path planning of a cooperative tandem formation in GNSS challenging environment. Path planning under non-nominal GNSS coverage for a single UAV is usually solved by designing a path that maximizes the GNSS coverage along the trajectory [13, 14], often modifying the preassigned path and not guaranteeing the mission to be fully accomplished. The proposed tandem planning techniques both for online and offline applications, ensure the son UAV to fly along the pre-assigned trajectory. Whilst, the cooperative vehicle is in charge of optimizing the navigation performance by realizing the relative geometry that maximizes the cooperation advantage thanks to the geDOP. An online Guidance, Navigation and Planning scheme is also designed for the two vehicles of the formation.

Low altitude mission in urban environments requires the UAV to fly along trajectory that are partially in GNSS challenging scenario. Following the aforementioned approach, to enable navigation in these segments one or more cooperative platforms are needed to support the flight of the son UAV. Whereas, the UAVs can execute the mission without the cooperative support under nominal coverage. It is intuitive that a mission in an urban environment, could be beneficial of reconfigurable vehicles that could either cooperate, or execute the mission independently based on the spatial distribution of the GNSS measurements. To fully exploit the potential of the UAV swarm a task assignment and a path planning technique has been developed for scenarios with heterogenous GNSS coverage with the aim of minimizing the mission time, and optimizing the resources among the task to be executed.

1.1.2 Navigation under nominal GNSS coverage

When under nominal GNSS conditions, the available cooperative information could be still used to increase the accuracy of the navigation solution. Due to the availability of a reliable position without cooperative information, the aim of cooperative navigation changes and is used to advantage the pointing accuracy that results in an increased navigation performance, also in positioning. The key concept of this approach, introduced in [12, 15], is to exploit Differential GPS (DGPS) among vehicles and vision-based tracking to build a virtual additional navigation information. The used method resembles multi-antenna attitude estimation architectures [16], and exploits DGPS measurement between GNSS antennas embarked on different vehicles. Differently from [16] the exact relative position between the antennas is unknown, and the line of sight between them can be estimated by vision sensors.

This thesis improves the accuracy of DGPS baseline estimation [12, 15] by using Carrier phase differential GPS (CDGPS) techniques that yields centimetric precision in 3D relative position. CDGPS requires accurate estimation of integer ambiguities that becomes a complex task when single frequency receivers are used. This thesis uses a CDGPS filter to estimate baseline between the antennas, exploiting partial validation tests for discriminating among the wrong and correctly fixed ambiguities.

The attitude measurement obtained integrating CDGPS and vision-based measurements are used as additional information source in an EKF, either in a loosely or tightly coupled architecture.

1.2 DISTRIBUTED SPACE PLATFORMS RELATIVE NAVIGATION

Many current and future space missions for Earth remote sensing [17], observation of universe [18] and mapping of earth gravity field [19] are carried out with distributed and cooperative formations of spacecrafts. The distributed platforms fly by maintaining prefixed relative orbital geometries to achieve specific mission objectives. The usage of spacecrafts' formation enables simultaneous data acquisition from two or more points in the space which distance could range from few kilometers to hundreds of kilometres. In addition, relying on a formation of satellites increases the observation rate that could be beneficial for many missions such as Cross-track interferometry (XTI) and bistatic SAR applications.

Scientific data postprocessing requires accurate positioning (centimeter level) of the relative formation. Even though this is needed off-line, the capability of determining the baseline onboard with an accuracy on the order of a decimeter can be of potential interest for future distributed systems based on flying multiple low-cost small platforms. GPS based relative navigation using carrier phase double differences (DD), is a promising strategy to enable very precise relative navigation. Indeed, the usage of double differenced carrier phase measurements exploits the integer nature of the cycle ambiguities that could be exactly estimated. Nevertheless, GPS relative navigation can be performed only in Low Earth Orbit (LEO) where GPS signal strength and the GPS constellation visibility and observation geometry are the most favourable. Several works [20, 21] designed Kalman filter exploiting CDGPS measurement for estimating relative positioning in LEO application. This resulted in centimetric precision in predicting the distance (baseline) between platforms.

CDGPS performance depends on correct estimation of the integer ambiguities. A fundamental contribution to the process of correctly determining the cycle ambiguities lies in the correct estimation of the DD ionospheric delay, especially when large baselines (>100 km) are taken into account. Indeed, in case of large baselines, ionospheric delay can be higher than several carrier wavelengths, thus seriously impacting the integer ambiguity solution.

This thesis tackles relative navigation for LEO missions over large baseline (hundreds of kilometres) and introduces a new model for estimating ionospheric delays that accounts for the ionospheric spatial difference. The introduced ionospheric model is tested in a Kalman filter and its performance compared with the classic model for ionosphere estimation [22].

1.3 THESIS OUTLINE

The present thesis includes cooperative navigation algorithms for UAVs and spacecraft and is organized as follows. Chapter from 2 to 6 introduces planning and cooperative navigation techniques for UAVs.

Chapter 2 remarks the motivations for using distributed UAV platforms and recall the main application and industries that could benefit from using UAV formation. A literature review of mission carried by UAV swarms and techniques used for enabling those applications is included.

The cooperative navigation architecture for GNSS challenging environments is described in Chapter 3. The chapter describes a general cooperative filter that is designed to use several cooperative measurements coming from one or more cooperative platforms. The concept of geDOP is also introduced in chapter 3 and used to compare the performance of the filter while using different sources of cooperative information, e.g. range or angular information. Navigation results for simulated and experimental data are shown.

Chapter 4 introduces a path planning technique for a tandem formation of UAVs, i.e. one son and one father. While the trajectory of the son is mission dependent, the trajectory of the father is designed to guarantee reliable state estimation of the son in the challenging area. Both offline and online approaches are reported in chapter 4. In view of a real-time implementation a conceptual scheme that includes guidance planning and navigation is also presented.

Chapter 5 tackles multi-UAV task assignment and path planning in environment with heterogenous GNSS coverage. In those missions the UAVs are demanded to collect targets, i.e. waypoints that could be located under nominal GNSS coverage or in challenging areas. It is intuitive that only in the case the UAV must reach a target in the challenging area the cooperative support is needed. Conversely, when the targets are under nominal GNSS condition no cooperation is needed and they can be used as independent systems to optimize the resource distribution and the overall mission time.

Chapter 6 describes the cooperative filter for improving the vehicle pointing accuracy. Attitude information are derived by coupling CDGPS and vision-based information, that creates a measure independent from magnetic and inertial effect. CDGPS filter and integer ambiguities validation techniques are described in chapter 6, and used with two filters architecture that integrates the CDGPS/vision measurement either in tightly or loosely coupled manner. The cooperative navigation performances are assessed using experimental data.

Chapter 7 deals with spacecraft relative navigation with CDGPS techniques. The problem of relative positioning estimation over large baseline in LEO is tackled by using a combination of EKF and Kinematic filter. A novel model for ionospheric delay estimation is introduced for enhancing the integer ambiguities estimation and improving the fixing rate. The proposed ionospheric model is compared with the classic model for ionosphere estimation introduced by Lear [22], using real flight data from GRACE mission [19].

Finally, Chapter 8 draws the conclusions of this thesis work.

Chapter 2: Cooperative UAVs: Motivation and Applications

In the last few years UAVs have gained popularity in many industries, due to their flexibility, level of autonomy and relatively low cost [23]. According to a PwC report [24], the market value of UAVs uses worth about $127 billion. Their potential can be exploited to perform several missions, reducing the human effort and avoiding exposing human beings to risky operation.

Nevertheless, several missions (e.g. long autonomy missions, delivery of multiple goods) often requires very expensive vehicles, that can embark a huge payload. As a solution of this problem, nowadays the UAS scientific community is oriented towards distributing the mission tasks among a swarm of cooperative UAVs. Two different architectures are available for cooperation, namely centralized and decentralized. The first assumes the decisional process occurs onboard a leader UAV or a ground control station (GCS). Whereas in decentralized approaches, every element of the formation is an intelligent agent and can make decision based on the formation's status.

Multi-UAV swarm can accomplish tasks which one UAV either fulfills with difficulty, such as mapping of a very huge area, accurate determination of the location for an object, search for a victim in short time, or fails to accomplish altogether, such as mapping of inaccessible caves or dense rain forest, navigation in GNSS challenging environments. Furthermore, compared to a one UAV, a UAV swarm is able not only to solve more tasks, but also to reduce the overall mission time. Additionally, if the task requires navigational autonomy within an unknown or difficult environment, a UAV swarm offers robustness through redundancy and self-organization, which cannot be achieved by deploying one UAV.

Missions involving the usage of multiple UAVs can be classified in seven categories that are highlighted in Figure 2.1:

1) Target search is a mission where the UAVs are demanded to explore an area and detect targets. People in danger are targets when dealing with search and rescue missions [25]. However target identification could be a part of military mission [26, 27], road patrol or surveillance (e.g. flying over

different road segment to stop vehicle for traffic violation [28]) and also includes precision agriculture as far as weeds detection is concerned [29].

2) Object tracking could be required in some missions after detecting the target and it is mainly needed to observe the target behavior [30]. It consist in using the UAVs to estimate the position and velocity of the target to eventually attack it when needed [27]. In the same way, environment monitoring aims at locating a certain element, e.g. wildfire [31], pollution [32], and monitor their propagation.

3) Mapping and data collection are missions that involve performing a global coverage of the selected environment. UAVs are used in these missions in different fields of applications, i.e. building inspection [33], precision agriculture, aerial mapping [34] and disasters monitoring [35].

4) Data collection could however be performed in a predefined location as occur for aerial photography of a certain target. Several missions deal with performing multiple tasks at a predefined location such as battery charging, highway velocity monitoring and flying dynamic traffic signal [28]. In addition, delivery and collection missions [36] assumes the UAVs have to pick the packages at a certain location and they have to be delivered in different points. Therefore, they can be included in this category.

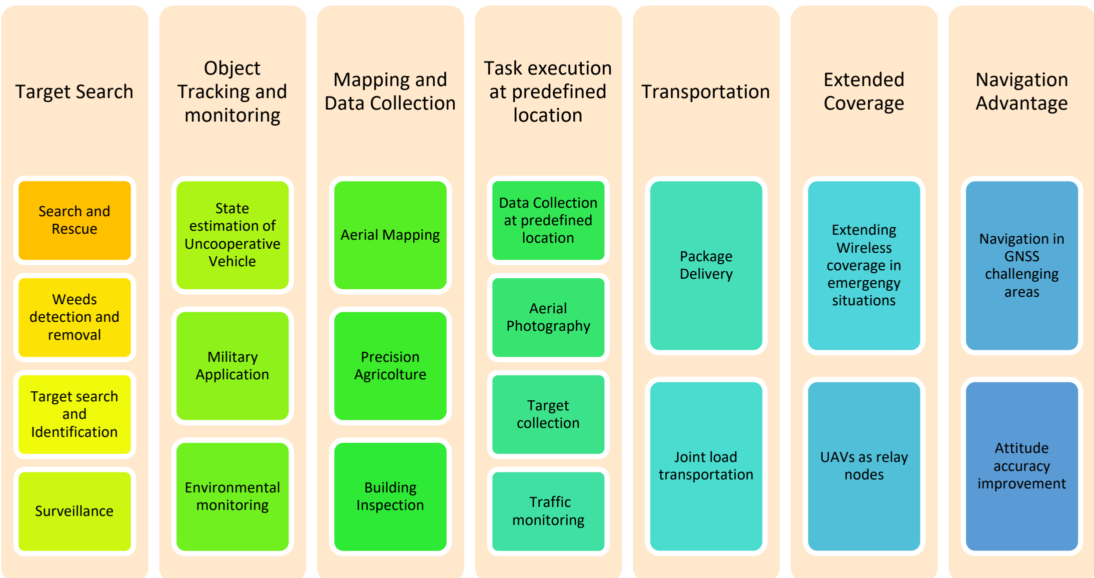

Figure 2.1 Multi-UAV Mission

5) On the other hand the second mission belonging to the transportation category involves the usage of cooperative UAVs to jointly transport a weight that is heavier than the maximum weight each UAV can load [37].

6) Another application that involves UAVs swarm consists in improving the coverage of a selected area or of a selected device. An example of that is the service recovery after disaster situation, where the UAVs of the swarm must be deployed in the environment to provide seamless coverage. On the other hand, UAVs can also be employed as communication relay [38] to extend the coverage of two or more distant platforms.

7) Finally, UAV swarms are used to the navigation advantage by the means of cooperative Navigation. Cooperative or networked navigation is a term used to describe an approach where a group of UAVs shares measurements and uses information exchange to the aim of enhancing the navigation performance.

In general, a multi UAVs mission could include the assignment of roles belonging to several categories of applications. As an example, Figure 2.2 includes an UAV swarm that is demanded to road patrol. In the figure the UAV 1 is performing data collection, UAV 2 is acting as communication relay and UAV 3 is both acting as a relay and collecting data at predefined location.

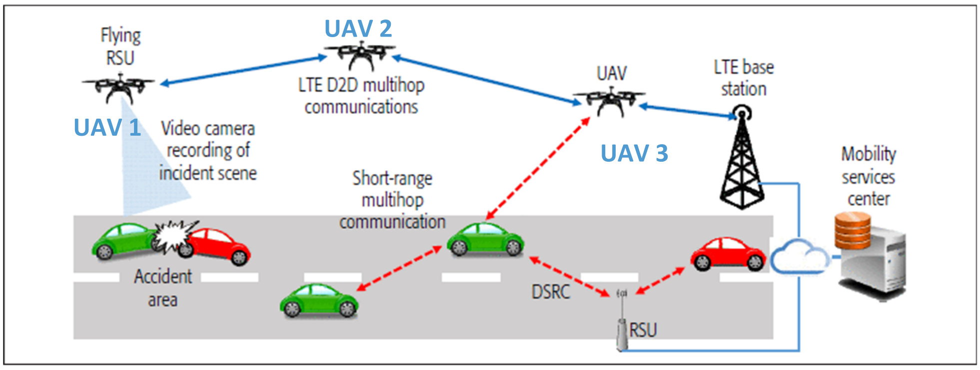

Figure 2.2 UAV Swarm for Intelligent transportation system [28]

This chapter is aimed to describe the past and current applications of multi-UAV swarm. To this end, the categories identified in Figure 2.1, whose potential fields of application are reported in Table 2.1 are detailed in sections from 2.1 to 2.7, where a literature review of the applications and the techniques used for multi-UAVs formation is given.

2.1 TARGET SEARCH

One of the main advantages of using a multi-UAV swarm is the capability to divide tasks among the platforms to optimize the overall mission time. Target search, and especially search and Rescue applications have as fundamental requirement the need for time minimization and can take advantage in the usage of multi-UAV swarms. Several techniques have been recently developed in this framework. The research conducted in [39] used preplanned trajectory to acquire a map of the whole environment scanning the selected region (Figure 2.3.a). When one of the UAV detects a target, it starts hovering on it, using the other UAVs of the swarm as relay to communicate its position with the ground control station. To this aim the others UAVs must leave their trajectory to reach the positions they are demanded to stay to act as relay platform (Figure 2.3.b). Also references [40, 41] use a cooperative framework for target search. In these research works the cooperation is not exploited to improve communication relay, but to optimize the exploration time. Each vehicle has a cognitive map of the environment that share with the other vehicles, path of each vehicle is defined in order to reduce the probability there is an undiscovered target in the searched area.

Differently from the cooperative approaches described above, [42] uses a un-cooperative decentralized approach for the search and rescue under canopy.

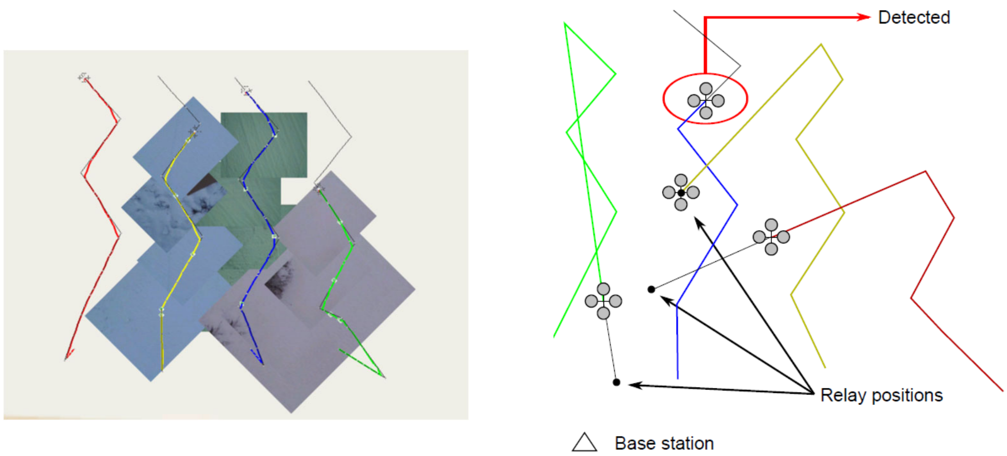

a) b)

Figure 2.3 Multiple UAVs search and rescue. a) preplanned path b) target detection and UAV swarm reconfiguration [39]

Table 2.1 Potential field of application for UAV swarms

Field of Application	**Missions**						
	Target Search	Object Tracking and Monitoring	Mapping and Data Collection	Task execution at predefined location	Transportation	Communication Relay	Navigation advantage
Delivery of Goods				Small Package delivery	Small package delivery, jointly load transportation		Delivery at low altitude
Precision Agriculture	Plant Disease detection [43]		Soil, field tile and crop maturity mapping	Irrigation, Pesticide spray			
Construction and Infrastructure Inspection			Oil/gas pipeline Inspection Critical land building inspection (e.g. cell towers)	Oil/gas pipeline Inspection Wind turbine inspection			Bridge or building inspection
Environment Monitoring		Wildfire, pollution monitoring	Aerial Mapping				
Search and Rescue	Search for human victims						Cooperative search in GPS-denied environment
Disaster Management [44]		People Tracking	Post disaster aerial management	Load transportation and deployment (food, water, medicines)	Load transportation and deployment	Wireless coverage improvement	Search at low altitude
Intelligent Transportation System [28]		Car tracking in occurrence of traffic violation	Monitor pedestrian traffic	Flying accident Report Agent Flying roadside unit Flying dynamic Traffic Signals			
Military application	Perimeter surveillance	Foe tracking and attack					
Homeland security	Border Surveillance						

This approach defines search area for each UAV, where each UAV has to plan online its trajectory with the aim of exploring all the assigned search area, without any knowledge of the path covered by the others member of the swarm. Therefore, cooperation is handled by the ground control station that defines the area to explore for each UAV and merges the acquired maps by detecting similar features. Whereas the UAVs act as independent platforms.

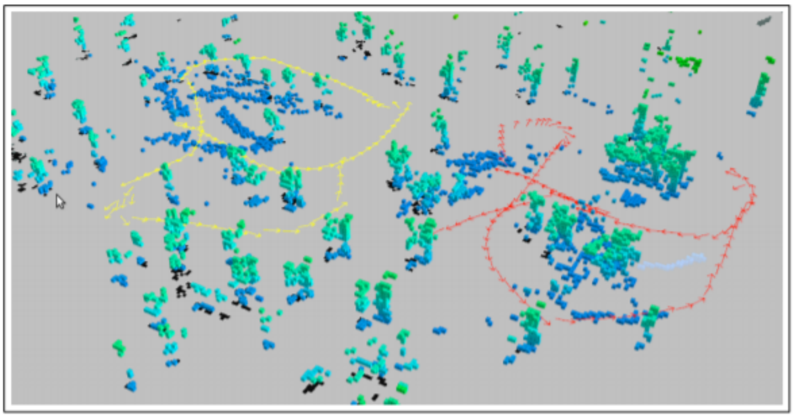

Figure 2.4 Multiple UAVs search and rescue, uncooperative planning of two UAVs. Maps collected by the two UAVs are merged at GCS level [42]

2.2 OBJECT TRACKING AND MONITORING

Object tracking is strictly related with Target Search and detection. Indeed, several missions, especially in the military applications, not only require detecting but also tracking the target to monitor its movements and behavior. A wide quantity of research papers is available in the open literature about this topic. In general, this problem is tackled using two approaches. The first one consists in using several UAVs to track the same target to better estimate its state. This is performed in [30, 45, 46], by optimizing the trajectory of the observers to track the target on the ground. Figure 2.5 shows a conceptual view of this approach, where the optimal position of the observer is strictly dependent on the onboard sensors used for estimating the target position.

The other approach assumes each target is tracked by a single UAV. Cooperation in this case aims at reducing the mission time, instead of the state estimation error. To this aim targets are distributed among the UAVs as shown in Figure 2.5. In general, The problem of defining the observer trajectory is tackled by using informative based planning [47, 48], genetic algorithms [49] receding horizon planning [50] and Markov Decision Process [51].

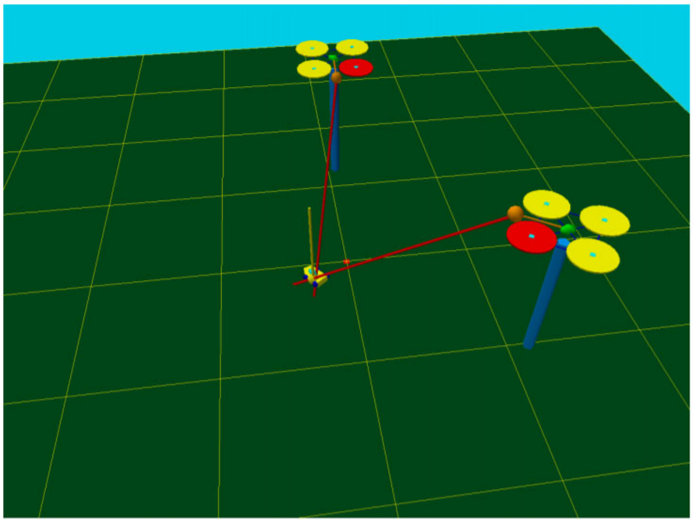

Figure 2.5 Cooperative Tracking: more observers for a single target [46].

Environmental monitoring of wildfire has been tackled in [31] with a swarm of small UAV. The mission aims to use the UAV swarm in a centralized way to track the flame perimeter. The information collected by the UAVs are sent to the ground control station and shared in the network to upload the path of the vehicle while the flame shape is changing. Figure 2.6 shows the path of six UAVs monitoring a flame while growing. A strategy for tracking and extinguishing fire is reported in [52].

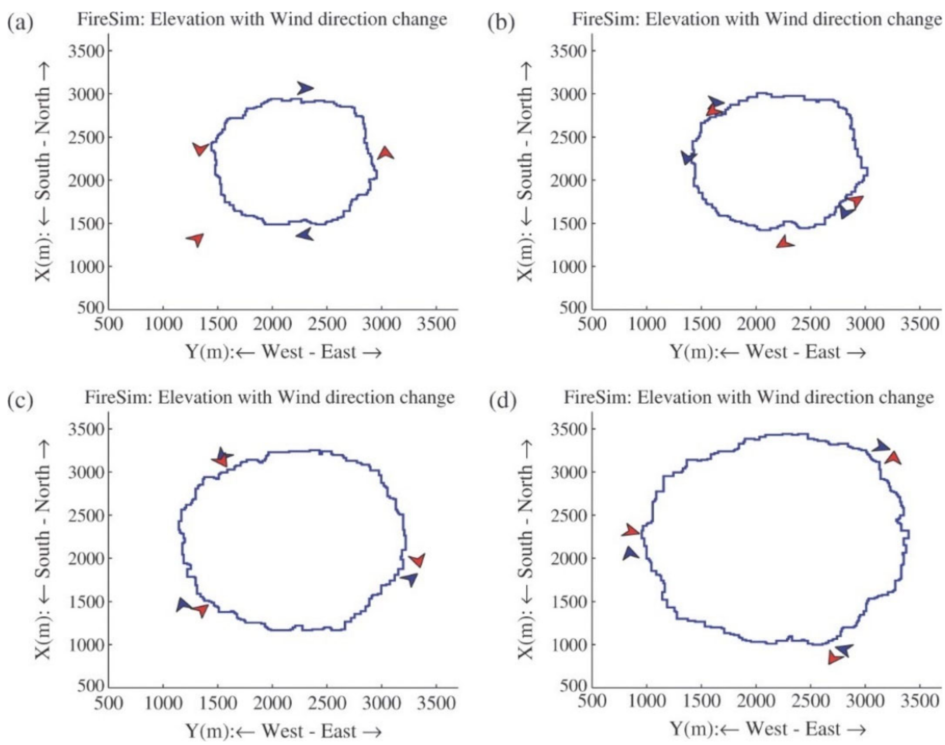

Figure 2.6 Monitoring of growing fire with 6 UAVs [31]

2.3 MAPPING AND DATA COLLECTION

Aerial mapping and data collection are in general very long and sometimes repetitive activities, that could take advantage of the usage of the UAVs. These missions are common to different fields of application, i.e. maritime surveillance, infrastructure inspection, precision agriculture and in general require performing observation in a selected area. Using a flying platform eases the mission and reduce its cost. In addition, using small platforms allow to monitor sites that either are not accessible or too risky for the human operator, i.e. bridge, pipelines, electric tower. As an example, Figure 2.7 shows the advantages and disadvantages of using an UAV, instead of satellite imagery or a manned vehicle for precision agriculture monitoring.

Issues	UAVs	Manned Aircraft	Satellite System
Cost	Low	High	Very High
Endurance	Short-time	Long-time	All the times
Availability	When needed	Some times	All the times
Deployment time	Easy	Need runway	Complex
Coverage area	Small	Large	Very large
Weather and working conditions	Sensitive	Low sensitivity	Require clear sky for imaging
Payload	Low	Large	Large
Operational complexity	Simple	Simple	Very complicated
Applications and usage	Carry small digital, thermal cameras & sensors	Spraying UAV system pesti-cide spraying	high resolution images for specific-area

Figure 2.7 Precision Agriculture Issues with different systems [53].

Cooperative mapping and data collection could be performed in an assigned area or at defined point location. The current subsection deals with the problem of collecting all the information in a predefined area, i.e. global coverage, whilst section 2.4 analyses the algorithms used when the location where data must be collected is defined a priori. Aerial mapping and global data collection include the need for performing a complete coverage of the selected environment. It is intuitive that allocating the mission among several UAVs will shorten the mission time.

One strategy used in this framework is defining a priori the area that each UAV has to explore as a subframe of the environment that the swarm is demanded to map [34, 54]. This approach is very similar to what described in the un-cooperative target detection. In this case there is no need to share real-time information among the vehicles and the union of the map estimated by each UAV can be computed in post-processing phase. Figure 2.8.a shows the predefined area that each UAV has to cover. Conversely another common approach [55, 56] is to use a cooperative network that uploads in real-time the exploration maps and defines the UAVs trajectory during the mission execution. A sketch of this approach is shown in Figure 2.8.b where different time epochs of the mission are shown. UAVs complete the mission when all the area has been inspected.

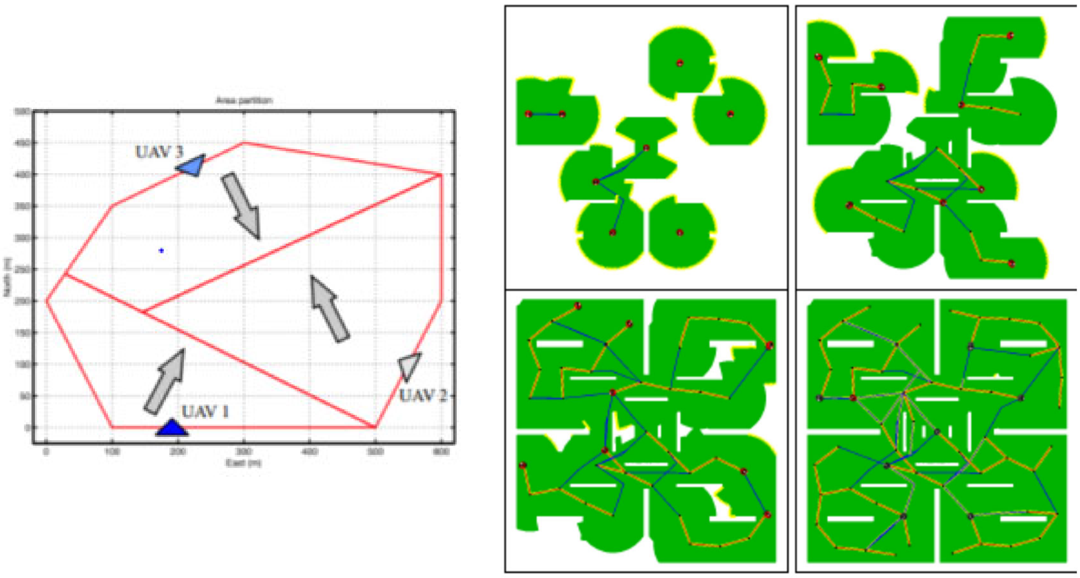

a) b)

Figure 2.8 Complete Coverage. with (a) [34] and without (b) [55] predefined area to explore.

2.4 TASK EXECUTION AT PREDEFINED LOCATION

The problem of performing tasks at a predefined location has been widely analyzed in the open literature and is known as Vehicle Routing Problem (VRP) [36]. VRP consists in routing a swarm of *n* UAVs to reach *m* targets at predefined locations and perform the mission they are demanded to execute at that location. Figure 2.9 depicts a concept of a mission where the UAVs have to collect object from a base station and deliver them to a predefined destination in an environment with obstacle. Several authors in the past years have focused on the problem of vehicle routing for multiple UAVs. The available strategies for VRP can be divided in exact and heuristic or metaheuristic methods [57–59]. Exact resolution problems [60, 61] are formulated as mixed-integer linear programming (MILP), and solved with branch and bound or set covering techniques [36]. These approaches yield the optimal solution by exploring all the feasible combinations, which suffers from scalability issues requiring a significant computational burden for increasing number of UAVs and/or target waypoints. When this occurs different heuristic [62] or metaheuristic [58, 62, 63] approaches can be applied. References [64, 65] use consensus based bundle algorithm to route a swarm of UAV in cluttered environment. Genetic algorithm and a discrete version of the particle swarm optimization (PSO), are used for assigning targets to UAVs in [66] and [67], respectively. However other techniques to solve that problem could include Markov processes, e.g. [68].

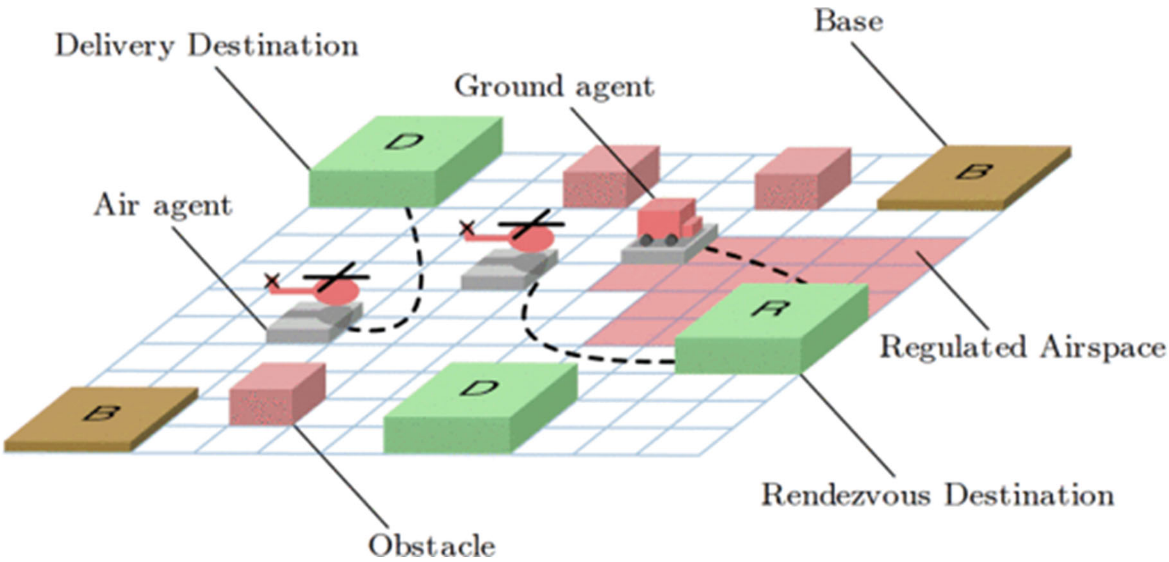

Figure 2.9 Data Collection at predefined location [68]

2.5 TRANSPORTATION

Package delivery is one of the most talked about application for unmanned aerial vehicles. The first America's drone delivery was performed in March 2019 by UPS and Matternet [69], and one month later Wing, a Google spinoff, received the first FAA approval for drone delivery [70]. Although no experiment has ever been performed using cooperative UAVs, it is clear that using a swarm of drones can enhance the delivery system method. However, this application is still at an early stage and a lot of issue concerning regulations and certifications must be solved.

On the other hand, joint load transportation has been extensively examined in the open literature. The problem of joint load transportation consists in defining the trajectory of the UAVs that allows equally distributing the weight during the transportation phase. A suitable approach for solving this problem is the leader-follower scheme, where the leader estimates the motion of the leader through the motion of the transporting object [71–73].

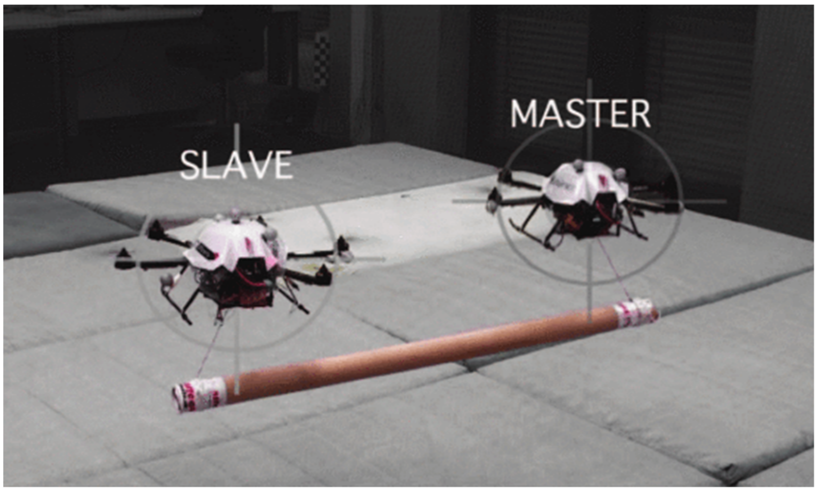

Figure 2.10 Cooperative Transportation [73]

2.6 EXTENDED COVERAGE

Swarms of UAVs are often demanded to provide wireless network to restore the coverage in a damaged area (Figure 2.11.a) or provide connection between too distant communicating platforms (Figure 2.11.b). The performance of the wireless network depends on the 3D placement of the UAVs. Different strategies for UAVs placement are available in the open literature that can be classified in three categories:

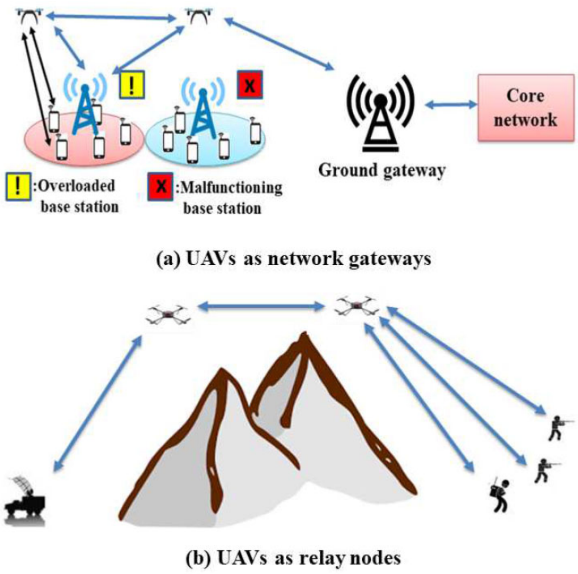

Figure 2.11 Typical Use Cases of UAV-Aided Wireless Communications [53]

- UAV placement aimed at minimizing the transmitting power of the UAVs [74],
- UAV placement aiming at maximizing the wireless network coverage [75],
- UAV placement aiming at minimizing the number of UAVs [76].

2.7 NAVIGATION ADVANTAGE

Cooperative navigation techniques consist in exploiting shared information to the navigation advantage. Two approaches exist in the open literature when dealing with this subject. Indeed, cooperative navigation can either be used as a mean to enhance the positioning performance of all the members of the cooperative formation [5], or can be used to advantage few elements of the formation [7, 12]. The key point of cooperative navigation is the usage of relative measurements as additional source of information to the aim of localization, e.g. range-based, angle-based or vision measurements.

2.7.1 Cooperative Navigation of Clustered Bodies

Missions involving vehicles' formation, usually requires to precisely estimate the inter-distance between the elements of the formation. An accurate estimate of the relative and absolute position of the platform can be accomplished by the mean of cooperative localization. Cooperative localization of clustered bodies it is nowadays a hugely discussed topic in the scientific community, especially for its application in environments where absolute localization systems, e.g. GNSS, are not available, i.e. underwater [77], in indoor environment [78], in the outer-space or GNSS-denied environments [79]. Without a reference absolute location, only the relative distance between the elements can be known, but their absolute position can be updated as soon as one of the elements of the formation receives the signal from an absolute source of positioning [80]. Due to the usage of additional measurements, cooperative navigation demonstrates outperforming the classic navigation solution also in presence of an absolute localization system, and reducing the error drift in the case an absolute solution is not available. Cooperative navigation architectures for clustered bodies can be classified in centralized [5] and decentralized [81, 82]. In centralized architectures each robot communicates its measurements to a leader robot that processes all the data and estimates all the states for the UAVs. On the other hand, in decentralized or multi-centralized [83] networks each UAV estimates its state using neighbouring measurements [84]. Even if centralized approaches have been demonstrated to achieve higher localization accuracy than the decentralized methods [85], they have several weaknesses. Indeed, state estimation requires a higher computational burden and becomes not available if the central processing unit is subject to a fault. A distributed processing was studied in [86] to reduce the computational burden of the leader platform. In addition, centralized approaches require all the UAVs to send simultaneously their data to the leader robot, that is affected to connectivity problems in communication network that could arise when a large distance interposes among the UAVs.

2.7.2 Improving cooperative localization performance of several elements of the swarm

Another, less used approach to cooperative navigation consists in using the relative information to the advantage of few elements of the swarm. The application of this technique follows a decisional process aimed at defining whose element of the formation are more in need of an external aiding. This approach could be in general applied in the case the navigation performance of some elements of the swarm are not compliant to the mission requirements.

An example of this application is the case of navigation in environments with heterogeneous GNSS coverage. In these missions, some members of the formation are demanded to fly in areas with non-nominal GNSS coverage, resulting in an unreliable navigation solution. Using cooperative measurements and the absolute position of the elements with good navigation solution allows the state estimation performance to be compliant with the requirements. Several mission have exploited this approach using as reference platforms for the absolute location mobile [7–9] and/or static platforms [87–89].

Nevertheless, cooperative navigation advantages are not only limited in scenarios where degraded performances are encountered. Indeed, also in the case of homogeneous coverage and navigation performances, it could be needed to improve the performance of only few elements of the formation to the mission advantage. As an example, mapping and reconstruction missions require the UAVs to achieve a pointing accuracy higher than the one that could be obtained with the stand-alone navigation, and cooperation could be a promising strategy to overcome this issue [12].

Chapter 3: Cooperative Navigation in GNSS Challenging Environments

The increasing interest in the usage of UAVs in daily life applications have recently posed the UAV community to new challenges mostly related to integrating the UAVs in urban scenarios. Mission such as mapping, aerial photography, search and rescue, package delivery, inspection could benefit from the usage of the UAV in terms of overall mission time and human effort reduction. Autonomy is the key feature to unleash the UAVs potential, allowing the final user to perform several missions, without having any particular skill.

Precise autonomous navigation is the main requirement for vehicle autonomy. Guidance and control outputs (path tracking and decision making [90]), indeed, are dependent on the position estimation's accuracy. Outdoor UAVs navigation is usually ensured coupling the Inertial Measurement Unit (IMU) with a GNSS receiver and a Magnetometer. Kalman filtering using these sources of information have been widely employed for high altitude flight, demonstrating good performances in positioning estimation.

Nevertheless, the integration of UAVs in urban environment requires them to operate at low altitude, where the GNSS signal is not nominal due to multipath or obstructed signal by the surrounding obstacles, i.e. buildings, hills, bridges, vegetation. In these scenarios, usually referred as GNSS challenging areas, the unreliable GNSS signals prevents the navigation filter to bound the error deriving from successive integrations of inertial sensor measurements, resulting in an unreliable position estimation solution [91, 92].

Due to its fundamental role in enabling a wide variety of services offered by the UAVs in the near future, navigation in GNSS challenging environments has been widely tackled in the open literature. The approaches used to solve this problem are reported in section 3.1.

This chapter presents an innovative solution to cooperate for enhancing navigation in GNSS challenging environments. As discussed in section 2.7, cooperative navigation solution could be used either to the advantage of each element of the formation or to improve navigation performance of a subsets of platforms. The latter approach is accounted for in this framework. It consists in improving the navigation performance of an UAV flying under non-nominal GNSS coverage by using additional measurements provided by cooperative platforms. Further details about the proposed cooperative navigation strategy are given in section 3.2. Hence, the proposed navigation solution, is detailed in section 3.3. Based on the navigation algorithm some conclusion can be drawn concerning the positioning of the cooperative platforms and its effects on the navigation performances. A wide description of this aspect is reported in section 3.4. The obtained results in simulation and with experimental data are reported in section 3.5 and 3.6, respectively.

3.1 RELATED WORKS

The problem of enabling navigation in GNSS challenging environment is usually approached by the UAS community at planning or at navigation level. This section gives a detailed overview of the already existing approaches, divided in the two categories and presented in sections 3.1.1 and 3.1.2.

3.1.1 Planning Level

Several works addressed the problem of navigating in GNSS challenging areas by planning for a trajectory that minimizes the covariance matrix and in general depends on the performance of the sensors on board of the UAV. [13, 14] define an occlusion map, based on Dilution of Precision of the current GNSS constellation. The occlusion map identifies the areas where the UAV is forbidden to fly due to the scarcity of the GPS coverage. Based on the updated obstacle a path planning to route the UAV from one point to another has been developed. In the case the UAV is obliged to pass through a challenging environment, a selection on the received measurement is performed, in order to prevent the usage of those affected by systematic GNSS errors, e.g. multipath [14]. A similar approach was used by [93], that also accounted for the divergency rate of the INS measurement. Indeed, the path planning technique proposed in [93] updates the occlusion map before taking each action. The area that ensure the INS (Inertial Navigation System) divergency to be below a certain threshold after the

UAV passage are excluded from the occlusion region. The problem of routing vehicles in GNSS denied environment, relying on landmark based absolute position has been tackled in [94], by finding a trajectory that minimizes the navigation error. However, navigation-aware planning is not always available, especially in the case when the UAV plan must be defined both to satisfy mission requirement and to be compliant with required navigation performances (RNP).

3.1.2 Navigation Level

Widely exploited in the open literature is the usage of navigation strategy to improve the state estimation performance of a UAV in GNSS challenging environments. References [95–97] developed techniques for detecting and removing multipath affected measurements to improve the navigation performance, based on terrain maps and/or cooperation, whilst [98] controlled the error divergence by adding velocity constraints. Those approaches bound the navigation error by optimizing the available measurements. Nevertheless, satellite removal could lead to a degraded dilution of precision (DOP) or even to the unavailability of positioning information if less than four satellites remain.

Therefore, a common solution to overcome the lack of GNSS satellites is using additional aiding information. Camera aiding has been extensively employed in this framework [11, 99–104]. Whereas, some works enables navigation in GNSS challenging environments by using as additional measurements: positioning based on phone signals [105], opportunistic navigation [106], radio beacon [94, 107], radar [108], laser [109], lidar [110, 111] measurements, or a combination of the aforementioned instruments [112]. [113] supported navigation in GNSS challenging environment using a hall effect sensor to act as flying odometer.

Cooperative navigation [114] represents a promising strategy to improve navigation performance [5, 6]. Different strategies have been proposed in the open literature, which are based on relative range and or angles measurements [5, 8] or on the observations of common ground areas by onboard optical sensors [114–116]. Reference [9] uses a cooperative UGV to simulate an additional satellite to the aim of navigating an UAV under non nominal GNSS coverage. RF ranging measurement is estimated on board the UAV and used along with the precise position of the UGV, shared in the network. Trajectory optimization of the UGV has been discussed in [117]. Conversely, relative angles (i.e. azimuth and elevation), estimated with a camera, are used in [7] to the same purpose. In this case a tandem UAV formation has taken into account. A similar approach is used by [8] to perform canyon mapping. In this case a formation of two UAVs is used. The UAV at low altitude is equipped with high power LEDs, that allow the highest UAV (under nominal GNSS coverage) to estimate its 3D relative position with a camera. Finally, relative range and camera (bearing angles only) measurements are used by [118] for a cooperative swarm of UAVs in GNSS denied environments, demonstrating reduction of error drift due to cooperation. [119] uses the same framework, setting the absolute reference with ground landmarks.

3.2 COOPERATIVE NAVIGATION CONCEPT

The technique described in this chapter defines a generalized approach to UAV cooperation in challenging environment, that can be adapted to different measurements sensors and increasing number of aiding platforms.

Specifically, cooperative navigation is used to enhance the navigation performances of a vehicle, termed “son”, that flies under non nominal GNSS coverage. To this aim, cooperative platforms referred as “fathers” are used. A conceptual scheme is reported in Figure 3.1, where the son is coloured in gray, while the fathers are highlighted in red.

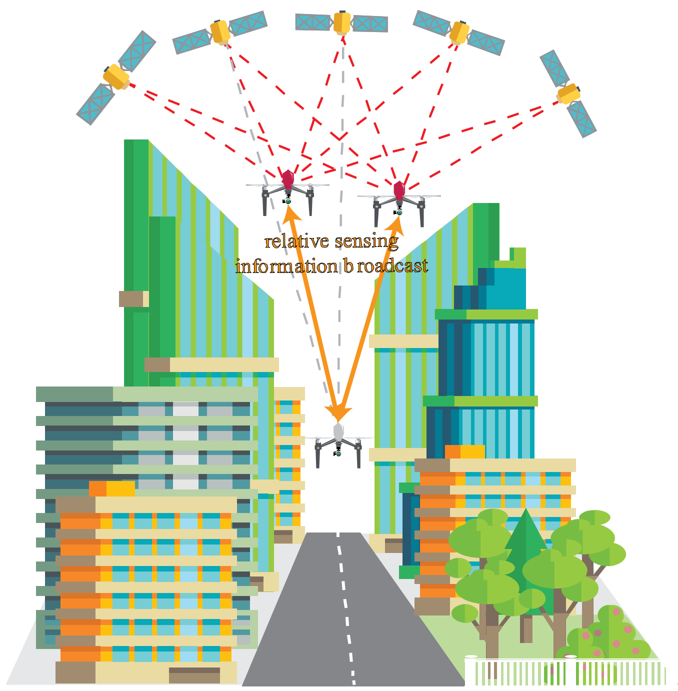

Figure 3.1 Cooperative Navigation Concept. Son vehicle in gray, Father vehicles in red. Signals' raypath are depicted with dashed lines.

Satellites to UAV ray-path are depicted with dashed lines, underlining the poor coverage of the son's UAV in these scenarios. The vehicles are equipped with sensor for estimating relative position measurements, which are used as navigation aid in the son's navigation algorithm. Relative sensing can be carried out exploiting different sensing technologies. Two sensors are taken into account in this research work: a camera for relative angles estimation between a father and the son, and an RF ranging that allows measuring with high accuracy the norm of the distance between the two platforms. Due to the analogy with the GNSS measurements, RF ranging have been extensively used [9] in this framework. On the other hand, camera, commonly embarked on the UAVs, represents a valid alternative to the more expensive RF ranging instrument, due to its low cost very small size, weight and power budget. Indeed, thanks to the very fast and accurate visual tracking algorithms, camera guarantees a very precise estimation of azimuth and elevation of the relative formation. Camera can be installed either on board the son (son-to-father visual tracking) or the father (father-to-son visual tracking).

The aforementioned sensors compose a couple of complementary measurements. Indeed, coupled information of camera and RF ranging allow to retrieve the complete distance information between the two UAVs.

To set an absolute reference for the relative (cooperative) measurement to be used in the son's navigation filter, the absolute position of the father is exploited. Hence, each father should share its positioning estimation to the cooperative navigation network, to let them be used by the son. This assumption poses two requirements for the father to be satisfied:

- The father must be always outside the GNSS challenging area. Indeed, it should be able to estimate very accurately its navigation state (position, velocity and attitude) relying only on non-cooperative measurements, i.e. GNSS, IMU and magnetometer.
- In order to guarantee sharing information among the UAVs among the network, line of sight (LOS) link between the fathers and the son must be maintained during the flight in the challenging area. This allow not only to ensure information broadcast, but it also enable relative sensing to be performed along the entire flight.

3.2.1 GNSS Challenging areas

Father's requirements impose the cooperative platforms to be always outside the challenging area. To guarantee the father to fulfill this requirement, the boundaries of the challenging area must be properly defined and set. As its definition suggests, the challenging area represents a portion of the space where the performance of GNSS measurement system are not nominal. Due to the wide usage of the concept of dilution of precision [120] to measure the performance of the GNSS instruments, it can be used as parameter to set the boundary of the challenging zone. However, in the case of a single constellation receiver a more intuitive and rapid method can discriminate about nominal and non-nominal GNSS coverage. Indeed, in this case the number of satellites in cluttered conditions usually goes below 4, that is the minimum to obtain the GNSS fix. Therefore, in this case a challenging area is defined as a portion of the space where the number of satellites seen by the platform is lower than 4.

3.2.2 Relative Sensing

The most used sensor for cooperative navigation application in GNSS challenging environments are RF ranging and camera that will be integrated in the son's navigation filter described in section 3.2. This section reports the difference in terms of processing, formation geometry and data exchange of the sensors used for relative sensing among the vehicles that are summarized in Table 2.1.

These sensors, even if complementary impose different requirement to the formation geometry. Indeed, camera observation requires the target UAV (father in the son-to-father tracking and son in the father-to-son tracking) to be always in the camera's field of view (FOV). In the case of a gimbaled camera this can be obtained by a tracking algorithm that follows the target motion along the trajectory. Nevertheless, the available relative geometries are limited to the gimbal motion and to the position where the camera is mounted. As an example, in the case the gimbal is below the UAV's main body it is impossible to track an object in the nadir direction. Whereas, when a strapdown camera is used the formation geometry between the target and the UAV that mounts the camera must be limited by the camera's FOV. In addition, camera requires an additional process to extract the needed information (azimuth and elevation) from the raw data. Conversely, the RF ranging does not limit the formation geometries and should be preferred to the camera for its continuous data availability, that are ready to be processed in the filter. Nevertheless, camera provides more information than RF ranging sensor, increasing the observability of the cooperative state.

Among the relative sensors used in this thesis work, the father-to-son visual tracking requires the largest amount of data to be broadcasted in the UAV network. Indeed, in both father-to-son visual tracking and RF sensing, only the father position is needed to set an absolute reference for the relative measurement. Whereas, in the case the camera is mounted on the father, the estimated relative angles must be broadcasted along the father absolute position.

As far as the camera is concerned, choosing between son-to-father and father-to-son visual tracking impacts not only the amount of data to be shared in the network, but also the accuracy of the estimated relative position. Indeed, to use the absolute reference given by the father's absolute position, the relative azimuth and elevation estimated by the camera must be converted using the UAV's rotation matrix. Therefore, the accuracy of the relative position depends on the platform's pointing accuracy and it is expected to be better for the UAV with better coverage, i.e. the father.

Finally, some conclusions can be drawn about the challenges associated to image processing and visual tracking function. It is well known that detect and tracking algorithms' performance depends on the illumination and on the image background. Target detection in cluttered environments or below the horizon could sometimes lead to missed or false detection. Whereas, detecting a target above the horizon has a low percentage of wrong detection. Due to the requirement to be outside the GNSS challenging area, it is reasonable to assume the father to have an altitude greater than the son. Therefore, son-to-father visual tracking should guarantee a higher percentage of correctly estimated azimuth and elevation, that the father-to-son approach. Indeed, the image containing the son is more likely to have a not-uniform cluttered background, that can spoil target detection. On the other hand, father-to-son visual tracking requires a conventional mounted camera that should point downwards and can be used for other applications, beside the cooperative tracking. Whereas, to track the father the son could need a dedicated camera.

Table 3.1 Comparison table of Relative Sensing instruments

Sensor	Processing platform	Number of measurements	Need of Cooperative Father	Data to be shared
RF Ranging	Son	1	Yes	Father positioning
Camera son-to-father	Son	2	No	Father Positioning
Camera father-to-son	Father	2	Yes	Father Positioning and relative azimuth and elevation

Furthermore, it is worth noting that both RF ranging and father-to-son visual tracking requires a cooperative platform that flies with the aim of aiding the son's platform. Whilst, son-to-father visual tracking allows the son to be independent from the cooperative platform. Indeed, it could exploit to the navigation advantage signals of opportunity coming from surrounding platforms, that could become "fathers of opportunity". These platforms don't need any specialized hardware, but they can communicate their position with ADS-B. Those position can be used with the camera's relative measurements as long as the "father of opportunity" is in the camera FOV.

3.3 COOPERATIVE NAVIGATION FILTER

This section describes the navigation filter used for cooperative navigation of the son's platform [121, 122]. A general formulation for the filter is derived. It includes the usage of *k* fathers, and all the sources of relative (cooperative) measurements discussed in the previous section. To this aim a tightly coupled Extended Kalman Filter (EKF) [120], whose scheme is depicted in Figure 3.2, has been designed. Its state vector includes 15 components which represent estimated error on vehicle absolute position **p** (composed by latitude l, longitude λ, and altitude h, in the WGS-84 ellipsoid), velocity **v**, attitude error vector **ρ** computed in local North East Down (NED) reference frame and accelerometer and gyroscope biases **b**.

$$\delta\mathbf{x} = \begin{bmatrix} \delta\mathbf{p} \\ \delta\mathbf{v} \\ \boldsymbol{\rho} \\ \mathbf{b} \end{bmatrix}; \quad \begin{array}{l} \delta\mathbf{p} = \begin{bmatrix} \delta l & \delta\lambda & \delta h \end{bmatrix}^T \\ \delta\mathbf{v} = \begin{bmatrix} \delta v_n & \delta v_e & \delta v_d \end{bmatrix}^T \\ \boldsymbol{\rho} = \begin{bmatrix} \varepsilon_n & \varepsilon_e & \varepsilon_d \end{bmatrix}^T \\ \mathbf{b} = \begin{bmatrix} b_{a,x}^{b_s} & b_{a,y}^{b_s} & b_{a,z}^{b_s} & b_{g,x}^{b_s} & b_{g,y}^{b_s} & b_{g,z}^{b_s} \end{bmatrix}^T \end{array} \tag{3.1}$$

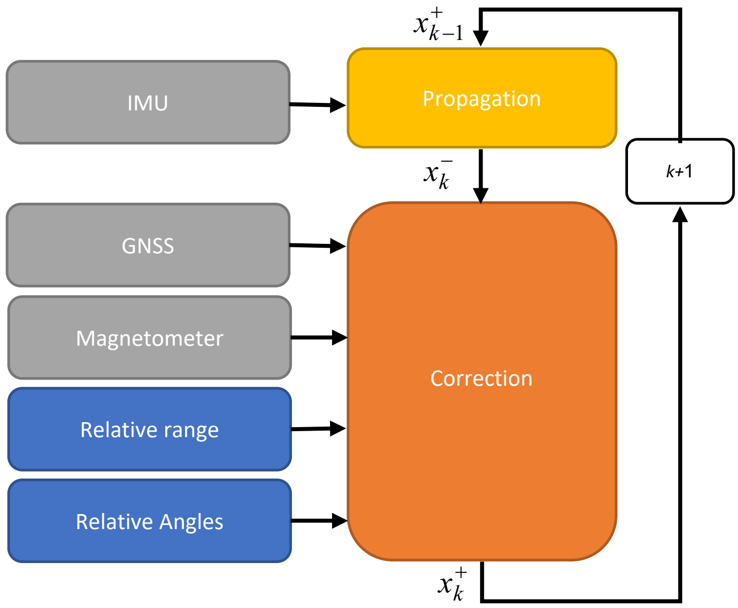

Figure 3.2 EKF architecture. The input, i.e. sensor measurements can be classified as cooperative (blue) and single-vehicle-based (gray).

The subscript n, e or d indicates one of the three axes of the NED frame. Whereas $b_{a,i}^{b_s}$ and $b_{g,i}^{b_s}$ indicates the accelerometer (a) and gyroscope (g) biases along the i-th axis of the son's body reference frame (BRF), respectively. The son's BRF is highlighted with the superscript b_s.

Filter's input measurement can be divided in two classes, i.e. cooperative (highlighted in blue in Figure 3.2) and non-cooperative (in gray). GNSS measurements are the pseudoranges of the satellites in view of the receiver, whereas the magnetometer outputs are the three components of the Earth's magnetic field. When under non-nominal GNSS coverage at least one cooperative measurement is needed to prevent filter divergence. The cooperative measurements depend on the sensor embarked on the UAVs, they can be distinguished in range distance, measured by RF ranging and angular distance measured by camera. However, as remarked before, due to its relative nature, the cooperative measurement is not able to correctly upgrade the absolute position of the son and must be complemented with the position of father in NED $\mathbf{x}_f^n$, that must be broadcasted with its covariance to the cooperative network.

Relative range represents the norm of the father-son distance. As far as the camera is concerned, in the case of son-to-father tracking camera measurements (referred as relative angles in Figure 3.2) represent the azimuth and the elevation of the father in the son's camera frame (CRF). Conversely, when the camera is mounted on the father, the measured azimuth and elevation in father's CRF are transformed in NED, with the accurate estimate of father's attitude, and then broadcasted to the cooperative network. This choice is made to reduce the computational burden on board the son's UAV and make the father position the only information that must be shared to convert the relative estimates in absolute position, velocity and attitude.

The filter state propagation occurs thanks to the classic INS mechanization equations [120], augmented with accelerometer and gyroscope bias estimation [123]. The filter's measurement vector is composed by measured residuals, estimated as the difference between the measured value and the predicted ones, and is:

$$\delta\mathbf{y} = \begin{bmatrix} \delta\mathbf{y}_{GNSS} \\ \hline \delta\mathbf{y}_{M} \\ \hline \delta\mathbf{y}_1 \\ \vdots \\ \delta\mathbf{y}_k \end{bmatrix} = \begin{bmatrix} \delta P_1 - \delta P_{m+1} \\ \vdots \\ \delta P_m - \delta P_{m+1} \\ \hline \varepsilon_{d,mag} \\ \hline \delta\mathbf{y}_1 \\ \vdots \\ \delta\mathbf{y}_k \end{bmatrix} \tag{3.2}$$

The magnetometer measurements are transformed in heading residuals $\delta\mathbf{y}_M$, thanks to the roll and pitch estimates, whose error can be reasonably assumed to be bounded. Whereas, $\delta\mathbf{y}_{GNSS}$, are the GNSS pseudorange residuals. In order to avoid including the receiver clock bias and the inter-constellation biases in the state estimation vector, GNSS residuals are obtained by using pivot satellites as detailed in section 3.3.1.1.

The residual vector of the cooperative measurements connected with the *j*-th father, i.e. $\delta\mathbf{y}_j$, in general includes RF residuals $\delta\mathbf{y}_{j,RF}$, son-to-father camera residuals $\delta\mathbf{y}_{j,EO}^{s\to f}$ and father-to-son camera residuals $\delta\mathbf{y}_{j,EO}^{f\to s}$.

$$\delta\mathbf{y}_{j,RF} = \delta r_j$$
$$\delta\mathbf{y}_j = \begin{bmatrix} \delta\mathbf{y}_{j,RF} \\ \delta\mathbf{y}_{j,EO}^{s\to f} \\ \delta\mathbf{y}_{j,EO}^{f\to s} \end{bmatrix}; \quad \delta\mathbf{y}_{j,EO}^{s\to f} = \begin{bmatrix} \delta Az_{s\to f_j}^{c_s} \\ \delta El_{s\to f_j}^{c_s} \end{bmatrix} \tag{3.3}$$
$$\delta\mathbf{y}_{j,EO}^{f\to s} = \begin{bmatrix} \delta Az_{f_j\to s}^{n} \\ \delta El_{f_j\to s}^{n} \end{bmatrix}$$

where $\delta\mathbf{y}_{j,RF} = r_j$ is the norm of the distance between the son and the j-th father. Whereas the camera measurement is composed by azimuth Az and elevation El. The apices c_s and n indicate respectively the son CRF and the NED frame where the azimuth and elevation are defined depending on which platform embarks the camera.

3.3.1 Measurement equations

In general, the linearized form of a measurement equation can be written as $\delta\mathbf{y}_h = H_h\delta\mathbf{x} + \mathbf{w}_h$. Where h indicates the generic sensor and $\mathbf{w}_h$ the noise associated to its measurement error, with covariance R_h. This section aims at defining H_h and R_h for each measurement source. Section from 3.3.1.1 to 3.3.1.4 derive the terms of measurement equation for each source of information. As far as R_h is concerned, one can observe that only for uncorrelated measurements, R_h can be defined accounting only for the current information and neglecting the others. Nevertheless, all the cooperative measurements depend on the father position, thus correlation among them exists. Section 3.3.1.5 derives the covariance of the cooperative measurement. Hence the covariance of the uncorrelated measurement, i.e. GNSS and Magnetometer are reported in the section where their measurement matrix are derived, i.e. 3.3.1.1 and 3.3.1.2, respectively.

3.3.1.1 GNSS

Derivation of GNSS measurement and covariance matrix has been widely discussed in the open literature for single and multi-constellation receiver. When dealing with multi-constellation satellites, an inter-constellation bias exist that must be compensated for. Inter-constellation biases are modelled as first order polynomial [124], whose daily coefficients are reported in the multi constellation broadcast ephemeris products, i.e. the brdm files [125], available at ftp://cddis.gsfc.nasa.gov/pub/gps/data/campaign/mgex/daily/rinex3/yyyy/brdm. The diversity between constellation biases affects the goodness of the GNSS fix. However, this term is constant for each constellation and is commonly grouped with the receiver clock bias. Therefore, the receiver delay for the satellite belonging to the g-th constellation can be written as [126]

$$\Delta t_g = \Delta t_r + T_g \tag{3.4}$$

where Δt_r is the receiver clock error and T_g is the time correction of the g-th GNSS system. $g = 1,\ldots,n_g$, with n_g indicating the number of constellation that the receiver observes. For each constellation couple (g-l) the receiver interconstellation bias is $\Delta t_{gl} = T_g - T_l$ For correctly solve the GPS pseudorange equation one must estimate with enough accuracy each Δt_g. Postprocessing application comes with the advantage of having already estimated coefficients to determine Δt_{gl}. Conversely, real time application requires to estimate those terms within a Kalman filter. Following the approach reported in [120] for the single constellation receiver, the model presented in this thesis uses pivot satellites for cancelling out every Δt_g. Therefore, a pivot satellite is chosen for each constellation and the measurement equations for the i-th pseudorange residual, i.e. $\delta\Delta P_i = \delta P_i - \delta P_{m_g}$, is:

$$\delta\Delta P_i = \frac{\partial \Delta P_i}{\partial \mathbf{x}_s^e} C_n^e G \delta\mathbf{p} \tag{3.5}$$

Where i = 1,…,m_g-1, and m_g is the number of the satellites available in each constellation. It is intuitive that m_g must be at least two in order to contribute at the pseudorange estimation, indeed the first measurements of each constellation is used to correct the receiver bias. $\mathbf{x}_s^e$ is the son's position of the UAV in the Earth Centered Earth fixed (ECEF) and C_a^b is the rotation matrix from the frame a to the frame b. In the specific case identified in equation (3.5), C_n^e identifies the rotation matrix from NED to ECEF frame. G is the matrix, that converts the local frame's error in geographic coordinates, that can be derived accounting for the concept of meridian and normal radii of curvature, i.e. R_M and R_N, respectively.

$$G = \begin{bmatrix} R_M + h & 0 & 0 \\ 0 & \cos l\left(R_N + h\right) & 0 \\ 0 & 0 & -1 \end{bmatrix} \tag{3.6}$$

$\frac{\partial \Delta P_i}{\partial \mathbf{x}_s^e}$ defines the derivative of the pseudorange residual with respect to the ECEF position of the son. It is a 1×3 matrix equal to

$$\frac{\partial \Delta P_i}{\partial \mathbf{x}_s^e} = \frac{\mathbf{x}_s^e - \mathbf{x}_i^e}{\left|\mathbf{x}_s^e - \mathbf{x}_i^e\right|} - \frac{\mathbf{x}_s^e - \mathbf{x}_{m_g}^e}{\left|\mathbf{x}_s^e - \mathbf{x}_{m_g}^e\right|} \tag{3.7}$$

where $\mathbf{x}_i^e$ is the ECEF position of the i-th GNSS satellite, and $|\ |$ indicates the operator that gives the norm of the vector.

Equation (3.5) remarks GNSS pseudorange measurements depend only on the position part of the state vector. Therefore, the matrix associating pseudorange residuals to $\delta\mathbf{p}$ is:

$$H_{GNSS\mathbf{p}} = \begin{bmatrix} H_{1\mathbf{p}} \\ \vdots \\ H_{n_g\mathbf{p}} \end{bmatrix} C_n^e G; H_g = \begin{bmatrix} \dfrac{\partial \Delta P_1}{\partial \mathbf{x}_s^e} \\ \vdots \\ \dfrac{\partial \Delta P_{m_g-1}}{\partial \mathbf{x}_s^e} \end{bmatrix} \tag{3.8}$$

$H_{GNSS\mathbf{p}}$ is a m×3 matrix, with $m = \sum_g m_g - n_g$. Indeed, due to the need for a pivot the number of measurements that effectively concur to the position estimation is equal to the number of the total satellites in view minus the number of used pivot satellites, that is equal to the number of GNSS constellation. The covariance matrix of the GNSS measurement is derived from the standard deviation (STD) of the pseudorange, i.e. σ_{Pr}, through the following relation:

$$R_{GNSS} = \left(\mathbf{I}_m + \begin{bmatrix} \mathbf{1}_{m_1-1} & 0 & 0 \\ 0 & \ddots & 0 \\ 0 & 0 & \mathbf{1}_{m_{n_g}-1} \end{bmatrix} \right) \sigma_{Pr}^2 \tag{3.9}$$

where $\mathbf{1}_a$ is a a×a matrix, whose elements are all set to one. Whilst $\mathbf{I}_a$ is an a×a identity matrix.

3.3.1.2 Magnetometer

As specified by equation in (3.2), the magnetometer residual represents a heading angle error. Therefore, the magnetometer measurement is coupled only with the attitude part of the state vector and is:

$$H_{M\mathbf{p}} = \begin{bmatrix} 0 & 0 & 1 \end{bmatrix} \tag{3.10}$$

The covariance matrix is a scalar identified by the square of the magnetometer heading angle STD, i.e. $R_M = \sigma_{\psi_M}^2$.

3.3.1.3 Camera

This section is in charge of deriving the measurement equation of the visual tracking algorithm in both son-to-father and father-to-son case. Before detailing the measurements equation used in the filter in sections 3.3.1.3.2 and 3.3.1.3.3, section 3.3.1.3.1 reports the line of sight measurement equation, that will be used for converting the estimated relative azimuth and elevation in relative positioning.

3.3.1.3.1 Line of sight measurements

The azimuth Az and elevation El of a vector $\mathbf{r}$ are defined to be

$$\begin{aligned} Az &= \tan^{-1}\left(\frac{r_x}{r_y}\right) \\ El &= -\sin^{-1}\left(\frac{r_z}{|\mathbf{r}|}\right) \end{aligned} \tag{3.11}$$

where the subscripts x,y and z highlight the three components of the vector. Inverting the relation in equation (3.11), and deriving with respect to $\mathbf{r}$, yields:

$$\begin{aligned} \frac{\partial Az}{\partial \mathbf{r}} &= \begin{bmatrix} -\frac{r_y}{r_x^2+r_y^2} & \frac{r_x}{r_x^2+r_y^2} & 0 \end{bmatrix} \\ \frac{\partial El}{\partial \mathbf{r}} &= \begin{bmatrix} \frac{r_x r_z}{|\mathbf{r}|\sqrt{r_x^2+r_y^2}} & \frac{r_y r_z}{|\mathbf{r}|\sqrt{r_x^2+r_y^2}} & -\frac{r_x^2+r_y^2}{|\mathbf{r}|\sqrt{r_x^2+r_y^2}} \end{bmatrix} \end{aligned} \tag{3.12}$$

3.3.1.3.2 Son-to-father

The two measurements residuals of the camera for the j-th father, i.e. azimuth and elevation, can be estimated in function of the distance between the j-th father's center of mass (CoM) and the origin of son's CRF. This distance, termed $\mathbf{r}_{s\to f_j}$, is:

$$\mathbf{r}_{s\to f_j} = \mathbf{x}_{f_j} - \mathbf{x}_s - \mathbf{r}_{c,s} \tag{3.13}$$

Where $\mathbf{x}_{fi}$ and $\mathbf{x}_s$ are the j-th father's and son's CoM, whilst $\mathbf{r}_{c,s}$ is the distance from son's CoM to the origin of its CRF. The error on a generic vector estimated in ECEF frame can be converted in the error in NED frame with:

$$\delta\mathbf{r}^n = C_e^n \delta\mathbf{r}^e - \delta C_e^n \mathbf{r}^e \tag{3.14}$$

where C_a^b is the rotation matrix from the frame a to the frame b, and n and e the apices indicating respectively NED and ECEF frames. Remembering that the NED coordinates of a point $\mathbf{x}^n$ are related to its ECEF coordinates $\mathbf{x}^e$ thanks to the ECEF location of the NED frame $\mathbf{x}_o^e$, i.e. $\mathbf{x}^n = C_e^n\left(\mathbf{x}^e - \mathbf{x}_o^e\right)$, eq. (3.13) can be substituted in eq. (3.14), yielding

$$\delta\mathbf{r}_{s\to f_j}^n = \delta\mathbf{x}_{f_j}^n - C_e^n\delta\mathbf{x}_s^e - \delta\mathbf{r}_{c,s}^n - \delta C_e^n\left(\mathbf{x}_o^e - \mathbf{x}_s^e\right) \tag{3.15}$$

δC_e^n is the error in estimating the rotation from ECEF to NED which is zero, being fixed the origin of the local NED frame, that is common for both the UAV. Hence, equation (3.15) becomes:

$$\delta\mathbf{r}_{s\to f_j}^n = \delta\mathbf{x}_{f_j}^n - C_e^n\delta\mathbf{x}_s^e - \delta\mathbf{r}_{c,s}^n \tag{3.16}$$

In analogy with equation (3.14), the error of a vector in NED frame can be estimated as a function of the error of the same vector in the BRF:

$$\delta\mathbf{r}^n = C_{b_s}^n\delta\mathbf{r}^{b_s} - \left[C_{b_s}^n\mathbf{r}^{b_s}\times\right]\boldsymbol{\rho} \tag{3.17}$$

where the apex b_s is used for the son's BRF and $\boldsymbol{\rho}$ is the angular error in son's state estimation. Whereas $[\mathbf{w}\times]$ is the skew symmetric matrix of the 3×1 vector **w**.

Being known the position of the camera origin in son's BRF, $\delta\mathbf{r}_{c,s}^n = -\left[C_{b_s}^n\mathbf{r}_{c,s}^{b_s}\times\right]\boldsymbol{\rho}$, and equation (3.16) becomes:

$$\delta\mathbf{r}_{s\to f_j}^n = \delta\mathbf{x}_{f_j}^n - C_e^n\delta\mathbf{x}_s^e + \left[C_{b_s}^n\mathbf{r}_{c,s}^{b_s}\times\right]\boldsymbol{\rho} \tag{3.18}$$

The position error of the son in ECEF frame $\delta\mathbf{x}_s^e$ can be expressed in function of the position error $\delta\mathbf{p}$, hence eq. (3.18) becomes:

$$\delta\mathbf{r}_{s\to f_j}^n = \delta\mathbf{x}_{f_j}^n - C_e^n\frac{\partial\mathbf{x}_s^e}{\partial\mathbf{p}}\delta\mathbf{p} + \left[C_{b_s}^n\mathbf{r}_{c,s}^{b_s}\times\right]\boldsymbol{\rho} \tag{3.19}$$

Transforming this expression in son CRF and converting the distance in angular measurements, thanks to equation (3.12), the measurement residual equation of the camera, when mounted on the son is:

$$\begin{aligned}\delta\xi_j = &-\frac{\partial\xi_j}{\partial\mathbf{r}_{s\to f_j}^{c_s}}C_{b_s}^{c_s}C_n^{b_s}C_e^n\frac{\partial\mathbf{x}_s^e}{\partial\mathbf{p}}\delta\mathbf{p} + \frac{\partial\xi_j}{\partial\mathbf{r}_{s\to f_j}^{c_s}}C_{b_s}^{c_s}C_n^{b_s}\left[\left(\mathbf{x}_f^n - \mathbf{x}_s^n\right)\times\right]\boldsymbol{\rho} + \\ &+\frac{\partial\xi_j}{\partial\mathbf{r}_{s\to f_j}^{c_s}}C_{b_s}^{c_s}C_n^{b_s}\delta\mathbf{x}_f^n + \delta_{cam}\end{aligned} \tag{3.20}$$

where ξ_j can be alternatively $El^{c_s}_{s\to f_j}$ or $Az^{c_s}_{s\to f_j}$ and δ_{cam} is the error of the camera in correctly detecting the father's location that has a standard deviation (STD) σ_{cam} equal to the dimension of the pixel (IFOV). The measurement matrix associated with the son-to-father measurement can be derived from eq. (3.20) and is:

$$H_{s\to f_j} = \begin{bmatrix} \dfrac{\partial Az^{c_s}_{s\to f_j}}{\partial \mathbf{p}} & 0_{1\times3} & \dfrac{\partial Az^{c_s}_{s\to f_j}}{\partial \boldsymbol{\rho}} & 0_{1\times6} \\ \underbrace{\dfrac{\partial El^{c_s}_{s\to f_j}}{\partial \mathbf{p}}}_{H^{s\to f}_{j,EO\mathbf{p}}} & 0_{1\times3} & \underbrace{\dfrac{\partial El^{c_s}_{s\to f_j}}{\partial \boldsymbol{\rho}}}_{H^{s\to f}_{j,EO\boldsymbol{\rho}}} & 0_{1\times6} \end{bmatrix} \tag{3.21}$$

where $0_{a\times b}$ is matrix of size $a\times b$, containing all zero elements, and

$$\begin{aligned} \frac{\delta\xi_j}{\partial \mathbf{p}} &= -\frac{\partial \xi_j}{\partial \mathbf{r}^{c_s}_{s\to f}} C^{c_s}_{b_s} C^{b_s}_n C^n_e \frac{\partial \mathbf{x}^e_s}{\partial \mathbf{p}} \\ \frac{\delta\xi_j}{\partial \boldsymbol{\rho}} &= \frac{\partial \xi_j}{\partial \mathbf{r}^{c_s}_{s\to f}} C^{c_s}_{b_s} C^{b_s}_n \left[\left(\mathbf{x}^n_f - \mathbf{x}^n_s\right)\times\right] \end{aligned} \tag{3.22}$$

The two terms not dependent from the state vector in δ**x** equation (3.20) are included in the measurement noise, that is:

$$\begin{aligned} \delta\tilde{\mathbf{y}}^{s\to f}_{j,EO} &= \frac{\partial \tilde{\mathbf{y}}^{s\to f}_{j,EO}}{\partial \mathbf{x}^n_{f_j}} \delta\mathbf{x}^n_f + \delta_{cam} \\ \frac{\partial \tilde{\mathbf{y}}^{s\to f}_{j,EO}}{\partial \mathbf{x}^n_{f_j}} &= \begin{bmatrix} \dfrac{\partial Az^{c_s}_{s\to f_j}}{\partial \mathbf{r}^{c_s}_{c_s\to f_j}} C^{c_s}_{b_s} C^{b_s}_n \\ \dfrac{\partial El^{c_s}_{s\to f_j}}{\partial \mathbf{r}^{c_s}_{c_s\to f_j}} C^{c_s}_{b_s} C^{b_s}_n \end{bmatrix} \end{aligned} \tag{3.23}$$

3.3.1.3.3 Father-to-son

The measurement equation for the camera when mounted on the father is derived in analogy with the previous section. The j-th father's camera measures the Azimuth and the Elevation in the father's camera frame, i.e. c_{fi}. To reduce the amount of information to be shared in the cooperative network the camera measurements are converted in Azimuth and Elevation in the NED frame thanks to the following formula

$$\mathbf{u}^n_{f_j\to s} = C^n_{b_{f_j}} C^{b_{f_j}}_{c_{f_j}} \begin{bmatrix} \cos El^{c_{f_j}}_{f_j\to s} \cos Az^{c_{f_j}}_{f_j\to s} \\ \cos El^{c_{f_j}}_{f_j\to s} \sin Az^{c_{f_j}}_{f_j\to s} \\ -\sin El^{c_{f_j}}_{f_j\to s} \end{bmatrix} \tag{3.24}$$

where $Az^n_{f_j\to s} = \mathrm{atan}\left(\mathbf{u}^{n,2}_{f_j\to s} \big/ \mathbf{u}^{n,1}_{f_j\to s}\right); El^n_{f_j\to s} = -\,\mathrm{asin}\left(\mathbf{u}^{n,3}_{f_j\to s}\right)$. $\mathbf{u}^n_{f_j\to s}$ is the unit vector originated at father's camera that points towards the son CoM, whose *l*-th component is $\mathbf{u}^{n,l}_{f_j\to s}$. Whereas, b_{fi} indicates the father BRF. It could be noticed that, if camera measurements were broadcasted by the father in CRF, the son would need the instantaneous attitude (or the corresponding rotation matrix) of the father to process them, increasing the amount of data to be shared among the cooperative network.

The error equation associated to eq. (3.24), allows converting the error of the camera measurement in CRF, i.e. δ_{cam}, in NED.

$$\Delta\chi^n_j = \frac{\partial \chi^n_j}{\partial \mathbf{u}^n_{f_j\to s}} C^n_{c_{f_j}} \frac{\partial \mathbf{u}^{c_{f_j}}_{f_j\to s}}{\partial \chi^{c_{f_j}}} \delta_{cam} - \frac{\partial \chi^n_j}{\partial \mathbf{u}^n_{f_j\to s}} \left[\mathbf{u}^n_{f_j\to s}\times\right] \boldsymbol{\rho}_{f_j} \tag{3.25}$$

where χ^n_j can be either $Az^n_{f_j\to s}$ or $El^n_{f_j\to s}$. $\boldsymbol{\rho}_{f_j}$ indicates the attitude error of the father.

In analogy with eq. (3.19), one can find an equation that connects the error on the distance between son CoM and father's camera, i.e. $\delta\mathbf{r}_{f_j\to s}$ to $\delta\mathbf{p}$:

$$\delta\mathbf{r}^n_{f_j\to s} = C^n_e \frac{\partial \mathbf{x}^e_s}{\partial \mathbf{p}} \delta\mathbf{p} - \delta\mathbf{x}^n_{f_j} \tag{3.26}$$

where $\mathbf{r}^{b_{f_j}}_{c,f_j}$ is the position of the father camera in father's BRF. Therefore, using equation (3.12) the measurement residual equation is:

$$\delta\chi^n_j = \frac{\partial \chi^n_j}{\partial \mathbf{r}^n_{f_j\to s}} C^n_e \frac{\partial \mathbf{x}^e_s}{\partial \mathbf{p}} \delta\mathbf{p} - \frac{\partial \chi^n_j}{\partial \mathbf{r}^n_{f_j\to s}} \delta\mathbf{x}^n_f + \Delta\chi^n_j \tag{3.27}$$

Only the first term of equation (3.27) it is included in the measurement matrix of the father-to-son visual tracking, $H_{f_j\to s}$, whereas all the other terms depending on the father position contribute to the covariance of the measurement shared by the father that is $R_{f_j \to s}$. Therefore:

$$H_{f_j \to s} = \begin{bmatrix} \underbrace{\begin{matrix} \dfrac{\partial Az^n_{f_j \to s}}{\partial \mathbf{p}} \\ \dfrac{\partial El^n_{f_j \to s}}{\partial \mathbf{p}} \end{matrix}}_{H^{f \to s}_{j,EO\mathbf{p}}} & \begin{matrix} 0_{1\times3} & 0_{1\times3} & 0_{1\times6} \\ 0_{1\times3} & 0_{1\times3} & 0_{1\times6} \end{matrix} \end{bmatrix} \tag{3.28}$$

As mentioned before, when dealing with relative measurements collected by a camera, on must account in the measurement matrix for the attitude of the body where the camera is mounted. In the father-to-son visual tracking, as expected the measurement equation is independent on the son attitude. Indeed, in contrast to (3.21), the measurement matrix reported in equation (3.28) does not present a coupling effect with the son attitude error, i.e. $\boldsymbol{\rho}$. The dependence from the father's attitude appears in the error the angular measurement within $\Delta\chi^n$ that is:

$$\begin{gathered} \delta\tilde{\mathbf{y}}^{f \to s}_{j,EO} = \frac{\partial \tilde{\mathbf{y}}^{f \to s}_{j,EO}}{\partial \mathbf{x}^n_{f_j}} \delta\mathbf{x}^n_f + \Delta\chi^n \\ \frac{\partial \tilde{\mathbf{y}}^{f \to s}_{j,EO}}{\partial \mathbf{x}^n_{f_j}} = \begin{bmatrix} -\dfrac{\partial Az^n_{f_j \to s}}{\partial \mathbf{r}^n_{f_j \to s}} \\ -\dfrac{\partial El^n_{f_j \to s}}{\partial \mathbf{r}^n_{f_j \to s}} \end{bmatrix} \end{gathered} \tag{3.29}$$

3.3.1.4 RF Ranging

The ranging measurement instrument is aimed at estimating the norm of the distance between the son and the supporting fathers. The measurement matrix for the *j*-th father H_{r_j} is a 1×15 matrix, and its associated covariance R_{r_j} is a scalar. Measurement equation and covariance are

$$\delta r_j = -\frac{\partial r_j}{\partial \mathbf{x}^e_s} \left(C^n_e\right)^T \frac{\partial \mathbf{x}^n_s}{\partial \mathbf{p}} \delta\mathbf{p} + \frac{\partial r_j}{\partial \mathbf{x}^n_{f_j}} \delta\mathbf{x}^n_{f_j} + \delta_{RF} \tag{3.30}$$

where δ_{RF} is the error of the RF ranging measurement. The terms not dependent on the state vector are lumped in the error on the residual that is:

$$\delta \tilde{\mathbf{y}}_{j,RF} = \frac{\partial \tilde{\mathbf{y}}_{j,RF}}{\partial \mathbf{x}^n_{f_j}} \delta \mathbf{x}^n_{f_j} + \delta_{RF}$$
$$\tilde{\mathbf{y}}_{j,RF} = r_j \tag{3.31}$$

The measurement matrix is:

$$H_{r_j} = \begin{bmatrix} \underbrace{\dfrac{\partial r_j}{\partial \mathbf{p}}}_{H_{j,R\mathbf{p}}} & 0_{1\times 3} & 0_{1\times 3} & 0_{1\times 6} \end{bmatrix}$$
$$\frac{\partial r_j}{\partial \mathbf{p}} = -\frac{\partial r_j}{\partial \mathbf{x}^e_s} \left(C^n_e \right)^T \frac{\partial \mathbf{x}^n_s}{\partial \mathbf{p}} \tag{3.32}$$

As regards ranging measurements, again they are independent from son attitude, therefore its contribution improves the position observability of the son's navigation filter without a coupling effect with the attitude.

3.3.1.5 Covariance of the Cooperative Measurements

Sections 3.3.1.3 and 3.3.1.4 shows correlation among the cooperative measurement, due to the dependence on the father position. This section is in charge of deriving the cooperative covariance matrix of the j-th father, i.e. R_{cj}. The residual error reported in equations (3.23), (3.29) and (3.31) can be lumped together in a 5×1 vector that is:

$$\delta \tilde{\mathbf{y}}_j = \begin{bmatrix} \delta \tilde{\mathbf{y}}_{j,RF} \\ \delta \tilde{\mathbf{y}}^{s\to f}_{j,EO} \\ \delta \tilde{\mathbf{y}}^{f\to s}_{j,EO} \end{bmatrix} = \begin{bmatrix} 0 \\ \hline 1_{2\times 1} \\ \hline 0_{2\times 1} \end{bmatrix} \delta_{cam} + \begin{bmatrix} 0 \\ \hline 0_{2\times 1} \\ \hline Az^n_{f_j\to s} \\ El^n_{f_j\to s} \end{bmatrix} + \begin{bmatrix} 1 \\ \hline 0_{2\times 1} \\ \hline 0_{2\times 1} \end{bmatrix} \delta_{RF} + \begin{bmatrix} \dfrac{\partial \mathbf{y}_{j,RF}}{\partial \mathbf{x}^n_{f_j}} \\ \dfrac{\delta \mathbf{y}^{s\to f}_{j,EO}}{\partial \mathbf{x}^n_{f_j}} \\ \dfrac{\partial \mathbf{y}^{f\to s}_{j,EO}}{\partial \mathbf{x}^n_{f_j}} \end{bmatrix} \delta \mathbf{x}^n_{f_j} \tag{3.33}$$

Hence, the error of the cooperative measurement is cross correlated only by the father's position error dependence. The covariance matrix associated to the cooperative measurements residuals is:

$$
R_{cj} = \left[\begin{array}{c|cc|cc}
\sigma_{RF}^2 & 0 & 0 & 0 & 0 \\
\hline
0 & \sigma_{cam}^2 & 0 & 0 & 0 \\
0 & 0 & \sigma_{cam}^2 & 0 & 0 \\
\hline
0 & 0 & 0 & \sigma_{\Delta Az^n_{f_j \to s}}^2 & 0 \\
0 & 0 & 0 & 0 & \sigma_{\Delta El^n_{f_j \to s}}^2
\end{array}\right] +
$$

$$
+ \begin{bmatrix} \dfrac{\partial \mathbf{y}_{j,RF}}{\partial \mathbf{x}^n_{f_j}} \\ \dfrac{\delta \mathbf{y}^{s\to f}_{j,EO}}{\partial \mathbf{x}^n_{f_j}} \\ \dfrac{\partial \mathbf{y}^{f\to s}_{j,EO}}{\partial \mathbf{x}^n_{f_j}} \end{bmatrix}
\begin{bmatrix} \left(\sigma^n_{f_j,1}\right)^2 & 0 & 0 \\ 0 & \left(\sigma^n_{f_j,2}\right)^2 & 0 \\ 0 & 0 & \left(\sigma^n_{f_j,3}\right)^2 \end{bmatrix}
\begin{bmatrix} \dfrac{\partial \mathbf{y}_{j,RF}}{\partial \mathbf{x}^n_{f_j}} \\ \dfrac{\delta \mathbf{y}^{s\to f}_{j,EO}}{\partial \mathbf{x}^n_{f_j}} \\ \dfrac{\partial \mathbf{y}^{f\to s}_{j,EO}}{\partial \mathbf{x}^n_{f_j}} \end{bmatrix}^T \tag{3.34}
$$

where σ_{cam} and σ_{RF} are respectively the STD on the son's camera and on the RF ranging measurements. $\sigma_{\Delta Az^n_{f_j \to s}}$ and $\sigma_{\Delta El^n_{f_j \to s}}$ are the standard deviation of the azimuth and elevation measured by the father camera in NED, which can be found applying the definition in equation (3.25). $\sigma^n_{f_j,l}$ is the l-th component of the father position STD in NED reference frame. Equation (3.34) demonstrates, the covariance matrix of the cooperative measurement is a block diagonal matrix except for the part that depends on father position that cross-correlates the measurements.

3.3.2 Measurement and Covariance matrix

This section, based on discussion of 3.3.1, reports the numerical formulation of the measurement and covariance matrix associated to the filter correction step. The measurement matrix H is

$$
H = \left[\begin{array}{cccc}
H_{GNSS\mathbf{p}} & 0_{m\times 3} & 0_{m\times 3} & 0_{m\times 6} \\
\hline
0_{1\times 3} & 0_{1\times 3} & H_{M\boldsymbol{\rho}} & 0_{1\times 6} \\
\hline
\multicolumn{4}{c}{H_1} \\
\multicolumn{4}{c}{\vdots} \\
\multicolumn{4}{c}{H_k}
\end{array}\right] \tag{3.35}
$$

where $H_{GNSS\mathbf{p}}$ and $H_{M\boldsymbol{\rho}}$ are derived in sections 3.3.1.2 and 3.3.1.3, respectively. The cooperative measurement matrix for the j-th father, i.e. H_j is

$$H_j = \begin{bmatrix} H_{j,RF\mathbf{p}} & 0_{1\times3} & 0_{1\times3} & 0_{1\times6} \\ H_{j,EO\mathbf{p}}^{s\to f} & 0_{2\times3} & H_{j,EO\mathbf{\rho}}^{s\to f} & 0_{2\times6} \\ H_{j,EO\mathbf{p}}^{f\to s} & 0_{2\times3} & 0_{2\times3} & 0_{2\times6} \end{bmatrix} \tag{3.36}$$

Equation (3.36) highlights the dependency of the measurement on son's attitude only in the case the camera is mounted on the son. In the other cases, i.e. father-to-son visual tracking and RF ranging, the aiding measurements contributes only to the positioning part. The components of H_j can be retrieved from equations (3.20), (3.28) and (3.32).

The covariance of the cooperative measurements for the j-th father, i.e. R_{cj}, is a 5×5 matrix, reported in equation (3.34). Using the covariance of the j-th father, one can derive the expression for the covariance matrix of the EKF, that accounts also for R_{GNSS} and R_M and is:

$$R = \begin{bmatrix} R_{GNSS} & 0_{m\times1} & 0_{m\times5} & \cdots & 0_{1\times5} \\ 0_{1\times m} & \sigma_{\psi_M}^2 & 0_{1\times5} & \cdots & 0_{1\times5} \\ 0_{5\times m} & 0_{5\times1} & R_{c1} & \cdots & 0_{5\times5} \\ \vdots & \vdots & \vdots & \ddots & \vdots \\ 0_{5\times m} & 0_{5\times1} & 0_{5\times5} & \cdots & R_{ck} \end{bmatrix} \tag{3.37}$$

3.4 COOPERATIVE NAVIGATION ACCURACY

The concept of Dilution of Precision (DOP) [120] is commonly adopted when analyzing accuracy in GNSS-based positioning. Even if the Geometric Dilution of Precision (GDOP) is usually employed in the stand-alone GNSS applications, this mathematical instrument could be used also in integrated framework, e.g. a Kalman filter using GNSS and IMU measurements, to set an upper bound for the expected navigation performance. With this approach, the performance of the navigation filter can be foreseen accounting for its measurement matrix. In general, this discussion can be extended to any source of measurement, whatever the measurement matrix is. To this aim [121] introduced the concept of Generalized dilution of precision, which can be used to estimate the expected positioning uncertainty in a cooperative scenario. The concept derives from applying the approach used for GNSS DOP definition, to the mathematical structure of cooperative navigation measurements. This section is aimed at deriving the mathematical formulation of the generalized dilution of precision (geDOP) and it is divided in two subsections. Section 3.4.1 introduces the theoretical framework of the Dilution of precision. Hence section 3.4.2 reports the mathematical formulation of the geDOP in its complete and simplified version.

3.4.1 Dilution of Precision

In GNSS-based navigation, the DOP is composed by four coefficients that relate the uncertainty on pseudorange measurements (σ_{Pr}) to the positioning errors in North, East, and Down components (σ_N, σ_E and σ_D) and the receiver clock bias error Δt. More relevant to the argument of this chapter is the concept of geometric dilution of precision that accounts only for the geometric part of the DOP. The generalized dilution of precision, i.e. D in equation (3.38), connects the pseudorange standard deviation to the NED STD through:

$$\begin{gathered}\boldsymbol{\sigma}^n = \begin{bmatrix} \sigma_n \\ \sigma_e \\ \sigma_d \end{bmatrix} = D\sigma_{Pr} \\ D = \sqrt{diag\left(\left(\left[H_{GNSS\mathbf{p}}G^{-1}\right]^T \left[H_{GNSS\mathbf{p}}G^{-1}\right]\right)^{-1}\right)}\end{gathered} \tag{3.38}$$

where the *diag* operator extracts the diagonal of the argument matrix, the square root operator works element-wise across the vector. The inverse of G allows to convert the geographic coordinate's error in local NED frame and is reported in (3.6).

3.4.2 Generalized Dilution of Precision

The geDOP $\breve{D}$, is defined in analogy with the geometric DOP, with the aim of mapping the pseudorange error in the NED positioning uncertainties

$$\boldsymbol{\sigma}^n = \breve{D}\sigma_{Pr} \tag{3.39}$$

Differently from the case of GNSS only measurements, the geDOP accounts for all the information coming from the aiding sensors, and it is based on the measurement matrix of the specific navigation algorithm. In this thesis the geDOP is derived with respect to the specific case of the filter described in section 3.3, but this discussion sets a general rule that could be applied to predict the performance of any navigation filter.

Being $\breve{H}$ a $n_y \times n_x$ subset of rows and columns of H, that allows to perform the inversion, similarly to equation (3.38), and $\delta\breve{\mathbf{y}}$ and $\delta\breve{\mathbf{x}}$ the subset of the measurement and the state vectors, respectively. The geDOP vector is given by:

$$\breve{D} = diag\left(\sqrt{\left(\left(\breve{H}\breve{G}\right)^T \left(\breve{R} / \sigma_{Pr}^2\right)^{-1} \breve{H}\breve{G}\right)^{-1}}\right)\Bigg|_{\mathbf{p}} \tag{3.40}$$

where the operator $\big|_{\mathbf{p}}$ extract only the positioning part from the diagonal elements of the resulting matrix, and $\breve{R}$ is the covariance associated to $\delta\breve{\mathbf{y}}$. $\breve{G}$ is a generalized version of the matrix G^{-1}, that accounts also for the non-positioning terms in the matrix $\breve{H}$.

$$\breve{G} = \begin{bmatrix} G^{-1} & 0_{3\times(n_x-3)} \\ 0_{(n_y-3)\times 3} & \mathbf{1}_{(n_y-3)\times(n_x-3)} \end{bmatrix} \tag{3.41}$$

Because the matrix H is often characterized by zeros columns and/or rows, preventing to perform the inversion in (3.40), the measurement matrix concurring to the geDOP definition, i.e. $\breve{H}$ should be carefully selected within the components of H. In this section, two approaches are reported to select the element of the matrix H used for the geDOP definition, leading to a simplified [121] and a complete [122] version of the generalized dilution of precision. Those concepts were discussed and introduced in sections 3.4.2.1 and 3.4.2.2.

With reference to the filter described in section 3.3, the measurement matrix H is detailed in equations (3.35) and (3.36), and it is reported herein for the sake of completeness

$$H = \left[\begin{array}{cccc} H_{GNSS\mathbf{p}} & 0_{m\times3} & 0_{m\times3} & 0_{m\times6} \\ \hline 0_{1\times3} & 0_{1\times3} & H_{M\mathbf{p}} & 0_{1\times6} \\ \hline H_{1,RF\mathbf{p}} & 0_{1\times3} & 0_{1\times3} & 0_{1\times6} \\ H_{1,EO\mathbf{p}}^{s\to f} & 0_{2\times3} & H_{1,EO\mathbf{p}}^{s\to f} & 0_{2\times6} \\ H_{1,EO\mathbf{p}}^{f\to s} & 0_{2\times3} & 0_{2\times3} & 0_{2\times6} \\ \hline & \vdots & & \\ \hline H_{k,RF\mathbf{p}} & 0_{1\times3} & 0_{1\times3} & 0_{1\times6} \\ H_{k,EO\mathbf{p}}^{s\to f} & 0_{2\times3} & H_{k,EO\mathbf{p}}^{s\to f} & 0_{2\times6} \\ H_{k,EO\mathbf{p}}^{f\to s} & 0_{2\times3} & 0_{2\times3} & 0_{2\times6} \end{array}\right] \tag{3.42}$$

As equation (3.42) suggests, the components made observables from the measurements used in the correction step of the Kalman filter are the position and the attitude elements. Whereas, all the other components of the state (i.e. biases and velocities) are made observables thanks to the variables' couplings in the filter's propagation step. Therefore, in order to guarantee inversion in (3.40) the subset of components of matrix H must be chosen neglecting the velocity and the biases part of the measurement matrix.

3.4.2.1 Simplified Generalized Dilution of Precision

The simplified version of the geDOP sets $\breve{H}_S$ as the H's sub-matrix which only includes entries related to positioning errors, due to the major interest is in estimating son positioning uncertainty. Indeed, GPS, cooperative ranging, and father-to-son visual tracking, provide measurements related (only) with son positioning error, while magnetometers outputs are clearly only dependant on attitude. On the other hand, cooperative visual measurements in son-to-father tracking scenarios are related to both positioning and attitude error. However, in common scenarios of interest it is possible to provide attitude estimates with bounded error exploiting inertial and magnetic sensors. In other words, the attitude can be deemed observable regardless of GPS and cooperative measurements, and the attention can thus be focused on the positioning contribution of son-to-father visual measurements. Therefore, to the scope of deriving the simplified version of the generalized DOP, only the first three columns, i.e. the part that depends on position are considered, neglecting the rows corresponding to measurements that do not contribute to positioning information, i.e. the magnetometer. The measurement and covariance matrix of the simplified geDOP are:

$$
\breve{H}_S = \left[\begin{array}{c} H_{GNSS\mathbf{p}} \\ \hline H_{1,RF\mathbf{p}} \\ H^{s\to f}_{1,EO\mathbf{p}} \\ H^{f\to s}_{1,EO\mathbf{p}} \\ \hline \vdots \\ \hline H_{k,RF\mathbf{p}} \\ H^{s\to f}_{k,EO\mathbf{p}} \\ H^{f\to s}_{k,EO\mathbf{p}} \\ \hline \end{array}\right] ; \breve{R}_S = \begin{bmatrix} R_{GNSS} & 0_{m\times 5} & \cdots & 0_{m\times 5} \\ 0_{1\times m} & R_{c1} & \cdots & 0_{5\times 5} \\ 0_{1\times m} & \vdots & \ddots & \vdots \\ 0_{5\times m} & 0_{5\times 5} & \cdots & R_{ck} \end{bmatrix} \tag{3.43}
$$

Hence, because only positioning part of matrix H and vector $\delta\mathbf{x}$ are used the expression of geDOP can be simplified to:

$$\breve{D}_S = diag\left(\sqrt{\left(\left(\breve{H}_S G^{-1}\right)^T \left(\breve{R}_S / \sigma_{Pr}^2\right)^{-1} \breve{H}_S G^{-1}\right)^{-1}}\right) \tag{3.44}$$

It is clear that in order to have an invertible matrix, for the geDOP estimation, $\delta\breve{\mathbf{y}}$ must be at least 3 components long. This means that, due to the mathematic formulation of the GNSS measurements in the proposed navigation algorithm this condition can be reached in the case of one father, when there are at least 2 satellites of the same constellation and 2 visual tracking measurement. In the case of RF-ranging only and one father at least 3 pseudoranges of the same constellation are needed $m \geq 2$. This result demonstrates that having two father and visual tracking capability allows directly triangulating son position.

3.4.2.2 Extended Generalized Dilution of Precision

In the previous section only the positioning part of the matrix H has been used to compute the geDOP, ignoring the coupling effect on the son's attitude, that holds only when the son-to-father tracking is used. Nevertheless, the attitude coupling with the measurement matrix reduces the cooperative effect on improving position performance when the distance between the two platforms arises, and there exists a maximum distance that guarantees camera measurement to be effective for the cooperative positioning sake. Therefore, in this section is introduced the extended generalized DOP that accounts also for angle dependency. To this aim the matrix $\breve{H}_E$ must include the positioning and the attitude columns of the matrix H and is:

$$\breve{H}_E = \begin{bmatrix} H_{coop} \\ H_{lev} \end{bmatrix}; \quad H_{coop} = \begin{bmatrix} H_{GNSS\mathbf{p}} & 0_{m\times 3} \\ 0_{1\times 3} & H_{M\boldsymbol{\rho}} \\ H_{1\mathbf{p}} & H_{1\boldsymbol{\rho}} \\ \vdots & \vdots \\ H_{k\mathbf{p}} & H_{k\boldsymbol{\rho}} \end{bmatrix} \tag{3.45}$$

$$H_{lev} = \begin{bmatrix} 0_{2\times 3} & \begin{matrix} 1 & 0 & 0 \\ 0 & 1 & 0 \end{matrix} \end{bmatrix}$$

where $H_{j\mathbf{p}}$ and $H_{j\boldsymbol{\rho}}$ are the positioning and attitude part of H_j, that are detailed in equation (3.36). H_{coop} comes from H removing the velocity and the biases columns. When only camera is used in the worst condition (k = 1, m = 1), H_{coop} is a 6×4 matrix and H_{lev} is mandatory to perform the inversion in equation (3.40). H_{lev} includes the geDOP dependency on roll and pitch angles, that comes from the filter's prediction equations. Indeed, roll and pitch angles are observables, and their error is generally bounded. This allows also in the case H_{coop} is not invertible to have a bounded filter error if the father is placed in the correct position [121]. Without the inclusion of H_{lev} in $\breve{H}$, at least four pseudoranges measurement (m = 3) would be needed to have a reliable geDOP value. Because the geDOP is an index of the son's filter performance, this would suggest cooperative filter error is bounded only if $m \geq 3$. Withal, [121, 127] demonstrate the cooperative filter performs well even if m = 1. To account this effect, H_{lev} is included in the extended form of the geDOP measurement matrix, associating to the horizontal rotations an empiric estimates of their error (σ_N and σ_E, respectively) in the geDOP covariance matrix, that is:

$$\breve{R}_E = \begin{bmatrix} (\mathbf{1}_m + \mathbf{I}_m)\sigma_{Pr}^2 & 0_{m\times1} & 0_{m\times5} & \cdots & 0_{m\times5} & 0_{m\times1} & 0_{m\times1} \\ 0_{1\times m} & \sigma_{\psi_M}^2 & 0_{1\times5} & \cdots & 0_{1\times5} & 0 & 0 \\ 0_{5\times m} & 0_{5\times1} & R_{c1} & \cdots & 0_{5\times5} & 0_{5\times1} & 0_{5k\times1} \\ \vdots & \vdots & \vdots & \ddots & \vdots & \vdots & \vdots \\ 0_{5\times m} & 0_{5\times1} & 0_{5\times5} & \cdots & R_{ck} & 0_{5\times1} & 0_{5\times1} \\ 0_{1\times m} & 0 & 0_{1\times5} & \cdots & 0_{1\times5} & \sigma_N^2 & 0 \\ 0_{1\times m} & 0 & 0_{1\times5} & \cdots & 0_{1\times5} & 0 & \sigma_E^2 \end{bmatrix} \tag{3.46}$$

3.5 SIMULATION RESULTS

As stated in the previous section, the geDOP is a useful mathematical concept that can be used to foresee the navigation filter's performance. To this aim an extensive analysis on geDOP behavior has been carried out in a simulation framework. This section is in charge of detailing with numerical simulation the meaning of the geDOP. Therefore, a comprehensive discussion about the geDOP properties is given in section 3.5.1. To complement the geDOP discussion, simulation results concerning the cooperative navigation filter are given in section 3.5.2.

3.5.1 geDOP Analysis

As suggested by its mathematical formulation the geDOP value and thus the filter cooperative performance depends on son position, 3D environment features, the consequently available GNSS satellites, and the embarked relative sensing systems.

3.5.1.1 Simplified geDOP

As first examples of generalized DOP exploitation, for the case of a single father, the simplified version of geDOP is used. The receiver is assumed to have GPS only capability, thus only the GPS satellites are simulated. Figure 3.3 and Figure 3.4 depict the norm of $\breve{D}_S$ as a function of father azimuth and elevation (in son-centered NED), for two common scenarios in low altitude UAVs missions. In particular, the first scenario (Figure 3.3) represents a building inspection mission, where the son vehicle is flying close (distance Δ = 5 m) to a south-north oriented building. The building is 60 m tall, and the son UAV flies at an above ground altitude of 20 m.

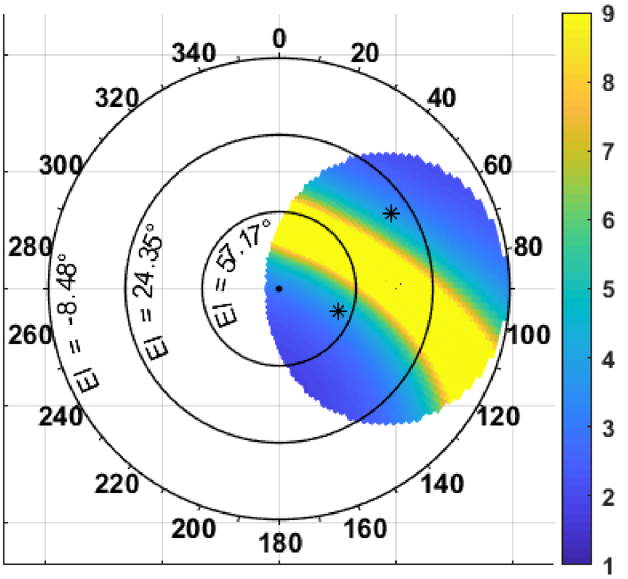

Figure 3.3 $\left|\breve{D}_S\right|$ as a function of azimuth and elevation, r = 40 m. Building inspection scenario: h = 20 m, Δ = 5 m. Son-to-father visual aiding only. Asterisks indicate GPS satellites in view of the son

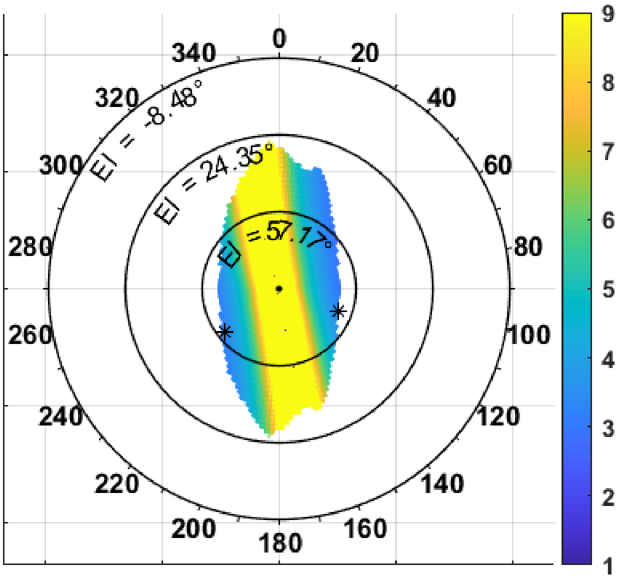

Figure 3.4 $\left|\breve{D}_S\right|$ as a function of azimuth and elevation, r = 40 m. Asterisks indicate GPS satellites in view of the son. Urban canyon scenario: h = 30 m, Δ = 15 m. Son-to-father visual aiding only.

The second scenario (Figure 3.4) simulates a mission within an urban canyon: the son UAV flies within a 30 m large south-north oriented urban canyon. Buildings are 60 m tall and son is flying at an above ground altitude of 30 m. In both cases, the distance between son and father, i.e. *r*, is set equal to 40 m. The geDOP graph is drawn in the worst time epoch, i.e. the one with the lowest dilution of precision. In this case only two GPS satellites are available to the son UAV (due to environmental obstructions). Son-to-father visual tracking is considered regarding cooperative aiding. The figures identify the available combination for the father while assisting the son UAV. Several combinations of azimuth and elevation are highlighted with a white color. Indeed, these specific combinations forbid the geDOP calculation, because identify relative formation that violates father requirements, i.e. father not in Line of Sight with the son and/or father in the challenging area. In the case of GPS only constellation the challenging area is defined as the area where the number of GNSS satellites it is lower than the one needed to perform position fix, i.e. 4.

Conclusion about the best relative geometry for the formation can be drawn from the geDOP plots. Therefore, the best father location is defined as the one that minimizes the norm of the generalized DOP. Figure 3.3 shows that for the building inspection scenario various azimuth-elevation combinations lead to good DOP values. Whereas, in the canyon scenario, even with the same number of available satellites and the same cooperative aiding technique, it is more challenging to find good DOP geometries and the functional dependences are clearly different, demonstrating that the GPS satellite geometry has a fundamental role in the definition of the optimal father-son geometry. It is worth noting that in both figures, yellow areas correspond to DOP divergence, i.e., the color scale limit has been chosen to allow better understanding of DOP variation for smaller values).

The geDOP can be used as an instrument to compare the performance of different relative measurement instrument to the aim of the cooperation. Figure 3.5, Figure 3.6, and Figure 3.7 and show the norm of the generalized DOP in the case of son-to father tracking, father-to-son tracking, and RF-based ranging in a building inspection scenario.

Son-to-father and father-to-son visual tracking scenarios (Figure 3.5 and Figure 3.6) yield similar results regarding the optimal father placement that optimizes cooperative aiding. The measurement equations are different in the two cases, but they adopt the same relative sensing system. In addition, measuring the navigation performance of the filter with the simplified version of the geDOP, allows to neglect the attitude coupling in the son-to-father visual tracking. This set a similarity between the son-to-father father-to-son visual tracking equation, that is demonstrated by the previous figures.

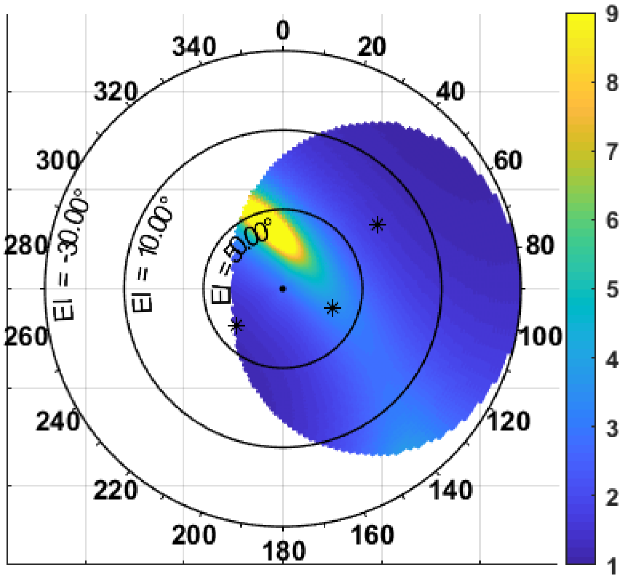

Figure 3.5 $\left|\breve{D}_s\right|$ as a function of azimuth and elevation, r = 40 m. Building inspection scenario: h = 30 m, Δ = 15 m. Son-to-father visual aiding only. Asterisks indicate GPS satellites in view of the son.

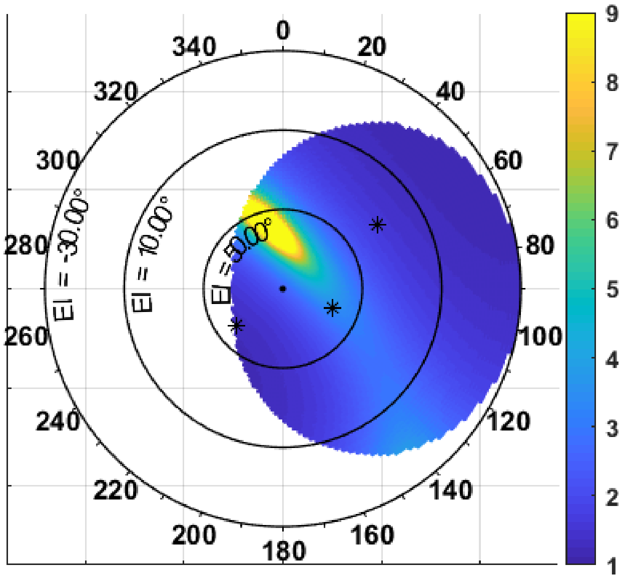

Figure 3.6 $\left|\breve{D}_s\right|$ as a function of azimuth and elevation, r = 40 m. Building inspection scenario: h = 30 m, Δ = 15 m. Father-to-son visual aiding only. Asterisks indicate GPS satellites in view of the son.

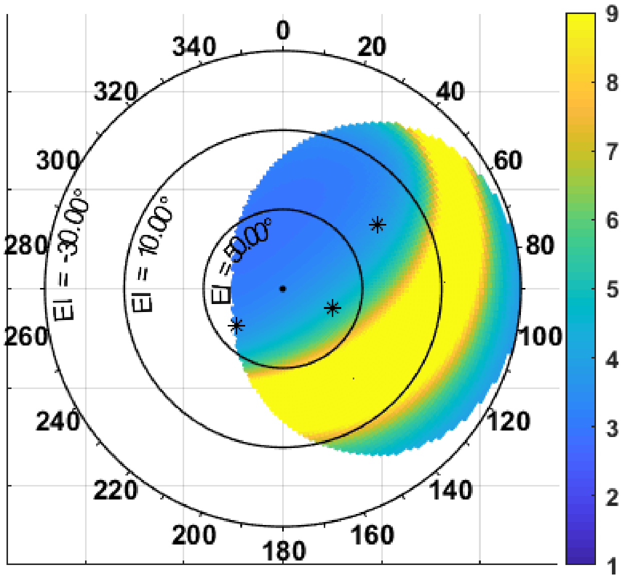

Figure 3.7 $\left|\breve{D}_S\right|$ as a function of azimuth and elevation, r = 40 m. Asterisks indicate GPS satellites in view of the son. Urban canyon scenario: h = 30 m, Δ = 15 m. RF-ranging only.

However, it is important to notice that the figures shown in this section are dependent on the onboard equipment, and thus differences can arise depending for instance on camera resolution.

Comparing the results obtained for visual aiding (Figure 3.5 and Figure 3.6) with those obtained with RF ranging (Figure 3.7), one can notice that on average the norm of generalized DOP is larger in the latter case. This mainly depends on the smaller number of observables contributing to cooperative navigation (one instead of two). Figure 3.7 also demonstrates the complementarity of the cooperative aiding approaches: RF-ranging systems improve the positioning accuracy along the father-to-son direction, while visual tracking provides information in the plane orthogonal to this direction. As expected, using together visual tracking (son-to-father aiding) and RF-ranging reduces dramatically the generalized DOP value, as shown in Figure 3.8 (color scale is different from the previous figures). Furthermore, no geDOP divergence is observed, which is an intuitive result considering that knowledge of father absolute position and of relative position vector in NED make son position observable whatever is the formation geometry.

The comparison between the previous figures of this section demonstrates the geDOP dependency on the used sensors (Figure 3.5, Figure 3.6, and Figure 3.7), the constellation of satellites and the 3D environment (Figure 3.3 and Figure 3.4) and the satellite constellation (Figure 3.3 and Figure 3.5).

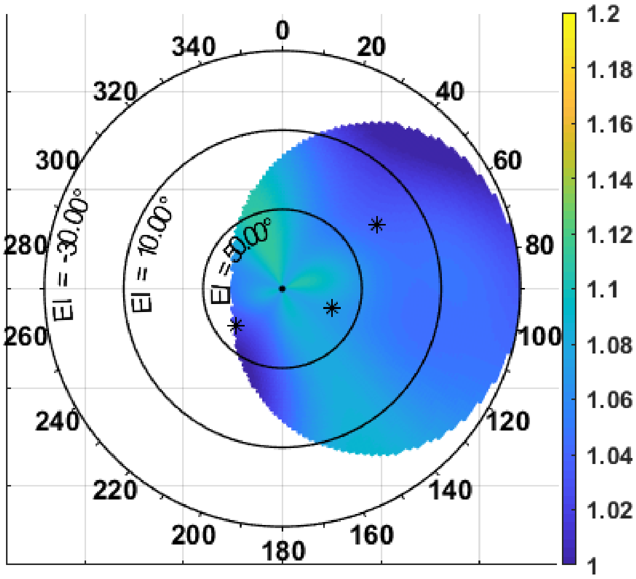

Figure 3.8 $\left|\breve{D}_S\right|$ as a function of azimuth and elevation, r = 40 m. Building inspection scenario: h = 30 m, Δ = 15 m. Son-to-father tracking and RF ranging aiding. Asterisks indicate GPS satellites in view of the son.

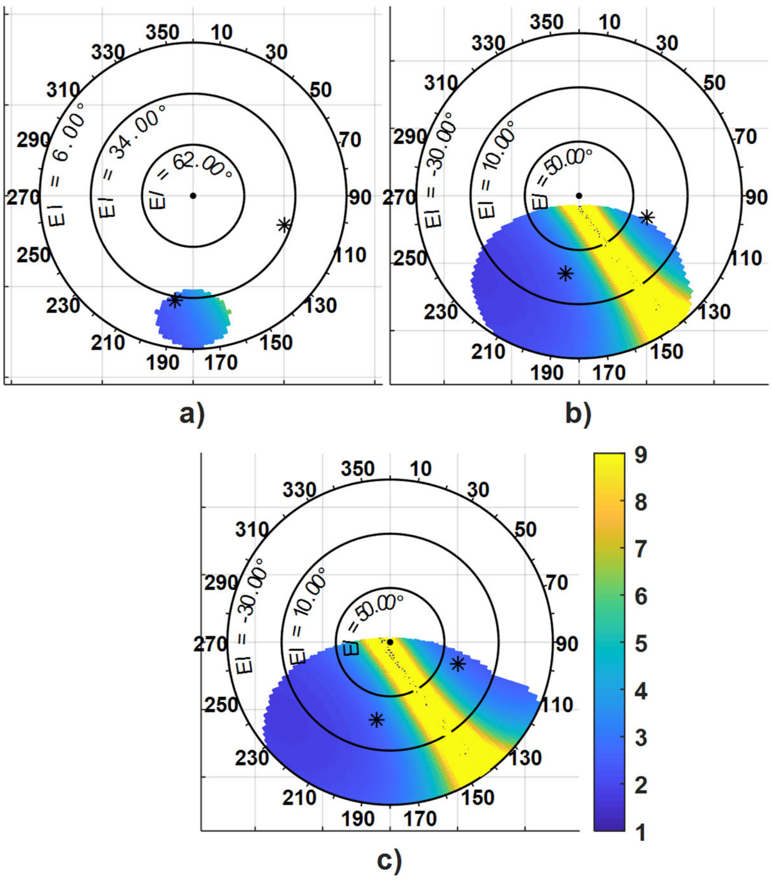

Figure 3.9 Norm of the generalized DOP in function of Azimuth and Elevation of the father with respect to the son. Son father range are a) 10 m, b) 20 m and c) 30 m. Son-to-father visual tracking and constant father positioning accuracy.

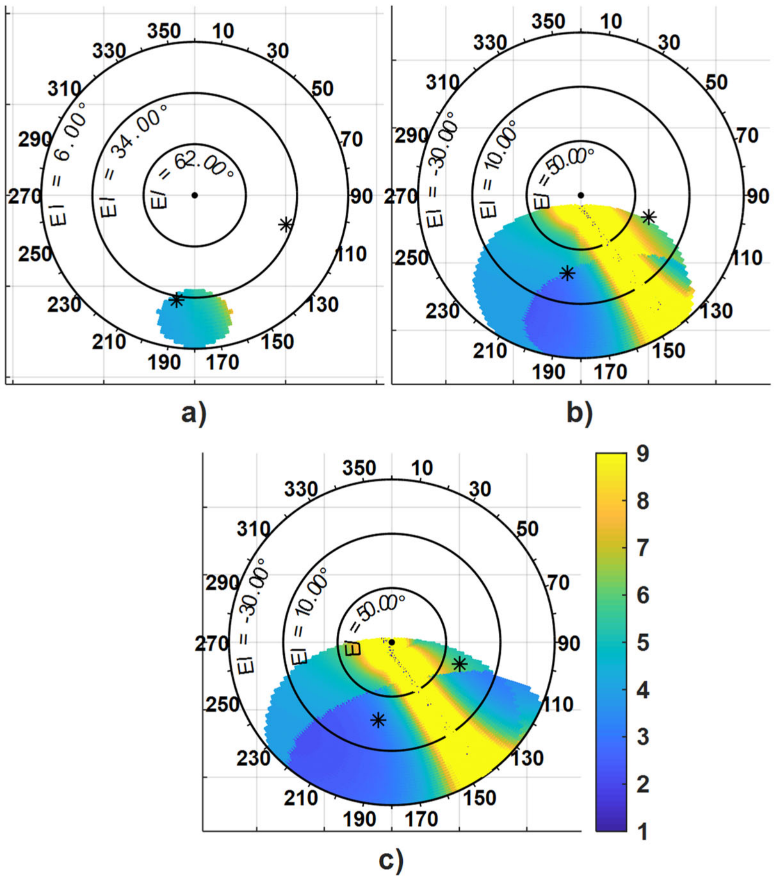

Figure 3.10 Norm of the generalized DOP in function of Azimuth and Elevation of the father with respect to the son. Son father range are a) 10 m, b) 20 m and c) 30 m. Son-to-father visual tracking. Father accuracy variation is taken into account.

Indeed Figure 3.3 and Figure 3.5, are drawn for different position of the son with respect to the obstacle, and therefore different available satellites and demonstrate as intuitive that increasing the number of satellite the good geDOP configurations increase.

Another interesting aspect to tackle is the dependency of the geDOP from the inter-range between the two platforms. To this aim Figure 3.9, reports three images evaluated assuming the father-son range to change. Specifically, it is assumed to be equal to 10, 20 and 30 m respectively. The son is assumed to hover at 30 m altitude holding a distance of 10 m from a building of 80 m height, oriented in the east-west direction. The building is 200 m wide in that direction. Son-to-father visual tracking has been considered. It can be seen that the generalized DOP mainly depends on azimuth and elevation. Even if admissible father positions reduce with the range, the value of the norm value of the generalized DOP does not change or slightly change with it. Nevertheless, Figure 3.9 has been drawn considering constant the accuracy on father positioning. This parameter plays a fundamental role in defining the covariance of the relative measurements and an therefore the geDOP, as remarked in equations (3.23), (3.29) and (3.31). A more realistic estimate of the geDOP should consider the accuracy on father positioning dependant on the current DOP, using equation (3.38).

Figure 3.10 reports again the norm of geDOP in function of the range, as Figure 3.9. In this case the accuracy of the father position has been estimated accounting for the actual DOP. The range increase sends away the father from the obstacle. This results not only in an increasing combination of available formation geometries for the father, but also in improved performance on cooperative aiding. Indeed, when the father goes away from the obstacle the number of in view satellites increases, leading to a DOP reduction and an improved positioning accuracy. Improved positioning accuracy of the father reduces the covariance of the measurement equations, returning a better geDOP.

3.5.1.2 Extended geDOP

The extended geDOP has been introduced in [122] to have a more reliable estimate of the filter performance, accounting also for the father coupling that holds true when son-to-father tracking is used. This section discusses the properties of the extended geDOP, in the most common GNSS challenging scenarios, i.e. building inspection, bridge inspection and urban canyon, that are described in 3.5.1.2.1. The results presented in this section assumes geDOP estimation is performed accounting for non-constant father accuracy, i.e. the accuracy on father positioning is based on the effective DOP and multi constellation configuration. Specifically, GPS and GLONASS satellites have been considered. It is reasonable to assume the multi GNSS receiver always has in view more than four satellites, also in challenging scenarios. Therefore, differently from the previous case the number of satellites cannot be anymore considered as reference for identifying challenging and non-challenging zones. Therefore, the DOP becomes a fundamental parameter to discriminate about the “challenginess” of the environment and a threshold can be set to delineate the boundary of the challenging areas. After introducing the simulated scenarios, section 3.5.1.2.2 presents the geDOP results.

3.5.1.2.1 *Simulation Scenarios*

As anticipated, the most common scenarios that could arise GNSS coverage problems are inspection of a high building, flight in urban canyon, and bridge inspection.

To the aim of a more realistic interpretation of the presented results simulation scenarios are taken from real world examples. Figure 3.11 depicts the building inspection scenario, that is a building in the Business District in Naples. Urban Canyon, represented in Figure 3.12, is a complex of some buildings near to south Cove park in lower Manhattan. Whereas, the Golden Gate bridge (San Francisco) in Figure 3.13 has been considered for the bridge inspection mission. The trajectory that the son UAV perform in each scenario is depicted with a blue line.

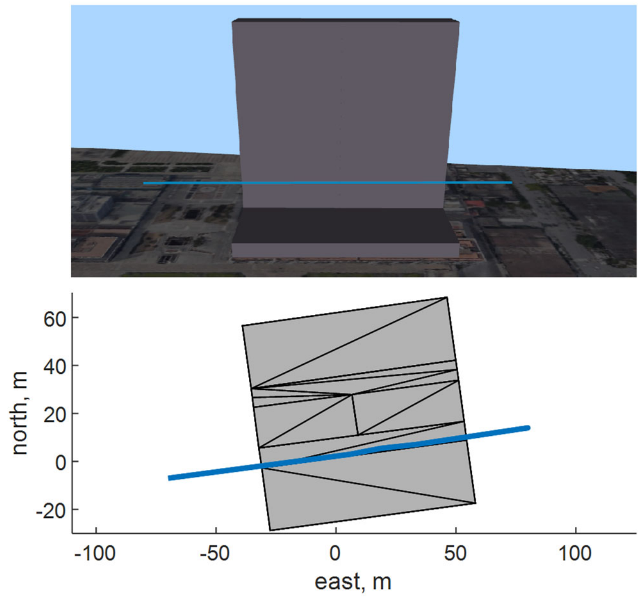

Figure 3.11 Building Inspection Scenario, the son's trajectory is depicted in blue.

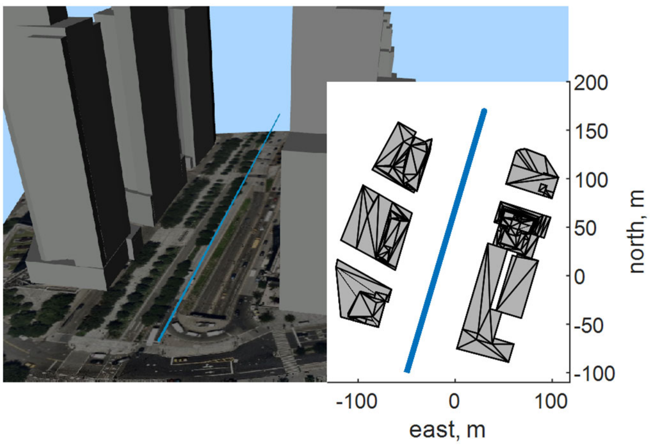

Figure 3.12 Urban canyon Scenario, the son's trajectory is depicted in blue.

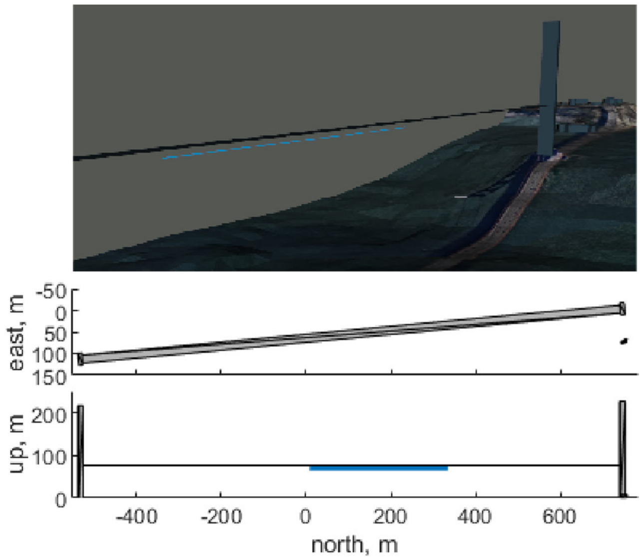

Figure 3.13 Bridge Inspection Scenario, the son's trajectory is depicted in blue

3.5.1.2.2 Extended geDOP results

To remark the relevance to the Extended geDOP, Figure 3.14 and Figure 3.15 reports the comparison between extended and simplified geDOP distribution in son-to-father and father-to-son visual tracking, respectively. Building inspection scenario in Figure 3.11 has been taken into account. The figures are derived considering the son is placed along the trajectory depicted in Figure 3.11, in the most critical point for navigation without any cooperation, i.e. the one with the maximum DOP. The maximum geDOP value represented in the two pictures is equal to 2.5, that has been set as threshold to identify the boundary of the challenging area. As expected, the multi constellation configuration improves the accuracy of the cooperative filter. Indeed, the improved number of satellites reduces the geDOP value, with respect to the single constellation case. Figure 3.14 underlines the coupling effect between the son-to-father visual tracking measurement and attitude. The geDOP value in Figure 3.14.a, estimated with the extended geDOP formulation is higher than what obtained in the simplified case, i.e. Figure 3.14.a. Conversely, when father-to-son visual tracking is taken into account (Figure 3.15), the geDOP slightly varies from the simplified to the extended definition, due to the lack of attitude coupling effect.

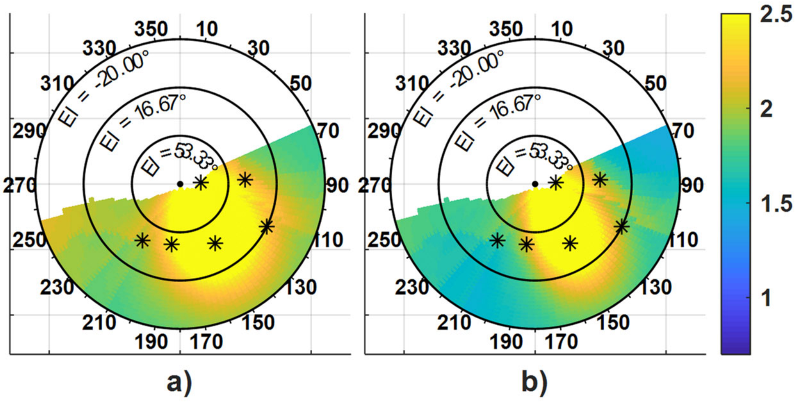

Figure 3.14 Comparison between a) extended and b) simplified geDOP norms, son-to-father visual tracking. r =40. Son is placed on the trajectory in Figure 3.11, in the most critical point, i.e. the one with the maximum DOP**.**

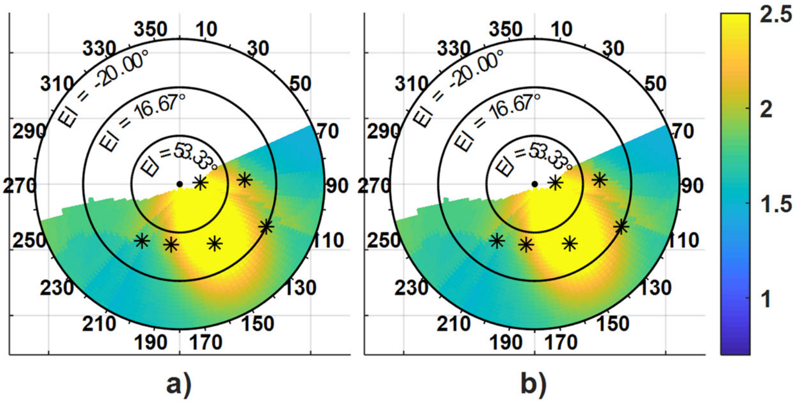

Figure 3.15 Comparison between a) Extended and b) simplified geDOP norms, father-to-son visual tracking. r =40. Son is placed on the trajectory in Figure 3.11, in the most critical point, i.e. the one with the maximum DOP.

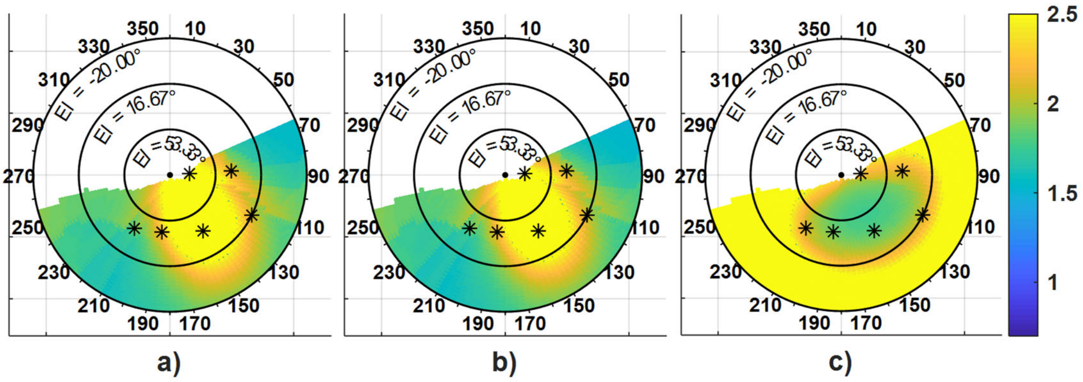

Figure 3.16 Extended geDOP norm as a function of Azimuth and Elevation in Building inspection scenario. a) son-to-father visual tracking, b) father-to-son visual tracking, c) RF-ranging. The distance of the cooperative formation has been set to 40 m.

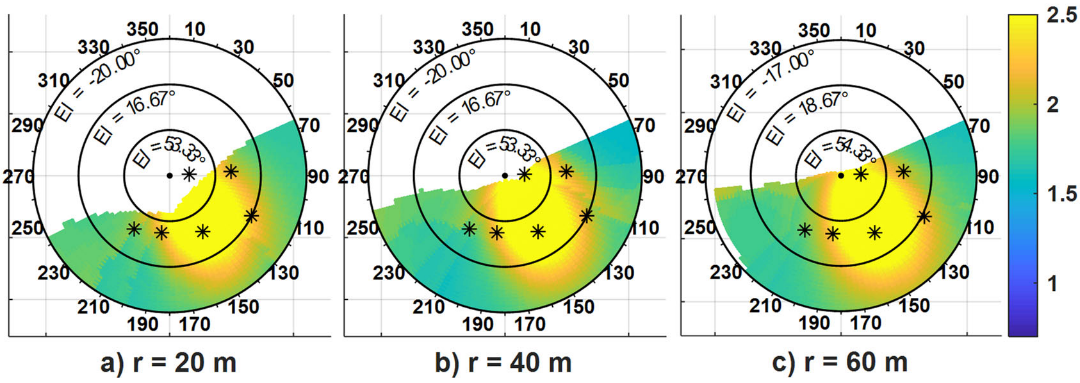

Figure 3.17 Extended geDOP norm as a function of Azimuth and Elevation in Building inspection scenario. Son-to-father aiding has been used as relative measurement and range variation has been taken into account, being the range 20, 40 or 60 m respectively in a), b) and c).

With reference to the building inspection scenario, Figure 3.16 reports the geDOP map, i.e. its variation in function of the relative azimuth and elevation with a) son-to-father, b) father-to-son, c) RF ranging aiding, in case a single father is used. The range is kept constant. White areas, breaching the father requirements, are forbidden to the cooperative vehicle. Yellow areas identify values for the geDOP higher than a threshold (i.e. 2.5), that must be avoided by the cooperative vehicle, to keep bounded the positioning error. Figure 3.16.a and Figure 3.16.b show a similar dependence in function of the relative geometry, because of the similarity in the position part of the measurement matrix of father-to-son and son-to-father visual tracking. However, camera on father yields more accurate estimation due to the lack of dependence on the son’s attitude, which provides an improved observability of the position part of the state. RF ranging aiding results are complementary to the cameras and offer a narrow area where the father can be placed. These results, although less performant than camera, show a region without discontinuity where the father can be placed. This property is essential when dealing with planning and guidance for father trajectory. Indeed, in the case a discontinuity (yellow area) exists in the geDOP diagram, father could easily fall during its motion in undesired conditions spoiling the advantage of cooperation. The inclusion of a more realistic father standard deviation in the geDOP estimation strengthens the geDOP dependency on the range. Figure 3.17 shows the geDOP when son-to-father camera aiding is used in the building inspection scenario by varying the distance between the two platforms. In Figure 3.17.a the available position for the father are limited due to the reduced distance between the platforms that makes the father fall in the challenging area. Non only does the range increase provide a larger amount of available formation geometries, but it also reduces the positioning error of the father, enabling its receiver to see more satellites. Nonetheless, when using camera, a large range is responsible of an increasing geDOP, spoiling the beneficial effect of the reduction of the father's position error. The geDOP increase in father-to-son tracking is due to the high camera measurement error, namely $\Delta\chi^n$ in equation (3.25), that linearly depends on the distance between the two platforms. This effect is stronger in son-to-father tracking, where the performance of cooperation in position aiding reduces in favour of an improved accuracy in angles estimation (see Figure 3.17.a and Figure 3.17.b). This is because of the coupling of the measured angles with the son's attitude.

Figure 3.18 and Figure 3.19 reports the geDOP map when more than a father is used and refers respectively to son-to-father aiding and rf-ranging aiding. The geDOP map of an additional father is drawn by fixing the position of the already used target, that are marked with red asterisks in these figures. As an example, Figure 3.19.a aimes at defining the position of a second father that uses RF ranging is derived by assuming the first father is placed in the position that minimizes the geDOP in Figure 3.16.c. Figure 3.18 and Figure 3.19 remark the camera effectiveness in cooperative navigation. Indeed, camera allows to get a value of the geDOP lower than the one the RF-ranging provides. In addition, RF-ranging's geDOP reaches a lower bound when two fathers are used, thus making ineffective the aiding of a third platform. Whereas, the positioning error of the son keep reducing when a new father is added. For the sake of completeness, Figure 3.20 depicts the geDOP map in a) urban canyon (Figure 3.12) and b) bridge inspection case (Figure 3.13). The son-to-father distance it is assumed to be 40 m and son to father tracking has been used.

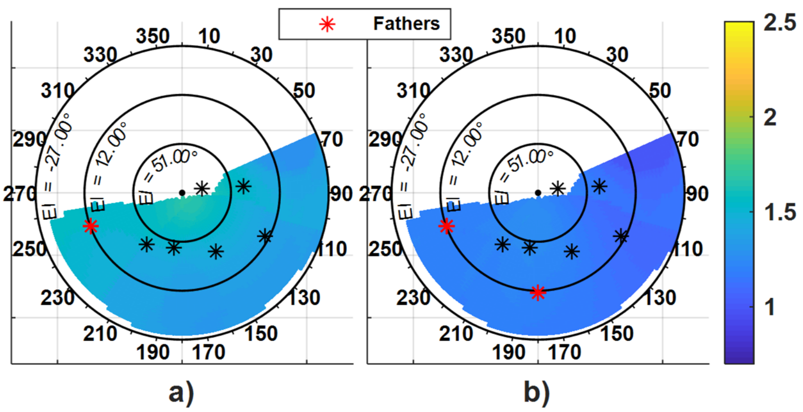

Figure 3.18 Extended geDOP norm as a function of Azimuth and Elevation with multiple fathers. Son-to-father camera aiding. a) and b) draw the geDOP maps for the second and the third father, respectively. The position of the already fixed fathers is highlighted with red asterisks.

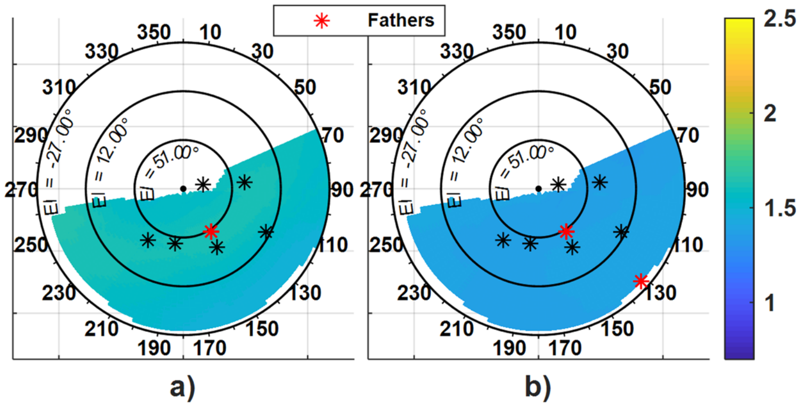

Figure 3.19 Extended geDOP norm as a function of Azimuth and Elevation with multiple fathers. RF ranging aiding. a) and b) draw the geDOP maps for the second and the third father, respectively. The position of the already fixed fathers is highlighted with red asterisks.

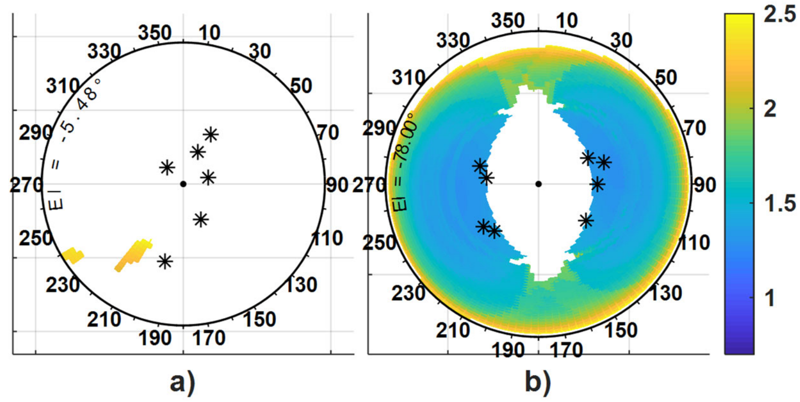

Figure 3.20 Map of extended geDOP norm in a) urban canyon and b) bridge inspection, using father-to-son tracking. The father-to-son range it is 40 m. The norm of dilution of precision without father ading is a) 3.86 and b) 5.34**.**

Formations yielding a high value for the geDOP (>2.5) have been included in the white area for the sake of visualization. The canyon is the most complex scenario where perform cooperation, due to the few available locations for the cooperative platform. In this specific scenario it is recommended to have an additional father.

3.5.2 Navigation Filter Results

The performance of the navigation filter are tested in single constellation (GPS only) and multi-constellation (GPS and GLONASS) scenarios, respectively in sections 3.5.2.1 and 3.5.2.2.

3.5.2.1 GPS Only

The simulated scenario assumes a building inspection mission. The son vehicle is assumed to fly with a very low velocity (2 m/s) along the north direction, parallel to the right face of the building $\Delta = 5$ m and $h = 20$ m are assumed. The available GPS satellites seen by the son during the flight close to the building are shown in Figure 3.21, along with its trajectory in the north-up plane. The figure highlights that as soon as the son vehicle reaches the building, the number of GPS satellites reduces. For this scenario, the minimum number of GPS SVs is two.

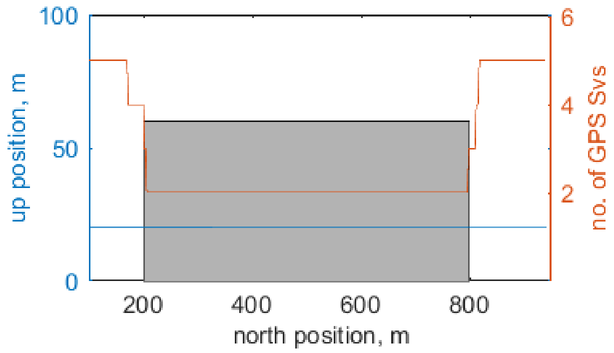

Figure 3.21 Number of satellites seen by the son vehicle during the flight. Building inspection scenario: $h = 20$ m, $\Delta = 5$ m

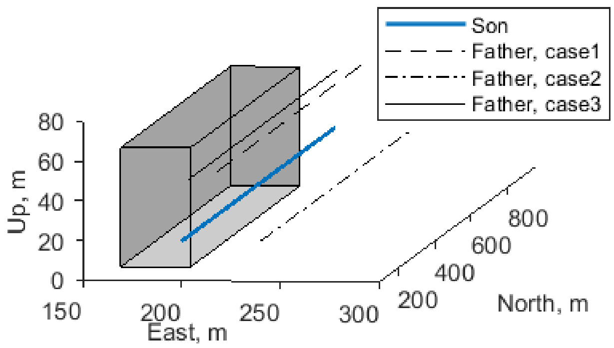

Figure 3.22 Trajectory of son and father vehicle in case 1) $Az = 60$ deg, $El = 60$ deg, $r = 40$ m, 2) $Az = 98$ deg, $El = 0$ deg, $r = 40$ m and 3) $Az = 170$ deg, $El = 50$ deg, $r = 40$ m. Building inspection scenario: $h = 20$ m, $\Delta = 5$ m

The generalized DOP in the worst case for positioning estimation is the one shown in Figure 3.3. Since the minimum number of GPS measurements is lower than 3, RF-ranging only aiding is not suitable for this scenario. With reference to Figure 3.3, three different father-son geometries are investigated within the filter, assuming the father flies parallel to the son with azimuth and elevation given as follows:

1) $Az = 60$ deg, $El = 60$ deg, $r = 40$ m. $\left|\breve{D}_S\right| > 9$

2) $Az = 98$ deg, $El = 0$ deg, $r = 40$ m. $\left|\breve{D}_S\right| = 6$;

3) $Az = 170$ deg, $El = 50$ deg, $r = 40$ m. $\left|\breve{D}_S\right| = 2$;

The ENU (East North Up) trajectories of the son and of the father in the three cases are depicted in Figure 3.22. They yield different generalized DOP values, which have been chosen to demonstrate how the filter performance is dependent on the father placement and is consistent with generalized DOP estimates. When the norm of the generalized DOP is higher than 9 (within the yellow area, case 1) the filter diverges. This basically means that the adopted geometry and relative sensing strategy do not make son position observable. Filter results for the geometries of case 2 and case 3, using only son-to-father aiding are given in Figure 3.23 and Figure 3.24. These figures show filter positioning error in cases 2 and 3, respectively. The figures show the 3σ bound that has been estimated accounting for the geDOP and the GPS pseudorange error, as described in equation (3.39). The figures also outline with different background colors the number of GNSS measurements used by the son's filter, *m*.

Figure 3.23 and Figure 3.24 highlight how the cooperative aiding is sensitive to the father position as predicted by the generalized DOP. Indeed, in case 3 all the errors in positioning estimation are bounded within 6 m.

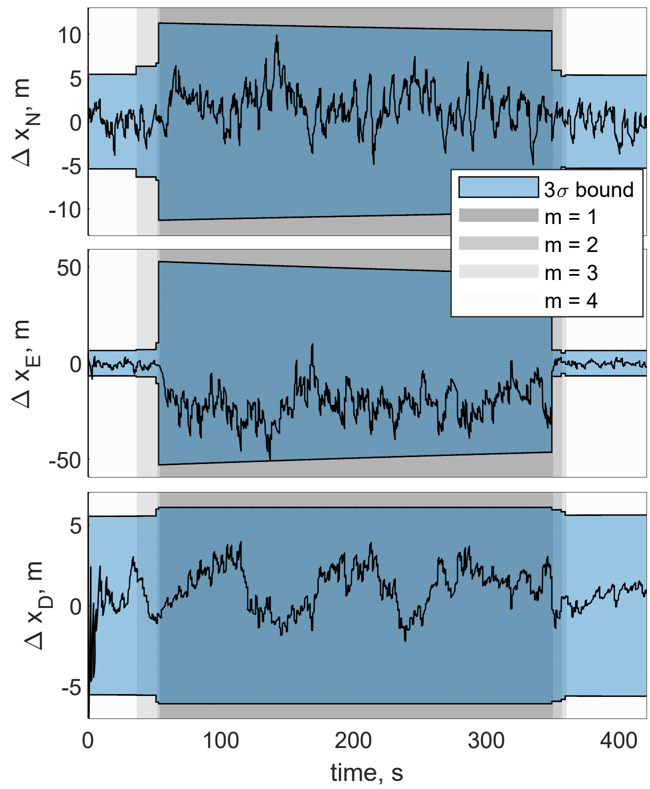

Figure 3.23 Filter NED Positioning errors. Building inspection scenario: h = 20 m, Δ = 5 m. Father has a trajectory parallel to the son with Az = 98 deg, El = 0 deg, r = 40 m. Son-to-father visual aiding only. The 3σ bound is estimated multiplying the predicted geDOP for σ_{Pr} and depicted in blue.

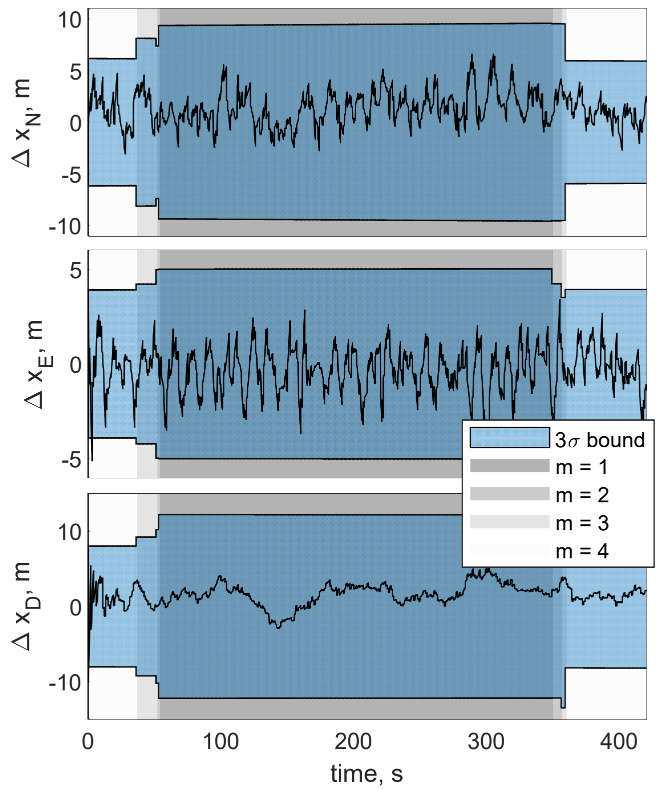

Figure 3.24 Filter NED Positioning errors. Building inspection scenario: h = 20 m, Δ = 5 m. Father vehicle has a trajectory parallel to the son with Az = 170 deg, El = 50 deg, r = 40 m. Son-to-father visual aiding only. The 3σ bound, estimated multiplying the predicted geDOP for σ_{Pr} is depicted in blue.

In case 2, a worse generalized DOP is achieved, and father aiding mostly helps North and Down position components. This is consistent with the fact that visual measurements provide information in the plane normal to the father-son direction, which is almost aligned with East direction. Thus, East error is large (it would actually lead to possible collision with the building) and can be reduced only once the number of GPS observables increase, i.e., a third satellite becomes available. When the generalized DOP assumes small values, as in case 3, filter performance is quite uniform along the simulation time span, showing less dependence on the number of available GPS satellites (case 2 vs. 3).

In summary, in all the considered cases the expected generalized DOP, as remarked from Figure 3.23 and Figure 3.24, is consistent with the accuracy of the navigation filter in estimating son position components.

3.5.2.2 Multiconstellation: GPS and GLONASS

To assess the effectiveness of the geDOP under multi-constellation scenario several simulations have been carried out. The performance of the navigation filter of the son with and without the father support have been compared. Son it is assumed to embark a consumer grade IMU, i.e. the Honeywell'HG1120CA50 [128]. The father(s) is flying along a trajectory parallel to the son, with a separation defined with the aim to minimize the geDOP. Figure 3.25 shows the accuracy of the son positioning that could be achieved using a cooperative father within the bridge inspection framework. Father-to-son camera aiding has been used. Father separation is mostly in the east direction. Therefore, when camera aiding is used, this makes unobservable the east component of the son's position which takes the least advantage from cooperation. Root mean square (RMS) and maximum errors are reported for each component. When son-to-father camera aiding is used, as in Figure 3.26 the performance of the cooperative navigation is spoiled by the unprecise son's pointing. However, a more performant gyroscope (i.e. tactical grade) mounted on the son could improve the cooperative formation performance, as highlighted in red in Figure 3.26.

Cooperative navigation performance in function of the father positioning and attitude errors is reported in Table 3.2, when camera is used. To this aim, Root Mean Square (RMS) and maximum error are used as reference parameters. The STD error on father position is given as scalar value, i.e. the user equivalent range error (UERE). This value has to be multiplied for the current father's DOP to obtain the error on each component.

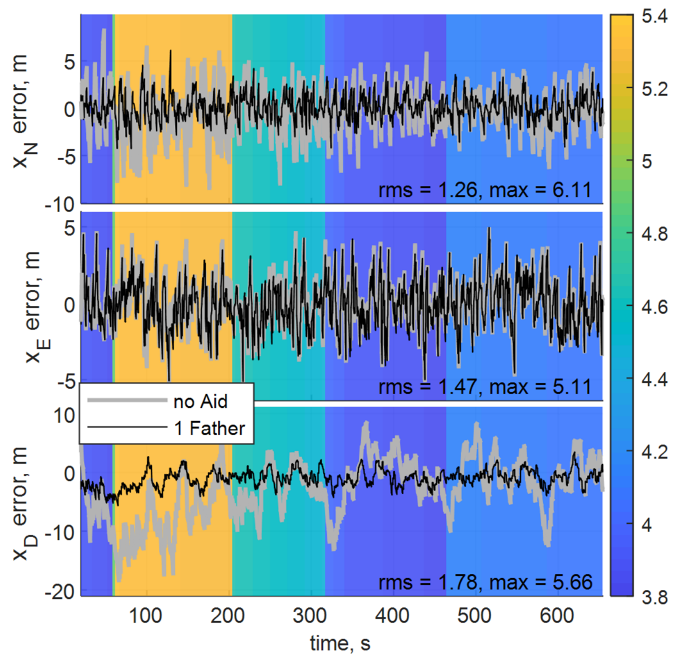

Figure 3.25 Son's navigation results, bridge inspection scenario. Father-to-son camera aiding. The relative formation assumes Az = 90°, El = 6°, r = 40. Background color represents the value of the DOP the son would encounter without father's support.

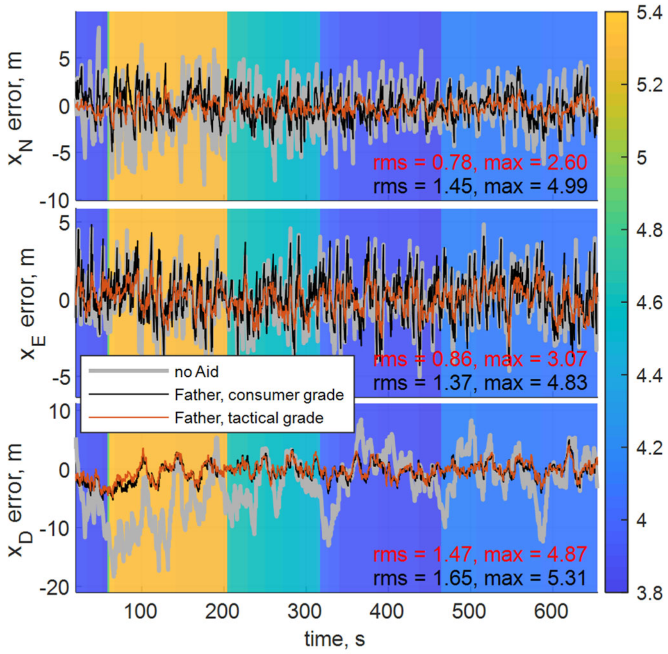

Figure 3.26 Son's navigation results, bridge inspection scenario. Son-to-Father camera aiding. The relative formation assumes Az = 90°, El = 6°, r = 40. Black and red lines represent camera aiding with two different gyroscope grades mounted on the son: consumer and tactical grade, respectively. Background color represents the value of the DOP the son would encounter without father's support.

Table 3.2 Cooperative navigation performance as a function of Father's Navigation errors. Camera Aiding it is accounted. Results refer to bridge inspection scenario. Relative formation: $Az = 90°$, $El = 6°$, $r = 40$.

Father Error Attitude STD, *deg* [φ, θ, ψ][a]	Position STD, *m*	**Cooperative Aiding**	**Navigation positioning performance**, *m* [x_N,x_E,x_D]
[0.5,0.5,1]	3	Father-to-son	RMS = [1.26, 1.47, 1.78] Max = [6.11, 5.11, 5.66]
		Son-to-father	RMS = [1.45, 1.37, 1.65] Max = [4.99, 4.83, 5.31]
		Father-to-son + RF ranging	RMS = [1.26, 1.05, 1.84] Max = [6.12, 3.81, 5.69]
[1,1,3]	3	Father-to-son	RMS = [1.44, 1.47, 1.86] Max = [5.39, 5.32, 5.96]
		Son-to-father	RMS = [1.45, 1.37, 1.65] Max = [4.99, 4.83, 5.31]
[0.5,0.5,1]	0.3	Father-to-son	RMS = [0.44, 1.46, 0.39] Max = [1.58, 5.24, 1.20]
		Son-to-father	RMS = [1.04, 1.29, 0.77] Max = [4.14, 4.66, 2.67]

[a] φ, θ, ψ are the roll pitch and yaw errors, respectively.

Result of Table 3.2 are obtained in a bridge inspection scenario with relative azimuth and elevation respectively equal to 90 and 6 deg. Hence the distance between father and son is 40 m. A better father's attitude accuracy affects only the father-to-son tracking, because the uncertainty on the camera mounted on the son is independent on the father's angular error. Whilst, both the tracking strategies benefit from an improvement in father position accuracy.

Therefore, differential or carrier phase differential GPS brings a huge advantage to the cooperative navigation strategy even if only used on the cooperative platform. However, Table I shows that the east component's error remains almost unaltered from father's accuracy variation because unobservable with the current geometry if a camera is used. On the other hand, complementing camera with RF ranging would make the error on that component reduces. Indeed, the RF-ranging increases the observability in the direction parallel to the UAVs separation.

Figure 3.27 shows the filter results in a building inspection scenario. The figure highlights the advantage in using an additional father. The two fathers are placed in the points highlighted in red in Figure 3.18.b.

For the analysed scenario, Figure 3.28 and Figure 3.29 shows the results when using father-to-son visual aiding and RF-ranging aiding. In the first case (Figure 3.28) the father is placed in the best position for the camera, i.e. the red asterisk in Figure 3.18.a. Due to the lack of the coupling effect with the attitude, the performance of the father-to-son visual aiding are better, than the son-to-father case.

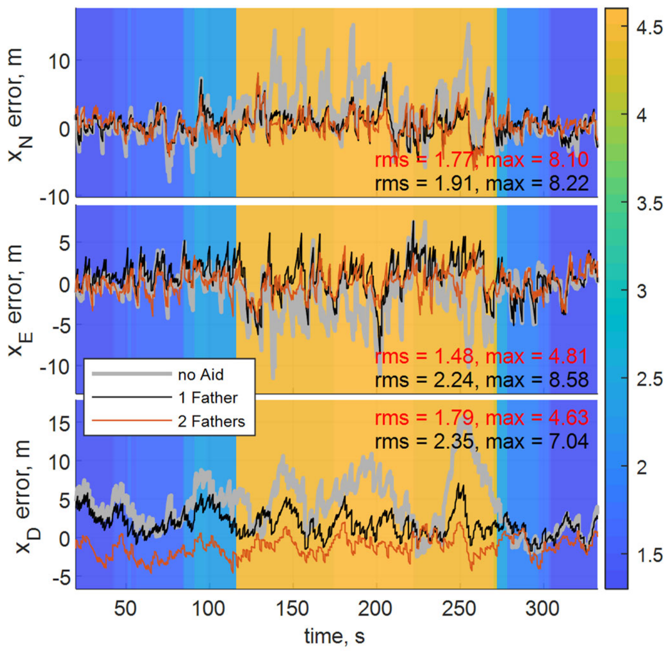

Figure 3.27 Son's navigation results, building inspection scenario. Son-to-Father camera aiding with one or two fathers. Father 1: Az = -110°, El = 12°, r = 40. Father 2: Az = 180°, El = 10°, r = 30. Background color represents the value of the DOP the son would encounter without father's support.

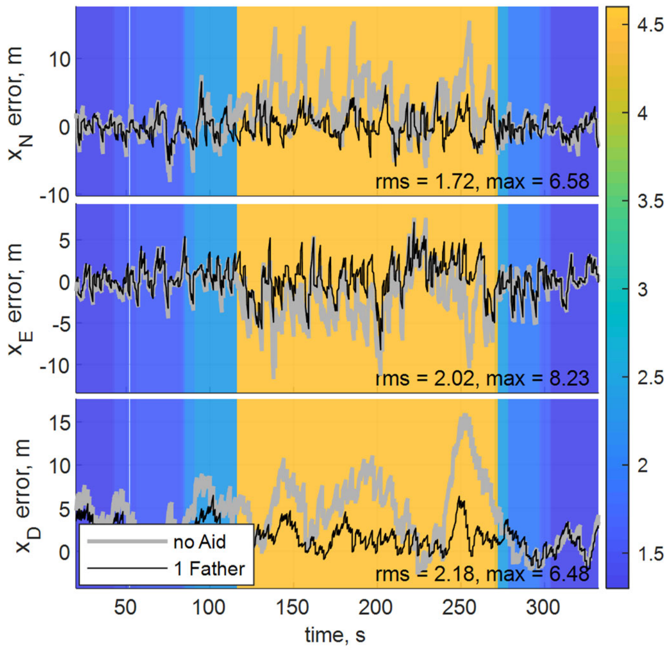

Figure 3.28 Son's navigation results, building inspection scenario. Father-to-son camera aiding. Father Az = -110°, El = 12°, r = 40. Background color represents the value of the DOP the son would encounter without father's support.

When RF-ranging is used two possible formation geometries are considered, namely α and β. The first case assumes the son-father formation geometry is the one that minimizes the camera geDOP, highlighted by the red asterisk in Figure 3.18.a. Whereas, case β assumes the father to be placed in order to minimize the geDOP when RF-ranging is used, i.e. the red asterisk in Figure 3.19.a.

As shown by Figure 3.29, formation α does not improve the filter performance with respect to the non-cooperative case, remarking the fundamental role of correctly choosing the position of the father based on the used sensor. Conversely formation β that has designed with the aim of exploiting RF-ranging measurements returns an improved performance of the cooperative navigation, with respect to the case without external aiding. This occurs especially in the north and down directions. Indeed, range aiding cooperation work mostly along the direction of the separation between the two platforms. Hence, having an azimuth of almost 180° means the two vehicles separation on the horizontal plane is along the north direction. In addition, having a non zero elevation means the vehicle separation has a component also along the vertical direction, which explain why the north and the down components are the most aided by this formation.

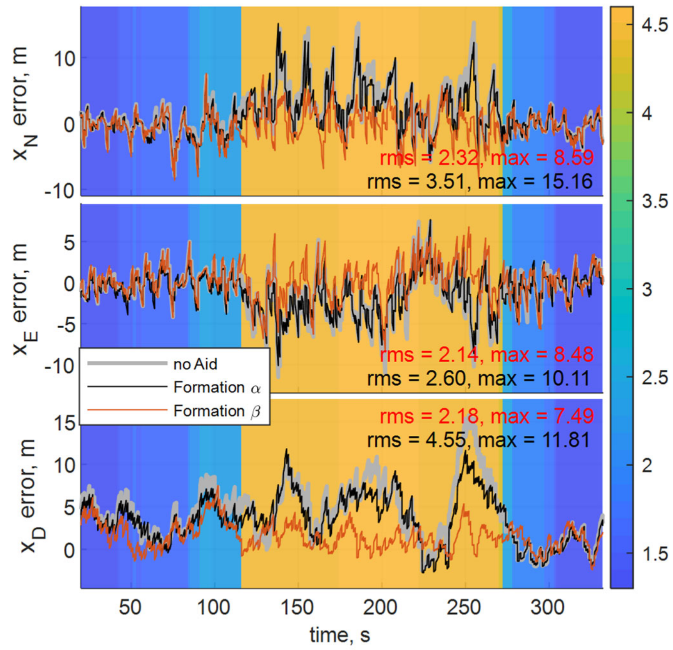

Figure 3.29 Son's navigation results, building inspection scenario. RF-ranging aiding. Formation α assumes father's Az = -110°, El = 12°, r = 40. Formation β assumes father's Az = 145°, El = 50°, r = 40. Background color represents the value of the DOP the son would encounter without father's support.

3.6 EXPERIMENTAL RESULTS

To assess the effectiveness of the proposed strategy in guaranteeing a bounded error in state estimation when flying under non nominal GNSS coverage, the navigation algorithm has been tested on experimental data. The flight test was conducted on June 17th 2019, outdoor in at a model aircraft airfield. The experimental setup used to collect data is described in section 3.6.1. Whereas, flight results are reported in section 3.6.2.

3.6.1 Experimental Setup

A couple of customized DJI™ M100 platforms has been used to conduct the experimental flight. In order to acquire data relevant for this thesis experiment, the two drones have been equipped with a camera and a raw GNSS receiver. Indeed, the DJI software development toolkit (SDK) does not provide the user with raw GNSS capabilities. The two drones, respectively named Eagle and Athena have been equipped with the following elements

- Eagle is a DJI™ M100 UAV equipped with an onboard computer (Intel NUC™ with an i7 CPU running Ubuntu 14.04). The drone embarks a CCD camera (PointGrey Flea™ FL3-U3-20E4C-C with 1600 X 1200 resolution in pixels and maximum frame rate of 59 fps, equipped with 8 mm focal length optics, with a resulting IFOV of about 0.030°) and a GNSS single frequency receiver (uBlox™ LEA-M8T) with raw measurements capabilities.

- Athena has as onboard computer an Intel NUC™ with an i5 CPU, running Ubuntu 16.04. It is equipped in analogy to is pair with a GNSS single frequency receiver (uBlox™ LEA-M8T) with raw measurements capabilities. The drone embarks as visual instrument a CCD camera (PointGrey Blackfly™ BFLY-U3-50H5C-C with 2448 X 2048 resolution in pixels and maximum frame rate of 7.5 fps, equipped with 6 mm focal length optics, with a resulting IFOV of about 0.022°).

The customized setups on board of the two M100 are reported in Figure 3.30 and Figure 3.31. The figures show the two drones embarking the PointGrey™ camera, the ublox™ receiver and its antenna the that has been mounted symmetrically to the DJI GPS antenna.

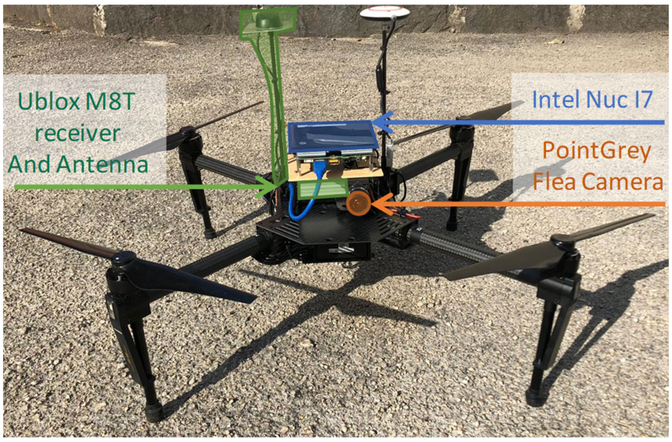

Figure 3.30 Costumized setup on-board the Eagle UAV

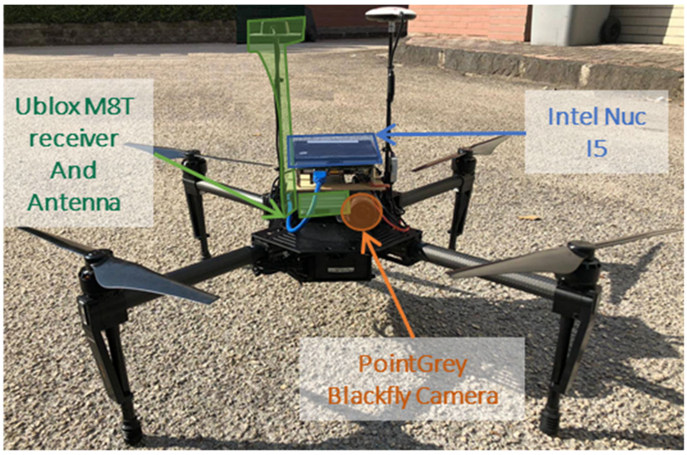

Figure 3.31 Costumized setup on-board the Athena UAV

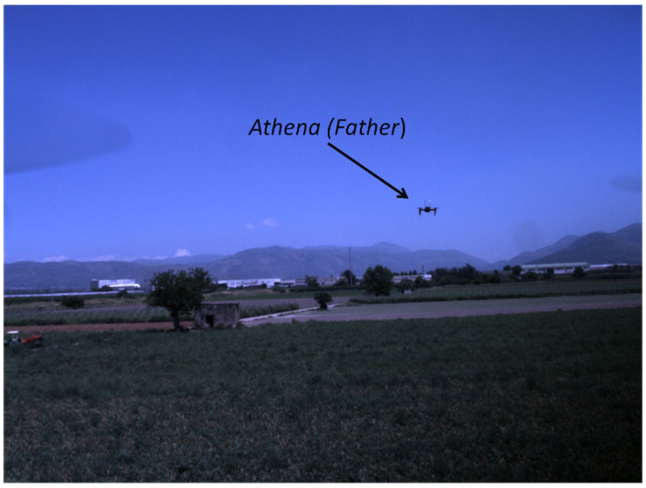

Figure 3.32 Flight Image taken by Eagle

Both the antennas have been placed on a carbon fiber rod higher than the DJI default, to prevent magnetic field interference that could arise in proximity of the onboard computer. In addition, an example of flight image taken by the Eagle's camera is reported in Figure 3.32.

On both the onboard computers, the data acquisition software has been developed in ROS (Robot Operating System). The ROS framework allows to timetag and synchronize data taken by ublox^{TM} receiver, DJI onboard SDK and Pointgrey^{TM} camera. In order to create communicating network between the UAVs and the user, that allows both the UAV to exchange information between themselves and to the user, a multi master network has been used. The network is needed to make the user able to send commands to the platform using a laptop. In addition, an user friendly RViz [129] based software has been developed to allow the user to see the UAV's trajectories in the 3D world where the experiment is conducted.

To the aim of collecting data, the following codes have been developed:

- A customized version of the DJI SDK node that allows retrieving telemetry data of the UAV, along with gyroscope and accelerometer measurements. This node uses the position estimated by the drone to localize itself in the user reference frame. Hence, the user has the full control on drone motion and can visualize its trajectory during the flight.
- The ROS node provided by Pointgrey^{TM} is used to save camera images.
- A ROS based node has been coded in C++ to process online the ublox^{TM} raw data, converting them in user readable variables [130].

The data acquired online have been processed offline and used in a MATLAB® implementation of the filter presented in section 3.3. The satellites position has been calculated using the multi-constellation broadcast ephemeris file. Precise satellite's positions and corrected pseudoranges from ionospheric and tropospheric errors have been obtained thanks to a customized version of the RTKLIB software [131]. Further activities are aimed at the online implementation of the navigation filter, and should include almanac decoding and online processing of the GNSS measurements.

3.6.2 Flight data and Results

As said before, the flight test has been performed outdoor under nominal GNSS condition, setting only GPS and GALILEO receiver capability on both the ublox™ devices. Performing the fight under nominal GNSS coverage allowed to have a very accurate estimate of the drone position through the DJI filter, to be used as benchmark. Therefore, GNSS-challenging condition have been simulated offline by assuming a virtual 3D environment and removing the satellites, whose ray-path intersects the surrounding obstacles. Specifically, a bridge inspection scenario, depicted in Figure 3.33, has been used.

Figure 3.33 shows the trajectories of the two vehicles (son and father) in the 3D environment, composed by a virtual bridge, located above the trajectory of the son. Eagle, whose trajectory is depicted in blue has been used as son, whereas Athena played the role of father. The DOP of the son with removed satellites is reported in Figure 3.33 with the colored dots, showing very bad navigation performance of the GNSS-IMU navigation filter. Conversely, using cooperation bounds the navigation error that is mostly inside the 3σ bound, as shown in Figure 3.34, including the East-North-Up components as estimated by the EKF. The figure compares the solution of the uBlox™ and DJI™ navigation filters estimated under nominal GNSS coverage, with the solution of the cooperative filter obtained using son-to-father visual tracking aiding. The filter solution is bounded. Seldom is the filter estimate outside the 3σ bound, that is reported in gray in the picture. It is estimated accounting for the predicted geDOP with equation (3.40). Those rare events are related to uncorrected pseudoranges and or sudden manoeuvres of the son. Due to the camera orientation, the value of the geDOP is higher on the east component, than in the north, because camera boresight is almost parallel to the east direction. However, using cooperative measurements allows reducing considerably the vertical error, even if compared with the performance of the stand-alone GNSS fix obtained under nominal coverage,

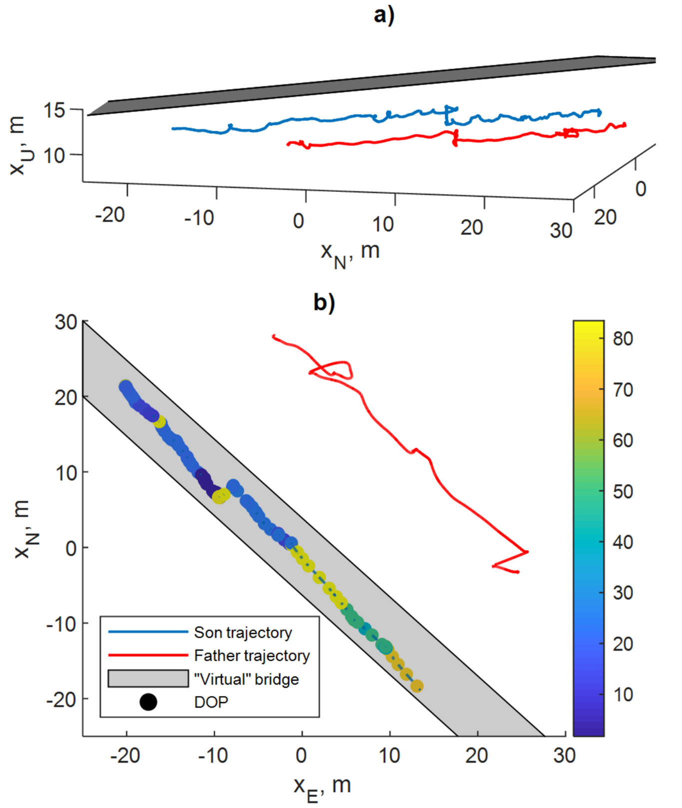

Figure 3.33 Trajectory of the two UAVs and simulated bridge. The colored dots represent the DOP of the son with removed satellites due to the obstacles.

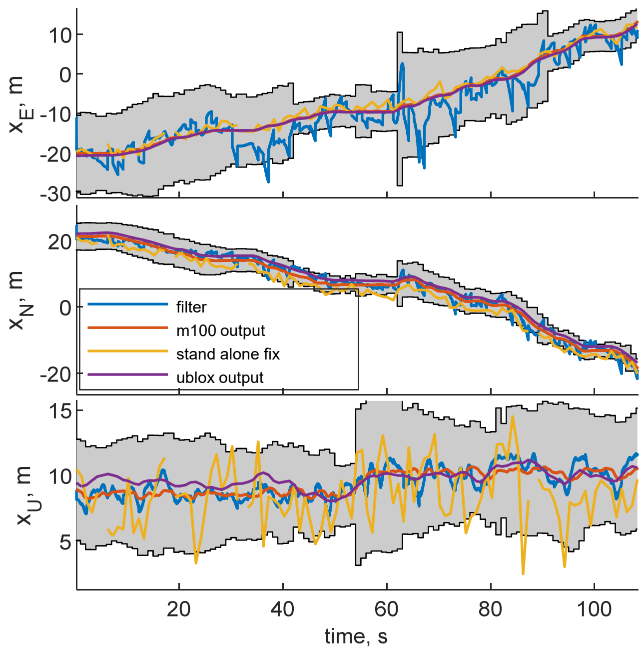

Figure 3.34 Results of the cooperative navigation algorithm using son-to-father visual tracking on experimental data. Galileo and GPS satellites are used. The gray background defines the 3σ bound interval

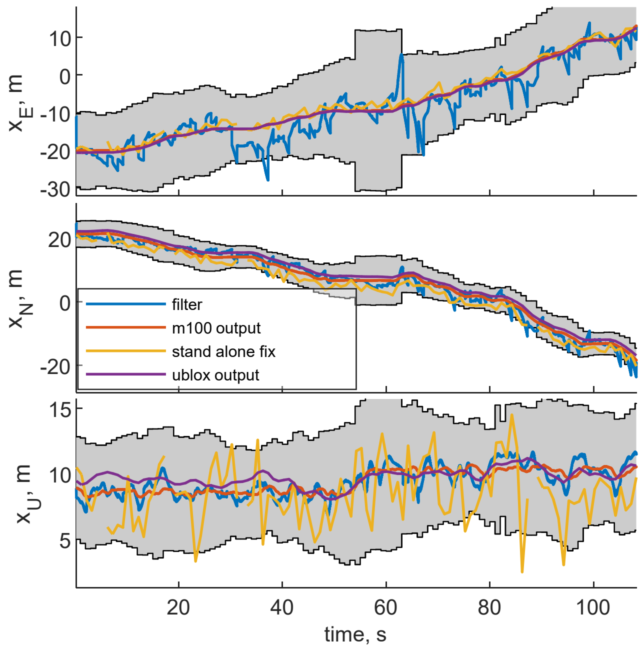

Figure 3.35 Results of the cooperative navigation algorithm using son-to-father visual tracking on experimental data. Only GPS satellites are used. The gray background defines the 3σ bound interval

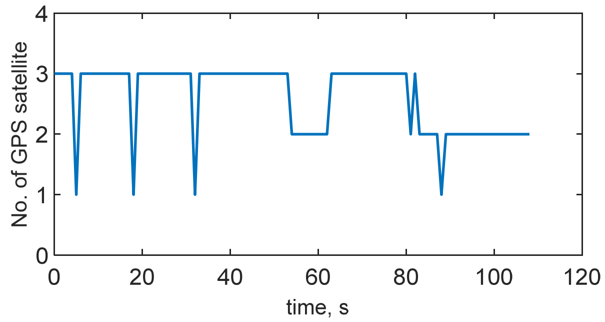

Figure 3.36 Number of GPS satellites seen by the son (Eagle) UAV under the simulated bridge.

reported with yellow line in the figure.

For the sake of completeness Figure 3.35 reports the filter solution if only the GPS satellites are used. As expected, removing the Galileo satellites increases the value of the geDOP, due to the reduced pseudoranges measurements, that reduces the filter observability. Nevertheless, the filter performance slightly differs from the case in which also Galileo satellites are used. Even without Galileo measurements, the filter errors are kept within the 3σ bound, demonstrating the effectiveness of the filter to operate in very challenging conditions. To remark this aspect Figure 3.36 shows the number of GPS satellites in view of the son. In the case only GPS constellation is used the number of the satellites is always below the prescribed value, i.e. 4, to perform the GNSS fix.

Chapter 4: Planning and Guidance of a Tandem UAV formation

The previous chapter described a navigation strategy for enabling navigation in GNSS challenging environment, by means of cooperative UAVs. Specifically, several relative measurement sources (i.e. camera and/or RF ranging) are used in the navigation filter, along with the GNSS satellites seen by the platform in the challenging area, termed "son". For cooperation to be effective, the relative geometries between the son UAV and the cooperative flying platforms (named "fathers") must be chosen properly [121]. To this aim the concept of generalized DOP (geDOP) has been introduced to quantify the navigation accuracy of the son in function of the relative positioning of the fathers. This chapter introduces a path planning algorithm for a tandem formation (one father and one son), which aims at defining the trajectory for the two vehicles in terms of 3D position and heading angle to maximize the son state estimation accuracy thanks to the father aiding.

First, an overview of planning techniques is given in section 4.1, hence section 4.2 includes assumption and discussion about the available formation geometries. Finally section 4.3 and 4.4 presents respectively an offline and online path planning strategy.

4.1 RELATED WORKS

The problem of planning in GNSS challenging or denied environments has often been tackled by routing a single UAV from a start to an end location using external fixed or mobile devices that aid its localization. In this case, planning consists in defining a trajectory that minimizes the state covariance [132–134]. However, when the mission of the UAV is not goal-oriented, and its path is defined to accomplish exploration or reaching multiple locations, this strategy is no longer available. References [94, 135] address the path planning problem when more than one target must be reached in the denied zone, by defining an optimization algorithm for placing fixed external positioning devices (landmarks). This technique implies that the fixed target must be moved when the planned path of the UAV changes, e.g. by considering a different position or number of targets.

Fixed landmark strategy requires precise knowledge of landmarks position that must be equipped with proper localization sensors. Moreover, the fixed landmarks must be positioned in the environment before the mission is executed by a ground robot or a human operator, increasing the mission time. Landmark positioning is limited by the accessibility of the target position by human or robot operator, and is not adaptive to online trajectory replanning. Using as landmark a mobile device, i.e. a collaborative ground or aerial vehicle, reduces the mission time and improves the performance of the navigation filter due to the increase of the available formation geometries. In addition, it allows to assist the UAV in the challenging area with a single platform, instead of multiple fixed devices.

Reference [9] introduced a planning technique for a ground cooperative platform (UGV) that assists an UAV during its flight in a challenging area. An RF ranging system measures the distance between the two vehicles that is used as cooperative measurement. The UGV defines its trajectory step by step with the aim of optimizing the cooperation effect in a local greedy manner. This technique is not directly applicable to a cooperative flying platform, also due to the need of ensuring small accelerations and thus smooth attitude dynamics. Indeed, large and quick attitude variations can affect the availability of cooperative measurements. As an example, in the case a strapdown camera is mounted on the father, a sudden manoeuvre could lead the son outside of the father's camera field of view.

4.2 TANDEM PLANNING CONCEPT

The technique presented in this chapter solves the problem of path planning in GNSS challenging environments using the father as external mobile device that is aimed at the son navigation performance improvement. On the other hand, the son is responsible solely for performing the required mission (through a 3D trajectory that can be pre-computed offline, or re-planned online), without considering its localization as an additional objective. The 3D trajectory planning algorithm for the son is thus independent from the knowledge of the GNSS constellation coverage and it only relates to mission accomplishment, e.g. classification, monitoring [29], searching, tracking, inspection [33], etc. Nonetheless a coarse map of the environment (non-detailed occupancy map of surrounding infrastructure, building and ground elevation) must be available to predict the extension of the challenging areas. Whereas, the planning strategy for the father UAV is aimed at minimizing the son navigation error and to avoid entering in challenging areas.

A forward-looking strapdown camera mounted on the son is used as relative sensing instrument. Using a strapdown camera prevents some relative geometries to be performed. As an example, forward looking camera cannot be used for a vertical geometry. Therefore, this restrict the scenarios of interest of the proposed planning technique to environments that require horizontal or quasi-horizontal baselines between the father and the son.

This section is in charge of defining the application scenarios and the available strategies for tandem planning, respectively in section 4.2.1 and 4.2.2. Then the son's navigation equations are detailed in section 4.2.3.

4.2.1 Application scenarios

In general, GNSS challenging scenarios can be divided in three classes:

- GNSS shadow from one side, e.g. building inspection
- GNSS shadow from above, e.g. flight under bridges
- GNSS shadow from two sides, e.g. flight in urban or natural canyon

Figure 4.1, Figure 4.2 and Figure 4.3 show the variation of geDOP norm with azimuth and elevation of the relative formation, respectively in building inspection, bridge inspection and canyon scenarios. In the canyon scenario the UAV is placed at the center of a canyon. Whereas the bridge inspection scenario assumes the UAV is flying under a bridge. The building inspection scenario assumes the UAV is flying parallel to a building with a variable distance (Δ). Figure 4.2 and Figure 4.3 analyse the variation of the geDOP map as a function of the width of the bridge or the canyon, respectively. The three figures have been estimated assuming a multi-constellation (GPS + GLONASS) receiver. Canyon enlargement, as well as increasing distance between building and UAV in the building inspection scenario produces, as expected an improved value of geDOP. Whereas, in the bridge inspection scenario a reduction of the bridge width increases the number of available relative formation and reduces the geDOP. Father placement in the canyon scenario become complex when the canyon width decreases and prefers formations with high elevation that cannot be fulfilled in the case of a forward-looking camera. On the other hand, bridge and building inspection scenarios allows the father to assume a low elevation with respect to the son that can be handled with a strapdown forward-looking camera.

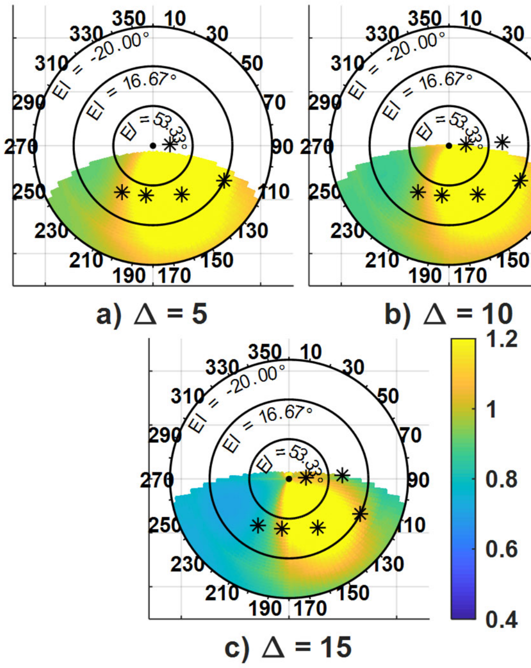

Figure 4.1 Norm of the geDOP as a function of elevation and azimuth of the father with respect to the son in building inspection scenario. The distance between the two platforms r = 40 m. The UAV is flying at with a distance from the building (Δ) equal to a) 5 m, b) 10 m, c) 15 m. Black asterisks indicate satellites seen by the son UAV.

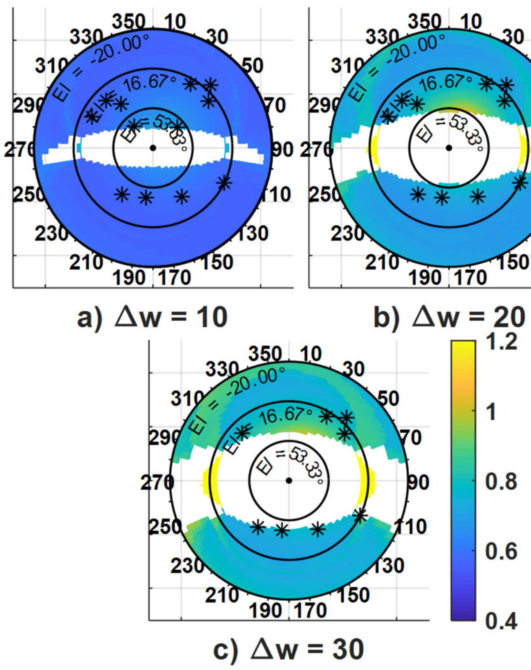

Figure 4.2 Norm of the geDOP as a function of elevation and azimuth of the father with respect to the son in bridge inspection scenario. The distance between the two platforms r = 40 m. The UAV is flying under a bridge with width (Δw) a) 10 m, b) 20 m, c) 30 m. Black asterisks indicate satellites seen by the son UAV.

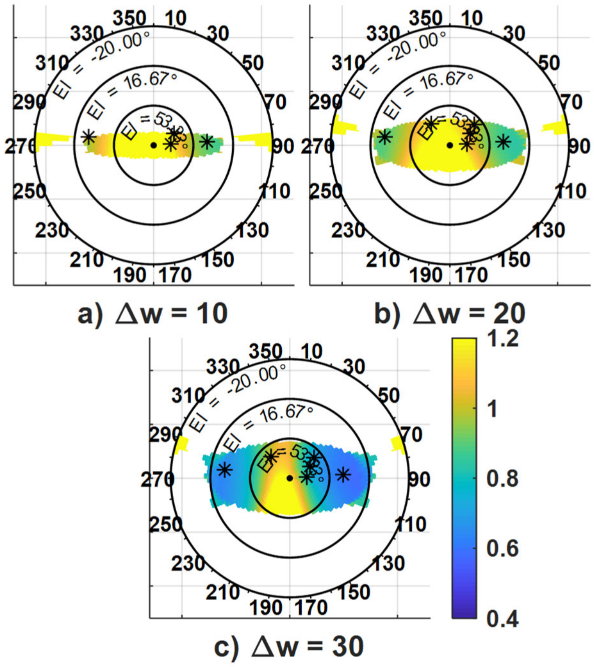

Figure 4.3 Norm of the geDOP as a function of elevation and azimuth of the father with respect to the son in canyon inspection scenario. The distance between the two platforms $r = 40$ m. The UAV is flying at the center of a canyon with width (Δw) a) 10 m, b) 20 m, c) 30 m. Black asterisks indicate satellites seen by the son UAV.

4.2.2 Cooperative Strategies

Father-to-son relative position can be defined accounting for the geDOP minimization. However constant relative position is hard to keep during the whole flight due to the complex shape of the challenging volume where the father should not enter. Very complex challenging scenarios could suggest using a static father and a moving son. Nevertheless, a static father could easily lead to cooperation failure. Indeed, the son motion changes the relative azimuth and elevation, that could bring the father in locations where the cooperation is not effective, i.e. the yellow areas in Figure 4.1 to Figure 4.3. In addition, father placement becomes even more complex due to the ever changing geDOP map as a function of the son's position and the in-view satellites. In view of this requirement a planning strategy that accounts for relative position variation along the trajectory is needed. Figure 4.4 shows the map of the challenging volume in an urban canyon environment, i.e. a complex of some buildings near to south Cove park in lower Manhattan, depicted in Figure 3.12. A case like the one in the figure can be solved by making the father fly at constant azimuth and elevation above the challenging volume. Nevertheless, one must avoid elevation higher than 70 degrees that are not advantageous for the cooperative navigation, as the geDOP plot in Figure 4.3 indicates. This requires a long range between father and son, especially when the son must fly near to the ground with high altitude of the canyon. However, an increasing range degrades the cooperative navigation performance especially in the son-to-father tracking. With a short and straight canyon, a viable option is to place the father at the end of the canyon, far from the challenging volume. The father UAV must move in a plane normal to the canyon direction to keep constant the relative azimuth and elevation, whilst the son's motion modifies the range. On the other hand, bridge and building inspection scenarios provide the father a wider range of positions from where assist the son during its flight and a less obstacle dense volume where the father can move. Those scenarios prefers small elevation of the relative formation, see Figure 4.1 and Figure 4.2 and suggest the father should move in a quasi-parallel trajectory with respect to the son.

Therefore, a general rule for father trajectory planning cannot be defined, but it does depend on the considered scenario and on the sensor used for relative positioning estimation. Planning and guidance strategies presented in the next sections (4.3 and 4.4) are aimed at planning for father's trajectory in case of:

- Tandem formation (one father and one son)
- Horizontal scenario (i.e. bridge or building inspection)
- Forward-looking camera mounted on the son used as relative sensor

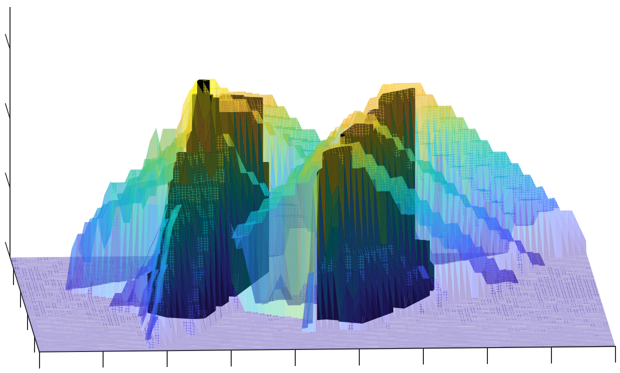

Figure 4.4 Map of the challenging volume in an urban canyon environment. Buildings are reported in black, and their shadows obtained with a DOP threshold equal to 1.2 is reported as colored in function of the challenging volume altitude.

4.2.3 Navigation equations

As assumed before, tandem path planning has been derived assuming the cooperative sensing is performed thanks to a strapdown camera mounted on the son. This section is in charge of detailing the measurement matrix of the son's navigation filter, that can be derived from the general mathematical formulation reported in equations (3.35). With the assumption of one father and son-to-father visual tracking, the measurement vector, to be used in the correction step of the EKF described in section 3.3 becomes:

$$\delta \mathbf{y} = \begin{bmatrix} \delta \mathbf{y}_{GNSS} \\ \hline \delta \mathbf{y}_{M} \\ \hline \delta \mathbf{y}_{EO}^{s \to f} \end{bmatrix} \tag{4.1}$$

Hence, the measurement matrix for the specific combination of sensor used for this application, is

$$H = \begin{bmatrix} H_{GNSS\mathbf{p}} & 0_{m\times3} & 0_{m\times3} & 0_{m\times6} \\ \hline 0_{1\times3} & 0_{1\times3} & H_{M\boldsymbol{\rho}} & 0_{1\times6} \\ \hline H_{EO\mathbf{p}}^{s\to f} & 0_{2\times3} & H_{EO\boldsymbol{\rho}}^{s\to f} & 0_{2\times6} \end{bmatrix} \tag{4.2}$$

4.3 OFFLINE TANDEM PLANNING

This section presents an offline approach to the tandem planning for cooperative platforms in GNSS challenging environment. A planning technique for generating the father's 3D trajectory, which aims at minimizing the son's state estimation error is introduced. Father planning should take into account the constraint that the two vehicles must remain within LOS and should ensures the father is always outside the GNSS challenging areas. In addition, to ensure that the cooperative measurements are always available, a yaw planning strategy for the son vehicle is introduced in order to guarantee continuous son-to-father visual tracking. Yaw planning is not needed in the case an omnidirectional or a gimbaled camera is used.

To the aim of defining the offline-planning strategy, GPS only constellation has taken into account. Section 4.3.1 analyzes how generalized DOP concept can be used to define the father's optimal position. Section 4.3.2 introduces the planning algorithm for father aiding, hence simulation results are described in Section 4.3.3.

4.3.1 Generalized DOP dependence on formation geometry

As demonstrated in [121], the Generalized DOP can be used as an instrument for defining the best position of the father with respect to the son. In general, the best relative geometry, i.e., the father position that minimizes the son estimation error is strictly related to the sensors that are used for the son's state estimation. This section aims at evaluating how the Generalized DOP, and thus the son's navigation accuracy with cooperative measurements, varies as a function of the relative geometry between the father and the son for the specific combination of sensors, whose measurements are reported in equation (4.1). In addition, the best position for the father is evaluated while changing the son's position. This step plays a fundamental role for assessing the father's path planning and defines the main parameters (relative geometry components) that must be considered when planning for the father trajectory. The results presented in this section have been evaluated for the specific combination of sensors described in Section 4.2.3, but a general rule of thumb can be obtained on the basis of the discussion that follows.

The planning described in this section uses the simplified version of the geDOP in order to define the optimal placement for the father platform, moreover the father position accuracy is assumed to be constant along the whole trajectory. Figure 3.9, that is reported here in for the sake of completeness (Figure 4.5), shows the Generalized DOP mainly depends on azimuth and elevation. Even if admissible father positions reduce with the range, the value of the norm value of the Generalized DOP does not change or change slightly with the range. Therefore, the main parameters that must be accounted for, while defining the best positioning of the father are the azimuth and the elevation, whereas the range must only be compliant with the main requirements that a vehicle must satisfy as a father, i.e., it must fly outside a challenging zone and must hold a LOS contact with the son. Figure 4.5 shows that the norm of the Generalized DOP can range from 1 to a value greater than 7 with azimuth and elevation. Ref. [121] demonstrates that the son filter performance is highly dependent on where the father is placed, e.g. if the father azimuth and elevation lean in the yellow area the son navigation filter will diverge even if the cooperative measurements are available. Hence, the azimuth and elevation parameters must be chosen properly to support son filter performance improvements.

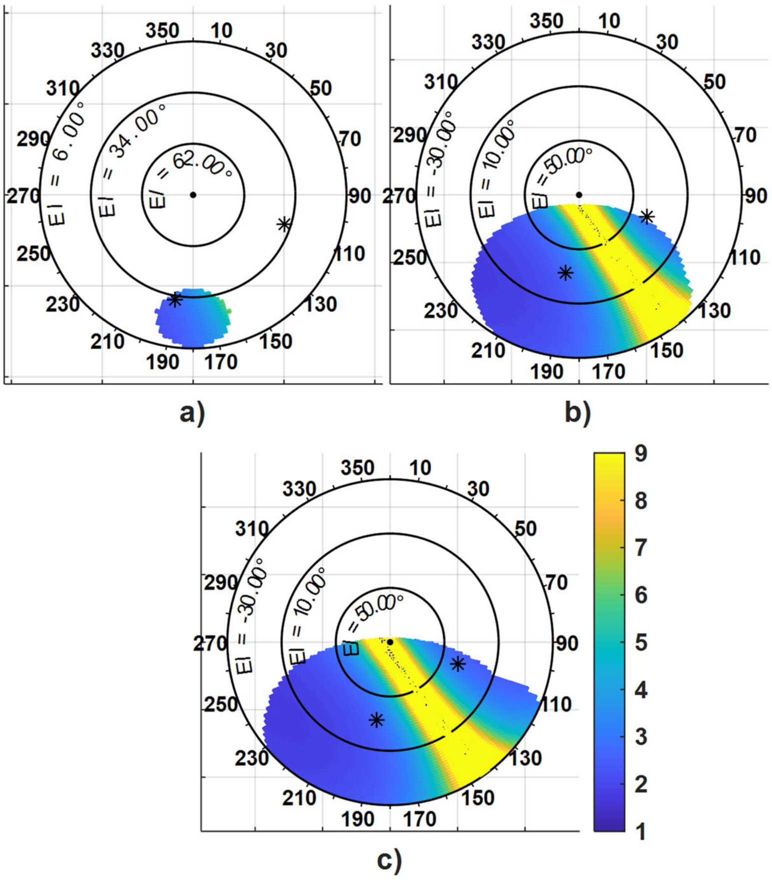

Figure 4.5 Norm of the generalized DOP in function of Azimuth and Elevation of the father with respect to the son. Son father range are a) 10 m, b) 20 m and c) 30 m. Son-to-father visual tracking and constant father positioning accuracy.

It is interesting to estimate how the main parameters for father planning, i.e. azimuth and elevation, vary with the available GNSS satellites. For this purpose, the son UAV is routed along a constant altitude (20 m) path in the proximity of the building, which north and east coordinates are shown in Figure 4.6.a. Figure 4.6.b and Figure 4.6.c show the optimal azimuth and elevation in function of the trajectory time. The background shade in these two subfigures highlights the number of satellites that the son observes along its trajectory. The best azimuth and elevation are shown only in the case the number of satellites is lower than four, i.e., when son requires the father for estimating its state with high reliability. Indeed, as said in section 3.2.1, when a single GNSS constellation, i.e. GPS, is used the challenging area is defined based on the number of satellites in view of the UAV, and 4 is the minimum number of satellite to deem a point in the space outside the challenging area.

It can be observed that the azimuth and the elevation of the father which optimize the son's navigation performance depend on the number of satellites seen by the son.

This implies that, for each interval in which the number of satellites is constant and lower than four, also the azimuth and the elevation of the father must be constant, so that their optimal values can be estimated once for each interval, e.g., by referring to the time instant when the number of satellite changes. In addition, in the area in which the number of satellites is greater than four, the son can estimate its state with high reliability without referring to cooperative measurements; in these regions, the father can have an arbitrary azimuth and elevation.

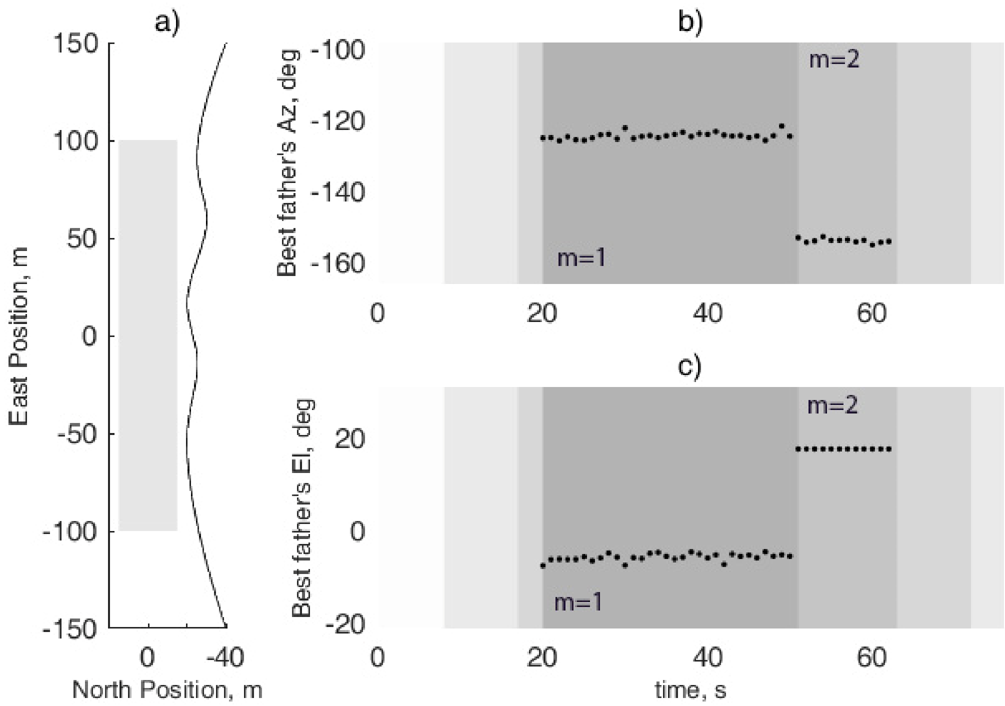

Figure 4.6 Best azimuth and elevation in function of the path performed by the UAV. a) shows the north and east coordinates of the path, hence b) and c) show the azimuth and elevation that the father must hold with respect to the son trajectory in order to maximize the accuracy of the cooperative navigation solution

4.3.2 Tandem Path planning

The tandem path planning assumes the son trajectory to be a polynomial 3D spline, which includes the 3D position of the UAV and the corresponding time stamp. This trajectory is obtained by optimizing the polynomial coefficients while fixing the first coefficient for each segment, i.e., the waypoints the UAV must visit [136, 137]. Knowing the son’s planned 3D trajectory, one can estimate the corresponding number of satellites observable at each time instant by simulating the GNSS constellation at a specific time epoch (day and hour) and removing all the GNSS measurements whose signal is obstructed by the surrounding environment. The estimation of the number of satellites seen by the son and the identification of the intervals in which this number remains constant is fundamental for tandem path planning, since it defines the interval in which the father's relative positioning with respect to the son must be constant, as stated in section 4.3.1. It is assumed that the trajectory planned for the son does not require a specific attitude, such that it can be defined to always point the son's camera towards the father. It is assumed that the son yaw angle has to guarantee that the father is always in the son's camera field of view (FOV) when father-to-son relative orientation changes, whereas roll and pitch angle are assumed to change in function of the UAV dynamics. In general they will be relatively small since the polynomial trajectory optimization has the purpose of minimizing the trajectory snap [136].

Algorithm 1 reports the pseudo code for the tandem path planning algorithm. It can be divided into three main steps: (1) identifying the interval in which the father's relative position, and thus the son's yaw, should be constant, (2) planning the father's trajectory, and (3) planning the son's yaw. These steps are described in the following sections.

Algorithm 1: Tandem Path Planning

Input: ***son3D*** **// 3D trajectory of the son**
time **// the time stamp of son trajectory**
B **// occupancy map of the surrounding environment**
day,hour **// day and hour at which the simulation is referred to**
orLlh **// geographic coordinates of local frame's origin**
(I_p, t_s, t_c, m_p) ← DEFINE_PLANNING_INTERVALS (*son3D*, *time*, *B*, *day*, *hour*, *orLlh*);
(Az_p, El_p, r_p, Δt_p, *fath3D*) ← FATHER_3D_PLANNING (*son3D*, *time*, *B*, *day*, *hour*, *orLlh*, t_s, t_c, m_p, I_p);
(*sonYaw*) ← SON_YAW_PLANNING (t_s, Az_p, El_p, r_p, Δt_p, *time*);
Return: ***fath3D*** **// 3D trajectory of the father**
sonYaw **// son yaw sequence**

4.3.2.1 Planning Interval Identification

Planning interval identification is responsible for defining the interval in which the main parameters of the relative father-son geometry, i.e., azimuth and elevation in the specific case of the presented algorithm, and the nominal yaw angle for the son are constant. In addition, the starting and characteristic times for each interval must be defined. The characteristic time specifies the reference time at which the optimal main parameters are estimated for each interval. The interval where the number of satellites is constant and equal to m+1 is named m-interval. For a generic trajectory, the plot of

m-intervals can be assumed as the one in Figure 4.7 a, where the number of m-intervals, i.e. I_m = 11.

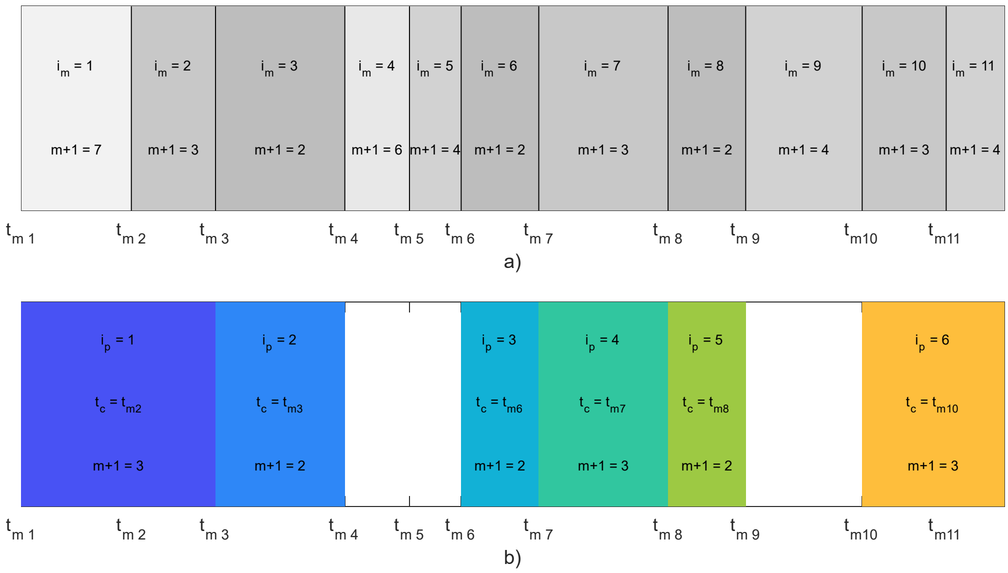

Figure 4.7 Interval procedure definition, a) identification of the m-interval at varying the number of satellites seen by the son, b) identification of the primary interval and definition of characteristic time t_c and m.

As stated above (see Section 4.3.1), it is assumed that whatever are the main parameters identifying father son relative position in the area in which the number of satellites is at least equal to four, the son is able to estimate its position with high reliability. Hence, the azimuth and the elevation of the father in these zones does not affect the cooperative navigation solution, thus can be set arbitrarily. In the zones where the number of satellites $(m+1)<4$, the azimuth and elevation of the father assume a critical role for the son's navigation. Therefore, in those intervals the azimuth and the elevation of the father must be set properly. The intervals where father's support is needed are deemed planning intervals (i_p), that are the colored sections in Figure 4.7.b. The number of planning intervals is equal to the number of the m-intervals where $m<3$. m-intervals with a duration shorter that 3 s are not accounted when defining the planning intervals even if the number of satellites is smaller than four, since the time in which the son remains in that area is negligible, and does not warrant moving the father. Those areas indeed are included in the near m-interval with the lowest m, named primary interval. The last planning interval extends until the trajectory is completed, this means in the last instants of the trajectory elevation, azimuth and range of the formation remains the same of the last interval when the father cooperation is needed even if the number of the satellites is enough to guarantee a reliable navigation solution. This occurs also for the first planning interval that is extended backward until the beginning of the trajectory. When considering merged intervals, e.g. $i_m = 10$ and $i_m = 11$ in Figure 4.7.a the relative formation to be considered is the one of its primary interval, i.e. $i_m = 10$. The characteristic time (t_c) of each planning interval is the starting time of its primary interval, as the number of satellites that identifies each planning interval is equal to the number of satellites of the corresponding primary interval. Figure 4.7.b identifies the planning intervals and defines the characteristic time and the number of satellites for each. The I_{nc} merged intervals where the father needs no cooperation are reported in white in Figure 4.7.b.

4.3.2.2 Planning for Father 3D Trajectory

As shown in Figure 4.7.b father 3D trajectory can be seen as decomposed in I_p segments, in which the father must have constant azimuth elevation and range with respect to the son, and I_{nc} intervals where the father can assume an arbitrary relative position with respect to the son. The father's trajectory planner is in charge of identifying the parameters that define the optimal relative geometry for each planning interval (azimuth, elevation and range of the father with respect to the son) and the trajectory needed for the father UAV to pass from the geometry required in the interval i_p to the one required in the interval i_p+1.

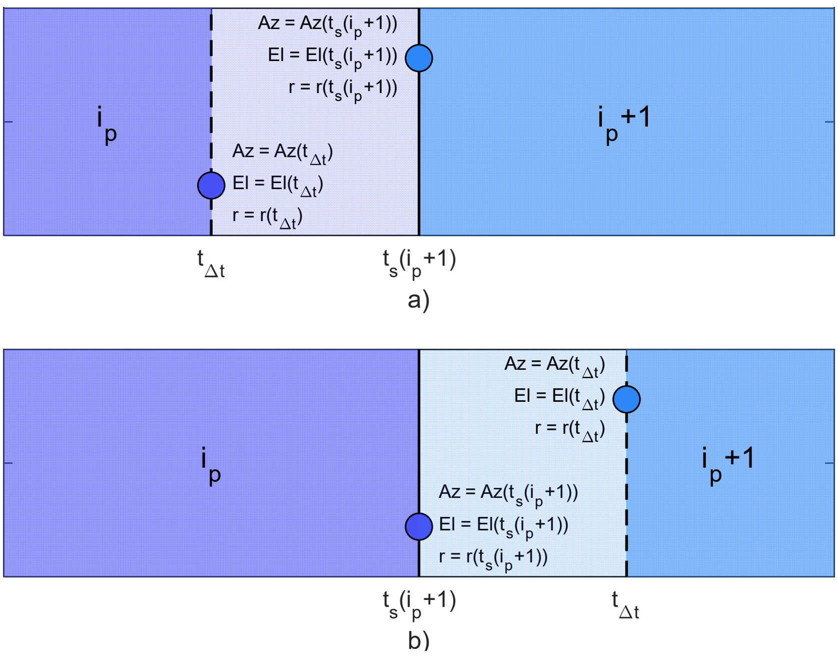

Figure 4.8 Transition between two subsequent planning intervals, i.e. i_p and i_p+1. Case a) $m(i_p+1) < m(i_p)$, case b) $m(i_p+1) > m(i_p)$.

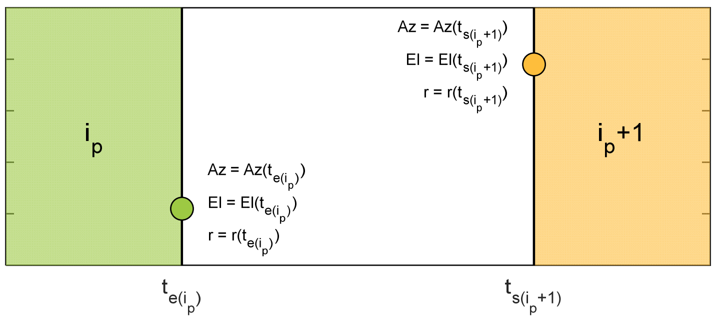

Figure 4.9 Transition between two non-contiguous planning intervals. t_e and t_s are the start and end time of the planning intervals.

The trajectory between two planning intervals is identified as transition. The transition can occur between two subsequent planning intervals, e.g. $i_p = 1$ and $i_p = 2$ in Figure 4.7.b, or between two non-consecutive planning intervals, e.g. $i_p = 2$ and $i_p = 3$ in Figure 4.7.b.

In the first case (see Figure 4.8) the transition between two given configurations occurs within the planning intervals and it is performed with the aim of reducing the time for transition, i.e. Δt_{i_p} named transition time. It is assumed the transition always occurs in the interval with the highest m. This is to ensure that, when the son is in an interval where the number of observed satellites is the lowest possible, the father is always placed in the relative geometry required in that interval for improving the son's navigation performance, without transitioning to another configuration.

Conversely in the case when two non-consecutive intervals are considered, as reported in Figure 4.9, the transition time is already defined by the time separation between the two intervals. Indeed, it can be defined as the time difference between the start time of the next planning interval $t_s\left(i_p+1\right)$ and the end time of the current one $t_e\left(i_p\right)$. The trajectory of the father in this interval is defined with the aim of minimizing the trajectory snap.

It is assumed that during its trajectory, excluded the transitions, the father has always the same velocity of the son in order to keep constant their relative position. The father path planning algorithm, whose pseudocode is in Algorithm 2, is divided in two steps. The first step is in charge of defining the optimal main parameters for each planning interval, i.e. azimuth and elevation, then the second step specifies the distances between the two UAVs (ranges) for each interval and the transition times, that are to be defined only in the case two contiguous planning intervals are taken into account.

The first step is performed by sequentially iterating through the planning intervals. It defines for each the optimal azimuth and elevation to minimize the norm of the Generalized DOP. This minimization is performed considering the constellation seen by the son at the characteristic time of each planning interval. Although, the azimuth can assume every value, the search space for the elevation is limited to the vertical camera FOV, assuming a camera mounted horizontally and relatively small roll and pitch angles. The best value for the main parameters is obtained using a particle swarm optimization algorithm (PSO) [138].

The second step defines the range and the transition time. The procedure reported in Algorithm **2**, i.e. OPTIMIZE_TRAJECTORY, is another PSO algorithm that aims at minimizing the overall transition time and the trajectory snap.

$$J = J_{pol} + k_t \sum_{i_p=1}^{I_p-1} \left(\Delta t_{i_p} \right)^2 \tag{4.3}$$

where J is the cost to minimize that includes the norm of the jacobian of the polynomial trajectory J_{pol} between the non-contiguous intervals [136], and the squared sum of the transitions time, that multiplies for a scale coefficient k_t.

Algorithm 2: Father 3D trajectory Planning

Input: ***son3D*** **// 3D trajectory of the son**
    time **// the time stamp of son trajectory**
    B **// occupancy map of the surrounding environment**
    day,hour **// day and hour at which the simulation is referred**
    orLlh **// geographic coordinates of local frame's origin**
    t_s **// starting time of the planning intervals**
    t_c **// characteristic time of the planning intervals**
    m_p **// characteristic number of satellites of the planning intervals**
    I_p **// number of intervals**
for $i_p = 1$ **to** I_p **do**
    $(Az_p(i_p), El_p(i_p))$ ← **FIND_BEST_MAIN_PARAMETERS(**$son3D$, $t_c(i_p)$, B, day, $hour$, $orLlh$**)**
end for
$(r_p, \Delta t_p)$ ← **OPTIMIZE_TRAJECTORY(**$son3D$, $time$, m_p, t_s, Az_p, El_p**)**
fath3D ← **FIND_TRAJECTORY(**$son3D$, $time$, r_p, Δt_p, Az_p, El_p**)**
Return: Az_p **// best azimuth for each planning interval**
    El_p **// best elevation for each planning interval**
    r_p **// best range for each planning interval**
    Δt_p **// transition between the planning intervals**
    fath3D **// 3D trajectory of the father**

Algorithm 3: Cost function for PSO algorithm of OPTIMIZE_TRANSITION

```
Input: r_p        // range for each planning interval
       Az_p       // best azimuth for each planning interval
       El_p       // best elevation for each planning interval
       t_s        // starting time of the planning intervals
       son3D      // 3D trajectory of the son
       time       // the time stamp of son trajectory
       I_p        // number of intervals
for i_p = 0 to I_p – 1 do
       Δt_p(i_p)  ← TRANSITION_FROM_RANGE(r(i_p ,i_p+1), Az_p(i_p ,i_p+1), El_p(i_p ,i_p+1),
                    m_p(i_p ,i_p+1),t_s(i_p+1), son3D, time, a_max, v_max) //Algorithm 4
       J          ← SNAP_COST_RANGE(r(i_p ,i_p+1), Az_p(i_p ,i_p+1), El_p(i_p ,i_p+1),
                    t_e(i_p),t_s(i_p+1), son3D)
end for
cost = J_pol + k_t Σ(Δt_p)^2;
Return: cost      // cost function of PSO algorithm
```

The transition time between two subsequent planning intervals, i.e. i_p and i_p+1, can be evaluated when the range, azimuth and elevation are defined, as explained in section 4.3.2.2.1. The PSO for trajectory optimization (OPTIMIZE_TRAJECTORY) thus, receives in input a guess of the range vector, i.e., the range of the father in each interval, and defines the transition time for each pair of contiguous planning intervals and the trajectory snap's cost J_{pol} for the non-contiguous planning intervals. Algorithm **3** shows the pseudocode that defines the cost function for the PSO aimed at trajectory optimization. The minimum range available for each planning interval, is the one which ensures that the father is always in the vertical FOV of the camera and does not enter in the challenging area if its azimuth and elevation are the optimal ones estimated for that interval. This value defines the lower bound for the PSO algorithm search space.

When the transition time between two consecutive intervals is greater than the half of planning interval time, it is not worthy to perform the transition and the consecutive intervals are merged together. The best azimuth and elevation for the merged interval are taken equal to these of the interval with minimum m. Penalization is added to transition cost.

Once the optimal values for the range and the transition time are estimated, these values along with the optimal azimuth and elevation, concur to identify the father trajectory for each planning interval excluded the transition zone. Indeed, the father trajectory in each planning interval is defined as the son's trajectory plus the 3D distance estimated on the basis of the best azimuth, elevation and range in that zone.

The trajectory in each transition zone is defined as the optimal polynomial trajectory [137] that allows for switching from the last position of the father's trajectory in previous planning interval to the first position of the father trajectory in the next planning interval within the transition time.

4.3.2.2.1 Definition of the transition time between two subsequent planning intervals

During each transition the father should move from the best configuration in interval i_p to the one required in the interval i_p+1. The time which identifies the boundary between these two intervals is $t_s(i_p+1)$. The time of transition is unspecified *a priori* but depends on the azimuth, elevation and range of the father in the two consecutive planning intervals, as well as the maximum allowed velocity and acceleration, as described in Figure 4.8. The transition time Δt is positive when the transition occurs in the i_p+1 interval, i.e. $m(i_p+1) > m(i_p)$, and is negative otherwise. It thus possible to define $t_{\Delta t} = t_s(i_p+1) + \Delta t$ that is with $t_s(i_p+1)$ one of the endpoints of the transition. $t_s(i_p+1)$ and $t_{\Delta t}$ are the start and the end points of the transition if $m(i_p+1) > m(i_p)$, and the end and start points otherwise, see Figure 4.8. The velocity $\mathbf{v}$ and the position of the son $\mathbf{p}^n$ at $t_s(i_p+1)$ are estimated by sampling the son trajectory.

The velocity of the father $\mathbf{v}_f$ at $t_s(i_p+1)$ is equal to the son's, whereas its position $\mathbf{p}_F^n$ is equal to the son's plus the 3D distance estimated with the azimuth, elevation and range of the interval i_p when $m(i_p+1) > m(i_p)$, or i_p+1 otherwise, see Figure 4.8. The transition time is defined as the minimum time that guarantees to transit from $\mathbf{p}_F^n(t_{\Delta t})$ to $\mathbf{p}_F^n(t_s(i_p+1))$ accounting for the maximum acceleration and velocity of the father, as stated in Equation (4.4).

$$\Delta t : \begin{cases} t_{\Delta t} = t(i_p+1) + \Delta t \\ \mathbf{v}_f(t_{\Delta t}) = \mathbf{v}(t_{\Delta t}) \\ \mathbf{p}_F^n(t_{\Delta t}) = \begin{cases} \text{if } m(i_p+1) > m(i_p) \\ \quad \mathbf{p}^n(t_{\Delta t}) + \mathbf{d}^n\left(Az(i_p), El(i_p), r(i_p)\right) \\ \text{if } m(i_p+1) < m(i_p) \\ \quad \mathbf{p}^n(t_{\Delta t}) + \mathbf{d}^n\left(Az(i_p+1), El(i_p+1), r(i_p+1)\right) \end{cases} \\ \dfrac{\left\|\mathbf{p}_F^n\left(t_s(i_p+1)\right) - \mathbf{p}_F^n(t_{\Delta t})\right\|}{v_{\max}} \le \Delta t - \dfrac{\left|2v_{\max} - \left\|\mathbf{v}_f(t_{\Delta t})\right\| - \left\|\mathbf{v}_f\left(t_s(i_p+1)\right)\right\|\right|}{a_{\max}}\kappa \end{cases} \tag{4.4}$$

where | | is the absolute value operator, κ is a constant that accounts the time needed for accelerate the father UAV to the maximum velocity and dn is the distance in the NED frame estimated considering a certain azimuth Az, elevation El and range r of the father son geometry. The pseudocode for the algorithm which defines the transition time from the range is defined in Algorithm 4.

Algorithm 4: Transition time from range

Input: Az_i, El_i, r_i **// azimuth elevation and range for planning interval** i
Az_j, El_j, r_j **// azimuth elevation and range for planning interval** $j= i+1$
t_j **// start time of the interval** j
m_i, m_j **// characteristic number of satellites of the** i **and** j **planning intervals**
son3D **// 3D trajectory of the son**
time **// the time stamp of son trajectory**
a_{max} **// maximum acceleration of the father**
v_{max} **// maximum velocity of the father**
if $m_i<m_j$
$Az_f = Az_i$; $El_f = El_i$; $r_f = r_i$;
$Az_m = Az_j$; $El_m = El_j$; $r_m = r_j$;
else
$Az_f = Az_j$; $El_f = El_j$; $r_f = r_j$;
$Az_m = Az_i$; $El_m = El_i$; $r_m = r_i$;
end
(p, v_f) ← SON_VEL_POS(*son3D*, *time*, t_i) **// is the function that samples the son trajectory at** t_i
p_f = p + DIST(Az_f, El_f, r_f);
Δt ← RETURN_DELTA_T(*son3D*, *time*, Az_m, El_m, r_m, a_{max}, v_{max}) **// implements equations (4.4)**
Return: Δt **// transition time between these two segments**

4.3.2.3 Planning for son yaw angle

The yaw angle planning is based on the results obtained in the previous section. Specifically, best azimuth of the father and transition time are accounted. Whereas the best elevation estimated for the father already ensure the son camera to always have it in its vertical FOV. The yaw is constant in each planning interval and is the responsible to direct the camera towards the father. During the transition between the planning intervals i_p and i_p+1 the yaw is planned to change smoothly using a 1D polynomial optimization algorithm [137]. Since is reasonable to assume small the pitch and the roll angles for the son, the yaw ψ of the son's camera in each planning interval is equal to the best azimuth.

$$\psi_p\left(i_p\right) = Az_p\left(i_p\right) \tag{4.5}$$

4.3.3 Results

The main purpose for the planning technique described in the current section is to define a flyable trajectory for the father that allows maximizing the accuracy in son positioning estimation when cooperative measurements are used to overcome the lack of GNSS reliable measurements. Therefore, planning algorithm performance and results are presented along with the performance of the son navigation filter when using cooperative measurement obtained flying the father through the planned trajectory. The simulation has been performed in MATLAB, using the Robotics System Toolbox for ROS/Gazebo interface and RotorS [139]. The simulation scenario represents a real-world environment including a building belonging to the "isola E" complex in the Naples' business center. The 3D geometry of the building, whose Google Maps visualization is shown in Figure 4.10.a, has been exported from the Open Street Map database (Figure 4.10.b) and loaded in Gazebo (Figure 4.10.c) as *.dae file. Two paths are considered as son's trajectories. In the first case, reported in Figure 4.11, the son flies beside the building along a straight line, at a constant altitude of 20 m. The polynomial path along this line has been defined using the start and end waypoints of the path as input of the polynomial optimization algorithm [137]. The son's path is depicted in Figure 4.11, where the top and the lateral view (Figure 4.11.a and Figure 4.11.b) are shown. Figure 4.11.c depicts the north and east position of the son with respect to the simulation time. The background colors in Figure 4.11.c corresponds to the number of satellites seen by the son during its path. The second case, assumes the son to perform a more complex trajectory that identifies more planning intervals than the first case, including both contiguous and non-contiguous. The trajectory is represented in Figure 4.12. The planning and navigation results of the cooperative formation under the two trajectories are reported in 4.3.3.1 and 4.3.3.2.

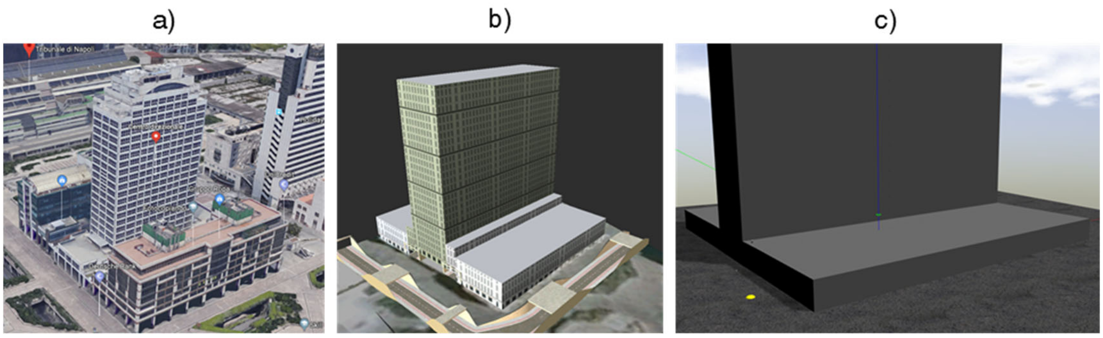

Figure 4.10 Simulation scenario, a) Google Maps, b) Open Street Map, c) Gazebo.

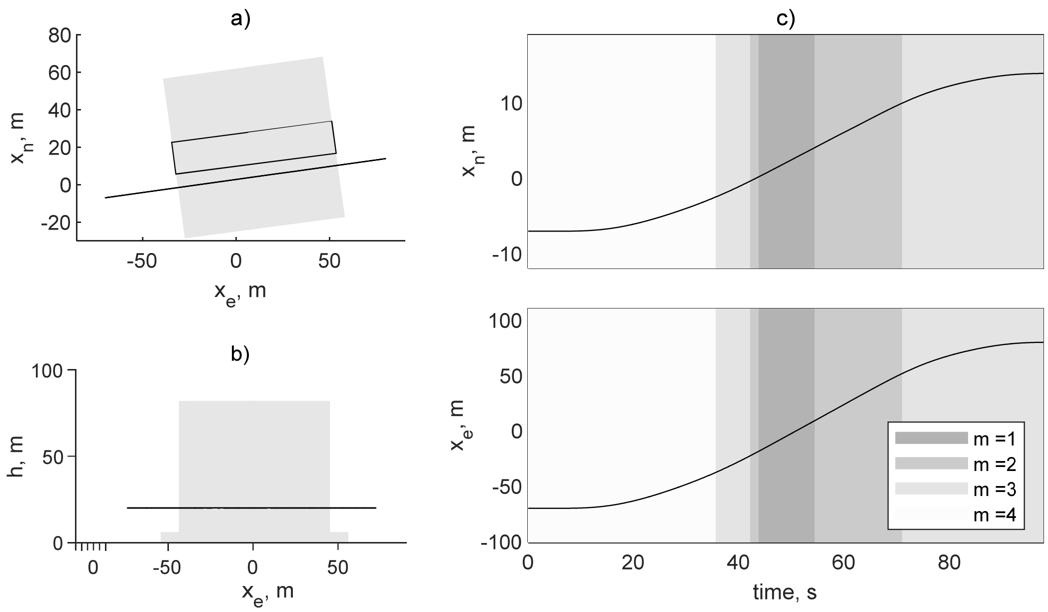

Figure 4.11 Son trajectory – case 1. a) top view, b) lateral view, c) north position and east position in function of time.

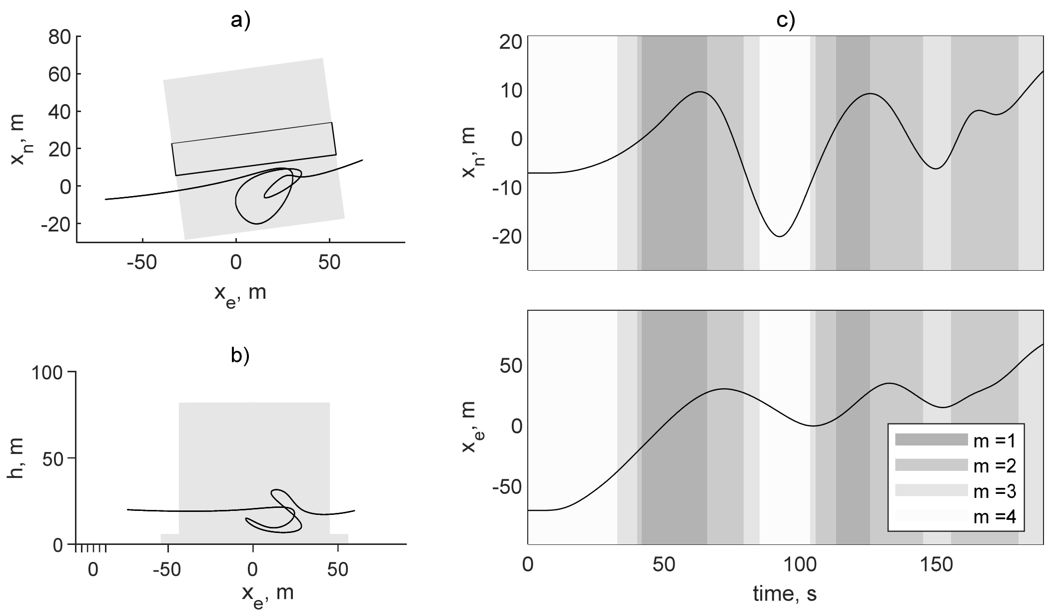

Figure 4.12 Son trajectory – case 2. a) top view, b) lateral view, c) north position and east position in function of time.

4.3.3.1 Case 1

4.3.3.1.1 Planning Results

In the son trajectory depicted in Figure 4.11 it is possible to identify two planning intervals, whose number of satellites are respectively 2 and 3. The planning intervals with their main characteristics are shown in Figure 4.13.a, with the outputs of father

3D trajectory planner depicted in Figure 4.13.b. Here, maximum acceleration and velocity limits have been set as 5 m/s^2 and 8 m/s respectively. The planner requires about 15 seconds to estimate the 3D father trajectory and the son's yaw sequence with MATLAB on Ubuntu 16.04 with a 2.20GHz processor and a RAM of 8GB. Time needed for the estimation of the main parameters (azimuth and elevation) is about 1.3 s for each planning interval.

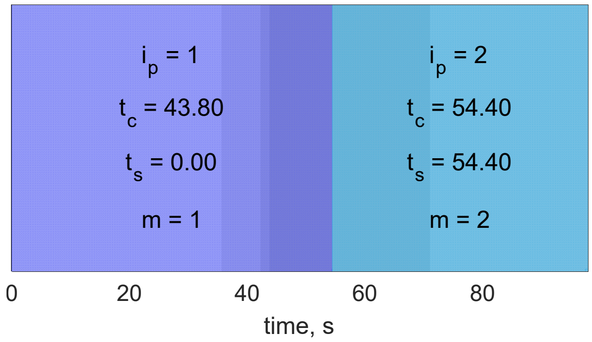

Parameter	i_p=1	i_p=2
Az_p	-124.59 °	-154.67°
El_p	-3.91 °	17.64°
r_p	22.20	31.18
$\lVert \breve{D} \rVert$	1.73	1.12

a) b)

Figure 4.13 Planning intervals for the simulated scenarios in case 1, a) planning intervals characteristics, b) best parameters for relative father-son geometry resulting from optimizing the father's trajectory.

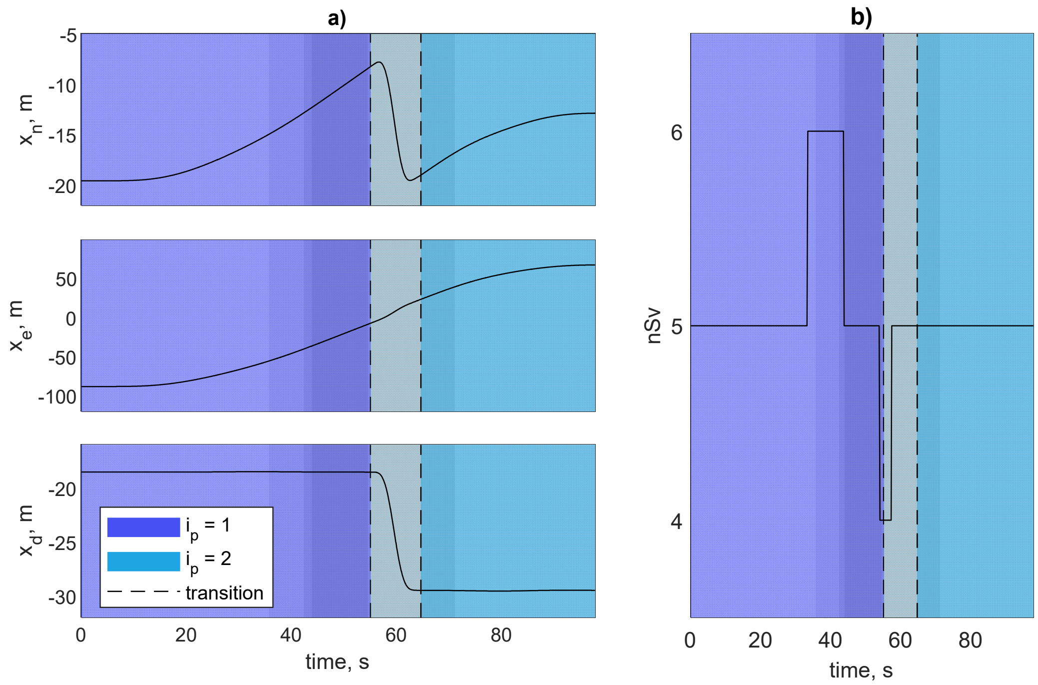

Figure 4.14 Planned trajectory for the father, a) north east and sown components, b) number of satellites seen by the father during its trajectory.

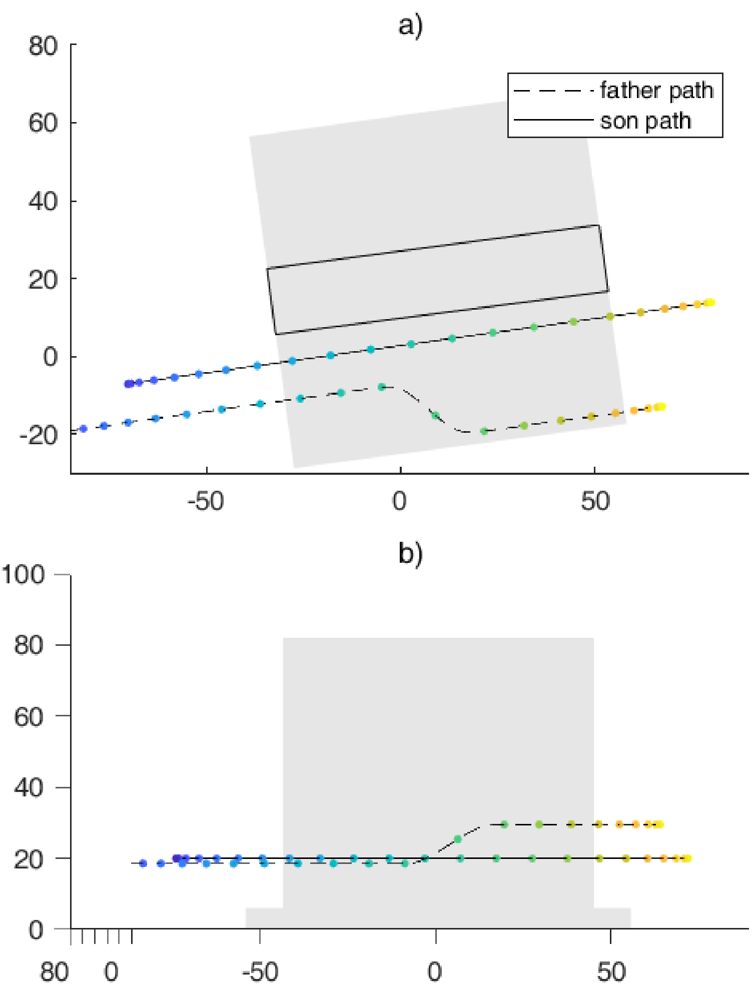

Figure 4.15 Path of the two UAVs in the simulated scenario. a) top view, b) lateral view. The two UAVs reach points with the same colors at the same time epoch.

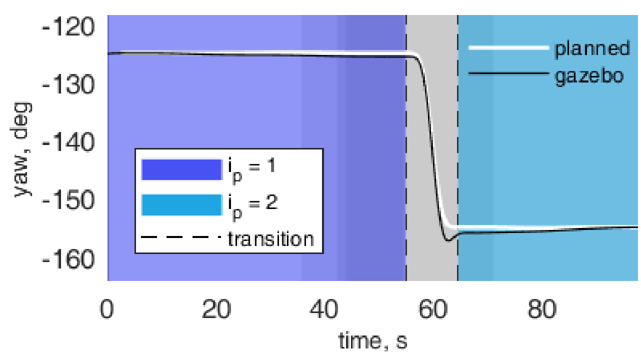

Figure 4.16 Yaw angle for the son, planned and obtained in Gazebo RotorS.

The resulting trajectory for the father is shown in Figure 4.14.a, and the planning and transition intervals are highlighted with different colored background. The transition time between the two planning intervals is 9.6 s and the distance that must be covered by the father during the transition is about 34 m.

Figure 4.14.b confirms that the planning module produces a trajectory that is it always outside the challenging area. Indeed, the number of satellites seen by the father is always greater or equal than 4. Figure 4.15 shows the top and the 3D view of the father and son trajectories in the simulated environment. The color of the dots indicates the time epoch at which the UAV reaches them, with dots of the same color indicating points that are reached at the same time epoch. The yaw angle sequence planned for the son vehicle, and obtained in RotorS after sending commands is shown in Figure 4.16. The simulation also validates that the yaw sequence maintains the father in the son's camera FOV.

4.3.3.1.2 Navigation Performance of the son with father aiding

This section is aimed at analyzing the performance of the son navigation filter, whose measurement equation are described in section 4.2.3, when the father trajectory is the one planned as described in the previous sections to improve the accuracy of son positioning in GNSS challenging environments.

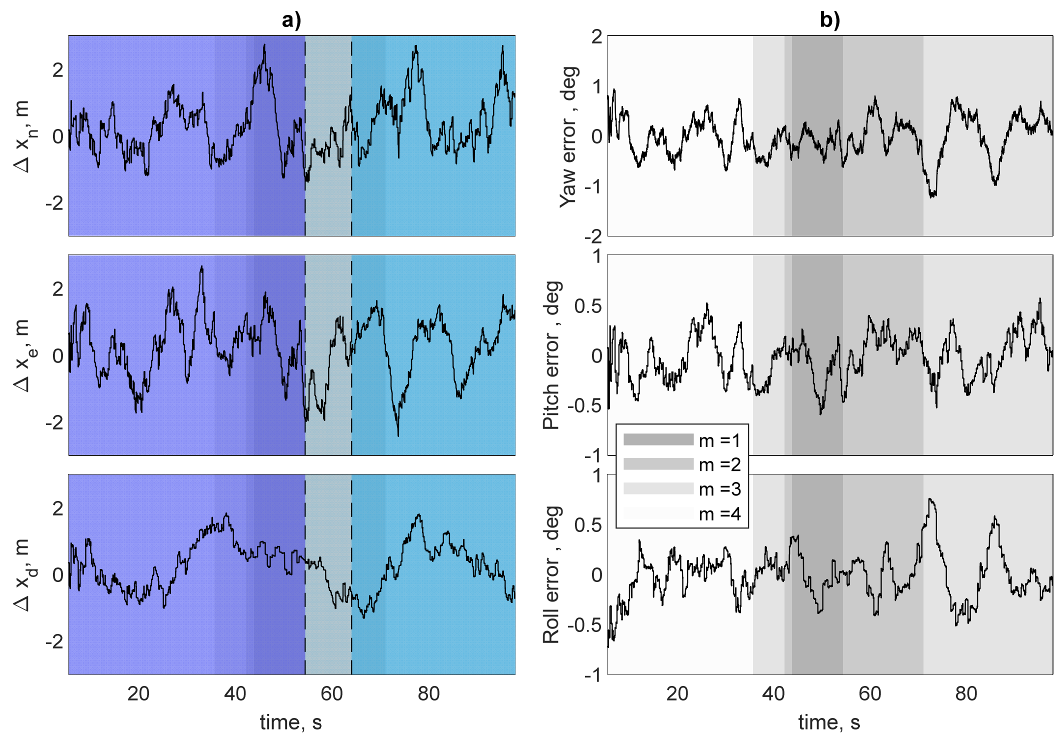

Figure 4.17 Son navigation results obtained with cooperative aiding. The father's trajectory and son's yaw are planned for improve son positioning accuracy, i.e. father trajectory is the one in Figure 4.14 and son yaw sequence is the one in Figure 4.19. a) Son's navigation NED error. The background colors highlight the planning intervals and the corresponding father trajectory parameters. b) son angular errors. The background colors indicate the number of satellites seen by the son along its trajectory. Yaw angle for the son, planned and obtained in Gazebo RotorS.

The father position transmitted to the son is assumed to be the position that will be estimated with a standalone GNSS/INS filter, whose STD error is in the order of 3 m along the horizontal directions and 6 m along the vertical. Cooperative measurements are available when father's data are received by the son, i.e. at an average frequency of 2 Hz. When those data are available, they are synchronized with the images acquired by the son camera and are used in the son filter for cooperative aiding. The results of that filter are shown in Figure 4.17, where Figure 4.17 a and b show the error in estimating the son NED position and attitude, respectively. The background color in Figure 4.17.a highlights the two planning intervals and the planning parameters (azimuth, elevation and range) that define the relative distance between the two platforms. The background colors of Figure 4.17.b remarks the number of satellites seen by the son along its trajectory. The presented strategy allows to keep the error of position and attitude estimation of the son bounded when it flies under a not nominal GNSS constellation. The maximum error in son position about 2 m for each component. This error can be reduced with the conventional instruments used for GNSS measurements improvement; e.g. differential GPS filter used in the father's sensor fusion algorithm guarantees to estimate father position with high accuracy that will improve cooperative navigation performances, and will reduce the error in son positioning estimation.

It is worth comparing the results of the son's navigation filter for different father trajectories. Figure 4.18 shows the NED errors in the cases a) the father flies along the trajectory for son navigation optimization, b) the father flies along a path that is parallel to the son with an azimuth and elevation that maximize the son performance in the planning interval when $m = 2$, c) cooperative measurements are not exploited, i.e., there is no father aiding. Case c shows that the son state estimation diverges in the challenging areas, and it is stabilized again when full GNSS coverage is available again. The father trajectory used in case b prevents the filter from diverging only in the area where $m = 2$, whereas the error when $m = 1$ increases dramatically, especially in the horizontal components. The results shown in Figure 4.18 remark that son-father cooperative navigation performance in a GNSS denied environment are strictly related to the father position. Therefore, choosing a father to support the navigation of the son does not guarantee improvement of son navigation performances unless the father position sequence is tailored to optimize the accuracy in the son's positioning.

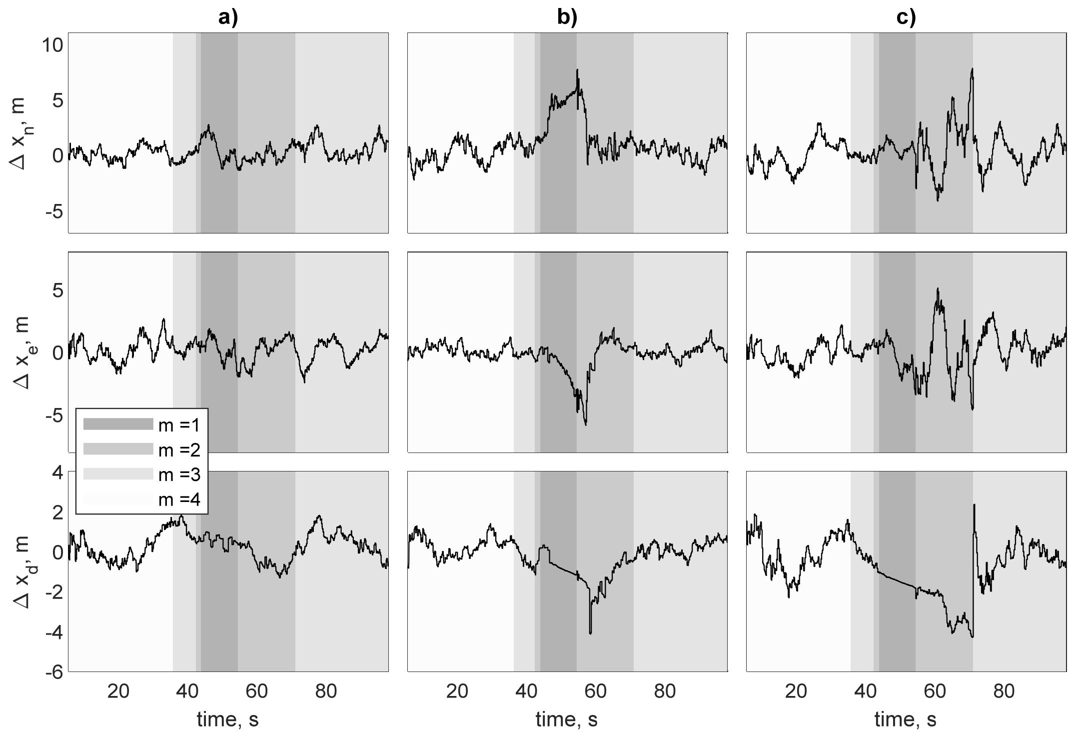

Figure 4.18 Son navigation results: NED position errors. a) Father trajectory is planned according to the son's state performance improvement, i.e., is as shown in Figure 4.14; b) Father moves along a trajectory parallel to the son, with azimuth and elevation equal to the best one in the challenging area when m = 2. c) Cooperative measurements are not used. planned and obtained in Gazebo RotorS.

4.3.3.2 Case 2

The planning intervals for case 2 are reported in Figure 4.19.a. The estimated best azimuth elevation and range to be hold in these intervals by the father are reported in Table 4.1.

Table 4.1 Best azimuth and elevation for each planning interval estimated with the PSO algorithm (FIND_BEST_MAIN_PARAMETERS) in Algorithm 2.

Parameter	Az_p	El_p
i_p=1	-122.76°	7.56°
i_p=2	-105.80°	17.64°
i_p=3	-118.41°	15.35°
i_p=4	-128.57°	4.29°
i_p=5	-102.04°	17.64°
i_p=6	-104.94°	17.64°

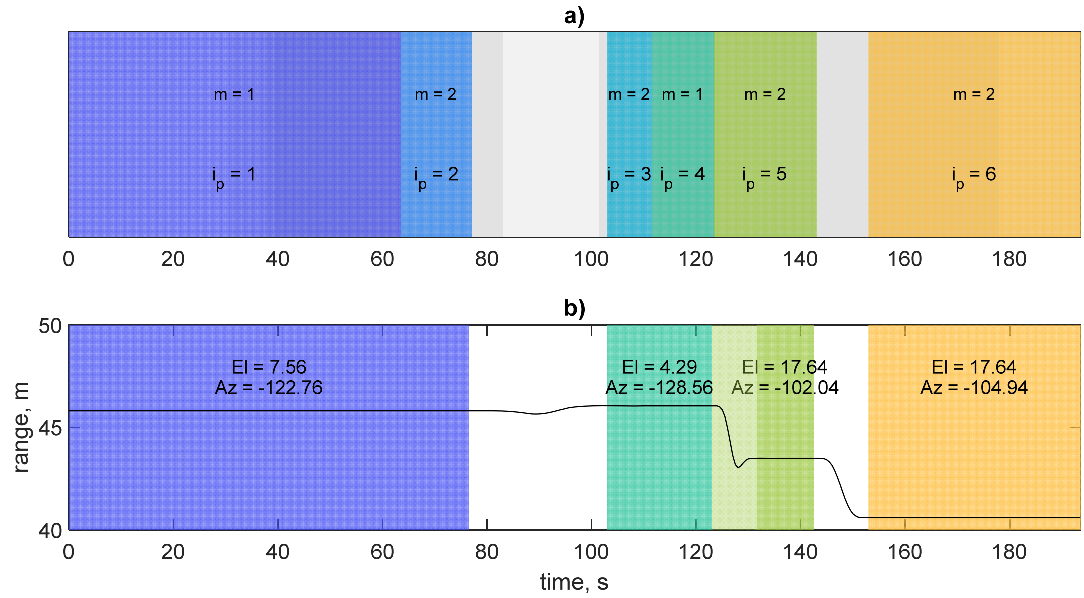

Figure 4.19 Planning intervals, for case 2. a) planning intervals for azimuth and elevation definition, b) merged planning intervals after trajectory optimization.

Intervals for which the needed transition time is higher than half of the planning interval duration are merged to their adjacent planning intervals with lowest *m*. Figure 4.19.b shows the merged planning intervals and the planned azimuth elevation and range of the relative formation. The father trajectory's components are reported in Figure 4.20, along with the number of in view satellites, showing the father is always outside the challenging area.

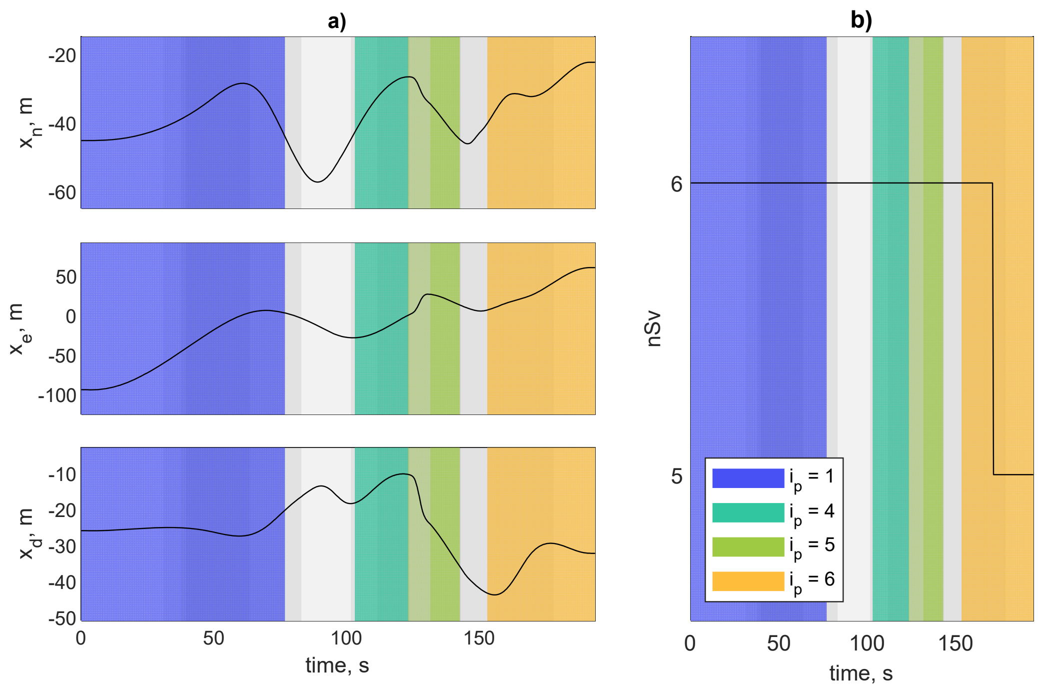

Figure 4.20 Planned path for the father, case 2. The background color identifies the planning intervals

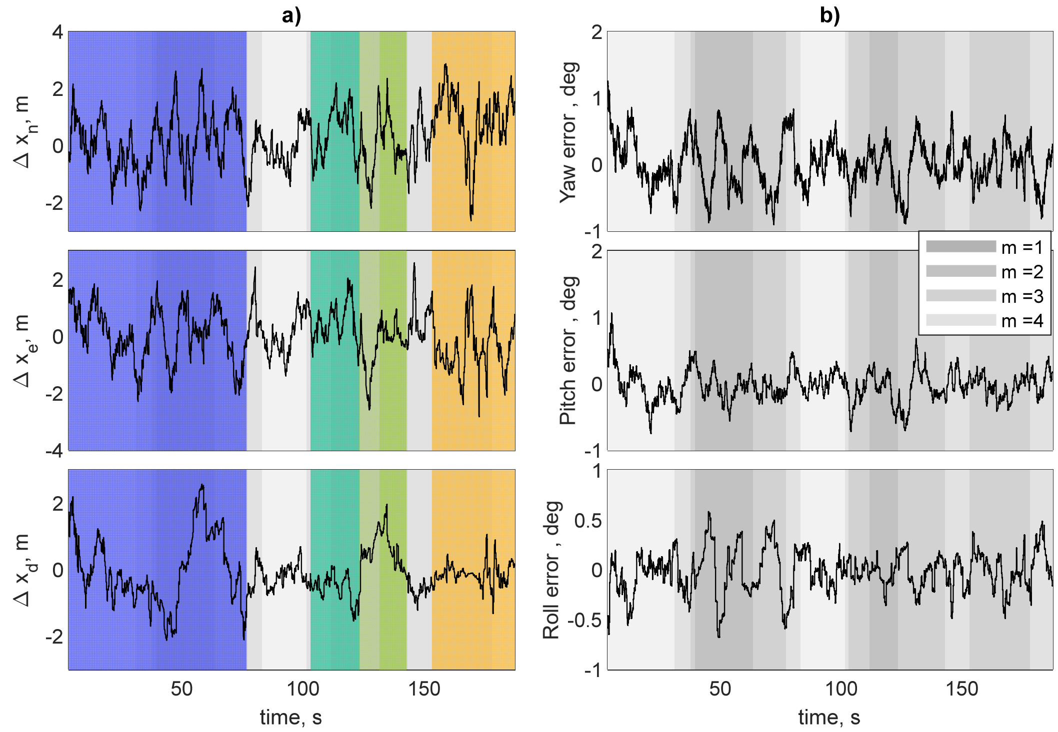

Figure 4.21 Son navigation results obtained with cooperative aiding. The father's trajectory and son's yaw are planned to improve son positioning accuracy, i.e. father trajectory is the one in Figure 4.20. a) Son's navigation NED error. The background highlights the planning intervals and the corresponding father trajectory parameters. b) son angular errors. The background indicates the number of satellites seen by the son along its trajectory.

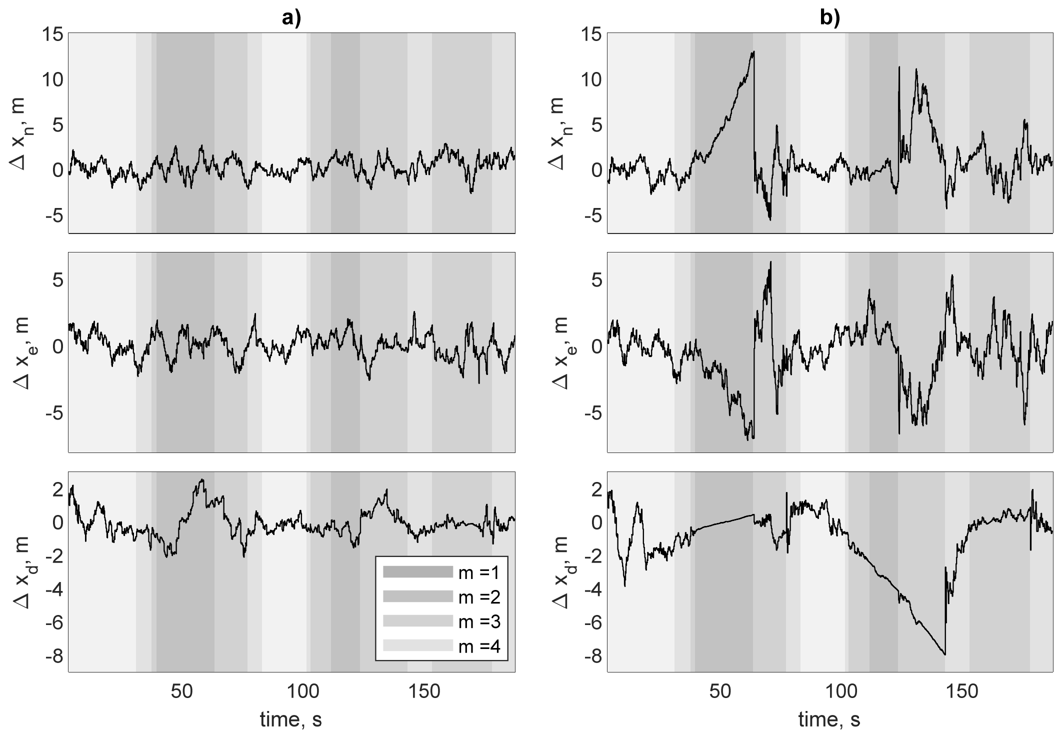

Figure 4.22 Son navigation results: NED position errors. a) Father trajectory is planned according to the son's state performance improvement, i.e., b) Cooperative measurements are not used.

The solution of the navigation filter allows also in case of a more complex trajectory for the son to keep small and bounded the navigation error. Figure 4.21 shows the filter results in terms of a) positioning and b) attitude errors. Hence, Figure 4.22 shows the filter results compared with the case no cooperation in exploited. Even if the number of planning intervals has been reduced due to the need for merging the intervals, the performance of the filter is satisfactory and keeps the positioning error bounded within 2 meters.

4.4 ONLINE TANDEM PLANNING AND GUIDANCE

Section 4.3 described an offline planning approach where the trajectory of the father is defined before the two platforms start the mission, based on the knowledge of the son's flight plan. The planning strategy [127] divides the trajectory of the father in several intervals, called planning intervals, where the elevation and the azimuth of the formation is constant and the father-son trajectories are parallel. The planning intervals are defined as a function of the number of satellites seen by the son, within a GPS-only framework.

This section [140] upgrades the approach presented in section 4.3 in various aspects. First, multi-GNSS constellation receiver are assumed, so that challenging volumes are defined in general based on the available Dilution of Precision (DOP), more than on the number of satellites in view. In addition, complex geometries for the obstacles and the challenging areas and/or complex son trajectories are considered, leading to a more general definition of father-son geometries. Finally, in view of real time implementation, off-line planning is complemented by a reactive guidance strategy that tries to prevent from loss of line-of-sight between UAVs. The upgraded version of the planner aims at minimizing the geDOP, defining the father's trajectory during the mission execution. The main innovation points of the presented strategy are:

- Usage of multi-constellation
- Definition of challenging volume that is seen as an obstacle by the father
- Sequential trajectory definition
- Usage of exended geDOP to quantify the cooperative navigation performances

The real time planning is introduced and described in section 4.4.1. Hence, section 4.4.2 reports simulation results.

4.4.1 Real time planning strategy

The on-line planner described in this section, assumes multi-GNSS constellation, therefore the number of satellites cannot be accounted anymore as indicator of the "challenginess" of a generic point of the environment. Conversely, the challenging volume is defined by means of dilution of precision, by grouping all the points whose geometric dilution of precision $|D|$ is below a certain threshold. D is the vector of the DOP that includes the north east and down dilution of precisions:

$$D = \begin{bmatrix} D_n & D_e & D_d \end{bmatrix}^T \tag{4.6}$$

To ease the definition of the forbidden points for the father, the presented planning technique uses a predefined map of the challenging volume, e.g. Figure 4.4, that is estimated at starting time of the mission. However, the challenging volume could be retained to be constant if the mission lasts less than 10 minutes and be updated otherwise.

Following the approach described in 4.3, the online trajectory planner decouples geDOP minimization and camera tracking control. Hence, geDOP minimization is handled by defining the optimized relative position and thus the father position during the flight as described in section 4.4.1.1. Whereas, a heading control is applied to rotate the vehicle equipped with the camera in order to always have the other vehicle (i.e. target vehicle) at the center of the image. The latter is based on a visual tracking algorithm that identifies the target vehicle and sends the command to modify the heading of the UAV that embarks the camera. Heading variation is dependent on the azimuth variation between the two vehicles along the trajectory. The azimuth variation must be kept bounded and compliant with the maximum heading velocity capability of the UAV, in order to allow the UAV to rotate toward the target. Nevertheless, the heading control guarantees to keep the target only in the camera's horizontal field of view (FOV). As the vertical direction as concerned, to make the target enter in the camera image some actions must be taken at position planning level:

- Limiting the relative elevation and range of the formation,

- Minimizing the trajectory snap that creates strong pitch and roll variation and modifies what the camera sees, especially in the case the camera is mounted on the father. To this aim we use polynomial planning [136, 137] to define smooth acceleration and velocity variations.

The minimum range and the maximum elevation between the two platforms are set by imposing the target UAV must be in the camera vertical FOV if its vertical position is estimated with an error equal to $D_d \cdot 2\sigma_{Pr}$. However, due to the degradation of cooperative filter performance with the range, a maximum range threshold has been used in the planning algorithm. Indeed, in the son-to-father tracking range increases produces a reduction of the navigation performances due to the degradation of the geDOP, depending on the attitude coupling, see Figure 3.17.

4.4.1.1 Position Planning

Position planning accounts for geDOP minimization along the trajectory. The optimization problem is constrained to the following requirements

- Minimize the roll and pitch digression
- Avoid entering in challenging volume
- Keep the relative separation norm between the minimum and the maximum range
- Prevent the relative elevation to go beyond vertical FOV limit
- Enable the camera to follow the target vehicle with a heading rotation, liming the relative azimuth rate.
- Guaranteeing the geDOP resulting from the relative geometry is below a certain threshold.

To comply with real time implementation, the trajectory of the father must be computed during the mission execution, optimizing the geDOP and defining the next moves based on the desired son's trajectory in the next step. Model Predictive Control is a powerful instrument that has been widely used for trajectory prediction in constrained optimization problems [141]. Nevertheless, it resolves only convex (or quadratic in the non-linear MPC version) problems and does not cater for geDOP minimization.

The proposed planer assumes sequential definition of the father trajectory. Therefore, it foresees real time computation and can adapt to son trajectory's changes. In addition, cooperation among the vehicles is exploited allowing the son to wait for the father while planning for its trajectory. It is assumed the son's trajectory can be defined as waypoints sequence $w = \{w_1, w_2, \ldots, w_n\}$ At each waypoint the son stops and wait for the father to compute the path required to assist the son until it reaches the next waypoint. Therefore, son and father trajectories are a polygonal chains. When the son reaches the w_k waypoint the father is in the waypoint w_k*, defined as the end of the optimal path computed at the previous step.

The trajectory of the father to support the son between w_k and w_{k+1} is a straight line, that is automatically defined from its end point w_{k+1}* and knowing the time Δt_k needed for the son to cover its straight line $\mathbf{p}(w_k, w_{k+1})$. w_{k+1}* definition proceed through the following steps:

1) The point with the maximum DOP $\overline{w}_k$ is estimated along the son's straight line $\mathbf{p}(w_k, w_{k+1})$.

A Particle Swarm Optimization algorithm (PSO) [138] is used to define w_{k+1}* so that the geDOP in $\overline{w}_k$ is minimized. This is done by locating the father point corresponding to $\overline{w}_k$ interpolating the father straight line between w_k* and w_{k+1}*. To speed up the optimization process, PSO searching space is reduced in range imposing a maximum distance between w_k* and w_{k+1}*, estimated accounting for Δt_k and the maximum velocity the father can fly.

The constrained problem is handled by preventing PSO to search for w_{k+1}* that fails the following conditions, the cost function pseudocode is summarized in Algorithm 5.

- The straight line w_k* to w_{k+1}* does not intersect neither the challenging volume, nor any other obstacle
- Acceleration, velocity and snap are bounded
- Elevation and range fulfill the camera's FOV requirements and are between their limits as previously defined.

- The two platforms are in LOS along the two straight lines. Because is w_k* in LOS with w_k, this is ensured by checking w_{k+1}* and w_{k+1} are in LOS.
- Azimuth velocity does not exceed the UAV's heading rate
- The geDOP is above a given threshold.

Algorithm 5: Transition time from range

Input: w_k, w_k* // starting son and father points
w_{k+1} // son's end point
w_{k+1}* // father candidate end point
Δt_k // time
svPos // satellite position
obst // challenging volume

$\bar{w}_k$ ← ESTIMATE_REF_POINT(w_k,w_{k+1}, Δt_k,*svPos*);
$F(1)$ ← IS_NOT_INTERSECT(w_k*,w_{k+1}*, *obst*)
$F(2)$ ← IS_ACC_VEL_SNAP_LIM(w_k*,w_{k+1}*, Δt_k)
$F(3)$ ← IS_EL_RANGE_BOUND(w_k*,w_{k+1}*,w_k,w_{k+1})
$F(4)$ ← IS_LOS(w_{k+1}*, w_{k+1})
$F(5)$ ← IS_AZ_RATE_BOUND(w_k*,w_{k+1}*,w_k,w_{k+1})

if *prod*(F)
  $\bar{w}_k$* ← ESTIMATE_FATHER_REF(w_k,w_{k+1}, $\bar{w}_k$ Δt_k);
  geDOP ← GEDOP($\bar{w}_k$*, $\bar{w}_k$, *svPos*); // Eq. (3.40)
else
  geDOP = nan;
end
Return: *geDOP* // norm of the generalized DOP

The algorithm described above is executed at each w_k*, being $k = 2,\ldots,n-1$. Whilst, at the first epoch the planned father trajectory until w_2* consist in a polygonal chain of two straight lines that are divided by the lock point w_l*, as shown in Figure 4.23. The lock point is the point where the father and the son encounter before entering in the challenging area. In that point the two UAVs check their connection and decide if perform the mission.

Father and son wait for connection in the lock point for 10 seconds, if no connection is received the UAVs abort the mission. The son's lock point w_l is defined along $\mathbf{p}(w_1, w_2)$, as the point that is along the line 5 meters before the challenging area. Hence w_l* is defined imposing $\mathbf{p}(w_l*, w_2*)$ is parallel to $\mathbf{p}(w_l, w_2)$ and selecting w_2* in order to minimize the geDOP in w_2. w_2* is selected imposing $\mathbf{p}(w_l*, w_2*)$ fulfills all the requirements indicated in Algorithm 5.

Differently from the path planner described in 4.3, the UAVs are not routed on parallel trajectories during the mission execution, this is done to prevent fast manoeuvres that could affect the father visual-tracking while performing transition manoeuvres between adjacent planning intervals. Conversely, the online planning strategy is constantly in search of a formation that produces a better geDOP, that complies with the problem's constraints and with the maximum distance the father could fly in Δt_k.

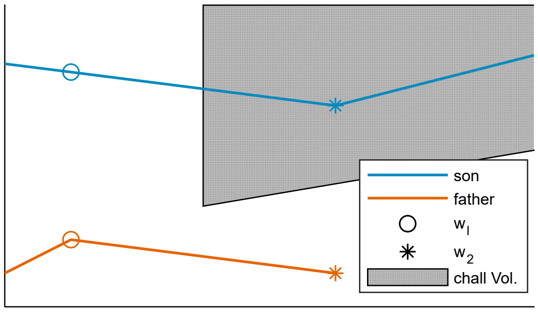

Figure 4.23 Trajectory of father and son with lock points

4.4.1.2 Guidance Strategy

This section summarizes the guidance strategy that the father and the son use to cover each trajectory piece, i.e. $\mathbf{p}\left(w_k, w_{k+1}\right)$. Figure 4.24 schematizes the planning and guidance strategies. When the father has estimated w_{k+1}*, it sends a message to the son that can start following its trajectory.

Using polynomial planning the trajectory of the son is fully characterized and velocity and position can be calculated at each time instant. Therefore a path following technique [142] can be implemented on board the son's UAV to give the velocity commands at the controller sampling time c_s. The son vehicle however should share with the father the position and the velocity at the next control instant, i.e. p_{i+1} and v_{i+1}.

Along the trajectory the position of the father can be easily derived from the position of the son observing that the relative position (azimuth, elevation and range) linearly varies in Δt_k. Therefore, one can define a function that describes between w_k* and w_{k+1}* the azimuth the elevation and the range variation between 0 and Δt_k, i.e. $Az_k(t)$, $Ez_k(t)$, $r_k(t)$, with $t \in [0, \Delta t_k]$. Hence, the father knowing p_{i+1}, v_{i+1} and t could derive p_{i+1}* and v_{i+1}* and send that command to the controller. In addition, the UAV embarking the camera must adjust the heading angle whenever a camera image is acquired, as highlighted by the black box in Figure 4.24.

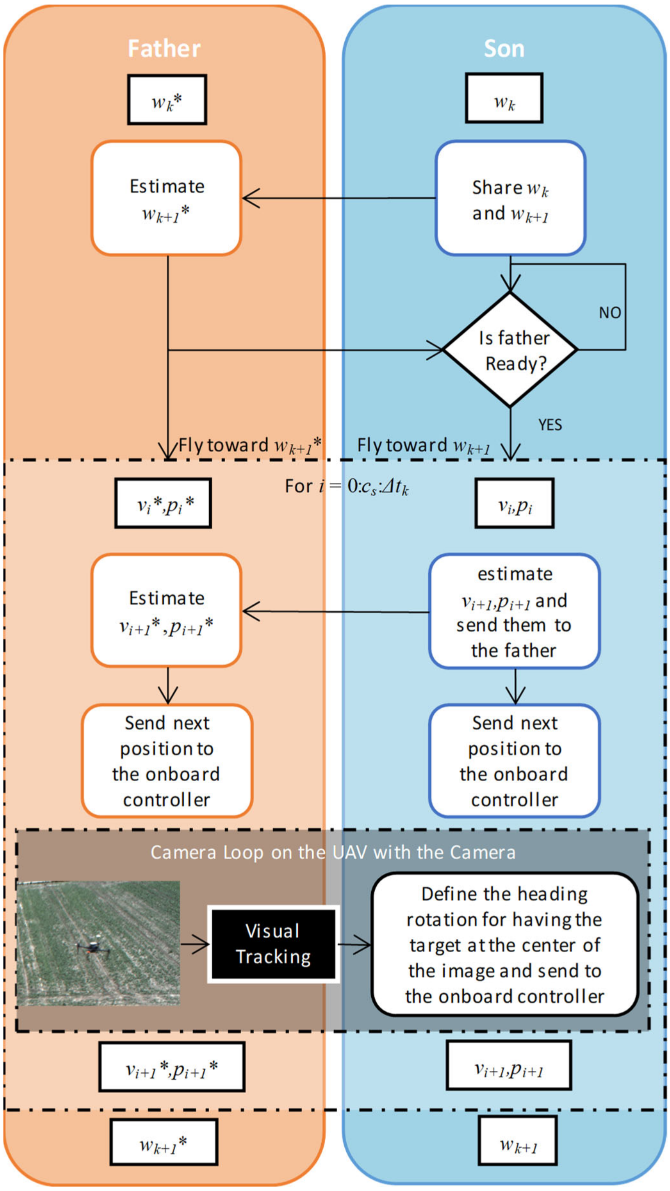

Figure 4.24 Planning and guidance conceptual scheme. Guidance strategy is highlighed with white shadowed background.

4.4.2 Results

This section reports the result of the planning algorithm in a building inspection scenario. The building used for this simulation belongs to the Business District in Naples, Italy, and it is represented in Figure 3.11. Figure 4.25 shows the used scenario, where the building is drawn in black and the challenging volume is shadowed with a color indicating its altitude. The planned father trajectory is reported in red. Cooperative navigation results are shown in Figure 4.26 where the cooperation advantage can be observed by comparing the filter results without aiding (gray) with those exploiting cooperative navigation (red and black). Specifically, the results in red are the obtained flying the father along the trajectory planned by the proposed algorithm. Whereas, the black line indicates the result of the cooperative filter if the father was flying along a trajectory parallel to the son, with azimuth elevation and range that minimize the geDOP in the point where the son's DOP is maximum. The latter is highlighted with a black line in Figure 4.25.

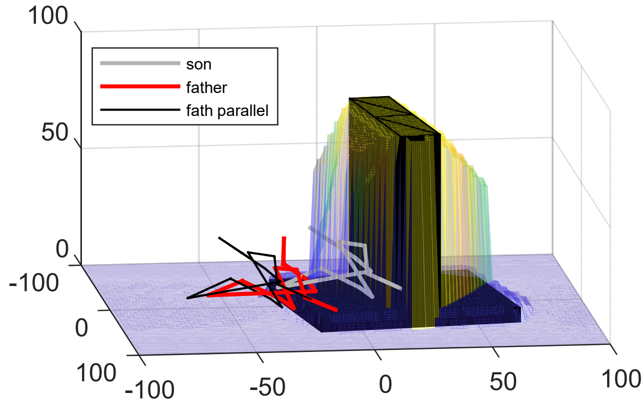

Figure 4.25 Simulated Planning Scenario and UAVs trajectories. Son's trajectory is in gray. Whereas the father trajectory obtained with the proposed planning technique is reported in red. Black trajectory is a trajectory for the father parallalel to the son that minimizes the geDOP in the point that requires to be aided the most (where the DOP is maximum) of the son's trajectory.

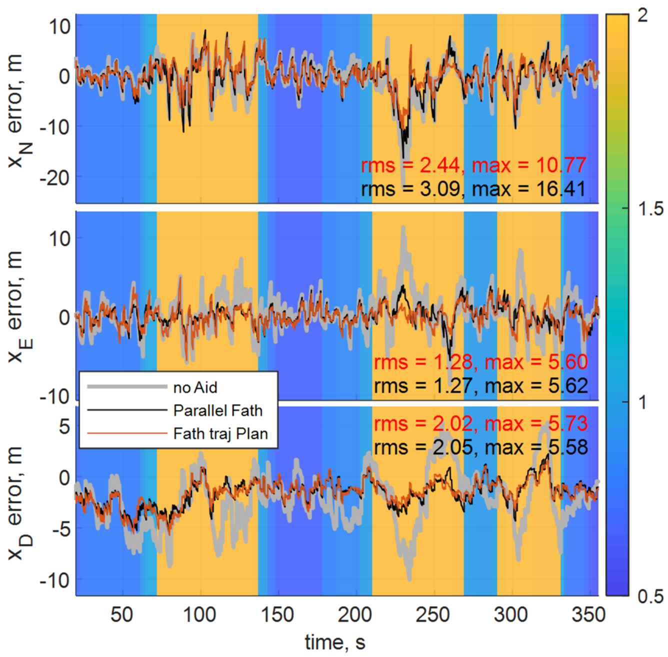

Figure 4.26 Cooperative Navigation Results. Filter results without coooperation are reported in gray. Whereas the red and the black lines are the results of a cooperative filter where the father trajectory is (red) set with the proposed algorithm and (black) parallel to the son. Background color indicates the DOP of the son, indicating its performances without cooperation.

The proposed planning technique provide a slightly improvement of the filter performance if compared with the parallel trajectory. However, it allows to define the trajectory on-line adapting to son's movements and foresee son's trajectory updates, e.g. consequently to a new waypoint assignment. Being the separation between the father and the son mostly along the north direction, the cooperation aiding is more effective in the east and down components, which are almost orthogonal to the UAVs separation. In the case son trajectory is composed by only two waypoints, the planning algorithm outputs a trajectory for the father, which is parallel to the son. However, to make the father planning more reactive to son's trajectory variation, the planning algorithm foresee a trajectory resampling that add intermediate waypoint to the trajectory, if the distance between them is higher than a threshold.

Due to the heuristic nature of the PSO algorithm, the planned trajectory changes at each run, but it satisfies all the imposed requirement, as shown in Figure 4.27.

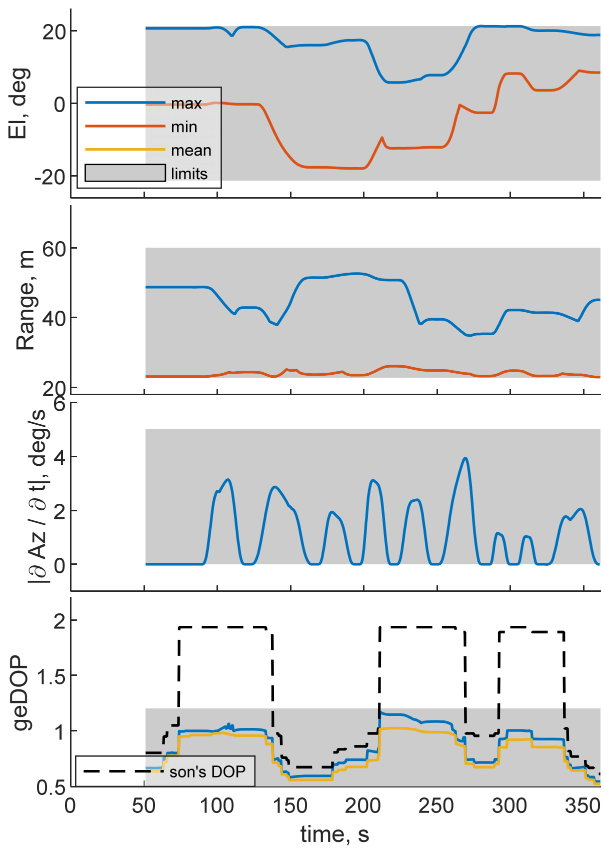

Figure 4.27 Mean, max and minimum relative formation parameter obtaining in multiple runs (20) of the planning algorithm. The limits imposed to the relative formation geometry are reported in gray. Figures shows Elevation, range, Azimuth (i.e. Heading) rate and obtained geDOP.

The figure reports values only during the cooperation phase (after 50 seconds), i.e. after the lock point. Indeed, relative formation limits could be violated in the first part of the trajectory where the two platform fly independently, especially in the case they have a large initial separation. Figure 4.27 shows the main parameters of the relative formation, i.e. range and elevation and Azimuth rate, reporting mean minimum and maximum value obtained among 20 runs of the planning algorithm. Range and elevation within predefined bounds prevent the target vehicle to be outside the camera vertical FOV. Whilst, azimuth rate’s limits bound the heading rotation, ensuring the UAV with camera to keep the target in its horizontal FOV. The last plot of Figure 4.27 compares the DOP of the son without cooperative aiding with the mean and the maximum value of the geDOP obtained along several runs of the planning algorithm.

Chapter 5: Multi UAV planning in environments with heterogenous GNSS coverage

This chapter presents an algorithm for multi-UAV path planning in scenarios with heterogeneous Global Navigation Satellite Systems (GNSS) coverage. In these environments, cooperative strategies can be effectively exploited when flying in GNSS-challenging conditions, e.g., natural/urban canyons, while the different UAVs can fly as independent systems in the absence of navigation issues (i.e., open sky conditions). These different flight environments are taken into account at path planning level, obtaining a distributed multi-UAV system that autonomously reconfigures itself based on mission needs.

Chapter 3 introduced a cooperative navigation strategy for improving navigation performances of a vehicle flying in GNSS challenging conditions, named "son". The proposed approach exploits information broadcast and relative sensing, using as visual features/trackers and/or transponders for radio frequency-based ranging vehicles flying in areas not susceptible to GNSS signal corruption, designed as "father" UAV(s). The positioning accuracy for the son UAV depends on several factors, including father-son and GNSS coverage geometry. However, the basic requirements that the father has to fulfill consist in keeping an unobstructed line-of-sight to the son, and flying under good satellite coverage (i.e., outside of the challenging areas) not too far from the son. Father(s) and son UAVs have to fly in a coordinated way to ensure success of the cooperative navigation strategy. As shown in chapter 4 [127, 140], for a tandem formation (one father one son), when an entire mission has to be carried out in a challenging environment (e.g., 3D mapping in a canyon), father and son UAVs keep their role during the whole mission. However, it is intuitive that this choice is non-optimal in scenarios with heterogeneous GNSS coverage conditions. In fact, coordinated flight and father/son task assignment is of interest only in some phases of the mission, while the different UAVs can be used as independent systems in absence of navigation issues. Thus, in these scenarios, the need to optimize the usage of available resources to minimize mission time while enhancing flight autonomy, naturally leads to an integrated approach to multi-UAV path planning, guidance, and navigation.

This chapter focuses on multi-UAV path planning for these mixed GNSS coverage scenarios. It aims at defining flyable trajectories for a swarm of UAVs, whose purpose is to reach several waypoints (also defined as “targets” in the following) and then performing actions at each location. Targets can lie in challenging or non-challenging areas. The proposed problem can be formulated as a customization of the vehicle routing problem (VRP) [36] that must account not only for target distribution amongst UAVs, but also on the need to ensure autonomous flight in challenging areas, associating to each son the needed number of fathers. The proposed approach can be thus defined as “navigation aware” path planning for multiple UAVs. The result is a multi-UAV system that is able to reconfigure itself during a mission, based on the operating environment.

In the open literature, “navigation aware” planning techniques for GNSS challenging environments are aimed at defining trajectories that minimize the state covariance [132–134], or that ensure a collision free path in the limits of the available GNSS measurements [93, 143]. These approaches adapt the trajectories not only to the mission requirement, but also account for the navigation state, which limits the areas the UAVs can reach. Exploiting cooperation, the proposed approach aims at defining trajectories that pass through mission defined targets, without forcing the trajectory of the vehicles to be modified because of navigation needs (in GNSS challenging areas), but using father(s) to reduce navigation state estimation covariance.

The VRP problem has been widely analyzed in the open literature, and solved with exact methods [60, 61, 144] and heuristic or metaheuristic methods [57, 59]. Exact resolution problems are formulated as mixed integer linear problems (MILP), which explores all the feasible solutions to return the optimum that solves the problem. These, method suffers from scalability problem when the number of combinations to explore increases, resulting in an increase of computational burden. Conversely, heuristic [62] or metaheuristic [58, 62, 63] methods return a solution in a short time even if a large amount of candidate solutions exist. Nevertheless, due to the heuristic nature of those method, they not always return the solution corresponding to the global minimum. Several heuristic and metaheuristic methods have been used in the open literature to solve the VRP problem. Bertuccelli et al. and Moon et al. [64, 65] use consensus based bundle algorithm to route a swarm of UAV in cluttered environment. Genetic algorithm and a discrete version of the particle swarm optimization (PSO), are used for assigning targets to UAVs in [66] and [67], respectively. The proposed method uses an iterative heuristic tecnhique, i.e., the insertion-based algorithm [145, 146], since the use of heuristics reduces the computation time, whilst, the sequential approach allows controlling which type of target is to be assigned after each iteration. As an example, the proposed algorithm assumes that after assignment of targets in a challenging area, the subsequent target to be assigned is a father one. Father locations (targets) are not defined *a priori*, but during target assignment, that makes unsuitable the usage of techniques that do not allow input data (i.e., targets) changing, e.g., PSO, MILP or genetic algorithm.

To ensure that each son is assisted by one or more fathers during the flight in its challenging zone, the VRP solution is then complemented with a proper timing strategy. Finally, flyable smooth paths are defined as polynomial trajectories based on the waypoint sequences and the timing solution. More in general, the conceived framework for autonomous multi-UAV missions in complex heterogeneous environments is depicted in Figure 5.1. It includes:

- Preprocessing operations aimed at evaluating the GNSS-challenging zones where UAVs cannot fly autonomously without support from other vehicles. They are based on the knowledge of a coarse representation of the 3D mission environment, and of the time and date the mission is performed (i.e., GNSS constellation geometry). Once the constellation of satellites and the surrounding environment are known, it is possible to define a 3D grid of the volume where the UAVs are designed to fly, in order to map the dilution of precision (DOP) and define the challenging areas as explained in Section 5.1;
- A multi-step path planning algorithm that assigns to all the UAVs flyable trajectories that fulfil mission and navigation constraints. This is discussed in detail in this chapter;
- An algorithm to refine the trajectories of the father UAVs when operating in challenging zones. This algorithm allows, once the trajectories of the sons in challenging areas are defined, shaping father trajectories based on the

navigation needs. This is oriented towards real time guidance and is described in [127].

The main contribution of the proposed technique is connected to the integration of cooperative navigation at planning level, thus enabling optimization of resources and autonomous flight through mission-defined targets in spite of navigation issues. The main innovation of the proposed planning approach is the introduction of a novel technique that solves together the problems of vehicle routing, task (father/son) assignment in challenging areas, and cooperative timing to ensure that father and son operate in the same challenging area at the same time. It uses a customized 3D fast insertion-based task assignment algorithm, with an adaptive cost function that is aimed at minimizing the total path length while also ensuring uniformity in load distribution amongst UAVs. Moreover, additional waypoints are defined during the planning process to account for cooperative navigation needs. Finally, it introduces an original timing strategy, that synchronizes UAVs motion accounting for the different speeds achievable in challenging areas or in open sky conditions.

The present chapter is organized as follows: Section 5.1 introduces the developed planning concept, its assumptions and the main processing steps. Algorithms are then detailed in Sections 5.2–5.5. Performance assessment is discussed in Section 5.6, where path planning is tested in a real-world scenario in the city of Naples.

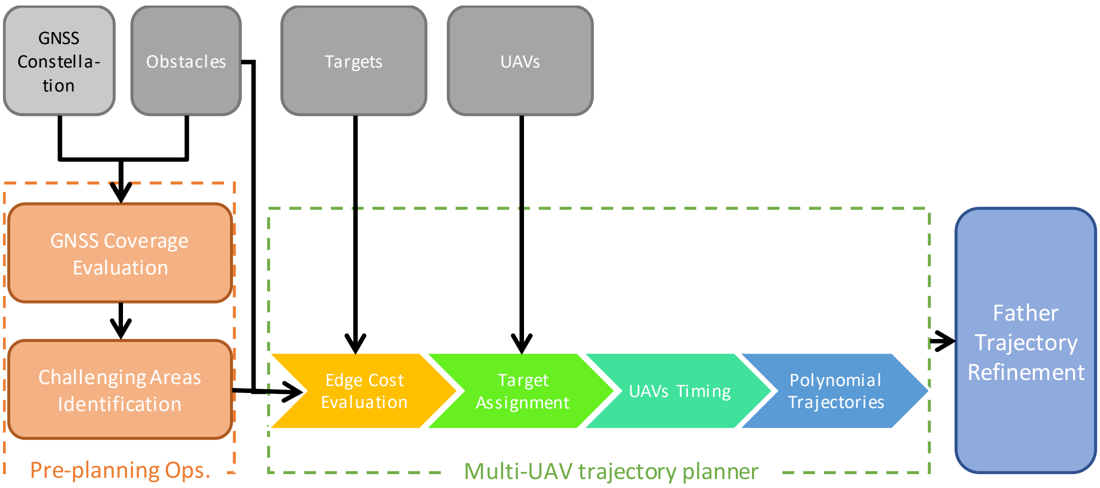

Figure 5.1 Scheme of path planning for a swarm of UAVs in a challenging environment, this chapter tackles the central step of the scheme termed as “Multi-UAV trajectory Planner”, while “Father Trajectory Refinement” is analyzed in [127], and details about pre-planning operations are given in [121] and summarized in Section 2.

5.1 PLANNING CONCEPT AND ASSUMPTION

The trajectory planning algorithm described in this chapter assumes that waypoints (targets) and service time, i.e., the time needed to perform the demanded mission at each waypoint, are provided as input data. Indeed, their definition usually depends on the specific mission under analysis and the adopted payload (e.g., infrastructure inspection [33]). In general, input data for the assumed multi-UAV path planning in heterogeneous environment include:

- A sequence of target positions, with the associated service time;
- Definition of GNSS-challenging areas (where navigation requirements cannot be fulfilled by single vehicle techniques), and of the number of fathers required at each of them for supporting the son flight. This information is the output of pre-processing operations based on a coarse knowledge of geometry of the three-dimensional (3D) environment (including obstacles), the GNSS geometry at the time the mission must be executed, and the assumed cooperative navigation sensors/approaches [121];
- Definition of eventual no-fly zones, which are seen as obstacles;
- Number and dynamic constraints (e.g., maximum speed) of the adopted UAVs. It is assumed that all the UAVs have the same constraints and capabilities.
- The definition of the challenging zones is performed analyzing which are the areas where GNSS satellites in view are not able to guarantee a certain navigation error. In those areas, the number of father vehicles depends on the available GNSS information and the adopted cooperative sensors. As a general concept, in GNSS-challenging areas, cooperative measurements are needed to provide given bounds for positioning error, complementing (eventual) pseudorange information from GNSS satellites. Available pseudorange information depends on the three-dimensional environment and the current GNSS coverage. Cooperative aiding measurements depend on which systems are adopted for relative sensing: cameras [147] (on board father or son) and/or RF-ranging systems can be used, that provide angular and/or range information. From a practical point of view, at least four scalar

measurements are needed to bound the positioning error. As an example, if the son has only two GNSS satellites in view, and RF-ranging is used for relative sensing, then two fathers are needed. In the same GNSS coverage conditions, a single father equipped with a camera (providing two angular measurements) can be able to fulfil navigation needs and bound the positioning error. It is clear that the quality of cooperative measurements, and the geometry of the problem, strongly impact the available positioning performance, which can be described by the concept of "generalized dilution of precision" [121].

For the sake of simplicity, it is assumed that both obstacles and challenging areas are prisms, and that variations in terrain elevation can be neglected. If there are no targets in a specific challenging area, that area is seen as an obstacle. It could be noticed that passing through a challenging area, instead of finding an avoidance path, could bring in theory an advantage in terms of mission time minimization. However, since father support is needed, then, the velocity of the son should be small enough to ensure father-son line of sight link to be always available, and one or more UAVs are needed for cooperation. Thus, even if the distance covered by the son to pass through the challenging area is lower than the one needed to avoid that zone, the overall mission time may be increased due to the reduced velocity and the need to use more than one UAV to pass that area. In addition, given the challenges of son-father formation flight, the proposed approach is thus to fly UAVs in challenging zones only if this is required by the mission. On the other hand, if the challenging area includes at least a target, only a single UAV, designed as son for that area, is allowed to access it. All the other UAVs see the considered area as a no-fly zone. This choice is made to avoid congestion in areas that are characterized by navigation challenges.

The start and the end point of the trajectory are the same for each UAV, and it is assumed that at $t = 0$ all the UAVs are at the start location. The velocity that son UAVs should not exceed during their flight in the challenging areas is defined as v_{chall}, while the cruise velocity, that is the one that should not be exceeded outside challenging zones, is named v_{cruise}. Due to the lack of reliable GNSS coverage and the need of maintaining unobstructed line-of-sight with the father(s), it is reasonable to assume that v_{chall} is relatively small, about 20–30% of the cruise velocity v_{cruise}.

Given this input information and assumptions, routing vehicles basically requires each selected target to be assigned to one UAV. Furthermore, in addition to classic VRP scenarios, when a vehicle flies inside a GNSS-challenging area (i.e., it is deemed as son for that area), one or more UAVs (father UAVs for that challenging area) need to "serve" the son supporting its flight by relative sensing and information broadcast. Therefore, planning is not limited to assign targets (waypoints) to each vehicle but must include a strategy to define, for each challenging zone, father UAV(s) and the associated waypoints. As far as this multi UAV planning technique is concerned, the definition of father waypoints is aimed at fulfilling the basic requirements recalled in the introduction (i.e., unobstructed LOS to the son, flight outside challenging areas at reduced distance from the son). Father trajectories can then be optimized in a refinement phase [127], which has negligible impact at planning level.

The strategy used for assigning targets consist in optimizing the resources (UAVs) to reduce the time of mission completion. Reducing mission time means reducing the overall distance covered by the UAVs and in addition equalizing the path length amongst the UAVs, to ensure the paths have more or less the same duration. Figure 5.1 shows the main steps of the path planner that are detailed in the following sections.

- The first step (edge cost evaluation, presented in section 5.2) is aimed at defining obstacle-free paths between each couple of targets, and evaluating their length;
- The second part of the path planning algorithm (target assignment, section 5.3) assigns all the waypoints and tasks to the UAVs, with the aim of minimizing the overall mission time. This is done minimizing the total path length while also ensuring uniformity in load distribution among UAVs. As an output of this step, each UAV is assigned a trajectory that is a polygonal chain composed by a number of waypoints and the edges between them;
- the timing step of the planning algorithm (section 5.4) consists in defining the velocity that each UAV must hold along its trajectory in order to synchronize son and father arrival and departure to/from the challenging zones;

- Finally, polynomial paths are defined for all the UAVs to connect waypoints with flyable and smooth trajectories (section 5.5). Polynomials allow easily deriving 3D position and its derivatives for each time epoch.

5.2 EDGE COST EVALUATION

Edge cost evaluation is aimed at estimating the cost to travel along each possible edge, i.e., the piece of trajectory between each couple of the available waypoints. For this specific application, the edge cost for each couple of targets i and j can be estimated as the length of the path between them, defined as d_{ij}. For the sake of edge cost evaluation, the path between two targets can be thought as an obstacle-free polygonal chain, with its length estimated as the sum of the lengths of its segments.

A multi-step process is adopted to obtain obstacle-free paths. The path between waypoints is initially defined as the straight segment that connects them. If the segment intersects an obstacle, auxiliary points are generated in proximity of obstacle corners. Different polygonal chains are thus obtained. These are then re-checked for obstacle avoidance, and further auxiliary points may have to be added. When all the potential paths are obstacle-free, the shortest one is selected, and a Fibonacci filter [65] is used to remove unneeded nodes. Within edge cost evaluation, challenging zones are considered as no-fly zones (i.e., an obstacle), when both targets i and j lie outside that area. The procedure is shown in Figure 5.2. The straight-line path between the two waypoints (indicated as circles) intersects the green obstacle on the top, and the two avoidance paths are defined in Figure 5.2.a. The avoidance paths are defined as the paths that travel around the obstacle passing through avoidance points (black crosses), that are points located at 3 meters along the bisector of each corner. One of the so defined paths (highlighted in red in Figure 5.2.a) still intersects the bottom obstacle, therefore two new paths avoiding the bottom obstacle are computed in Figure 5.2.b. Figure 5.2.c shows all the generated obstacle-free paths that connect the two waypoints, where the black is the one with minimum length. Figure 5.2.d shows the Fibonacci filter application to the path with the minimum length, which removes an unneeded point from the trajectory.

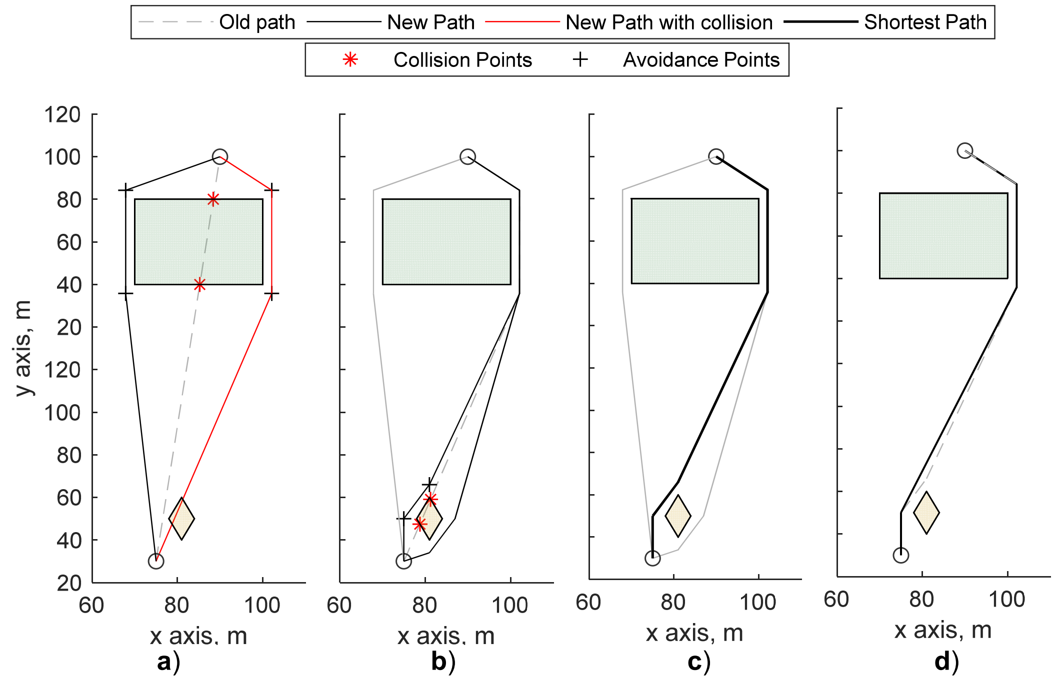

Figure 5.2 Definition of obstacle-free path between two waypoints. a) avoidance of green obstacle, on the top. Two avoidance paths are depicted, the black one is obstacle-free, the red one intersects the bottom obstacle; b) avoidance of the orange (bottom) obstacle: the two avoidance paths (in black) are not intersecting any other obstacle; c) Among the three non-colliding paths that connects the two waypoints (circles) the one with the minimum path length (black) is selected. d) Fibonacci filtering is applied to remove the unneeded point from the selected trajectory.

5.3 TARGET ASSIGNMENT

The insertion-based algorithm used to sequentially assign target to the trajectory aims at optimal distributing the resources amongst the targets. Let n be the number of targets, m the number of available UAVs, A_c the c-th challenging zone, with $c = 1, \ldots, C$. The targets to be assigned are named $\underline{w}_i = 1, \ldots, n$, and include the start and the end waypoints, that are common to all the UAVs. The waypoints that are sequentially assigned to the trajectory are indexed with an apex k, i.e., $\underline{w}^k$, that indicates the step of the task assignment algorithm at which they are assigned. The assignment sequence is not known *a priori*. The target/task assignment algorithm at step k is shown in Figure 5.3.

There are three possible cases. If the waypoint assigned at the previous step ($\underline{w}^{k-1}$) lies within a challenging area A_c, and no other waypoints in that area need to be assigned, the targets to be assigned at step k are father waypoints, whose definition and assignment procedure is reported in Section 5.3.2. If $\underline{w}^{k-1}$ lies within a challenging area A_c and other waypoints lie in the same challenging zone which have not been assigned yet, these other waypoints are assigned to the UAV already designated as son for that zone. Finally, if $\underline{w}^{k-1}$ does not belong to any challenging area, the waypoint insertion procedure described in Section 5.3.1 is applied.

5.3.1 Waypoint Insertion Procedure

Let $\mathbf{p}_h^{k-1}\left(\mathbf{w}_h^{k-1},\mathbf{e}_h^{k-1}\right)$ be the trajectory of h-th UAV at step $k-1$ that includes a set of waypoints ($\mathbf{w}$) and edges ($\mathbf{e}$) currently assigned to that UAV. The sorted sequence of waypoints assigned to the h-th UAV at step $k-1$ can be written as $\mathbf{w}_h^{k-1}=\left[\underline{w}_h^1 \quad \dots \quad \underline{w}_h^{h_{k-1}}\right]$, where h_{k-1} is the number of waypoints assigned to that UAV at step $k-1$. At step zero, each UAV trajectory includes only the start and the end waypoints of the trajectory and the edge defined in between them. The waypoint insertion procedure consists in choosing the target to be added to the trajectory set, and selecting the UAV to which this waypoint must be assigned to. It is based on minimizing a proper cost function.

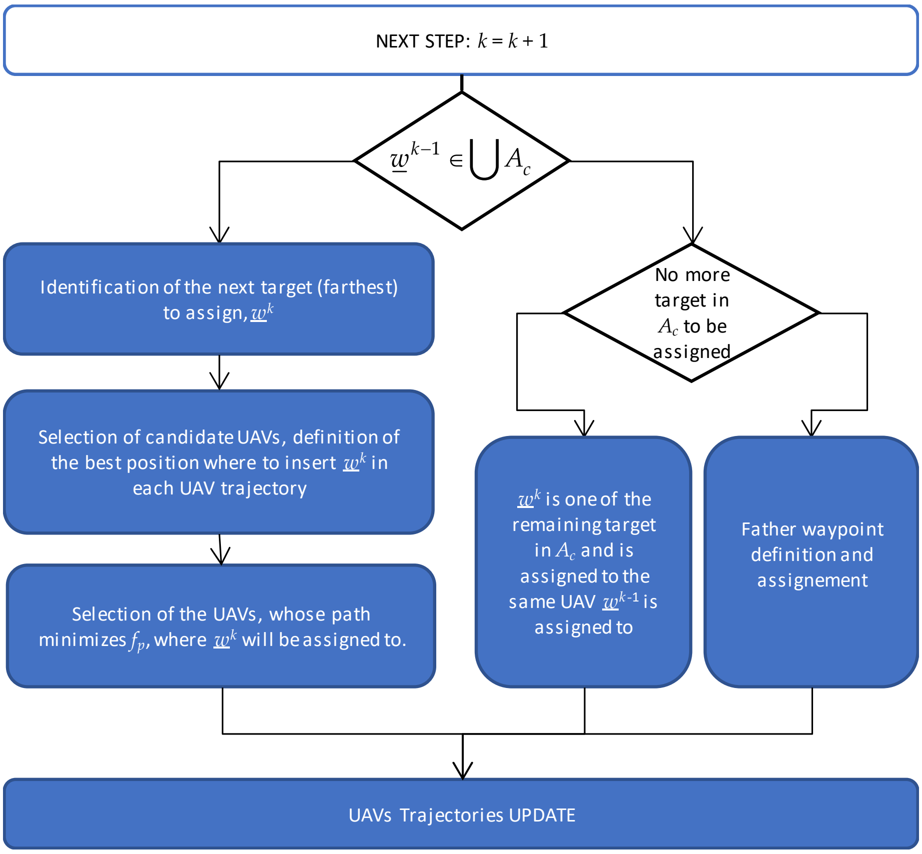

Figure 5.3 Target Assignment algorithm.

At each step, the target to be assigned is the "farthest" target, defined as the target that maximizes the distance from all the assigned waypoints and edges, while the cost function aims at minimizing the sum of path lengths for the different UAVs and keeping uniformity in the path length distribution. As it will be shown in the following, the assignment of the farthest target to the UAV with the minimum path length increase is a strategy that mimics optimal approaches such as MILP. In details, waypoints insertion procedure consists in the following three steps, also summarized in Figure 5.3:

1) Select the target i to be added ("farthest" target) as the one that maximizes f_T:

$$f_T = \frac{1}{J}\sum_{j=1}^{J} d_{ij} + \frac{1}{L}\sum_{l=1}^{L} D_{il} \tag{5.1}$$

where d_{ij} is the distance (computed along the relevant edge) between the not yet assigned target i, and the already assigned target j. j enumerates the already assigned waypoints (including fathers' ones) and l the already assigned edges, whose distance from the target i is named D_{il}.

2) Find the three edges that are closest to the farthest target, and the UAVs whose trajectories at k-1 include at least one of the endpoints ($\underline{w}_e$) of these edges. For each UAV, the farthest target is tried to be inserted before and after the point $\underline{w}_e$. The resulting paths that intersect the path of the other UAVs are discarded to avoid that targets could be assigned to farther trajectories when the path equalizing logic prevails. In addition, this improves the capability of the algorithm to mimic optimal techniques. Then, the best insertion location is defined as the one that minimizes path increase. The trajectory obtained by adding the farthest target to the path of the g-th UAV is defined as $\breve{\mathbf{p}}_g^k\left(\breve{\mathbf{w}}_g^k, \breve{\mathbf{e}}_g^k\right)$.

3) The UAV which the target is assigned to, is selected minimizing the cost function f_p, reported in Equation (5.2). This cost function is composed by two terms aimed at minimizing the overall distance and reducing the standard deviation (std) among UAV path lengths, thus ensuring (up to a certain level) uniformity in load distribution among UAVs. This is an innovative point of the target assignment procedure. The cost function is written as:

$$f_p = \frac{\frac{1}{\alpha}\mathrm{std}\left(\left[d\left(\mathbf{P}^{k-1}/\mathbf{p}_g^{k-1}\right); d\left(\breve{\mathbf{p}}_g^k\right)\right]\right) + \alpha \cdot \left(d\left(\breve{\mathbf{p}}_g^k\right) - d\left(\mathbf{p}_g^{k-1}\right)\right)}{\mathrm{mean}\left(\left[d\left(\mathbf{P}^{k-1}/\mathbf{p}_g^{k-1}\right); d\left(\breve{\mathbf{p}}_g^k\right)\right]\right)} \tag{5.2}$$

where $d\left(\mathbf{P}^{k-1}/\mathbf{p}_g^{k-1}\right)$ is the vector containing path lengths at step k-1 for all UAVs excluding the g-th UAV, for which path length is computed accounting for the farthest target added at the k-th step and defined as $d\left(\breve{\mathbf{p}}_g^k\right)$. $d\left(\mathbf{p}_g^{k-1}\right)$ is the path length of the g-th UAV at time step $k-1$. *mean* is the operator that yields the mean of the variables, α is a tuning coefficient whose role is relevant to the trade-off between path lengths uniformity and minimization.

In fact, the first term at the numerator is the standard deviation of the path lengths and is used to make as uniform as possible the distribution of path lengths among trajectories. The second term at numerator aims at assigning the waypoint to the UAV that has the minimum path increase after the waypoint is added to its trajectory and is thus aimed at minimization of total path length. These two elements are weighted by the coefficient α that is small at the first and last steps of assignment procedure, where the logic that prevails is to make trajectories as uniform as possible.

In the central steps of assignment procedure, α is higher and the aim of assignment procedure is biased towards minimization of the overall distance to be covered. α is a quadratic function of k and it is equal to α_{max}, when $k = n/2$ and equal to α_{min} when k is 1 or m. α_{min} and α_{max} are set by the user.

Figure 5.4 shows an example of waypoint assignment procedure applied for the sake of simplicity at 2D scenario (i.e., the altitude of the target is the same) with 14 targets and 3 UAVs (n = 14 and m = 3). In the case depicted in the figure, seven targets (2-4-5-7-10-11-12) have already been added to the trajectory, thus k = 8. The farthest target at this step is the waypoint 3, and the three closest edges are 1-10, 1-7, 5-2, that belong to the current trajectories of UAV 1, UAV 2 and UAV 3, respectively. In Figure 5.4.b the farthest target is tried to be inserted before and after each endpoint of the three closest edges, resulting in an increment of the path of the UAV where the endpoint belongs. Figure 5.4.b depicts the possible insertions for the three UAVs. For each UAV the unfeasible paths (those that intersect the trajectory of the others) are removed. In the specific case in the figure, all the paths of UAV 3 must be removed since they intersect the already defined path of UAV 2. Then the shortest path is estimated for each UAV, as in Figure 5.4.c. Figure 5.4.d represents the final trajectory after the insertion of the farthest target to the UAV, which path minimizes Equation (5.2) (UAV 1 in the considered example).

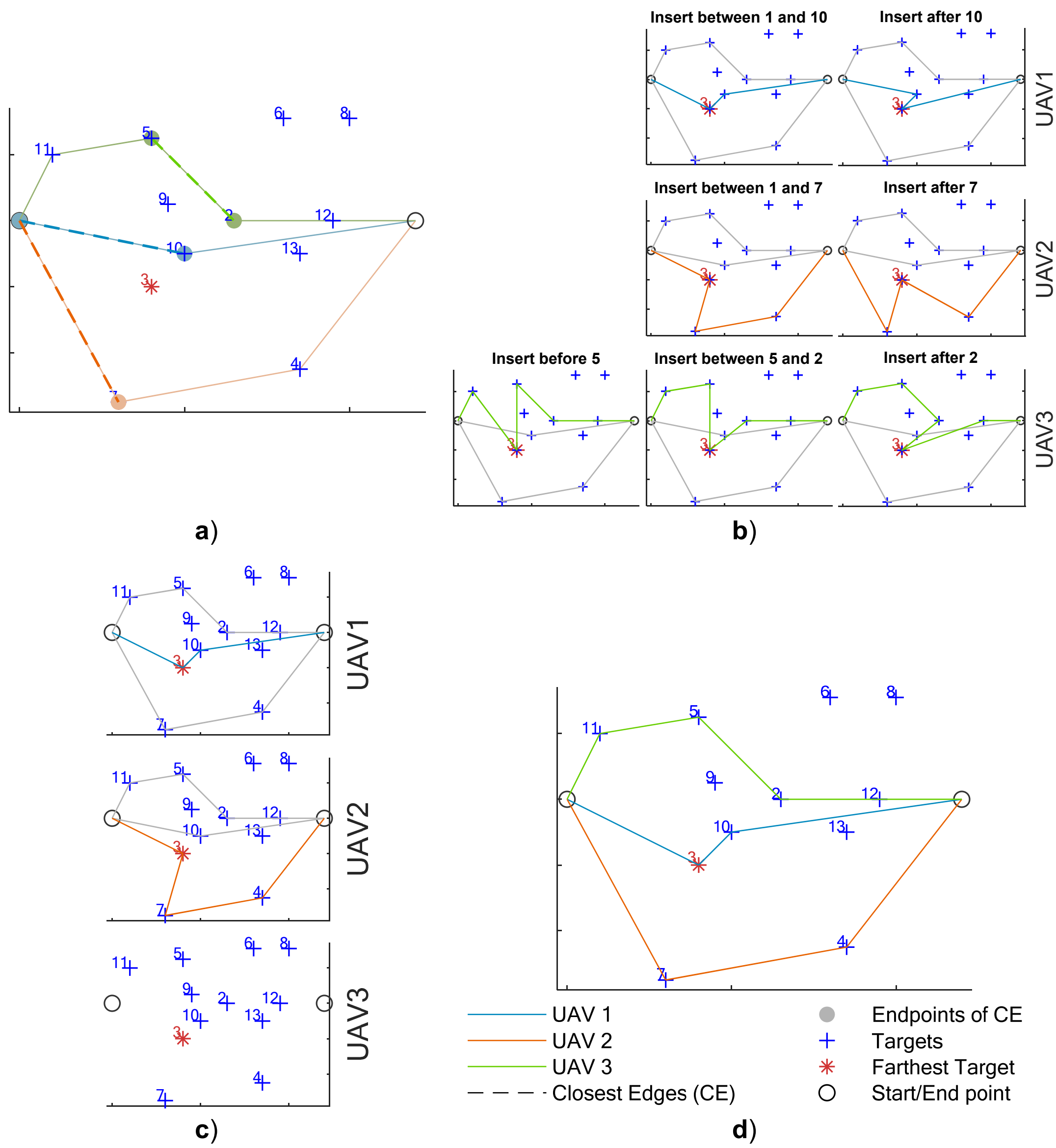

Figure 5.4 Example of waypoint insertion procedure with 1 target and 3 UAVs (n = 14 and m = 3). a) selection of the farthest target and definition of the three closest edges and their endpoints $\underline{w}_e$, b) Insertion of the farthest target before and after $\underline{w}_e$, c) identification of the shortest path for each UAV, neglecting the paths that intersect those of the other UAVs. d) Assignment of the target to the UAV whose path minimizes the cost function $\boldsymbol{f_p}$ in Equation (5.2).

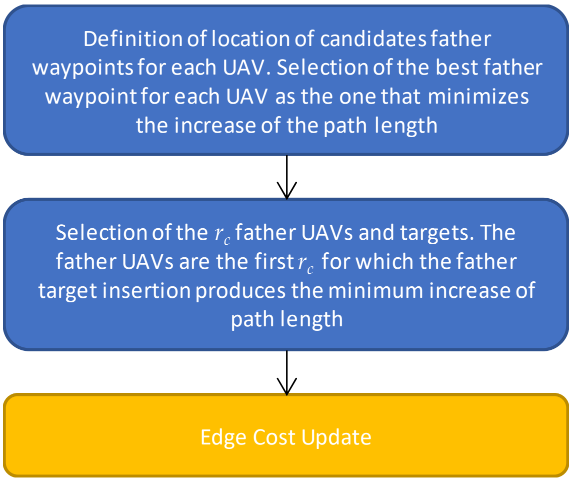

Figure 5.5 Father Waypoint Definition and Assignment procedure.

5.3.2 Father waypoints definition and assignment procedure

As anticipated above, when more than one target is inside a challenging area, all these targets are assigned to the same UAV that is designed as the son UAV for that zone. When the target assigned at step $k-1$ lies in a specific challenging zone A_c and no other targets in that zone need to be assigned, the next step consists in defining father waypoints for that challenging zone, and assigning them to specific UAVs. These are auxiliary waypoints, not foreseen in the initial targets definition and directly related to navigation needs. The basic input information from cooperative navigation approaches concerns the number of father UAVs required for a given zone. As in other processing steps, definition and assignment of father waypoints is done according to path length minimization principles. The main steps that compose fathers' assignment strategy are summarized in Figure 5.5, and described in the following:

1) For the c-th challenging zone, candidate father waypoints $\mathbf{x}_c = \left[\underline{x}_c^1 \quad \dots \quad \underline{x}_c^{o_c}\right]$, are estimated assuming that father(s) can be placed on an open face of the c-th challenging volume, where o_c is the number of open faces of that volume. Since that volume is a prism, one can easily identify the open faces as the ones not adjacent to any obstacle. For each open face, the candidate waypoint is defined projecting the barycentre of the targets inside the challenging area on a plane parallel to the face and located at a distance of 3 m from it (outside the challenging zone). It is assumed that the UAV designed as father must hold that position for the whole time required to the son UAV for flying inside the challenging zone, unless the father

target is located on top of the challenging volume. In that case the father UAV flies over the challenging area passing by the father waypoints. Candidate father UAVs are all the UAVs, excluding the one that is son for the c-th challenging zone. For each candidate UAV, all the possible father waypoints are tried to be inserted in between all the waypoints belonging to the trajectory at step k-1. The best insertion is defined, along with the best father, as the couple that minimizes the increase of path length Δ_{c,i_c}^{h,i_h} :

$$\begin{aligned} \delta_{\min,h} &= \min_{i_h,i_c} \Delta_{c,i_c}^{h,i_h} \\ \Delta_{c,i_c}^{h,i_h} &= \Delta\mathbf{w}_{c,i_c}^{h,i_h} + \Delta_{v_c} \\ \Delta\mathbf{w}_{c,i_c}^{h,i_h} &= \left\| \underline{w}_h^{i_h+1} - \underline{w}_c^{i_c} \right\| + \left\| \underline{w}_c^{i_c} - \underline{w}_h^{i_h} \right\| - \left\| \underline{w}_h^{i_h+1} - \underline{w}_h^{i_h} \right\| \end{aligned} \tag{5.3}$$

where Δ_{v_c} is the increase of the h-th UAV trajectory length due to adding i_c father point after the i_h element of the $\underline{w}_h^{k-1}$ sequence. $\| \ \|$ is the Euclidean distance, used instead of the distance on the obstacle-free polygonal chain, to simplify operations and reduce the computational burden. Δ_{v_c} is the total distance between the targets served by the son UAV in the c-th challenging zone, that is summed up to the Euclidean increase of trajectory length. Δ_{v_c} is added to $\Delta\mathbf{w}_{c,i_c}^{h,i_h}$, to take into account the fact that the father trajectory must be defined to serve the son UAV within the challenging zone, and the time spent to do this is strictly connected with the time the son UAV requires to fly inside the challenging area. Indeed, when planning the father trajectory, one must account for the time spent to serve the son, when the father must fly over or hover next to the challenging area.

The UAVs to which father targets are assigned are the first r_c for which $\delta_{\min,h}$ is smaller, where r_c is the number of required fathers for the c-th challenging zone. If more than one UAV choose the same father position, i.e., the same face from where to serve the son, evenly spaced points around the initially considered father position are designed as UAV father points to prevent those UAVs from holding the same position during son operations. Therefore, father assignment yields r_c new points to the UAVs trajectory, even if some of the fathers serve the son using the same face. As previously pointed out, father waypoints are only an indicative location for the true father trajectory in servicing the son. The definition of the specific father/son aiding geometry can be left to cooperative navigation studies [127], while the presented definition of father waypoints has sufficient level of detail in view of path planning aims.

The last step consists in updating the edge cost definition including the r_c father waypoints. The cost to travel from the newly defined father targets to the already defined $\underline{w}_i$ targets is estimated, in order to account also for the father waypoints in the definition and assignment of the farthest target for the next steps of the assignment procedure.

5.4 UAV TIMING

The previous processing steps define son and father(s) that operate in each challenging zone. UAV Timing, whose flow chart is depicted in Figure 5.6, defines the time the UAVs arrive and depart from a certain location (target) so that father and son arrive and leave the challenging zones at the same time. UAV timing can be divided in two steps. The first described in section 5.4.1 that yields the time of arrival and departure of the UAVs from the challenging areas. The second (Section 5.4.2) is aimed at defining the time of arrival and departure of each UAV at any waypoint of its trajectory.

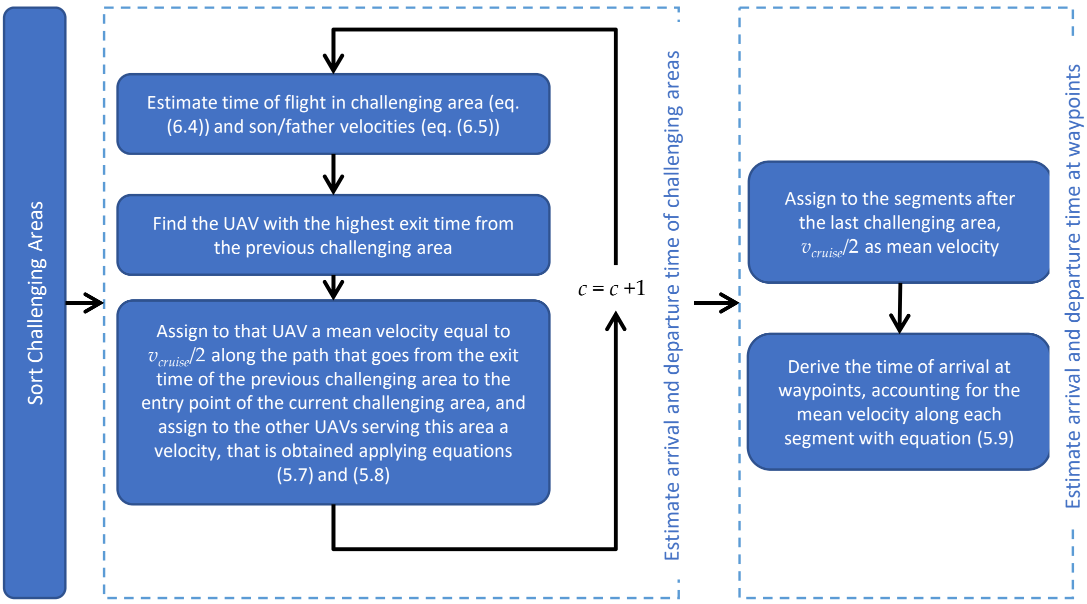

Figure 5.6 UAV Timing Strategy.

5.4.1 Arrival and Exit Time of the Challenging Areas

Assignment of the required time to fly from one challenging area to the following one occurs sequentially. Thus, the challenging areas are sorted based on the order in which they are served by the UAVs. Operation time in each challenging area depends on son UAV parameters, such as path length in the challenging zone and service time at each target. Whereas, the time of arrival at the challenging area depends on the exit time from the previous challenging areas. Especially in complex scenarios with several challenging zones, it is likely that the UAVs serving the *c*-th challenging area are coming from different challenging areas, with different exit times. As an example, in Figure 5.7 all three available UAVs used for the mission are needed to support the flight in challenging area 3. Although the previous challenging area both for UAV 1 and UAV 2 is the area number 4, the UAV 3 comes from area number 3.

The arrival time is evaluated as follows. First, the UAV with the maximum exit time from the previous challenging areas is considered. This UAV is assigned an average velocity along the path from the previous to the current challenging area, which defines its arrival time. Then, velocities for the other UAVs operating at the challenging area are evaluated imposing that all the arrival times should be the same. If one of these velocities exceed the dynamic capabilities of the aircraft, it is set equal to the UAV maximum speed, and both the arrival time and the average velocity of the other UAVs are updated.

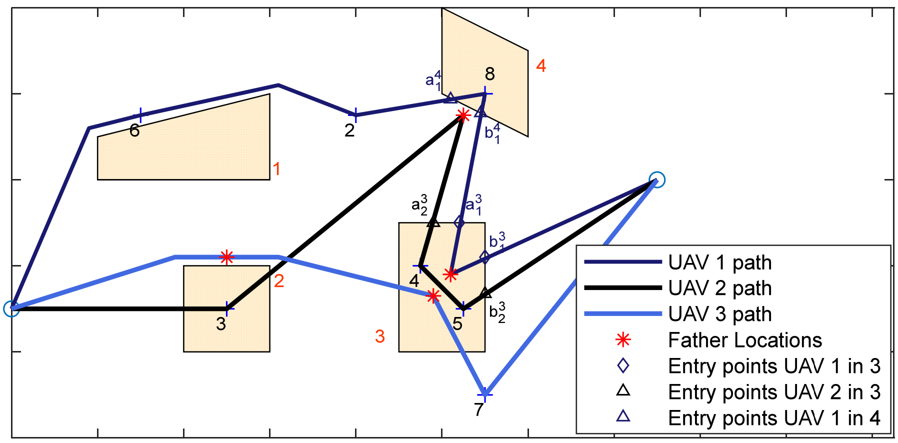

Figure 5.7 Path of three UAV in performing mission in an environment with heterogeneous GNSS coverage (horizontal view). Orange areas are GNSS challenging zones where cooperative navigation is required. The figure shows the distribution of the target amongst the UAV. The father for challenging area 2 is UAV 3, that is serving the son laterally. The fathers for challenging area 3 are UAVs 1 and 3 that fly above that zone, whilst UAV 2 is father for challenging area 4.

In details, the time of flight of the son UAV in the c-th challenging area, and thus the time of father(s) aiding for that area, is equal to:

$$\Delta t_c = d\left(\mathbf{p}\left(\underline{a}_S^c : \underline{b}_S^c\right)\right)\frac{2}{v_{chall}} + t_w\left(\underline{a}_S^c : \underline{b}_S^c\right) \tag{5.4}$$

where $\mathbf{p}\left(\underline{a}_h^c : \underline{b}_h^c\right)$ is the path of the h-th UAV from the entry point ($\underline{a}_h^c$) to the exit point ($\underline{b}_h^c$) of the c-th challenging area, and $d(\ )$ is the length of this path. Δt_c is obtained by summing up the time required to cover the path inside the zone and the servicing time of the waypoints inside the challenging zone, i.e., $t_w\left(\underline{a}_S^c : \underline{b}_S^c\right)$. Indeed, each waypoint is related to a servicing time that is the time required for the UAV to perform operation on that target, e.g., acquiring remote sensing data, performing surveillance related operations, carrying out delivery and/or pickup.

To estimate the flight time of the son in the challenging area, the overall distance of the son in that area is divided by $v_{chall}/2$, which is selected as mean velocity to guarantee that despite the velocity variations (e.g., in proximity of the targets, if the son must stop) the maximum velocity of the son in the challenging zone is not greater than v_{chall}. In summary, the mean velocities of the father(s) and the son in the challenging area are:

$$\begin{aligned} \bar{v}_S^c &= v_{chall}/2 \\ \bar{v}_F^c &= \frac{d\left(\mathbf{p}\left(\underline{a}_F^c : \underline{b}_F^c\right)\right)}{\Delta t_c} \end{aligned} \tag{5.5}$$

In general, father does not enter the GNSS challenging area. When the father flies above the challenging area, its "entry" and "exit" points (i.e., $\underline{a}_F^c$ and $\underline{b}_F^c$) are points whose x and y coordinates are given by the intersection of the horizontal projections of father trajectory and the top face of the challenging zone, while the vertical coordinate is given by selecting along the father path the point with those x and y coordinates. In the case the father location is lateral to the challenging area, no entry and exit points exist for the father that must hover in its location waiting for the son (thus, $\bar{v}_F^c = 0$). For the sake of clarity, Figure 5.7 shows the path of three UAVs, whose flights intersect a challenging area. UAV 1 and UAV 2 play the role of fathers for challenging zones 3 and 4, respectively, where their father waypoints are above and lateral with respect to the challenging area. With reference to challenging area 4, UAV 2 hovers at its father location when UAV 1 covers the path from $\underline{a}_1^4$ to $\underline{b}_1^4$. Instead, in the challenging zone 3 the father, i.e., UAV 1, moves from $\underline{a}_1^3$ to $\underline{b}_1^3$.

The time required by the son to fly in the challenging zone, i.e., Δt_c, connects the exit and entry time of the h-th UAV in the c-th challenging zone, respectively ($t\left(\underline{b}_h^c\right)$ and $t\left(\underline{a}_h^c\right)$, respectively):

$$t\left(\underline{b}_h^c\right) = t\left(\underline{a}_h^c\right) + \Delta t_c \tag{5.6}$$

Equations (5.4) and (5.6) guarantee that father and son will be at the same time at the exit point of the challenging area, if they are at the same time in the entry points. As stated above, to ensure the entry time in the challenging zone is the same for father(s) and son vehicle, one must account for the paths those UAVs have covered before arriving in that area.

Let $h = 1,\ldots,H$ be the index defining the UAVs that serve the c-th challenging zone as fathers and son. The arrival time of the h-th UAV at $\underline{a}_h^c$ is:

$$t\left(\underline{a}_h^c\right) = t\left(\underline{b}_h^{c-1}\right) + \frac{\bar{v}\left(\mathbf{p}\left(\underline{b}_h^{c-1} : \underline{a}_h^c\right)\right)}{d\left(\mathbf{p}\left(\underline{b}_h^{c-1} : \underline{a}_h^c\right)\right)} + t_w\left(\underline{b}_h^{c-1} : \underline{a}_h^c\right) \tag{5.7}$$

where $t\left(\underline{b}_h^{c-1}\right)$ is the exit time of the h-th UAV from the challenging zone that is in its trajectory before c. $\mathbf{p}\left(\underline{b}_h^{c-1} : \underline{a}_h^c\right)$ is the path covered by the UAV from the exit point of the previous challenging zone to the its entry point in c and $t_w\left(\underline{b}_h^{c-1} : \underline{a}_h^c\right)$ is the time required to serve waypoints (if any) during this path. $\bar{v}(\ )$ defines the mean velocity of the UAV along the path. The entry time is the same for each UAV that serve the c-th challenging zone if:

$$t\left(\underline{a}_1^c\right) = t\left(\underline{a}_2^c\right) = \cdots = t\left(\underline{a}_H^c\right) \tag{5.8}$$

The definition of the time at the entry point of the challenging zone occurs sequentially, therefore once solved the entry time definition at the previous challenging zone, $t\left(\underline{b}_h^{c-1}\right)$ is known with Equation (5.6), and the only unknowns of the combination of Equations (6.7) and (5.8) are the $\bar{v}\left(\mathbf{p}\left(\underline{b}_h^{c-1} : \underline{a}_h^c\right)\right)$. They are solved assigning $v_{cruise}/2$ to the UAV with the highest $t\left(\underline{b}_h^{c-1}\right)$ and then calculating the velocities for the other UAVs.

5.4.2 Time of Arrival and Departure for Each Waypoint

The previous step estimates the arrival time at the exit and entry points of the challenging zones, therefore for the h-th UAV $t\left(\underline{b}_h^c\right)$ and $t\left(\underline{a}_h^c\right)$ are known $\forall c = 1,\ldots,c_h$, where c_h is the number of challenging areas where the h-th UAV passes. This is in general smaller or equal than C, i.e., the number of all the challenging areas. As stated in the assumptions, the time of departure from the first waypoint is set as $t\left(\underline{w}_h^1\right) = 0$. The time of arrival at the last waypoint $t\left(\underline{w}_h^{n_h}\right)$ is estimated assuming that after the last challenging zone, the mean velocity of the vehicle is assigned to be equal to $v_{cruise}/2$, and the time for flying along the path is defined dividing by the path length (n_h is the number of assigned targets to the h-th UAV). Let us call $\underline{\omega}_h^{i_\omega}$ with $i_\omega = 0,1,\ldots,2c_h+1$, the waypoints for which the arrival time is already known, where $\underline{\omega}_h^{i_\omega=2c-1} = \underline{a}_h^c$ and $\underline{\omega}_h^{i_\omega=2c} = \underline{b}_h^c$ (note that omega is used instead of w). The sorted sequence of waypoints and exit and entry points of challenging areas is for the h-th UAV is:

$$\begin{gathered}\tilde{\mathbf{w}}_h = \Big[\underline{\omega}_h^0 \quad \cdots \quad \underline{w}_h^{\Delta c_1} \quad \underline{\omega}_h^1 \quad \underline{w}_h^{\Delta c_1+1} \quad \cdots \quad \underline{w}_h^{\Delta c_2} \quad \underline{\omega}_h^2 \quad \cdots \\ \cdots \quad \underline{\omega}_h^2 \quad \underline{w}_h^{\Delta c_2+1} \quad \cdots \quad \underline{w}_h^{\Delta c_3} \quad \underline{\omega}_h^3 \quad \cdots \quad \underline{\omega}_h^{2c_h} \quad \cdots \quad \underline{\omega}_h^{2c_h+1}\Big] \\ \underline{\omega}_h^{2c_h+1} = \underline{w}_h^{n_h},\ \underline{\omega}_h^{2c_h+1} = \underline{w}_h^1\end{gathered} \tag{5.9}$$

where Δc_{i_ω} is the number of waypoints covered by the UAV before the i_ω-th points with already known arrival time. Hence for the k-th waypoint, where $\Delta c_{i_\omega} + 1 \le k \le \Delta c_{i_\omega+1}$, the arrival time is evaluated as:

$$t\left(\underline{w}_h^k\right) = t\left(\underline{\omega}_h^{i_\omega}\right) + t_w\left(\underline{\omega}_h^{i_\omega} : \underline{w}_h^{k-1}\right) + \frac{d\left(\mathbf{p}\left(\underline{\omega}_h^{i_\omega} : \underline{w}_h^k\right)\right)}{\bar{v}\left(\mathbf{p}\left(\underline{\omega}_h^{i_\omega} : \underline{\omega}_h^{i_\omega+1}\right)\right)} \tag{5.10}$$

and the departure time is the arrival time plus $t_w\left(\underline{w}_h^k\right)$. The mean velocity along the path is obtained with Equations (5.5) and (6.7), respectively inside and outside the challenging areas.

5.5 POLYNOMIAL PATHS

The polygonal trajectory obtained in Section 5.3 connects the waypoints by polygonal chains and no information about velocity (except for the mean velocity) is available for each segment. To produce smooth trajectories and have a punctual information about the velocity and the acceleration that the UAV is experiencing, polynomial trajectories [136, 137] are defined, using for each UAV the assigned waypoints and their time of arrival and departure that are estimated in sections 5.3 and 5.4. To obtain the polynomial trajectory the method described in [136, 137] is used, which results in a UAV path, that is for each position component (x, y and z) a sequence of polynomial segments each of them defined in between two subsequent waypoints. The method described in [136] allows getting a closed-form solution to the quadratic program for polynomial optimization, which aims at minimizing the trajectory snap. The problem can be formulated as linear when the time in between two subsequent waypoints is known, and then easily inverted to obtain the polynomial coefficients [137].

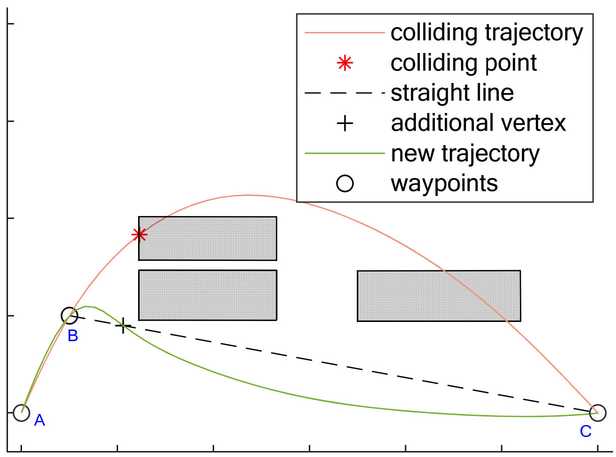

Figure 5.8 Logic to define an additional vertex to ensure that polynomial path does not collide with obstacles, represented in gray. The polynomial trajectory passing through A, B and C, resulting as linear solution of the polynomial trajectory optimization problem, is the one depicted in orange. This trajectory intersects one of the obstacles (red point). The projection of this point on the straight line (black cross) is computed and the obtained point is added to the original sequence of waypoint between B and C with the proper arrival time.

[136, 137] assume as problem unknowns not only the polynomial coefficients but also the time to transverse each segment, which turn the problem into a nonlinear optimization problem. In the application presented in this chapter the segment time is strictly dependent on the UAV synchronization performed in section 5.4. Hence, the solution of the linear problem gives a polynomial trajectory that passes for the desired waypoint at the desired time epoch.

Polynomial generation is not only accounting for the waypoint sequence that is defined in (5.9), but also includes the obstacle avoidance points that are derived in the section 5.2. It is assumed that the UAVs fly along the obstacle avoidance waypoints without stopping there. Using smooth polynomials instead of straight lines does not guarantee that the trajectories are still collision-free. This is handled adding additional vertices on the path in case of collisions. These vertices are computed as projections of the collision points along the polynomial trajectories, see Figure 5.8. In [137] a similar strategy is adopted, where the new added vertices slow down the trajectory. Due to the need for synchronization among the UAVs, the time of arrival at the new vertices is estimated based on Equation (5.10), thus avoiding changes in the arrival times at challenging.

5.6 PERFORMANCE ASSESSMENT

The planning algorithm presented in this chapter offers a solution for routing vehicles in an heterogenous environment with the aim of distributing the resources among the targets and using them together when is needed to pass through a challenging area. In this section, the algorithm is tested comparing its performance with those of optimal and heuristic techniques (Section 5.6.1) and then using it in an applicative example simulating a real-world scenario (Section 5.6.2).

5.6.1 Comparison with optimal and heuristic techniques

The target assignment algorithm is tailored to assign the farthest target in order to minimize the overall path length and to equalize paths. In facts, this solution allows obtaining, when the MILP hypotheses are valid, the same results of this optimal technique in terms of targets distribution among the UAVs. This section aims at comparing the performance of the proposed algorithm with optimal techniques, specifically analyzing:

- The classical MILP formulation [36], whose solution is a binary variable x_{ij}^{h} that is 1 if the edge from the target i to the target j is included in the h-th UAV path;
- The MILP formulated as set-covering [36], e.g., Multi-dimensional Multiple-choice Knapsack Problem (MMKP), that instead of the edges assumes the solution for each UAV connected to a circuit, i.e., a feasible sequence of edges. Therefore, the binary variable y_{l}^{h} is 1 if the l-th circuit is assigned to the h-th UAV, 0 otherwise.

Due to the limitations of the MILP algorithm, a heuristic technique, i.e., Particle Swarm Optimization, has been used to evaluate the performance of the multi-UAV for increasing number of targets and UAVs, using the approach described in [67] for discretizing the PSO algorithm.

To allow comparison with MILP, the assignment problem described in the chapter has been simplified and no challenging areas have been considered, due to the impossibility of linearizing the formula for father location identification and assignment. In fact, the proposed task assignment algorithm is adaptive, and minimizes in central steps of the assignment process, the sum of the distances covered by all the UAVs, while in the first and last steps provides path equalization as reported in Equation (5.6). Whereas, the MILP cost function cannot be tuned adaptively.

Thus, in this section, first we compare MILP (with and without set covering) and PSO aimed at global distance minimization with a customized version of the algorithm presented in this chapter which uses a constant high value for α. Then, we analyze the performance of the proposed algorithm (using the cost function reported in Equation (5.6) with varying α) in optimizing the overall time, comparing its results with those of the optimal algorithm described in [144]. Performance reported in this section is evaluated on 10 randomly generated scenario, i.e., waypoints location.

When dealing with overall distance minimization, the solutions of the proposed algorithm (insertion based), classic MILP and set-covering MILP (MMKP), are the same in terms of target assignment, whilst PSO rarely (i.e., only when the number of UAVs and targets is small) yields the optimal solution. Figure 5.9 shows the mean computation time, i.e., the mean time needed to for the problem to be solved in the ten randomly generated scenarios, for the four different techniques, with different numbers of UAVs. Computational times have been obtained with MATLAB® (The MathWorks, Inc., Natick, MA, United States) on a Windows PC with CPU at 2.20 GHz. In both MILP cases (with and without set covering) the running time is very sensitive to the number of targets, so that no solution is actually available when more than nine targets are considered. In case MILP is formulated as MMKP, the computational burden is not dependent on the number of the UAVs. As for the insertion-based techniques, the computational time is almost independent from the number of UAVs, while it increases for increasing number of targets. However, a reasonably fast solution can be obtained even with a relatively large number of targets. Contrarily, computation time for the PSO solution is strictly dependent on the number of UAVs, and almost constant as a function of the number of targets. To assess the performance of the algorithm in terms of overall time minimization (i.e., "optimality"), it is compared with the MILP algorithm described in [144], that assumes constant velocity. Thus, the overall time minimization can be reduced to minimizing the maximum path length among the UAVs.

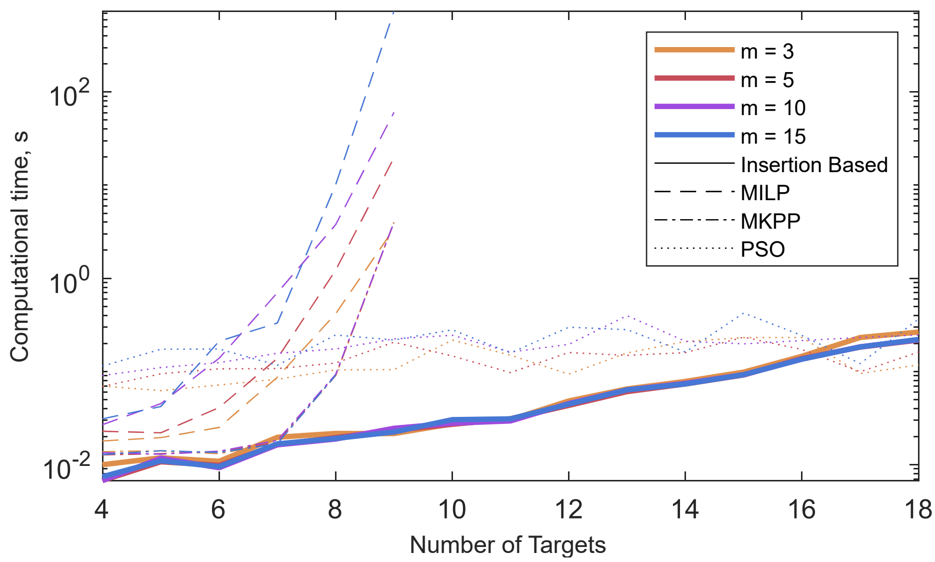

Figure 5.9 Mean computational time, i.e., running time for obtaining the solution of the VRP, with four different techniques: The method proposed in this chapter (Insertion Based), the classical MILP technique (MILP), the MILP formulated as set covering problem (MMKP) and the PSO algorithm. The time is estimated as a mean of the computation time among ten randomly generated sets of waypoints. The edge cost is estimated once for all the techniques and only target assignment time is considered in the picture, to ensure the results are only dependent on the number of targets, and not on the selected scenario. Different number of UAVs (m) are used for the simulation identified by different colored lines.

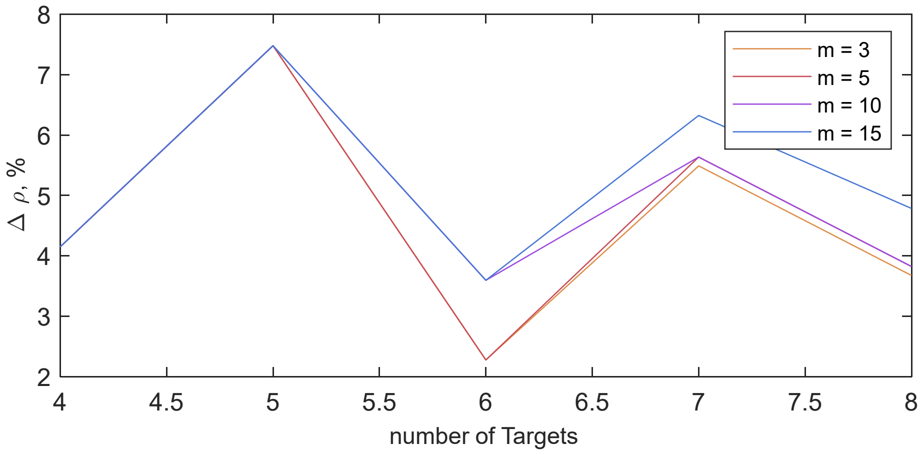

Figure 5.10 $\Delta\rho$, i.e., Percentage difference between the maximum path length obtained using the algorithm described in the chapter, and the one calculated by an optimal technique aimed at minimizing the maximum path length (and thus the overall mission time if velocity is assumed constant). $\Delta\rho$ is estimated as a mean in ten randomly generated sets of waypoints.

Figure 5.10 quantifies the capability of the described algorithm to mimic optimal overall time minimization, reporting the mean among the 10 randomly generated scenarios of the normalized difference between the maximum path length obtained with our algorithm and with the one described in [144]; i.e., $\Delta\rho$. Being ν the optimal maximum path length, one can define:

$$\Delta\rho = \frac{\max\left\{d\left(\mathbf{p}_1\right), d\left(\mathbf{p}_2\right), \ldots, d\left(\mathbf{p}_n\right)\right\} - \nu}{\nu} \tag{5.11}$$

As far as the optimal solution is available, the algorithm proposed in this chapter is able to guarantee a maximum path length that is at maximum 8% higher than the optimal. The increment of the maximum path length with respect to the optimal case it is not dependent on the number of UAVs, nor on number of targets.

5.6.2 Results of Routing Algorithm in Real-World Scenario

After analyzing the performance of the proposed algorithm in terms of computational cost, in this section it is tested in a real-world scenario (simplified just neglecting topography variations and considering buildings as prisms).

5.6.2.1 Scenario

The selected scenario is a portion of the Centro Direzionale (Business District) in Naples, i.e., isola C and a portion of isola E. Specifically it is a rectangular region of 300 × 280 m. Within a quasi-unsupervised workflow, the scenario has been imported using freely available 3D maps and commercial software tools, i.e., Open

Street Maps (OSM) and Autodesk® Infraworks® and 3ds Max®. The 3D representation of the considered scenario in Google Maps is shown in Figure 5.11, whilst the simulated scenario imported in MATLAB is shown in Figure 5.12, where the blue crosses represent target waypoints (n = 16) and the gray circles identify start and end location.

Figure 5.11 Google Earth's 3D view of the environment considered for Path Planning, isola C and E of Business district in Naples.

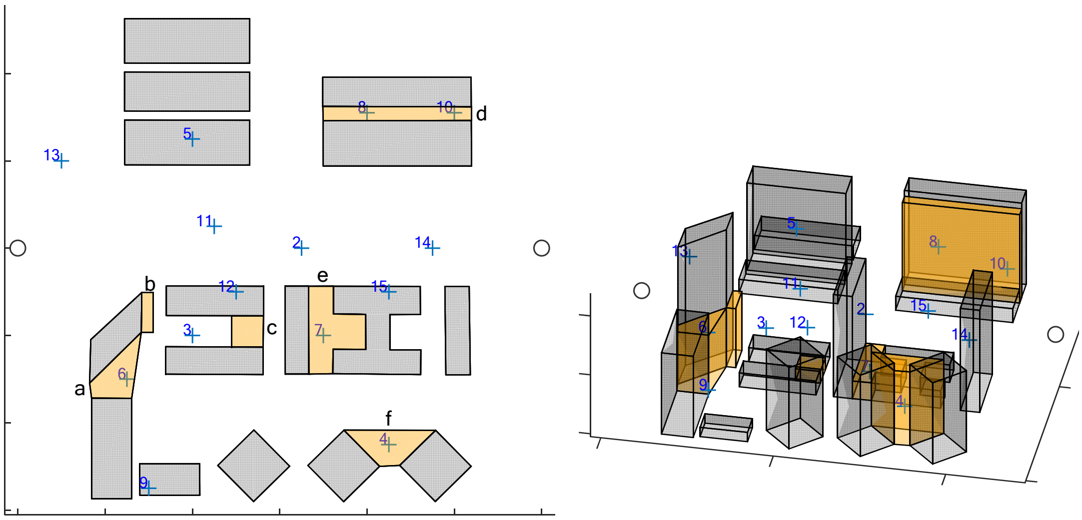

a) b)

Figure 5.12 Simulation scenario, a) top view and b) 3D view. Buildings are gray. The Orange areas are GNSS challenging areas. Blue crosses are the targets, whilst gray circles are the starting and ending points that are common to all the UAVs.

Buildings and challenging zones are respectively drawn in gray and orange. From the 3D view of the simulation scenario (Figure 5.12.a), it can be noticed that the challenging zones have in general an altitude that is lower than the adjacent buildings. Challenging zones are enumerated with letters. Waypoints 4,6,7,8,10 fall within a challenging area. All the challenging zones contain a waypoint except for *b* and *c*, that are thus seen as obstacles by all the UAVs. In each challenging zone one father is required, except for zone *e* where it is assumed that two fathers are required. Cruise velocity and challenging velocity are respectively $v_{cruise} = 8\ m/s$ and $v_{chall} = 2\ m/s$, whilst the service time is 0 *s* for the waypoints outside the challenging, and 1 *s* for those within these areas.

5.6.2.2 Results

First, the algorithm has been tested on the selected scenario setting the minimum number of UAVs to fulfill mission requirements. Since zone *e* requires two fathers (and one son), this minimum number is three. UAV trajectories resulting from the algorithm in are shown in Figure 5.13 (x-y plane), and in Figure 5.14 (3D). The UAVs paths are smooth due to the usage of polynomial planning.

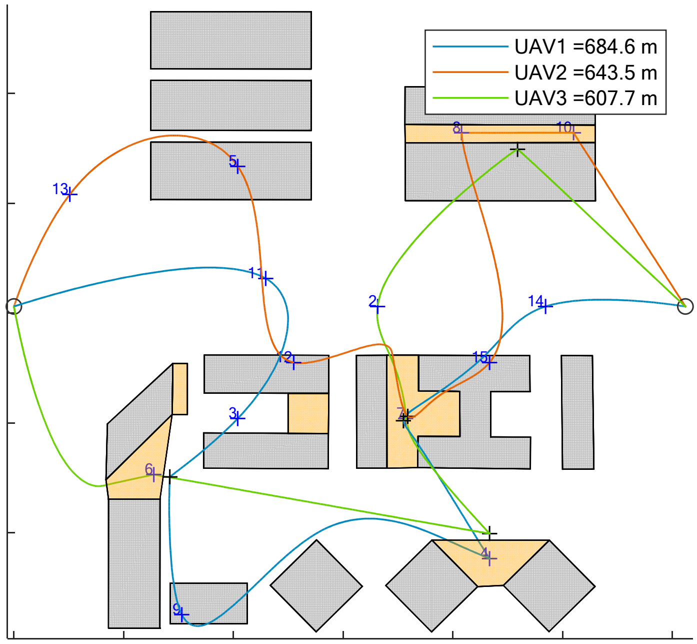

Figure 5.13 Top view of trajectory generated by the proposed path planning algorithm, for the proposed scenario. n = 16, m = 3. Father waypoints are highlighted with black crosses. The path length of the UAVs is reported in the legend.

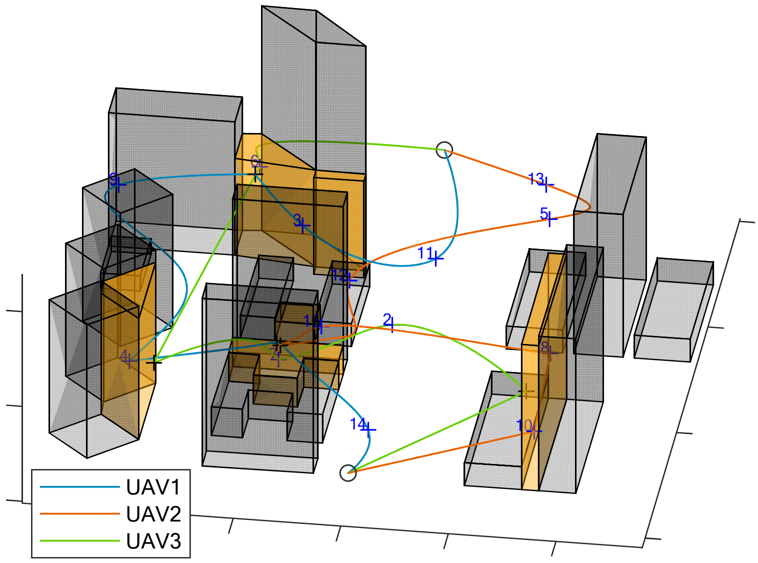

Figure 5.14 3D view of trajectory generated by the proposed path planning algorithm, for the proposed scenario. $n = 16$, $m = 3$. Father waypoints are highlighted with black crosses.

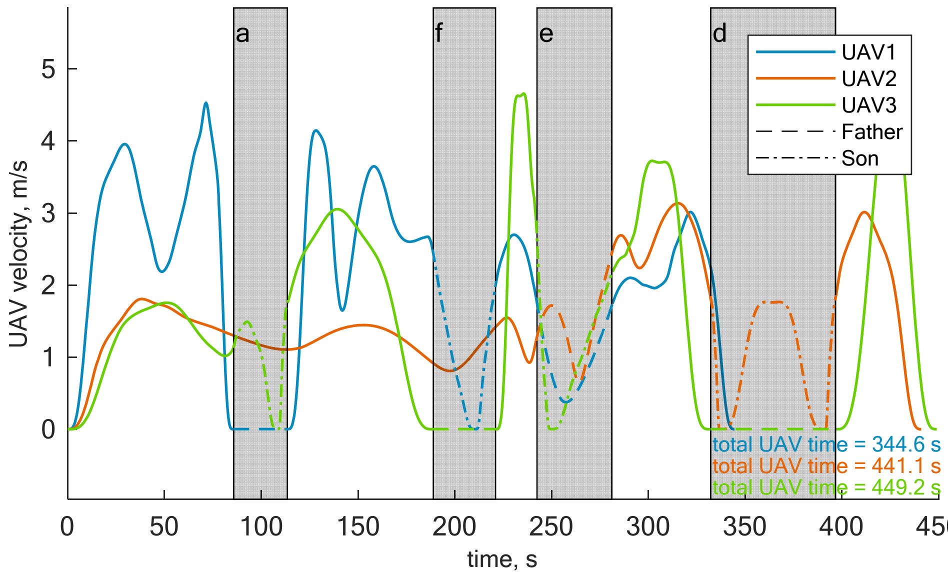

Figure 5.15 Velocity module of the UAVs during their trajectories, the time to flight along the trajectory is reported in the figure highlight by the corresponding color of the UAV. The challenging area are highlighted by gray background. Note that the challenging areas are sorted in the same order of Table 5.1. Father and son UAV are highlighted in the challenging area by dashed and dot-dashed lines.

Figure 5.15 shows the velocities of the UAVs during their paths. In the challenging areas (gray background) the son and father UAVs are highlighted with dashed and dash-dotted lines, respectively. The velocity of the son in the challenging area is always smaller than v_{chall}, whilst the velocity of the fathers and of all the UAVs outside the challenging area is below v_{cruise}. Synchronization results are reported in Table 5.1 highlighting times of arrival and departure of fathers and the son are the same for each challenging area. The mission total duration is about 8 min. Table 5.1 reports the UAVs that are assigned as father and son in the challenging areas, that are sorted in the same order the UAVs pass through them. Challenging areas b and c have no data since there is no waypoint lying there and no UAV is demanded to fly in there. The path length of the three UAVs, reported in Figure 5.13 is almost the same, as guaranteed by path equalization in Equation (5.2). As shown in Figure 5.15, the flight time is shorter for UAV 1 than for UAVs 2 and 3.

Table 5.1 Challenging Areas' characteristics and arrival and departure time

Challenging Zone	Father(s) ID	Son ID	Arrival time, s	Exit time, s
a	1	3	24.06	36.35
e	2,3	1	65.80	78.15
f	3	1	90.45	98.96
d	3	2	125.39	151.91
b	-	-	-	-
c	-	-	-	-

5.6.2.3 Algorithm performances with varying m and n

The computational burden of the algorithm in the simulated scenario (n = 16) with varying number of UAVs is analyzed in Table 5.2, which reports the computation time needed for each phase of the path planning algorithm along with the total time for running the simulation, as a function of the number of the UAVs (m) used to accomplish the mission. The path planning phase that mostly concurs to the computational burden increase is the target assignment. As expected, the computation time is slightly dependent on the number of UAVs used. Indeed, the proposed insertion-based technique sequentially adds target to the trajectory and the computation time for each step (i.e., waypoint insertion) is almost constant. Table 3 shows the target sequence assigned to each UAV varying m from seven to 20, the UAVs saturation point is obtained at m = 11. For the sake of brevity, the targets distribution among the UAVs is reported in Figure 5.16 only for m = 5 and m = 11. The only factor that can lead to an increase of computation time is the increase of the number of waypoints, which is analyzed in Figure 5.17. For the sake of completeness different m values are considered, resulting in a very slight variation of the computational burden when the number of UAVs that composes the fleet varies. The minimum number of targets to assign is equal to 3 since the trajectory is always composed by the start and the end point. The computational burden increases by increasing the number of targets, as expected.

Table 5.2 Algorithm performances by varying the number of UAVs used for performing the mission. It is assumed the number of targets is the same defined in used scenario in Section 7.2.1, n = 16. The computation time has been estimated for each phase of the planning algorithm. Mission time is the time for mission competition that is the maximum time of flight among the UAVs.

m	Computation Time[1], s					Mission Time, s
	Edge Cost	Target Assignment	UAV Timing	Polynomial Trajectory	Total Time	
3	0.23	0.78	0.01	0.07	1.09	496.46
4	0.22	0.65	0.01	0.06	0.94	394.27
5	0.23	0.68	0.01	0.08	1.00	333.39
6	0.23	0.72	0.01	0.05	1.01	321.64
7	0.22	0.75	0.01	0.06	1.04	265.74
8	0.23	0.75	0.01	0.06	1.05	265.74
9	0.23	0.75	0.01	0.06	1.05	265.74
10	0.23	0.79	0.01	0.08	1.11	265.74
11	0.22	0.78	0.01	0.08	1.09	265.74
12	0.22	0.80	0.01	0.08	1.11	265.74
13	0.24	0.88	0.01	0.08	1.21	265.74
14	0.23	0.83	0.01	0.08	1.15	265.74
15	0.23	0.83	0.01	0.08	1.15	265.74
16	0.23	0.83	0.01	0.08	1.15	265.74
17	0.23	0.81	0.01	0.08	1.13	265.74
18	0.22	0.83	0.01	0.09	1.15	265.74
19	0.22	0.87	0.01	0.09	1.19	265.74
20	0.22	0.85	0.01	0.08	1.17	265.74

[1] The computation time has been evaluated with MATLAB running on a Windows PC at 2.2 GHz.

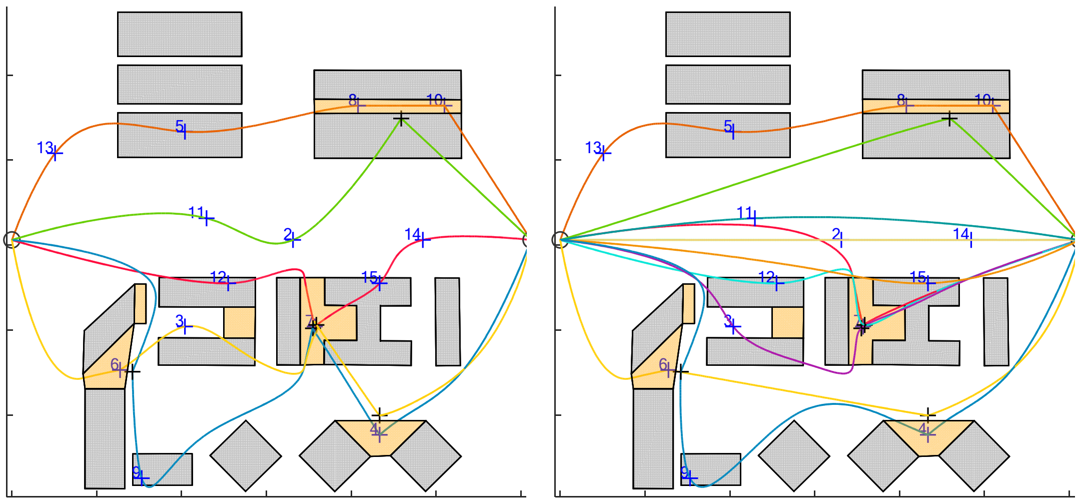

a) b)

Figure 5.16 Top view of trajectory generated by the proposed path planning algorithm, for the proposed scenario with n = 16 and a) m = 5, b) m = 11. Black crosses are father waypoints.

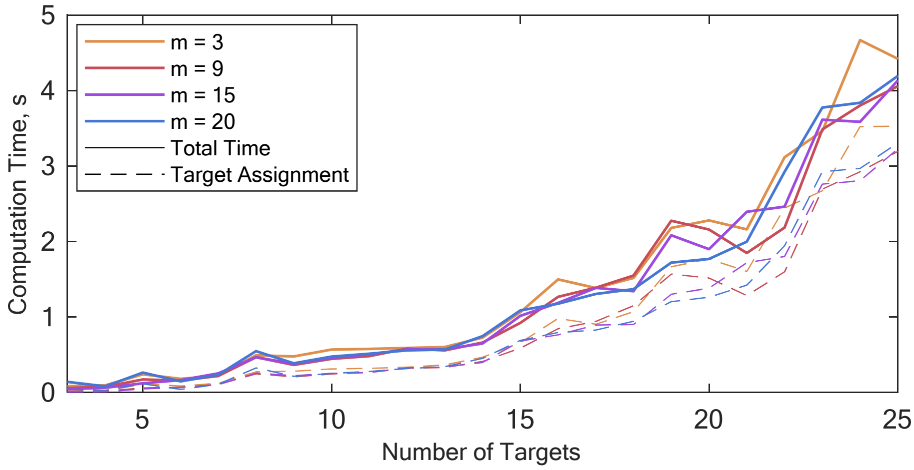

Figure 5.17 Computation time of the proposed algorithm by varying the number of targets, the total time and the time required for target assignment have been considered. The simulated environment is the one depicted in Figure 5.12.

Table 5.3 Target distribution among the UAVs, for a fleet composed by seven to 20 UAVs, $n = 16$. The number of targets with higher index are father targets (target id to 17 to 21).

	Numbers of UAVs (*m*)				
UAV id	**8**	**9**	**10**	**11**	**11-20**
1	1-3-19-9-4-16	1-3-19-9-4-16	1-3-19-9-4-16	1-19-9-4-16	1-19-9-4-16
2	1-13-5-8-10-16	1-13-5-8-10-16	1-13-5-8-10-16	1-13-5-8-10-16	1-13-5-8-10-16
3	1-17-16	1-17-16	1-17-16	1-17-16	1-17-16
4	1-6-18-16	1-6-18-16	1-6-18-16	1-6-18-16	1-6-18-16
5	1-7-15-16	1-7-16	1-7-16	1-7-16	1-7-16
6	1-12-20-16	1-12-2-20-16	1-12-2-20-16	1-12-20-16	1-12-20-16
7	1-3-21-16	1-3-21-16	1-3-21-16	1-3-21-16	1-3-21-16
8	1-11-2-14-16	1-11-14-16	1-11-16	1-11-16	1-11-16
9	-	1-15-16	1-15-16	1-15-16	1-15-16
10	-	-	1-14-16	1-14-16	1-14-16
11	-	-	-	1-2-16	1-2-16
12-20	-	-	-	-	1-16

While Figure 5.17 reports only the target assignment and the total computation time, the time needed to perform each phase of the algorithm are exploded in Figure 5.18, when $m = 3$. The increase of the number of targets mainly affects the target assignment time. Polynomial trajectory computation and UAV timing are not affected by the increment of n, whilst the edge cost definition rises, due to the increase of the target couples to be considered. The computation time for a larger number of targets (from 25 to 90) is reported in Table 5.4. The table shows that even with a high number of targets the computation time is compliant with the requirements for pre-mission planning. It could be noticed that in case of UAV failures during the mission, if the number of remaining targets is small (up to 20), the algorithm could be used to re-plan the path, since the running time is compliant with near real time requirements.

For the sake of completeness, Table 5.2 also shows the mission time, i.e., the maximum flight time among the UAVs. For the analyzed scenario, the mission completion time decreases with the number of UAVs, since path equalization is enhanced by an increasing number of UAVs. Nevertheless, mission time reduction with UAVs number remains constant after m = 7. Indeed, even adding more UAVs the minimum path length and thus the minimum travelling time depends on the distance between the start and end point. It is important to notice that for each scenario, (i.e., number of targets, targets location, obstacles and challenging zones) there exists a UAV saturation point, which is the number of UAVs above which, even adding more UAVs to the fleet the target distribution remains the same. In facts, the UAVs beyond the saturation point are not needed for target collection and are demanded only to cover the distance from the start to the end point.

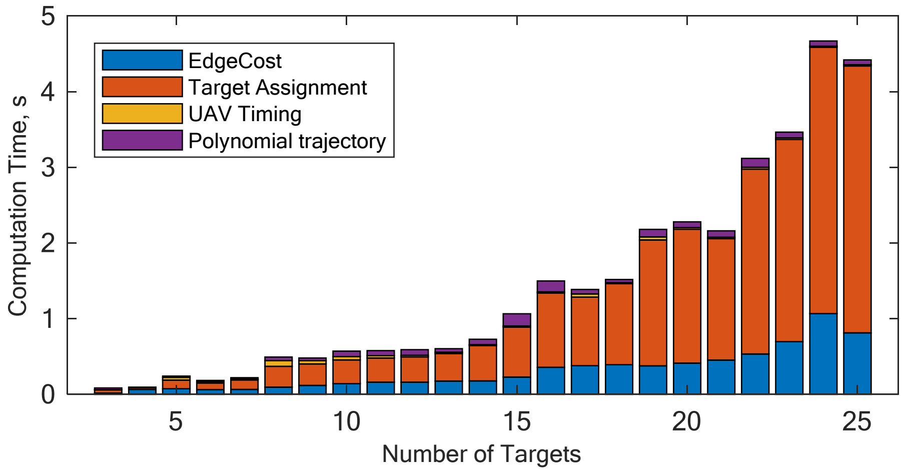

Figure 5.18 Computation time of the proposed algorithm by varying the number of targets, with m = 3. The time required to compute each step of the planning algorithm is stacked in bars, yielding as result the total computation time. The simulated environment is the one depicted in Figure 5.12.

Table 5.4 Computation Time varying the number of targets and UAVs, simulated scenario is depicted in Figure 5.12.

		Computation Time, *s*			
	Numbers of UAVs (*m*)	**3**	**9**	**15**	**20**
Number of Targets	30	7.41	7.35	7.18	7.14
	35	12.53	12.39	11.74	11.55
	40	19.04	20.35	20.0	19.83
	50	58.75	60.84	55.35	60.03
	60	109.54	108.90	108.84	108.95
	70	223.12	225.89	224.79	226.57
	80	339.47	336.90	337.45	338.40
	90	594.79	595.54	593.70	596.80

Chapter 6: Cooperative Navigation for pointing accuracy

Navigation of commercial small UAS is typically based on the integration of low-cost avionics systems, such as consumer grade Micro Electro-Mechanical Systems (MEMS) inertial sensors and Global Navigation Satellite Systems (GNSS) receivers. MEMS-based magnetometers are also usually adopted to estimate heading. This results in position accuracies of the order of 5-10 *m* and attitude accuracies of approximately 1°-5°, with possibly larger errors on heading [148]. This accuracy level suffices for real time stabilization and control, but it is not suitable for applications that require precise positioning and fine sensor pointing, such as high accuracy 3d mapping which represents an important application field for small UAS.

In fact, direct georeferencing strategies adopted in LIDAR-based mapping create a strong link between navigation performance and accuracy in 3d reconstruction [10, 149]. Furthermore, accurate estimates of position and attitude may also play a key role in photogrammetric processing, potentially limiting the need of Ground Control Points (GCPs) for given reconstruction accuracy requirements, helping tie points matching, and reducing the computational time for bundle adjustment [150].

Recent technology trends have led to an increasing availability of accurate positioning solutions onboard mini- and micro- Unmanned Aerial Vehicles (UAVs). As a consequence, miniaturized multi-frequency GNSS receivers are becoming more affordable [151], and recent experimental analyses have shown the potential of single frequency (L1 only) receivers in the framework of differential architectures [152]. In all cases, accurate positioning is achieved using a ground antenna as reference, and carrier-phase differential approaches either in real time (RTK - real time kinematic) or off-line (PPK - post processing kinematic). These approaches lead to cm-level positioning accuracy even for relatively large distances from the ground antenna used as reference [153, 154], which typically fulfills application requirements.

As regards attitude estimation, accuracy can be improved by exploiting high performance avionics, with relatively high hardware costs. Possible approaches comprise integration of miniaturized tactical grade Inertial Measurement Units (IMU), which are accurate enough to perform initial north-finding independently of magnetometer output, and/or dual antenna GNSS architectures (only for heading). Nevertheless, the attainable performance does not completely fulfil requirements in some application fields. As an example, again considering photogrammetric 3d mapping, attitude estimates may still be too inaccurate to be assigned with a high weight during the 3d reconstruction process [155].

A different strategy consists in adopting a multi-UAV approach, exploiting spatial diversity of measurements obtained by a formation of cooperating aircraft. [12, 15, 156] presented the concept of integrating GNSS (in particular, GPS) and vision-based measurements to provide inertial- and magnetic-independent attitude information (which can be defined as "DGPS/Vision" processing). Ref. [12] discussed direct attitude estimation based on two cooperating deputies, while in [156] the focus was set on integrating the attitude information within a navigation algorithm based on Extended Kalman Filtering (EKF). Then, Ref. [15] presented a tight integration scheme to combine GNSS and vision-based information. In these papers, code-based differential GPS (DGPS) was used as GPS information source. DGPS provides a reliable solution based on kinematic processing, with meter-level accuracy. Baselines of the order of 100 m are needed to convert the meter-level positioning error into sub-degree angular uncertainty [12].

Following this line of research, this chapter presents an algorithm that exploits carrier phase differential GPS (CDGPS) measurements as GNSS information source, to improve the pointing accuracy with respect to the techniques proposed in [12, 15, 156]. Therefore, a CDGPS/Vision technique it is introduced and analysed within a loosely [157] and a tightly coupled [158] integration scheme, reported respectively in sections 6.4 and 6.5. The cooperative navigation concept is described in section 6.1. CDGPS processing aimed at estimating the baseline between two receivers is described in section 6.3, whereas some introductive remarks about GPS measurement and their combinations are reported in 6.2. The proposed CDGPS/Vision technique has been tested on real data acquired during a flight campaign conducted on November 22th, 2016. Flight experiment results are reported in section 6.6.

6.1 COOPERATIVE NAVIGATION CONCEPT

The key idea to estimate attitude of a "chief" UAV is to exploit a number of "deputy" UAVs acting simultaneously as flying antennas and as visual features. CDGPS processing provides chief-to-deputies baselines (and thus, the corresponding unit vectors) directly in a stabilized North-East-Down (NED) reference frame, $\mathbf{r}_k^n$, while vision processing gives unit vectors in the chief body reference frame (BRF) $\mathbf{r}_k^b$, where the *k* index indicates the *k*-th deputy UAV; *k=1:K*. Thus, combining the two measurements, it is possible to infer information on chief attitude. In fact, CDGPS and Vision Based unit vector are related through the equation:

$$\mathbf{r}_k^b = C_n^b \mathbf{r}_k^n \tag{6.1}$$

where C_n^b is the NED to BRF attitude matrix, and the superscript *b* and *n* indicate respectively the vector expressed in the NED and BRF frames.

Theoretical performance limits can be discussed by considering angular uncertainties of differential GPS estimates as a function of the norm of the baseline **b** among UAVs. At a first level of approximation, if the baseline is large enough, and assuming that the CDGPS error distribution is the same in all horizontal directions, angular uncertainties are given by

$$\begin{aligned} \sigma_{CDGPS,angle,hor} &\cong 2\arctan\left(\frac{\sigma_{CDGPS,lin,hor}}{2|\mathbf{b}|\sqrt{2}}\right) \\ \sigma_{CDGPS,angle,vert} &\cong 2\arctan\left(\frac{\sigma_{CDGPS,lin,\mathrm{vert}}}{2|\mathbf{b}|}\right) \end{aligned} \tag{6.2}$$

where | | indicates the Euclidean norm. Whereas, $\sigma_{CDGPS,lin,hor}$ and $\sigma_{CDGPS,lin,ver}$ are the CDGPS uncertainties in the horizontal and vertical direction, respectively. Assuming CDGPS and camera measurements are uncorrelated, the angular error resulting from CDGPS/Vision processing can be derived summing up the error of the CDGPS processing (equation (6.2)) with the camera error, that is basically dependent on the camera instantaneous field of view (IFOV). It is:

$$\begin{aligned} \sigma_{CDGPS/Vision,angle,hor} &\cong \sqrt{\sigma_{CDGPS,angle,hor}{}^2 + IFOV^2} \\ \sigma_{CDGPS/Vision,angle,ver} &\cong \sqrt{\sigma_{CDGPS,angle,ver}{}^2 + IFOV^2} \end{aligned} \tag{6.3}$$

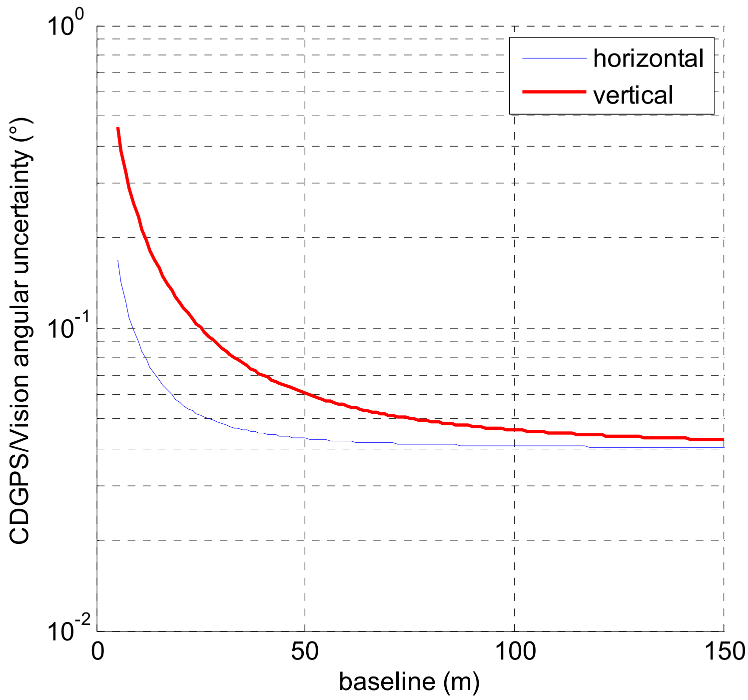

Figure 6.1 Theoretical performance limits for CDGPS/Vision processing

Using CDGPS uncertainties typically attained after successful integer ambiguities fixing (0.02 and 0.04 m for horizontal and vertical directions, respectively) and a camera IFOV of 0.04° we get the results shown in Figure 6.1. The potential of CDGPS/Vision for high accuracy attitude estimation can be appreciated from the diagrams: a baseline of a few tens of meters enables angular uncertainties of the order of 0.05°, and for increasing baseline the error is actually bounded by the assumed camera IFOV.

6.2 GPS OBSERVATIONS

GPS observation can be usually divided in three types: pseudorange or code observations, carrier phase observations and doppler observations. This section describes pseudoranges and carrier phase observations (section 6.2.1) and how their combined formulations can contribute to the formation of the single and double difference measurements, respectively in sections 6.2.2 and 6.2.3.

6.2.1 Pseudorange and Carrier Phase observation

The code observations are direct measurements of the signal's travelling time. Multiplying the code observation with the speed of light yields the pseudorange (PR) measurement

$$P_r^s = \rho_r^s + c\left(\delta t_r - \delta t^s\right) + I_r^s + T_r^s + \sigma_r^s + \left(b^{Pr}\right)_r + \left(b^{Pr}\right)^s \tag{6.4}$$

The superscript *s* and the subscript *r* indicate respectively the satellite and the receiver, whose spatial separation (range) is ρ_r^s. The pseudorange measurement P_r^s includes the receiver and satellite clock biases δt_r and δt^s, which multiply the speed of light *c*, the ionosphere I_r^s and troposphere T_r^s error that can be usually predicted with empiric models [159] and the measurement thermal noise σ_r^s, which is assumed to be a pure random with zero mean gaussian noise. All the other biases and dispersive receiver and satellites hardware effect can be included in the *b* terms, for the receiver and the satellite.

The carrier phase (CP) measurements are derived from tracking the carrier onto which the code is modulated, being λ the signal wawelenght the carrier phase measurement can be expressed as

$$L_r^s = \rho_r^s + c\left(\delta t_r - \delta t^s\right) - I_r^s + T_r^s + \lambda \psi_r^s + \varepsilon_r^s + \left(b^{Cp}\right)_r + \left(b^{Cp}\right)^s \tag{6.5}$$

ε_r^s is the carrier phase thermal noise, hence ψ_r^s is the phase ambiguity that is a real valued constant parameter along the tracking arc.

6.2.2 Single Difference Measurements

The single difference (SD) observation is obtained by subtracting the same GPS observation taken by two GPS receiver at the same time. Assuming to have two receiver A and B, the single difference with respect to the satellite *s* is given by $\square_{AB}^{s}=\square_{B}^{s}-\square_{A}^{s}$, the pseudorange and carrier phase measurements on the L1 and L2 frequencies are:

$$\begin{aligned}
\left(P_1\right)_{AB}^s &= \rho_{AB}^s + c\delta t_{AB} + I_{AB}^s + T_{AB}^s + \left(\sigma_1\right)_{AB}^s + \left(b_1^{Pr}\right)_{AB} \\
\left(P_2\right)_{AB}^s &= \rho_{AB}^s + c\delta t_{AB} + \left(\frac{\lambda_1}{\lambda_2}\right)^2 I_{AB}^s + T_{AB}^s + \left(\sigma_2\right)_{AB}^s + \left(b_2^{Pr}\right)_{AB} \\
\left(L_1\right)_{AB}^s &= \rho_{AB}^s + c\delta t_{AB} - I_{AB}^s + T_{AB}^s + \lambda_1 \cdot \left(\psi_1\right)_{AB}^s + \left(\varepsilon_1\right)_{AB}^s + \left(b_1^{Cp}\right)_{AB} \\
\left(L_2\right)_{AB}^s &= \rho_{AB}^s + c\delta t_{AB} - \left(\frac{\lambda_1}{\lambda_2}\right)^2 I_{AB}^s + T_{AB}^s + \lambda_2 \cdot \left(\psi_2\right)_{AB}^s + \left(\varepsilon_2\right)_{AB}^s + \left(b_2^{Cp}\right)_{AB}
\end{aligned} \tag{6.6}$$

where $\square_1$ and $\square_2$ refers to the quantities related to L1 or L2 frequencies. All the terms depending only on the satellite (e.g. the satellites clock bias) are cancelled out from this combination of measurements.

6.2.3 Double Difference Measurements

The double difference (DD) measurement is formed by subtracting two SD observations of two different satellites, named *i* and *j*. Double differenced measurements are given by $\square_{AB}^{ij} = \square_{AB}^{j} - \square_{AB}^{i}$. Applying this scheme to equation (6.6) yields:

$$
\begin{aligned}
\left(P_1\right)_{AB}^{ij} &= \rho_{AB}^{ij} + I_{AB}^{ij} + T_{AB}^{ij} + \sigma_{AB,P_1}^{ij} \\
\left(P_2\right)_{AB}^{ij} &= \rho_{AB}^{ij} + \left(\frac{\lambda_1}{\lambda_2}\right)^2 I_{AB}^{ij} + T_{AB}^{ij} + \sigma_{AB,P_2}^{s} \\
\left(L_1\right)_{AB}^{ij} &= \rho_{AB}^{ij} - I_{AB}^{ij} + T_{AB}^{ij} + \lambda_1 \cdot \left(n_1\right)_{AB}^{ij} + \varepsilon_{AB,L_1}^{ij} \\
\left(L_2\right)_{AB}^{ij} &= \rho_{AB}^{ij} - \left(\frac{\lambda_1}{\lambda_2}\right)^2 I_{AB}^{ij} + T_{AB}^{ij} + \lambda_2 \cdot \left(n_2\right)_{AB}^{ij} + \varepsilon_{AB,L_2}^{ij}
\end{aligned}
\tag{6.7}
$$

All receiver common contributes are removed by double differenced observations. In addition, using double difference measurements allows to remove the non-integer terms in the carrier phase ambiguities, that becomes a integer number value that is reported in the equations with n_1 and n_2, respectively for L1 and L2 frequencies.

6.3 CDGPS FILTERING

CDGPS techniques are widely used in both terrestrial, airborne and space application to improve the accuracy of baseline determination. The advantage of CDGPS processing is related to integer ambiguities that can be exactly estimated. The ambiguities are constant as long the satellite tracking is not lost, or a cycle slip occurs. Hence, once an ambiguity is correctly estimated and validated it can be used to correct the GPS measurement as long the tracking exists. Ambiguities validation process depends on the receiver type. When dual-frequency GPS receivers are available, standard Real-Time Kinematic (RTK) techniques can be used to perform robust integer ambiguities estimate. When only single frequency receivers are available, no standard solution exists to deal with the problem of integer estimation especially when moving receivers are considered, some promising results on this framework have been obtained for static platforms in [160], which uses L1 receivers.

The CDGPS problem can be modelled considering a couple of UAVs (chief c and deputy d) as reported in Figure 6.2. Assuming that the distance between the two UAVs is relatively short, i.e. in the order of 100 m at most, CP and PR observation equations can be written neglecting both ionospheric and tropospheric DD delays [161] yielding:

$$\begin{aligned}
(P_1)_{cd}^{ij} &= \rho_{cd}^{ij} + (\sigma_1)_{cd}^{ij} \\
(P_2)_{cd}^{ij} &= \rho_{cd}^{ij} + (\sigma_2)_{cd}^{ij} \\
(L_1)_{cd}^{ij} &= \rho_{cd}^{ij} + \lambda_1 \cdot (n_1)_{cd}^{ij} + (\varepsilon_1)_{cd}^{ij} \\
(L_2)_{cd}^{ij} &= \rho_{cd}^{ij} + \lambda_2 \cdot (n_1)_{cd}^{ij} - \lambda_2 \cdot (n_w)_{cd}^{ij} + (\varepsilon_2)_{cd}^{ij}
\end{aligned} \tag{6.8}$$

where P and L are the pseudo-range and carrier-phase DD measurements respectively, estimated assuming that i is the pivot satellite and $j=1,\ldots,n_{DD}$ is the index of any other satellite in view by the chief-deputy couple. Hence, $n_{DD}+1$ is the number of common satellites in the chief and the deputy UAVs FOV (Field of View).

The subscript 1 and 2 indicates the frequency of the acquired measurements, i.e. L1 and L2. In equation (6.8) σ and ε are the measurement thermal noises for PR and CP respectively. $(n_1)_{cd}^{ij}$ is the double difference ambiguity on L1 and n_w are the wide lane ambiguities. The wide lane objects are obtained subtracting L2 observation, from L1 observation. Therefore, $n_w = n_1 - n_2$.

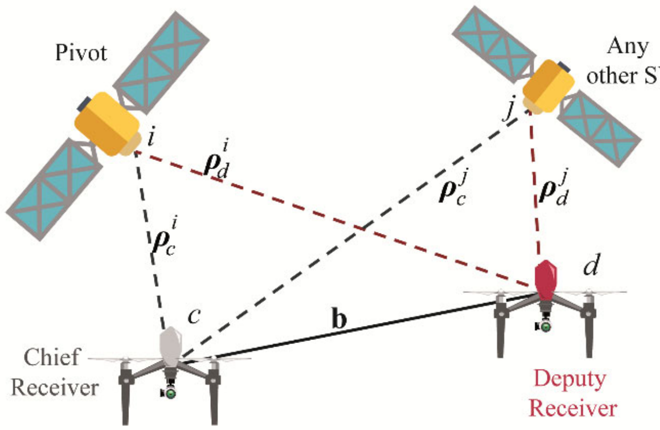

Figure 6.2 CDGPS observation geometry

ρ_{cd}^{ij} is the DD geometrical term, that can be estimated assuming that $\boldsymbol{\rho}_r^s$ is the LOS distance travelled from the SV *s* to the receiver *r*, see Figure 6.2. And ρ_{cd}^{ij} is

$$\begin{aligned}
&\rho_{cd}^{ij} = \left\|\rho_d^j\right\| - \left\|\rho_d^i\right\| - \left\|\rho_c^j\right\| + \left\|\rho_c^i\right\| \\
&\rho_c^j = \mathbf{R}^j - \mathbf{r}_c \\
&\rho_d^j = \mathbf{R}^j - \mathbf{r}_c - \mathbf{b}
\end{aligned} \tag{6.9}$$

where $\mathbf{R}^j$ is the position of the *j*-th satellite of the GPS constellation which can be retrieved from ephemeris data. Equation (6.9) states the unknown of equation (6.8) are the baseline and the double difference ambiguities. Baseline determination based on CDGPS processing is commonly solved using an Extended Kalman Filter (EKF), being the state vector **x** composed by the baseline **b**, its derivative and the unknown ambiguities. The measurement vector **y** is composed by the GPS measurements. The EKF estimates the ambiguities as real numbers. The difference between the float and the true but unknown integer ambiguities generates an error in the baseline estimation that affects filter performance. For reducing baseline error, the integer nature of DD ambiguities must be exploited. A common way to retrieve integer numbers from the real estimates of the integer ambiguities is to use a least square estimator, e.g. LAMBDA [162]. The ambiguities estimated with LAMBDA can be fixed in the state vector, assumed their value constant and reducing the error in baseline estimation. When an ambiguity is fixed, its associated covariance is set zero preventing it to change in time until a cycle slip occurs. However, fixing wrong estimated ambiguities produces a huge degradation of filter's performance. Thus, a validation technique is required. Integer ambiguities validation techniques can be divided in partial or global tests [163].

This section reports the dual frequency CDGPS filter algorithm used in [161] (section 6.3.1). Hence, the single frequency filter used in the cooperative navigation strategies reported in sections 6.4 and 6.5 is introduced in 6.3.2.

6.3.1 Dual Frequency CDGPS filter

The dual frequency CDGPS filter reported in Figure 6.3, has been demonstrated to have satisfactory results in baseline estimation for ground and mobile receivers [161]. The state vector reported in equation (6.10) includes both the L1 and the wide lane (WL) ambiguities, that are considered unknowns to estimate, thanks to the GNSS measurements. a_1 and a_w represents the float ambiguities. State and measurement vectors are:

$$\begin{array}{l}\mathbf{x} \in R^{(6+2n_{DD})\times 1} \\ \mathbf{y} \in R^{4n_{DD}\times 1}\end{array} : \mathbf{x} = \begin{bmatrix} \mathbf{b} \\ \dot{\mathbf{b}} \\ (a_1)_{cd}^{i1} \\ \vdots \\ (a_1)_{cd}^{in_{DD}} \\ (a_w)_{cd}^{i1} \\ \vdots \\ (a_w)_{cd}^{in_{DD}} \end{bmatrix}, \ \mathbf{y} = \begin{bmatrix} (P_1)_{cd}^{i1} \\ \vdots \\ (P_1)_{cd}^{in_{DD}} \\ (L_1)_{cd}^{i1} \\ \vdots \\ (L_1)_{cd}^{in_{DD}} \\ (P_1)_{cd}^{i1} \\ \vdots \\ (P_2)_{cd}^{in_{DD}} \\ (L_2)_{cd}^{i1} \\ \vdots \\ (L_2)_{cd}^{in_{DD}} \end{bmatrix} \tag{6.10}$$

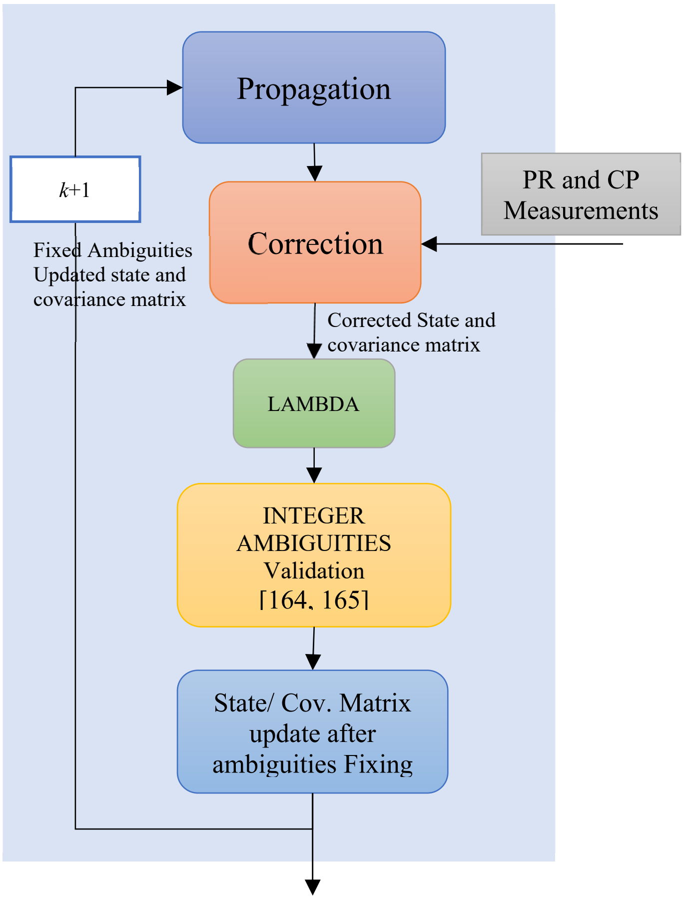

Figure 6.3 Dual Frequency CDGPS filter

When dual frequency receivers are employed, well assessed techniques exist for validating integer ambiguities, that return centimetric or millimetric precision in baseline estimation. The filter reported in Figure 6.3 provides partial ambiguities validation capabilities [161], thanks to the standard Melbourne-Wübbena tests [164, 165].

6.3.2 Single Frequency CDGPS filter

This section introduces the single frequency CDGPS EKF that is used to estimate the GNSS information source to be used in order to improve the UAV pointing accuracy with cooperation. In the single frequency case, equation (6.8) becomes:

$$\begin{aligned}\left(P_1\right)_{cd}^{ij} &= \rho_{cd}^{ij} + \left(\sigma_1\right)_{cd}^{ij} \\ \left(L_1\right)_{cd}^{ij} &= \rho_{cd}^{ij} + \lambda_1 \cdot \left(n_1\right)_{cd}^{ij} + \left(\varepsilon_1\right)_{cd}^{ij}\end{aligned} \tag{6.11}$$

As reported before, the problem in using single frequency CDGPS filter lies in the lack of a standard validation method for the ambiguity validation. Without a reliable validation technique, it is not advisable to fix the integer ambiguities, since an error in integer ambiguity fixing can result in filter divergence. That prevents the full exploitation of the CDGPS potential.

This chapter describes two version of the EKF. The first version (section 6.3.2.1) uses float ambiguities. Hence, section 6.3.2.2 integrates the EKF with a integer ambiguity estimator (LAMBDA) and introduces a novel version of the ambiguity validation test to be used when single frequency receivers are taken into account. The two sections are aimed at highlighting the structural differences between these two solutions, i.e. EKF and EKF + LAMBDA, hence their performance comparison will be discussed in section 6.6.2. Section 6.3.2.3 define a method for self-estimating the accuracy of the CDGPS output to be used in the cooperative navigation processing.

6.3.2.1 EKF

The EKF used to estimate CDGPS-based baseline, whose flow chart is depicted in Figure 6.4, uses the DD GPS measurements presented in equations (6.11) in the correction step. Thus, the measurement vector **y** includes the n_{DD} PR and CP measurements. Whereas the filter state vector **x** includes the unknown of equations (6.11), and is composed by 6+n_{DD} components, i.e. the baseline **b**, its derivative $\dot{\mathbf{b}}$ and the n_{DD} L1 float ambiguities a_1.

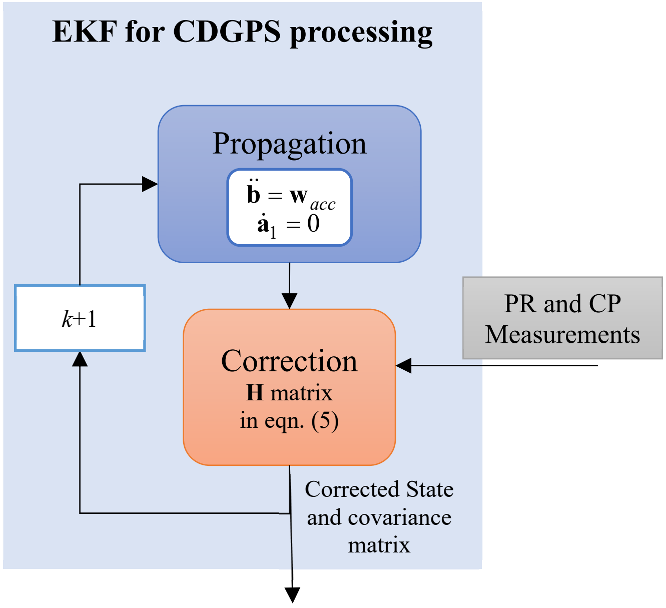

Figure 6.4 Single Frequency CDGPS filter with float ambiguities

$$\begin{matrix} \mathbf{x} \in R^{(6+n_{DD})\times 1} \\ \mathbf{y} \in R^{2n_{DD}\times 1} \end{matrix} : \mathbf{x} = \begin{bmatrix} \mathbf{b} \\ \dot{\mathbf{b}} \\ (a_1)_{cd}^{i1} \\ \vdots \\ (a_1)_{cd}^{in_{DD}} \end{bmatrix}, \mathbf{y} = \begin{bmatrix} (P_1)_{cd}^{i1} \\ \vdots \\ (P_1)_{cd}^{in_{DD}} \\ (L_1)_{cd}^{i1} \\ \vdots \\ (L_1)_{cd}^{in_{DD}} \end{bmatrix} \tag{6.12}$$

No dynamics is provided for the baseline except that its derivative propagates as a random walk: $\ddot{\mathbf{b}} = \mathbf{w}_{acc}$, where $\mathbf{w}_{acc}$ is the white noise on the baseline's acceleration. Whilst, the ambiguities are assumed to be constant characterized by unknown initial value. The measurement matrix **H** used to estimate the Kalman relates the measurements to the state vector **y=Hx** and is evaluated performing linearization of equations (6.11) around the available baseline estimate, that is:

$$\mathbf{H} = \left(\begin{array}{c:c:c} \begin{matrix} \left(\nabla_{b\langle j=1\rangle}\right)_{1,3} \\ \vdots \\ \left(\nabla_{b\langle j=n_{DD}\rangle}\right)_{1,3} \end{matrix} & 0_{n_{DD},3} & 0_{n_{DD},n_{DD}} \\ \hdashline \begin{matrix} \left(\nabla_{b\langle j=1\rangle}\right)_{1,3} \\ \vdots \\ \left(\nabla_{b\langle j=n_{DD}\rangle}\right)_{1,3} \end{matrix} & 0_{n_{DD},3} & \begin{pmatrix} \lambda_1 & & 0 \\ & \ddots & \\ 0 & & \lambda_1 \end{pmatrix} \end{array} \right) \tag{6.13}$$

where

$$\nabla_{b\langle j\rangle} = \frac{\partial (P_1)_{cd}^{ij}}{\partial \mathbf{b}} = \frac{\partial (L_1)_{cd}^{ij}}{\partial \mathbf{b}} = \frac{\partial \rho_{cd}^{ij}}{\partial \mathbf{b}} = \frac{\rho_d^i}{\left\|\rho_d^i\right\|} - \frac{\rho_d^j}{\left\|\rho_d^j\right\|} \tag{6.14}$$

6.3.2.2 EKF integration with lambda

The EKF presented in the previous section estimates the ambiguities as real numbers. The difference between the float and the true but unknown integer ambiguities generates an error in the baseline estimation that affects filter performance. For reducing baseline error, the integer nature of DD ambiguities must be exploited. However, the costs to pay for baseline accuracy improvement by estimation of integer ambiguities include:

1) a more complex filter to be implemented, able to integrate LAMBDA into the EKF

2) a significant loss of robustness against wrong integer estimates that can easily leads to filter divergence.

The scheme in Figure 6.5 integrates the EKF in Figure 6.4 with the LAMBDA estimator. The integer ambiguities estimated by LAMBDA are validated and used to correct the current state vector. Hence, the validated integer ambiguities are assumed to be correct and are fixed in the following time epoch, as far as satellite is tracked.

The central step in this algorithm is the integer ambiguities validation step, which is in charge of avoiding wrong integer ambiguities to be fixed. When dual-frequency GPS receivers are available, standard Real-Time Kinematic (RTK) techniques can be used to perform robust integer ambiguities validation. When only single frequency receivers are available, as in the present case, no standard solution exists to deal with the problem of integer validation especially when moving receivers are considered.

The use of integer ambiguity tests is the standard solution in dual-frequency receivers. Tests can be classified as in Global and Partial Tests. The Global approaches test if all the IA are simultaneously valid (a list of the most common Global validation tests can be found in [166]). These “vector” validation tests operate on the whole vector of IA, and do not discriminate between IA within the vector: if only one IA within the vector is deemed erroneous, the whole IA vector does not pass the test.

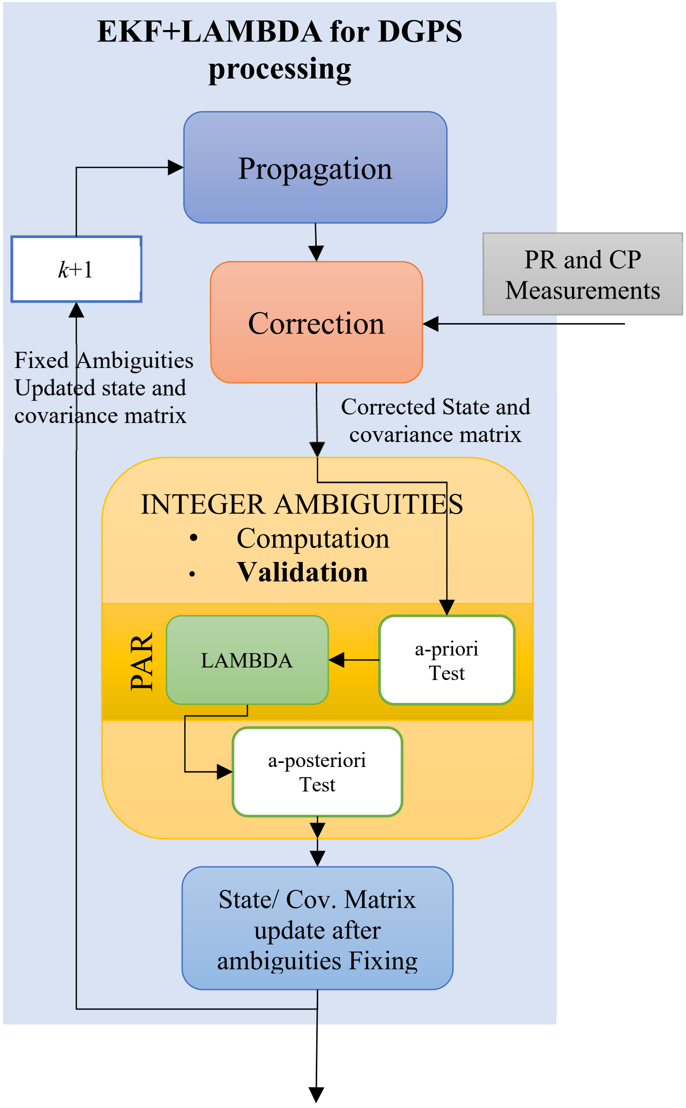

Figure 6.5 Single Frequency CDGPS filter + LAMBDA with fixed ambiguities

On the other hand, when not all the IA are correctly fixed, there is the possibility that a subset of the IA vector is instead correct. Partial IA validation tests are concerned with discriminating between the single IA, i.e. separating the correct from the incorrect ones. The partial integer validation allows therefore to fix the correct integer ambiguities before all the ambiguities in the vector become correct, easing the filter estimation, and, as a consequence, this approach should be preferred with respect to the Global one. Most of the partial tests available in literature allow correctly estimating the ambiguity for dual frequency receivers [164, 165].

The LAMBDA 3.0 software [167] includes the possibility to operate with partial estimation, i.e. Partial Ambiguity Resolution (PAR) in the single frequency receiver case using the partial ambiguity test presented in [163, 167], to which we refer the interested readers. PAR consists in two steps. The first step acts on the float decorrelated ambiguities [167] by selecting the best candidates to be converted in Integer ambiguities. PAR test aims at selecting the largest subset of decorrelated ambiguities, whose probability to be fixed to the correct integer is above a threshold. Those float ambiguities are fed to the LAMBDA estimator to compute their integer counterpart.

PAR algorithm discriminates the ambiguities a-priori, acting on the float component and accounting for their probability to be correctly fixed. Following [168, 169] a novel approach is tested in the present work, aimed at improving the success rate of the ambiguity fixing. This complements the a-priori PAR validation test with an a-posteriori test performed on the integer ambiguities, as shown in Figure 6.5. As stated in [168] combining a-priori test on float ambiguities and a-posteriori test on Integer ambiguities is expected to improve the overall PAR success rate, and it represents the most promising solution for the case of multiple constellation GNSS application. Specifically, integer estimation and validation proceed through the following steps:

- **A-priori (PAR) test** selects $n_{\mathrm{ILS}} \leq n_{\mathrm{DD}}$ ambiguities among the float ones, for which the probability that their integer counterpart is correct is greater than a threshold.
- **The LAMBDA estimator** computes the n_{ILS} integer ambiguities, from the float ones.
- **A-posteriori Integer validation test** defines the correct ambiguities to be fixed among the n_{ILS} integer ambiguities estimated by LAMBDA.

A-posteriori integer ambiguities validation test is twofold and accounts for the residuals on measurements and the difference between Integer and float ambiguities. As a result, the integer ambiguity $\left(n_1\right)_{cd}^{ij}$ is deemed valid if

$$
\begin{gathered}
\left|\left(n_1\right)_{cd}^{ij}-\left(a_1\right)_{cd}^{ij}\right|<d_a \\
\frac{\left(\Delta \tilde{L}_1\right)_{cd}^{ij}-\left(\Delta \hat{L}_1\right)_{cd}^{ij}}{\left|\left(\Delta \hat{L}_1\right)_{cd}^{ij}\right|}<d_b
\end{gathered}
\tag{6.15}
$$

where $(a_1)_{cd}^{ij}$ is the float ambiguity corresponding to the integer $(n_1)_{cd}^{ij}$, $(\Delta L_1)_{cd}^{ij}$ is the residual on the CP measurement. ˜ and ˆ defines the residual estimated with integer and float ambiguities, respectively; d_a and d_b are the two thresholds. The test on the residuals checks if the residual estimated with the integer ambiguity is lower than the residuals with the float ambiguity: in that case the integer ambiguity is deemed wrong and thus it is not fixed. Ambiguities test states that if the difference between the float and the integer ambiguity is too high the integer ambiguity is wrong; usually d_a is set lower than one to avoid selecting an integer ambiguity very different from its float counterpart.

All the integer ambiguities passing the a-posteriori test are fixed, i.e. they are kept constant, in the following steps until a cycle slip occurs or the satellite signal is lost. The state vector can be thus partitioned in two components: the ambiguities vector $\boldsymbol{a}$ and the vector including the baseline and its derivative $\boldsymbol{\beta}$. The symbols ˆ and ˘ discriminating between estimates before and after the ambiguities estimation and validation step. The j-th element of the ambiguities vector $\breve{\boldsymbol{a}}$ is:

$$\breve{\boldsymbol{a}}_j = \begin{cases} (n_1)_{cd}^{ij} & \textit{if a-posteriori validation test is satisfied} \\ (a_1)_{cd}^{ij} & \textit{otherwise} \end{cases} \tag{6.16}$$

Finally, the updated ambiguities vector $\breve{\boldsymbol{a}}$ is used to correct both the state vector and the covariance matrix, C, of the EKF, thus realizing a closed-loop EKF+LAMBDA scheme [20]. This correction is performed partitioning the covariance matrix estimate of the EKF, i.e. $\hat{C}$, in the relevant component depending on $\boldsymbol{\beta}$ and $\boldsymbol{a}$

$$\hat{C} = \begin{bmatrix} \hat{C}_{\beta\beta} & \hat{C}_{\beta a} \\ \hat{C}_{a\beta} & \hat{C}_{aa} \end{bmatrix} \tag{6.17}$$

where $\hat{C}_{\beta\beta}$ is a 6×6, $\hat{C}_{aa}$ is a n_{DD}×n_{DD} matrix, $\hat{C}_{\beta a}$ and $\hat{C}_{a\beta}$ are, respectively, a 6×n_{DD} and a n_{DD}×6 matrix. Based on equations (6.16) and (6.17), the estimate of $\boldsymbol{\beta}$ after ambiguities estimation and validation, , i.e. $\breve{\boldsymbol{\beta}}$, is

$$\breve{\boldsymbol{\beta}} = \hat{\boldsymbol{\beta}} + \hat{C}_{\beta a}\hat{C}_{aa}^{-1}(\breve{\boldsymbol{a}} - \hat{\boldsymbol{a}}) \tag{6.18}$$

and the relevant components of the covariance matrix can be updated as

$$\breve{C}_{\beta\beta} = \hat{C}_{\beta\beta} - \hat{C}_{\beta a}\hat{C}_{aa}^{-1}\hat{C}_{a\beta} \tag{6.19}$$

6.3.2.3 Baseline Accuracy Estimation

To the sake of cooperative navigation, the GNSS information source must be complemented with its accuracy, that impacts the cooperative measurement covariance matrix [170] . Baseline errors resulting from EKF depend on CP residuals and the satellites-receivers geometry. The CP residuals are obtained by substituting EKF estimates in the second equation reported in (6.11). They quantify the level of uncertainty of filter state vector components. The CP residuals $\left(\Delta L_1\right)_{cd}^{ij}$ are mapped into baseline error thanks to Dilution of Precision (DOP) coefficients extracted from a submatrix of **H**, namely $\breve{\mathbf{H}}$. Extending equation (6.13) to the residuals yields:

$$\begin{bmatrix} \left(\Delta L_1\right)_{cd}^{i1} \\ \vdots \\ \left(\Delta L_1\right)_{cd}^{in_{DD}} \end{bmatrix} = \breve{\mathbf{H}} \cdot \Delta\mathbf{b} \; ; \breve{\mathbf{H}} = \begin{bmatrix} \left(\nabla_{b\langle j=1\rangle}\right)_{1,3} \\ \vdots \\ \left(\nabla_{b\langle j=n_{DD}\rangle}\right)_{1,3} \end{bmatrix} \tag{6.20}$$

The error on CDGPS residual ΔL_1 is estimated as the mean of the $\left(\Delta L_1\right)_{cd}^{ij}$, and mapped in the north east and down error, thanks to the horizontal and vertical dilution of precision D_H and D_V. Vertical and horizontal dilution of precision are obtained from matrix **P**, that is:

$$\mathbf{P} = \left(\left(\breve{\mathbf{H}}G^{-1}\right)^T \breve{\mathbf{H}}G^{-1}\right)^{-1} = \begin{bmatrix} \mathbf{P}_{11} & \mathbf{P}_{12} & \mathbf{P}_{13} \\ \mathbf{P}_{21} & \mathbf{P}_{22} & \mathbf{P}_{23} \\ \mathbf{P}_{31} & \mathbf{P}_{32} & \mathbf{P}_{33} \end{bmatrix} \tag{6.21}$$

Where G is the matrix that converts ECEF error in north east down components, see equation (3.6). Therefore, D_H and D_V are:

$$D_H = \sqrt{\mathbf{P}_{11} + \mathbf{P}_{22}} \; ; D_V = \sqrt{\mathbf{P}_{33}} \tag{6.22}$$

Hence the error on the baseline $\Delta\mathbf{b}$ is

$$\Delta\mathbf{b} = \begin{bmatrix} D_H \\ D_H \\ D_V \end{bmatrix} \Delta L_1 \, ; \Delta L_1 = \frac{1}{n_{DD}} \sum_{j=1}^{n_{DD}} \left(\Delta L_1\right)_{cd}^{ij} \tag{6.23}$$

6.4 LOOSELY COUPLED CDGPS/VISION

This section discusses the loosely coupled integration of the CDGPS/Vision measurement. The proposed technique is based on [12, 156] and aims at defining the orientation of the aircraft using the TRIAD/QUEST [171, 172] methods. The measured orientation is forwarded to the Kalman filter to be used as measurement in the correction step. This technique processes the CDGPS/Vision in a loosely manner obtaining the desired information, i.e. the orientation outside the filter. The logical architecture of the proposed navigation algorithm is depicted in Figure 6.6.

The logical architecture in Figure 6.6 is used on board a vehicle of the formation, named "chief", that uses the cooperative measurements coming from cooperative platforms ("deputies"). It includes:

- A CDGPS filter, described in section 6.3, used for accurately estimating the baseline between the "chief" and the cooperative platforms in NED frame
- A visual tracking algorithm that extracts the relative positioning of the cooperative platforms in the "chief" BRF from camera images. As regards vision-based tracking, the considered architecture can work for both strapdown and gimbaled cameras installation. In both cases, it can be assumed that the camera-to-body rotation matrix is known.
- A TRIAD/QUEST algorithm that concurs to cooperative attitude estimation

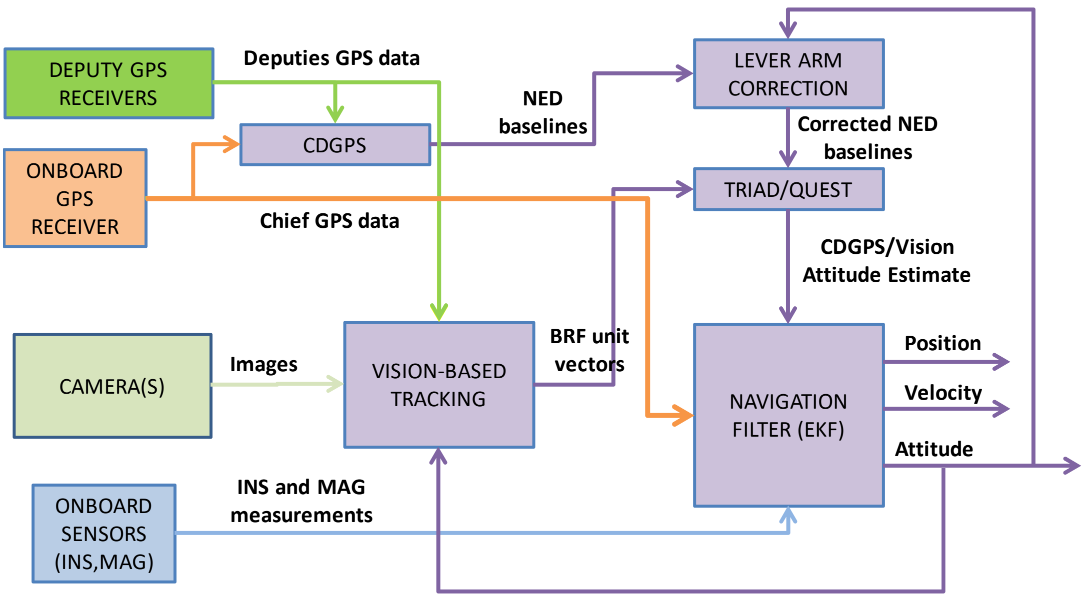

Figure 6.6 Loosely coupled CDGPS/Vision cooperative filter

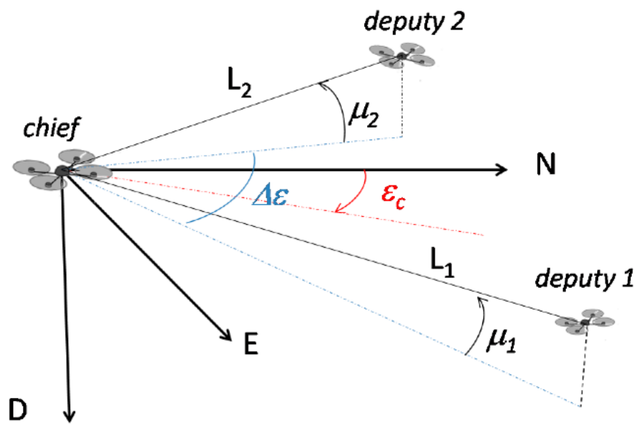

Figure 6.7 Cooperative navigation for attitude improvement, visual concept

- An Extended Kalman filter that integrates cooperative (orientation estimated via CGDPS/Vision) and non-cooperative measurements for the navigation sake. Non cooperative measurements include GPS, IMU and Magnetometer measurements.

As far as the orientation error minimization is concerned, the core of the proposed algorithm lies in the TRIAD/QUEST block. Indeed, the cooperative aiding information comes from using together camera and CDGPS measurement, to obtain an additional attitude measurement, independent from IMU and Magnetometer. Section 6.4.1 describes the attitude determination technique implemented in the navigation architecture.

6.4.1 Attitude Estimation

Three-Axis Determination (TRIAD) and Quaternion Estimation (QUEST) methods are analytical methods to determine the rotation matrix between two reference frames and can be used when two or more direction are available. Specifically, TRIAD method works with two deputies, whereas quest is a TRIAD extension when more than two direction are available, based on minimum least square approach. The current approach uses as reference directions the unit vectors from the chief to the deputies as reported in Figure 6.7. When only one deputy is available a straightforward strategy is to integrate the only relative measurement in the navigation filter as performed in [15, 173] and described in section 6.5.

6.4.1.1 Triad

Given two non-parallel unit vectors $\mathbf{v}_1^f$ and $\mathbf{v}_2^f$ in the frame *f* and their respective representation ($\mathbf{v}_1^g$ and $\mathbf{v}_2^g$) in the frame *g*, TRIAD [171] defines two orthonormal triads of vectors: $\{\mathbf{r}_1, \mathbf{r}_2, \mathbf{r}_3\}$ and $\{\mathbf{s}_1, \mathbf{s}_2, \mathbf{s}_3\}$:

$$\begin{aligned} \mathbf{r}_1 &= \mathbf{v}_1^f, \mathbf{r}_2 = \frac{\mathbf{v}_1^f \times \mathbf{v}_2^f}{\left|\mathbf{v}_1^f \times \mathbf{v}_2^f\right|}, \mathbf{r}_3 = \mathbf{r}_1 \times \mathbf{r}_2 \\ \mathbf{s}_1 &= \mathbf{v}_1^g, \mathbf{s}_2 = \frac{\mathbf{v}_1^g \times \mathbf{v}_2^g}{\left|\mathbf{v}_1^g \times \mathbf{v}_2^g\right|}, \mathbf{s}_3 = \mathbf{s}_1 \times \mathbf{s}_2 \end{aligned} \tag{6.24}$$

The unique rotation matrix that performs transformations from *f* to *g* is defined as [12]:

$$C_f^g = \{\mathbf{s}_1, \mathbf{s}_2, \mathbf{s}_3\}\{\mathbf{r}_1, \mathbf{r}_2, \mathbf{r}_3\}^T \tag{6.25}$$

6.4.1.2 Quest

When more than two vectors are available the problem posed in the previous section is overdetermined and one can solve for the rotation matrix by minimizing a loss function

$$J\left(C_f^g\right) = \frac{1}{2}\sum_{k=1}^{N} w_k \left|\mathbf{v}_k^g - C_f^g \mathbf{v}_i^f\right| \tag{6.26}$$

where *N* is the number of the available measurements and w_k is the weight given to the *k*-th unit vector. The least square problem in equation (6.26) can be solved numerically with the Newton's method, exactly with the q-method or using QUEST [172], that is and efficient approximation of the q-method.

6.4.1.3 Vector Specification for attitude determination

TRIAD and QUEST algorithms are used in the architecture depicted in Figure 6.6 with the aim of estimating the rotation from the local navigation frame (NED) to the body reference frame (BRF), i.e. C_n^b. The unit vector in body reference frame is estimated with the aid of a camera mounted on the UAV that is able to track the deputies. The unit vector in camera reference frame $\mathbf{v}_i^c$ can be converted in the BRF $\mathbf{v}_k^b$ thanks to the body to camera rotation matrix C_b^c, that can be obtained performing camera extrinsic calibration in a strapdown configuration. Whilst, the gimbaled camera returns C_b^c history over time.

$$\mathbf{v}_k^b = \left(C_b^c\right)^T \mathbf{v}_k^c \tag{6.27}$$

The vector in the camera frame can be obtained by retrieving from the visual tracking algorithm the azimuth *Az* and the elevation *El* of the pixel identifying the center of the deputy.

$$\mathbf{v}_k^c = \begin{bmatrix} \cos El \cos Az \\ \cos El \sin Az \\ -\sin El \end{bmatrix} \tag{6.28}$$

The unit vector in NED frame $\mathbf{v}_k^n$ is the baseline **b** estimated with the CDGPS filer divided by its norm.

6.5 TIGHTLY COUPLED CDGPS/VISION

CDGPS/Vision information can be processed in different ways. The loosely coupled approach, described in section 6.4 consists in estimating attitude (by algorithms such as TRIAD and QUEST [171, 174]) and then integrating this estimate in the navigation filter, while a tightly coupled strategy (based on [15]) corresponds to directly integrating line-of-sight (LOS) information within the filter. The tight integration approach provides several advantages, such as the capability to automatically take into account different LOS uncertainties for different deputies, and the possibility to work with any number of deputies. Indeed, the exploitation of a single deputy UAV still allows CDGPS/Vision technique to be applied. Specifically, even though a single chief-to-deputy LOS does not give any information about rotations around the LOS (i.e., it does not enable complete attitude estimation), it can still provide useful in all the scenarios in which it is important to improve attitude estimation accuracy with regard to some angles (e.g., heading) only.

The logical architecture of the tightly coupled CDGPS/Vision technique is reported in Figure 6.8 and includes:

- A CDGPS filter, described in section 6.3 in order to provide accurate estimates of the baselines among antennas
- A vision-based tracking algorithm that analyzes images in order to track deputies and thus extract angular position of their antennas. It is assumed that the camera-to-body rotation matrix, needed to convert unit vectors from

camera reference frame (CRF) to BRF, is accurately known. Thus, the considered architecture can work for both strapdown and gimbaled cameras installation, provided that, in the latter case, estimates of gimbal rotation angles are accurate enough. Knowledge of chief and deputies positions given by the GPS data, and the predicted chief attitude, can be used to predict angular position of deputies within camera images, and thus to build relatively small search windows for vision-based detection and tracking. This makes image processing task easier, reducing the computational time and increasing robustness with respect to tracking losses or false detections. Also, knowledge of the baseline among flight platforms, and of the deputies configuration, can be exploited to the tracking advantage, enabling prediction of deputy appearance. In general, the trade-off between angular coverage and detection range can be tackled by exploiting higher resolution sensors and/or multiple/gimbaled camera systems.

- A sensor fusion algorithm based on standard EKF, that is aimed at estimating the chief navigation state (position, velocity, and attitude). The cooperative multi-sensor fusion integrates the non-cooperative measurements, i.e. GNSS, Magnetometer and IMU measurement, with the cooperative measurements. Differently from the filter described in section 6.4, the sensor fusion algorithm used in this section directly process the CDGPS and Vision measurements, i.e. chief-to-deputy unit vectors in NED and BRF respectively. Indeed, the scheme depicted in Figure 6.8 lacks of the TRIAD processing step. Therefore, the cooperative measurements are directly forwarded to the filter that integrates them in the correction step in a tightly coupled manner. Section 6.5.1 details the tightly coupled navigation filter using the Vision and CDGPS measurement, providing an improvement of the attitude estimation performances.

6.5.1 Tightly Coupled EKF

The tightly coupled CDGPS/Vision EKF is based on the equations presented in [15]. The filter described in this section uses CDGPS instead of DGPS baselines, as performed in [15], returning a more precise estimate of the chief orientation. The extended Kalman filter includes in its state vector **x**:

- the errors on geographic positions (latitude, longitude and altitude), i.e. $\delta\mathbf{p}$.
- the errors on NED velocity components, $\delta\mathbf{v}$.
- the attitude error: $\boldsymbol{\rho}$.
- The accelerometer and gyroscope biases, $\mathbf{b}$.

The measurement vector includes GPS measurements, CDGPS/Vision and magnetometer measurements. Measurement equation for GPS and magnetometer can be derived in section 3.3.1. Hence, 6.5.1.1 reports CDGPS/Vision measurements integration.

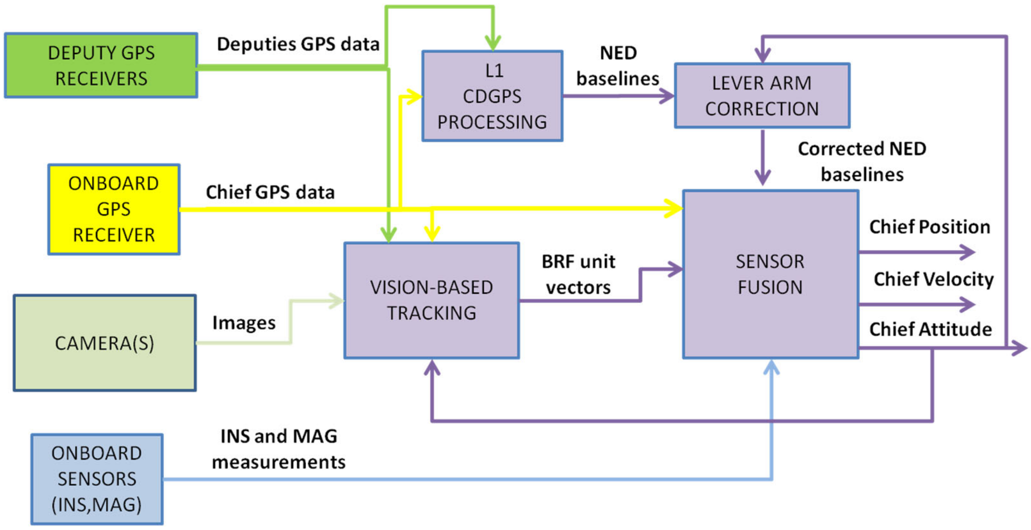

Figure 6.8 Tightly coupled cooperative navigation architecture for attitude accuracy improvement.

6.5.1.1 CDGPS/Vision Measurement update

Equation (6.1) represent the key equation of the CDGPS/Vision approach, estimated for the *k*-th chief deputy couple. The error form of this equation can be derived based on the attitude error equation [120]:

$$\hat{C}_n^b = C_n^b(\mathbf{I} + [\boldsymbol{\rho}\times]) \tag{6.29}$$

where the symbol ˆ indicates the predicted quantity that depends on the true one C_n^b, through the attitude error. $\mathbf{I}$ is the 3×3 identity matrix.

Based on (6.29) is possible to rewrite (6.1) as:

$$\hat{\mathbf{r}}_k^b = \hat{C}_n^b(\mathbf{I} - [\boldsymbol{\rho}\times])\hat{\mathbf{r}}_k^n \tag{6.30}$$

Manipulating equation (6.30) yields:

$$\hat{\mathbf{r}}_k^b - \hat{C}_n^b \hat{\mathbf{r}}_k^n = \hat{C}_n^b [\hat{\mathbf{r}}_k^n \times] \boldsymbol{\rho} \tag{6.31}$$

$\delta \mathbf{z}_{CV,k} = \hat{\mathbf{r}}_k^b - \hat{C}_n^b \hat{\mathbf{r}}_k^n$ is deemed as the CDGPS/Vision residual including the difference between the CDGPS and Vision measurements. The CDGPS/Vision measurement depends only on the attitude part of the state vector, where:

$$\frac{\partial \mathbf{z}_{CV,k}}{\partial \boldsymbol{\rho}} = H_{CV,k\boldsymbol{\rho}} = \hat{C}_n^b [\hat{\mathbf{r}}_k^n \times] \tag{6.32}$$

Therefore, the CDGPS/Vision measurement matrix for the k-th chief-deputy couple is:

$$H_{CV,k} = \begin{bmatrix} 0_{3\times3} & 0_{3\times3} & H_{CV,k\boldsymbol{\rho}} & 0_{3\times6} \end{bmatrix} \tag{6.33}$$

Therefore, the generic k-th deputy provides a (vectorial) measurement residual which is linearly related to the attitude error vector.

6.6 EXPERIMENTAL RESULTS

The CDGPS/Vision technique has been tested on experimental data. The experimental setup is reported in Section 6.6.1. The output of the CDGPS filter that is in common to the two processing schemes, i.e. loosely and tightly coupled are reported in section 6.6.2. Hence, loosely and tightly coupled results are discussed in sections 6.6.3 and 6.6.4, respectively.

6.6.1 Experimental Setup and Flight Test

A customized version of the Pelican quadrotor (Figure 6.9) from Ascending Technologies has been selected as chief UAV in the flight tests. The Pelican quadrotor designed as is equipped with an autopilot, an onboard computer (AscTec Mastermind™), a GPS receiver, and a set of low-cost MEMS sensors. Furthermore, the platform has been customized with an additional GPS single frequency receiver (uBlox LEA-6T™) with raw measurements capabilities, an auxiliary GPS antenna, and a CMOS camera. The additional GPS receiver and the camera have been connected to the Mastermind computer via a USB link. A customized version of the 3DR X8+™ has been used as flying deputy (Figure 6.10). In particular, it has been equipped with an auxiliary GPS system (the same installed on the chief) and an Odroid XU4™ embedded CPU for data processing and storage.

Two ground antennas/receivers have also been used. In particular, one of them has been used as a surrogate deputy UAV (2-deputy architecture has been considered to analyze cooperative navigation potential for complete attitude estimation). The second ground antenna/receiver has not been exploited to provide cooperative measurements, but just to have a ground reference for attitude accuracy evaluation, as detailed in section 6. Both ground systems have been equipped with the BD960™ receiver from Trimble, a Trimble AV59™ antenna model, and a laptop to save all GPS raw data as it has been done on the multirotors. BD960™ is a dual frequency receiver, however only L1 signals have been processed in the presented experiment.

Figure 6.9 Customized Asctec Pelican™ used as chief.

Figure 6.10 Customized 3DR X8+™ used as flying deputy.

The adopted test strategy is based on the concept of data acquisition for off-line processing. Thus, no real time data link among the UAVs is needed, and proper acquisition software have been developed in C/C++ in order to save all the data with an accurate time-tag based on the CPU clock. This time-tag is also associated to GPS measurements (including GPS time) gathered with very small latency, which enables accurate synchronization of all data acquired on each flying platform. During experimental tests, images acquired by the (forward-looking) camera and GPS data have been gathered on-board the chief at 1Hz frequency and IMU data at about 100Hz, in addition, GPS data have been stored on-board the flying deputy at 1Hz while GPS measurements from the ground antennas have been acquired at 5Hz. Flight geometry is depicted in Figure 6.11 which is an image acquired from the chief vehicle (Pelican).

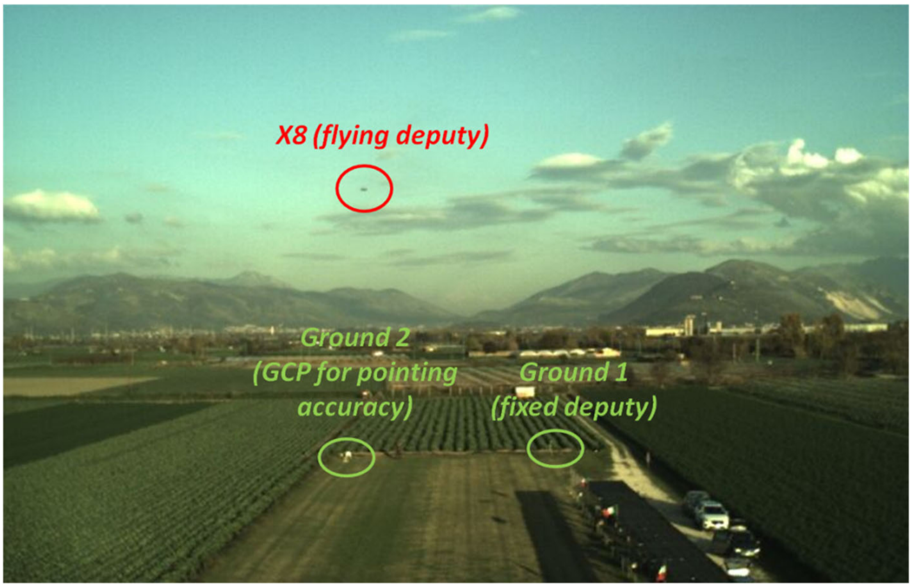

Figure 6.11 Example image acquired on the chief UAV showing flight geometry

In the following, experimental data are analyzed to highlight CDGPS accuracies in estimating chief-to-deputy baselines, and to show the beneficial effects of using these baselines to estimate chief attitude through the CDGPS/Vision approach.

6.6.2 CDGPS

To assess the performance of the filters described in sections 6.3.2.1 and 6.3.2.2, the baseline is estimated in static and dynamic conditions. CP residuals are used as index of the filters' performance. The static configuration is assessed using data acquired by two ground antennas (Trimble AV59^{TM}), whose results are depicted in Figure 6.12. The figure shows (with different colors) the CP residual for each available couple of GPS satellites, when the simple EKF (Figure 6.4) filter and the filter that complements EKF with LAMBDA (Figure 6.5) are used. When static receivers are used, the filter that fixes the ambiguities (EKF+LAMBDA) shows an advantage in baseline estimation. The ambiguities that are correctly estimated show a sudden drop of the corresponding CP residuals (see red and purple lines in Figure 6.12).

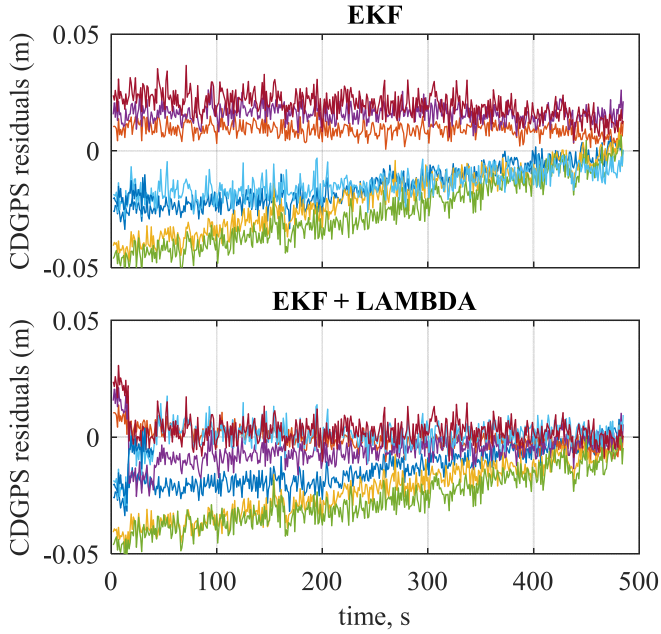

Figure 6.12 CP residuals of Single Frequency CDGPS filter and Single Frequency CDGPS filter + LAMBDA for static receivers.

It is important to note that not all the ambiguities are fixed: this is the case of yellow and green lines that do not show any jump. This means that the relevant ambiguities are not fixed in the processed time span. Indeed, the ambiguity thresholds d_a and d_b have been carefully selected to avoid false ambiguities fixing, while guaranteeing that a reasonably large set of ambiguities is fixed and thus improving the performance in baseline estimation with respect to the simple EKF filter. CP residuals of baseline estimation for two flying receivers are shown in Figure 6.13, in this case data from GPS receivers of Pelican and X8 are used to compare the filters' performance. Comparing the two plots in Figure 6.13 it can be seen that no improvement is provided by combining the EKF with LAMBDA. During the experiment, the uBlox™ receivers suffered, indeed, from signal tracking deficiency, experimenting a significant amount of cycle slips (both on Pelican and on X8). Recurring slips (one each 4 seconds on average) cancel out the advantage of the combined EKF + LAMBDA filter because the high slip rate makes the correct ambiguities estimation and fixing harder and even if ambiguities are fixed, they are rapidly discarded because of the occurrence of a new slip.

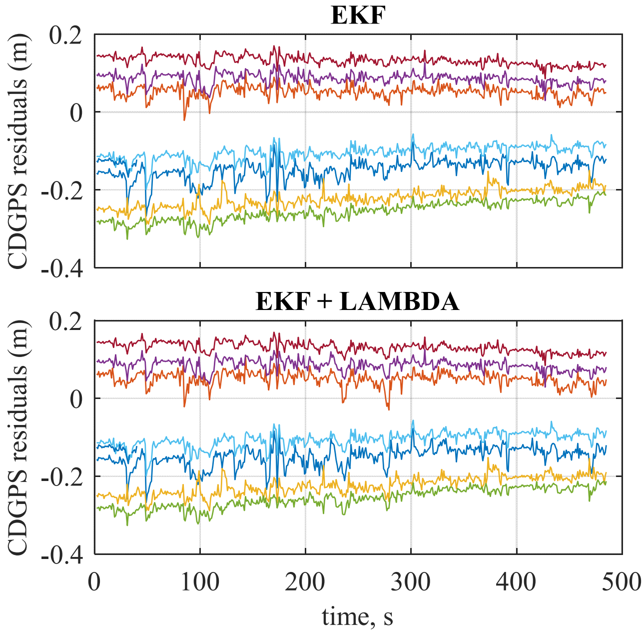

Figure 6.13 CP residuals of Single Frequency CDGPS filter and Single Frequency CDGPS filter + LAMBDA for flying receivers.

In summary, in the performed experiments, the filter combining EKF with LAMBDA has demonstrated to work well with Trimble^{TM}, static receivers. On the other hand, using ambiguity fixing on flying UAVs gives no clear advantage because of the significant amount of cycle slips. As a consequence, the EKF-only algorithm depicted in Figure 6.4 has been preferred due to the lower computational burden, and is used to estimate the CDGPS baselines in the reminder of this work.

At this regard, it is important to underline that the experimented hardware issues are believed to be strongly related to the specific experimental conditions of our dataset, and the relevant installation challenges for GPS receivers and antennas. In other words, these issues do not affect in general single frequency receivers embarked on board small/micro UAVs. In fact, recent results from the geomatics community [152] clearly show that effective ambiguities fixing by LAMBDA techniques enables cm-level baseline estimation accuracy even in the case of low cost receivers flying on micro UAVs. Thus, the choice of using EKF-only CDGPS processing for the current dataset, does not reduce the general interest in integrating EKF+LAMBDA processing within CDGPS/Vision cooperative navigation for a multi-UAV system.

The baseline norm of the receiver couples estimated with CDGPS technique is shown in Figure 6.14, in black and it is compared with standard DGPS processing (DD pseudo-range measurements [12]). As expected, even if CDGPS and DGPS solutions are in general in good agreement, CDGPS is much smoother than DGPS one. Specifically, DGPS results are obtained by applying a weighted least square (WLS) technique on the first equation of (6.11), using only pseudo-range measurements for estimating the baseline. The results suggest, as shown in Figure 6.15-Figure 6.18 that using the CDGPS, the accuracy in estimating the baseline is an order of magnitude better than the DGPS one. Figure 6.15, Figure 6.16 and Figure 6.17 depict the baseline components of the X8-pelican, pelican-ground antenna 1 and pelican-ground antenna 2 couple in ENU. Figure 6.15 highlights that during the flight, the vertical separation between the two flying platforms is almost constant, with a more dynamic evolution in the horizontal plane. The last plot of Figure 6.15 underlines the noisy behaviour of the DGPS solution with respect to CDGPS.

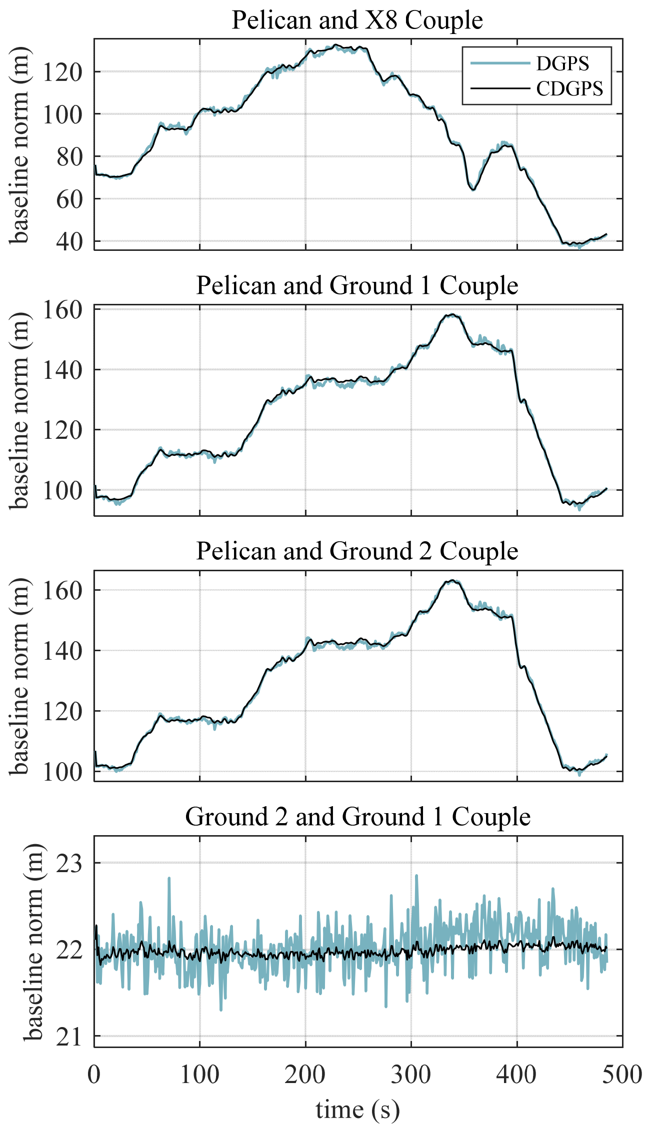

Figure 6.14 Estimated CDGPS and DGPS Baseline Norm.

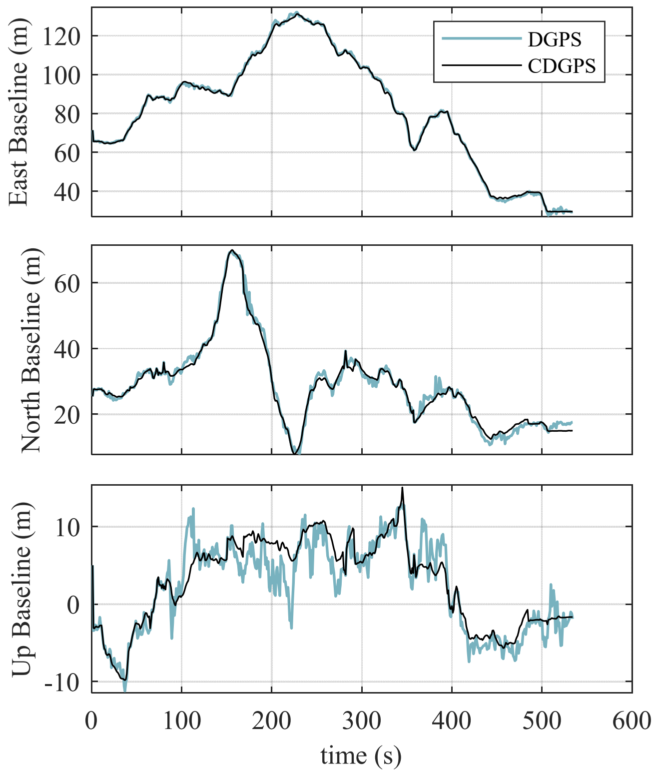

Figure 6.15 Pelican-X8 couple’s baseline components in ENU.

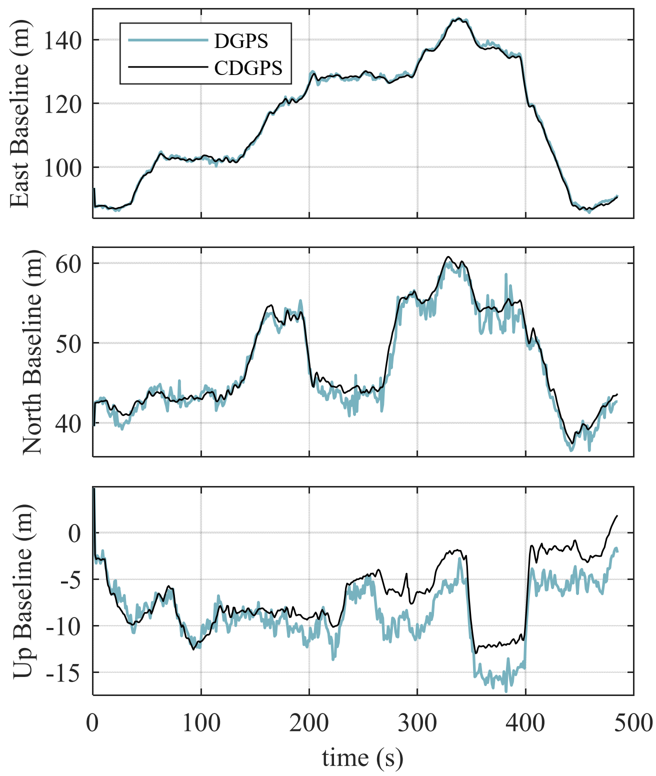

Figure 6.16 Pelican-Ground 1 couple’s baseline components in ENU.

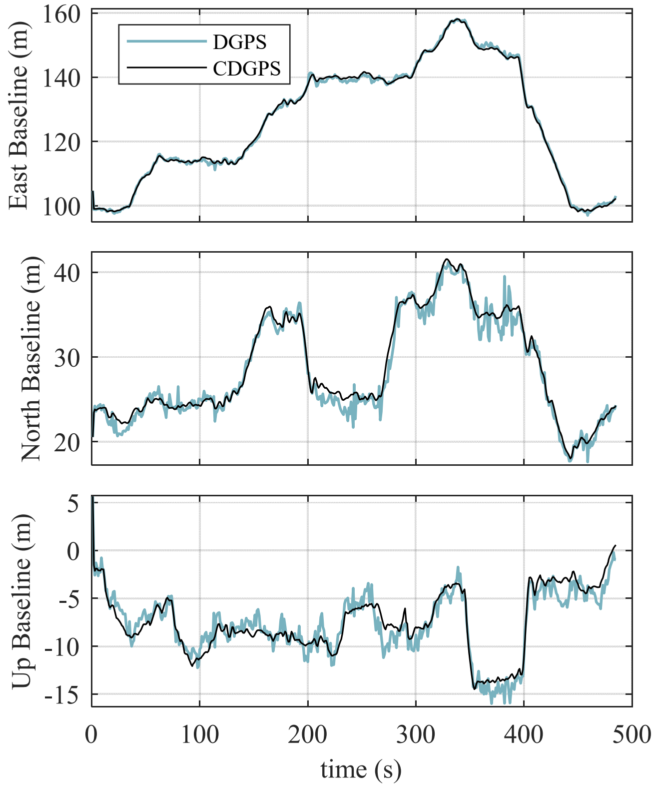

Figure 6.17 Pelican-Ground 2 couple's baseline components in ENU.

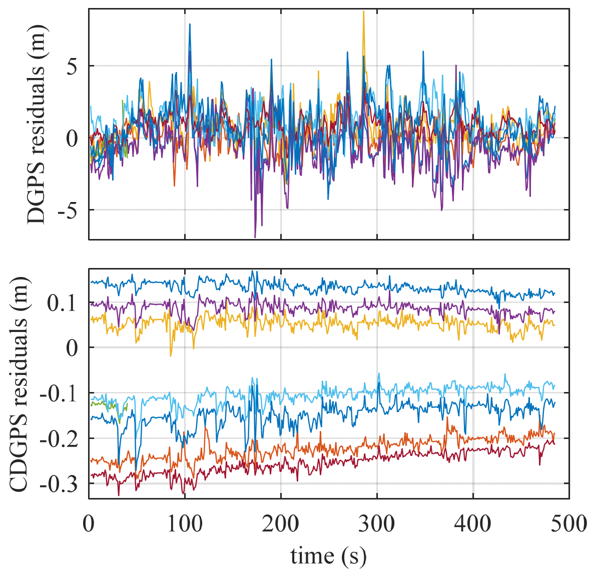

Figure 6.18 Pelican-X8 couple's DGPS and CDGPS residuals.

For the sake of brevity, the residuals and the baseline's errors are shown in this section only for the Pelican-X8 couple, but similar results are obtained for all the considered couples. The CDGPS residuals depicted in the second plot of Figure 6.18 are in the order of ten centimeters, which is ten times smaller than the DGPS ones. More importantly, CDGPS residuals are in good agreement with the expected DD carrier phase noise (i.e. in the order of centimeters) leading to the consideration that float ambiguities should differ from integer ones for an amount that is not significantly larger than an L1 cycle (i.e. 19 cm). Finally, Figure 6.19 depicts the predicted horizontal and vertical errors on baseline estimation with CDGPS filter for the Pelican-X8 couple.

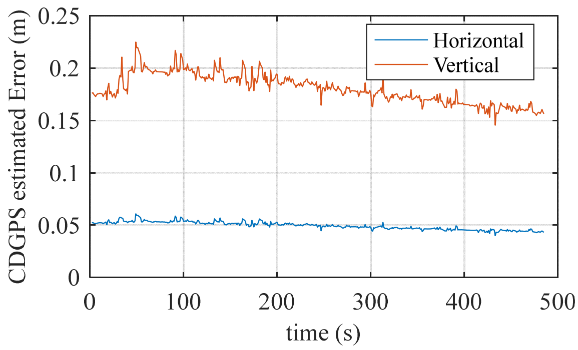

Figure 6.19 Pelican-X8 couple's estimated Horizontal and vertical errors.

6.6.3 Loosely coupled Integration

This section estimates the performances of the loosely CDGPS/Vision integration within the EKF, assuming the pelican as chief platform. To this aim the solution of the navigation approach described in section 6.4 is compared to the one given by the Pelican navigation filter (running onboard the autopilot). To this end, the focus is set on a time frame of about 80 seconds (540 seconds whole flight) during which the Pelican was commanded to slowly change its heading while keeping the deputies within the camera FOV. The results are obtained assuming the X8 and the ground antenna 1 to be respectively a flying and a fixed deputy for the pelican.

The maximum baseline length (about 130 m) between the chief (Pelican) and the flying deputy (X8) is reached in the initial phase of the considered time frame and slowly decreases with time to about 90 m (Figure 6.20). On the contrary, the maximum baseline of about 160 m between the chief and the fixed deputy used for attitude estimation (ground antenna 1) is reached at the end of the considered time frame (Figure 6.21).

Heading behaviour is analysed in Figure 6.22. The figure compares the heading resulting from the EKF augmented with the cooperative measurements (EKF CDGPS/Vision) with the results of the TRIAD algorithm in the case DGPS (DGPS/Vision) and CDGPS (CDGPS/Vision) measurements are used as GPS information source. In addition, Pelican's navigation filter and magnetometer output are considered. The EKF is initialized with the first Pelican's navigation filter output, and is propagated using accelerometers and gyroscopes measurements. During the propagation phase, the heading estimated by the EKF follows the one estimated by the Pelican navigation filter.

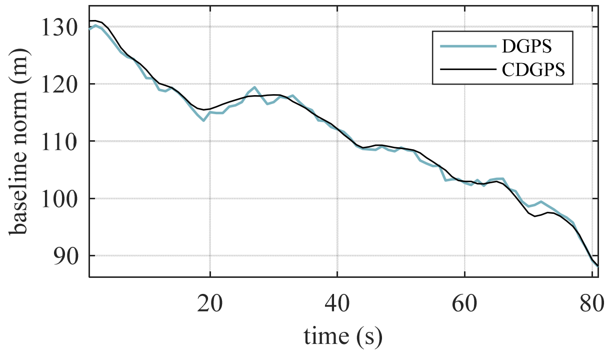

Figure 6.20 Pelican-X8 baseline in the considered time frame.

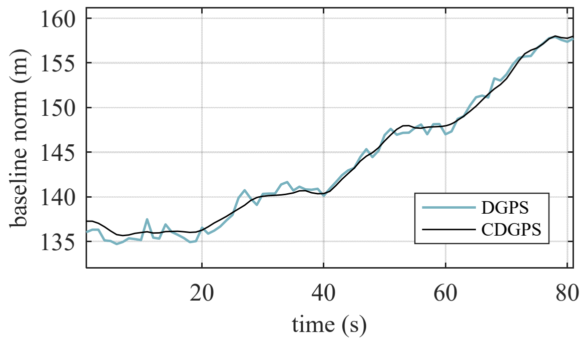

Figure 6.21 Pelican-ground antenna 1 baseline in the considered time frame.

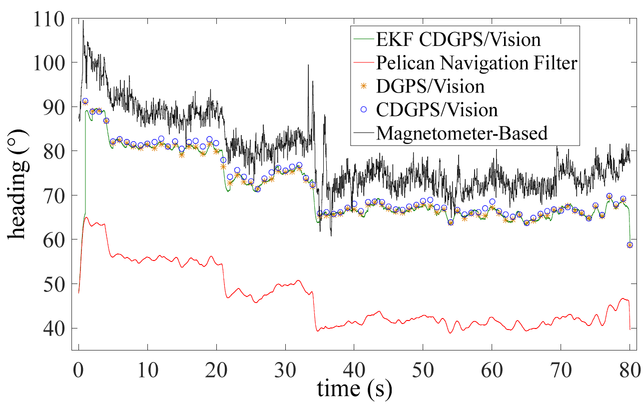

Figure 6.22 Heading as a function of time. The figure compares the Heading predicted with the proposed technique (loosely coupled CDGPS/Vision EKF) with those estimated by the Pelican navigation filter and by the magnetometer. In addition, the DGPS/Vision and CDGPS/Vision outputs of the TRIAD algorithm are reported.

Table 6.1 Mean Value of the heading angle during the analysed time frame.

Angle [°]	Estimation Method		
	Loosely coupled EKF-DGPS/Vision	*Loosely coupled EKF-CDGPS/Vision*	*Pelican Navigation filter*
Heading	71.9	71.3	79.4
Pitch	5.5	4.5	4.4
Roll	1.4	-1.3	-0.3

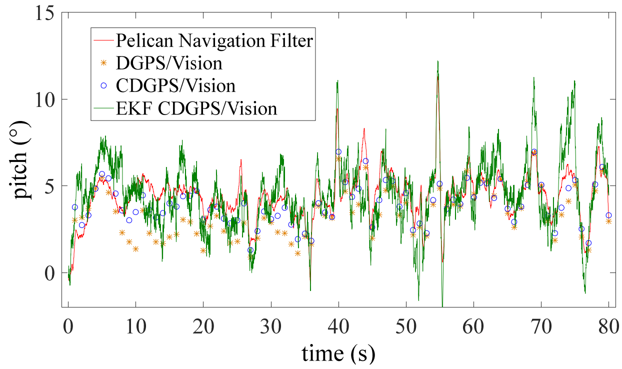

Figure 6.23 Pitch as a function of time. The figure compares the pitch angle predicted with the proposed technique (loosely coupled CDGPS/Vision EKF) with the one estimated by the Pelican navigation filter and the DGPS/Vision, CDGPS/Vision outputs of the TRIAD algorithm.

This behaviour changes completely as soon as CDGPS/Vision measurements are integrated in the EKF where a difference of several degrees is generated with respect to the pelican data fusion. This difference is mainly related to several heading rotation manoeuvres that have been commanded prior to the considered time frame which significantly affect the heading estimated by the Pelican navigation filter [12]. As regards the comparison of the EKF output with the magnetic heading, also in this case a difference of about 8° (Table 6.1) is experienced mainly due to magnetic biases and IMU-camera residual misalignment. As regards the pitch estimate (Figure 6.23), the EKF-CDGPS/Vision provides an output that is similar to the one provided by the Pelican navigation filter and in both cases, the mean value over the time frame is about 4.5° (Table 6.1), on the contrary, the EKF based on DGPS/Vision is characterized by a mean of 5.5° due to the higher impact of formation geometry and DGPS vertical accuracy on this angle estimate. A similar behavior is shown for the estimate of the roll angle (Figure 6.24) where in this case the CDGPS/Vision outperform the DGPS/Vision thanks to the higher vertical accuracy achievable with the CDGPS solution.

In order to have a benchmark for comparing the accuracy of the CDGPS/Vision with DGPS/Vision and the Pelican Navigation Filter, a pointing accuracy analysis has been performed following the concept proposed in [12]. However, while in [12] a map-georeferenced Ground Control Point (GCP) was used to evaluate the accuracy of the proposed method, here the ground antenna not involved in the attitude estimation process (ground antenna 2) and CDGPS-based relative positioning have been used. In more details, CDGPS-based azimuth and elevation of the GCP in the chief-based NED reference frame can be used as a reference for the pointing angles calculated converting image-based azimuth and elevation in BRF through the estimated attitude matrix. Figure 6.25 shows the computed azimuth error for the CDGPS/Vision, DGPS/Vision and the onboard navigation filter. It is clear how the CDGPS/Vision and the DGPS/Vision errors do not show a dependence on flight dynamics history. Whereas, the onboard navigation filter exhibits a significant pointing error because of these effects.

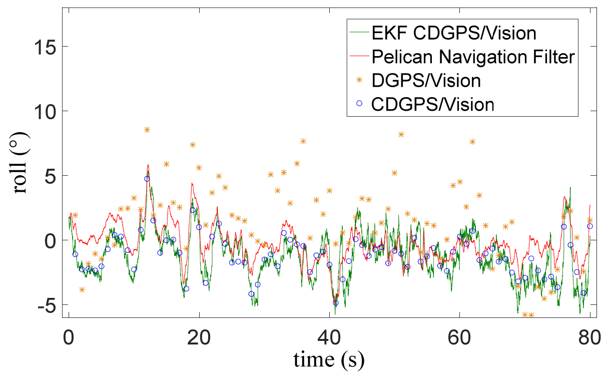

Figure 6.24 Roll as a function of time. The figure compares the roll angle predicted with the proposed technique (loosely coupled CDGPS/Vision EKF) with the one estimated by the Pelican navigation filter and the DGPS/Vision, CDGPS/Vision outputs of the TRIAD algorithm.

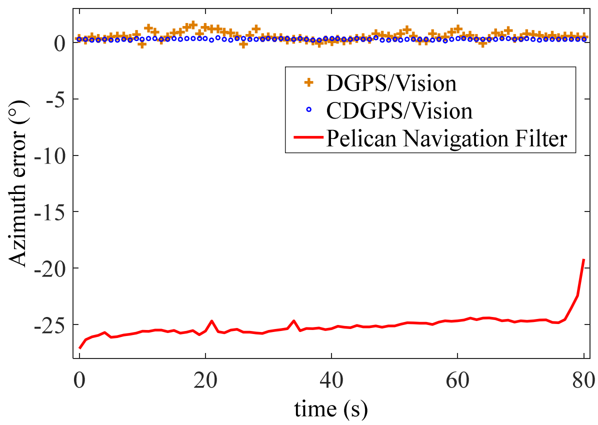

Figure 6.25 Comparison of the pointing accuracy of the loosely coupled CDGPS/Vision DGPS/Vision and Pelican Navigation Filter, in terms of Azimuth error.

6.6.4 Tightly coupled Integration

This section analyses the performance of the tightly coupled CDGPS/Vision navigation filter described in section 6.5. As in section 6.6.3, the results obtained using the customized filter are compared to those given by the Pelican navigation filter that runs onboard the autopilot. The focus is set on the entire flight of about 500 seconds during which the Pelican was commanded to perform heading rotation manoeuvres with different rates. Several fast 360 degrees heading rotations have been commanded while most of the flight was characterized by slow heading rotations in order to keep the deputies within the chief camera FOV. Baseline variation of the chief with respect to the flying deputy (X8), the fixed deputy (ground antenna 1) and the ground control point (ground antenna 2) are shown in Figure 6.26. As for the loosely coupled results, the second ground antenna is used as GCP to assess the performance of the technique. Figure 6.27 shows a zoom of the heading behaviour during the 500 seconds flight. The zoom has been performed to allow focusing on the parts with almost constant heading, highlighted by the red circles, and to assess the performance of the proposed technique. The figure reports the magnetic heading compared with that predicted by the pelican's filter. The result of the tightly coupled CDGPS/Vision filter with two deputies (flying and fixed deputies) is reported in the legend of Figure 6.27 as 2 LOS. This is because the CDGPS filter is using two information, i.e. the line of sight (LOS) direction from two deputies as cooperative aiding. Some observation about the flight dynamics and Pelican's filter results can be made by analyzing the three time intervals highlighted with the red circles in Figure 6.27.

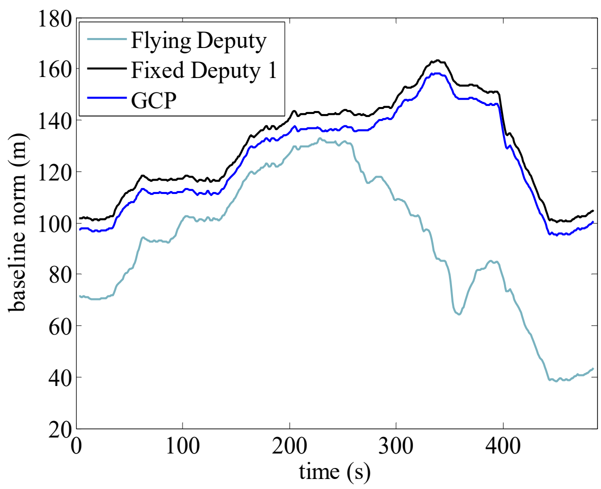

Figure 6.26 Baseline variation of the chief platform, with respect to the deputies along the entire flight.

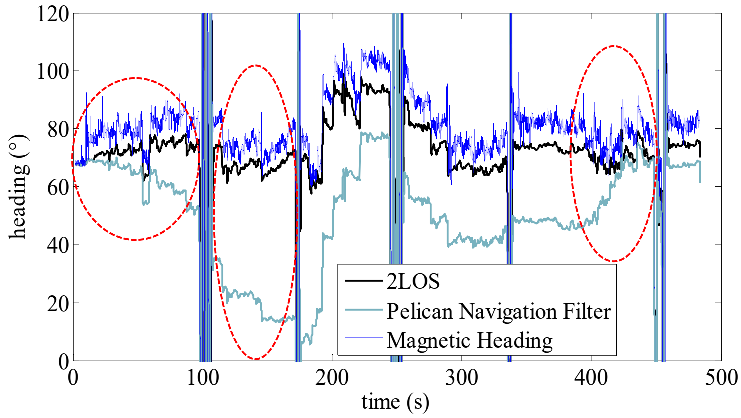

Figure 6.27 Heading as a function of time. 2 LOS indicated the results of the tightly coupled CDGPS/Vision filter when two deputies (fixed and flying deputies) are used.

During the first flight segment (0-100 seconds) the Pelican navigation filter presents a significant drift, and a difference of about 22 degrees is established with respect to the EKF. On the contrary, an almost constant difference, of about 8 degrees, stands between the EKF and the magnetic heading. The drift of the Pelican navigation filter is mainly due to the commanded slow heading rotations that create angular velocities which are not tracked by gyroscopes due to the large sensors noise. On the other hand, the proposed EKF aided by CDGPS/Vision measurements is able to accurately follow the heading dynamics and does not present any drift. In addition, the almost constant difference between the EKF and the magnetometer-based heading is mainly due to on board uncompensated magnetic disturbances. The flight segment between 100 and 170 seconds, after the 360 degrees heading rotations, highlighted by the second red ellipse in Figure 6.27, shows a similar behaviour. The offset between the EKF and the Pelican navigation filter increases (up to about 60 degrees) due to the drift accumulated during fast rotations. As before, CDGPS/Vision EKF and magnetometer-based estimates (which are both insensitive to the flight history) present an absolute difference of about 8 degrees. The third red circle in Figure 6.27 shows that fast heading rotation can help the Pelican's navigation filter to reduce the drift and get back to an almost constant separation between the estimated heading and those estimated by magnetometer and CDGPS/Vision. Pitch and roll estimated angles are reported in Figure 6.28 and Figure 6.29 respectively.

Using as ground control point the second ground antenna, Figure 6.30 and Figure 6.31 show the computed azimuth and elevation errors for the navigation filter exploiting CDGPS/Vision measurements, and the onboard navigation filter.

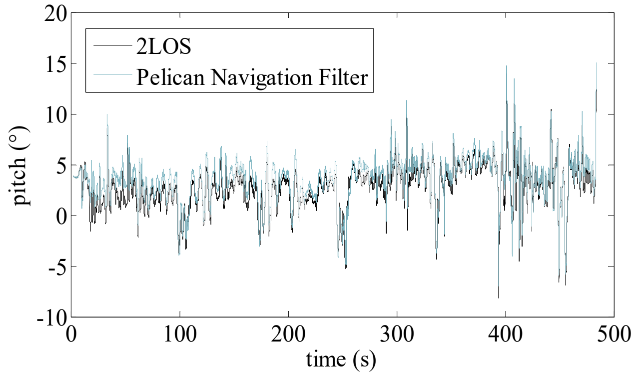

Figure 6.28 Pitch as a function of time. Tightly coupled CDGPS/Vision EKF results (2 LOS) are compared with the output of the Pelican's filter.

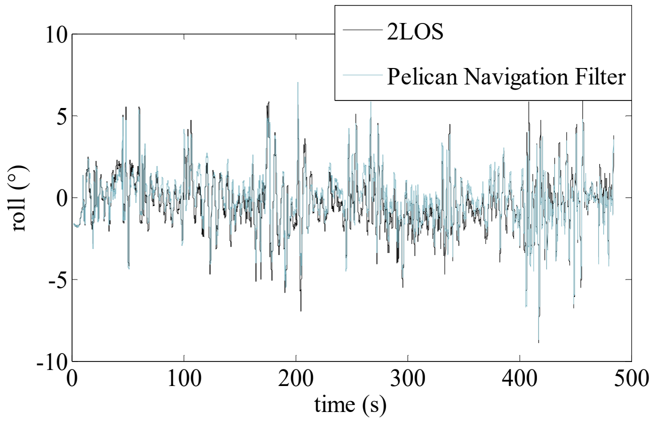

Figure 6.29 Roll as a function of time. Tightly coupled CDGPS/Vision EKF results (2 LOS) are compared with the output of the Pelican's filter.

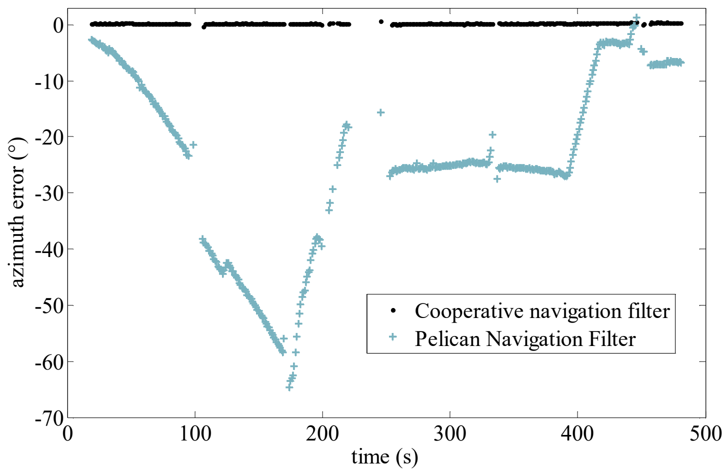

Figure 6.30 Comparison of the pointing accuracy of tightly coupled CDGPS/Vision EKF and Pelican Navigation Filter, in terms of Azimuth error.

As [12] demonstrates, the azimuth accuracy depends primarily on heading measurements performance, while the elevation accuracy is connected with pitch and roll errors. Differently from the Pelican's onboard navigation filter, the tightly coupled CDGPS/Vision EKF accuracy does not depend on flight dynamics history.

Indeed, the azimuth error the proposed EKF presents a mean error of about 0.1 degrees with a standard deviation of about 0.08 degrees, on the contrary, the Pelican navigation filter produces azimuth errors with mean and standard deviation of -24.1 and 15.6 degrees respectively. A similar result is shown for the elevation error (that is connected to pitch and roll performance), where a significant improvement is provided by the CDGPS/Vision measurements due to the increased vertical accuracy of the CDGPS solution with respect to the DGPS one, see Figure 6.23 and Figure 6.24. Indeed, the standard deviation of the CDGPS/Vision elevation error is 0.18 degrees (Table 6.2) while the Pelican navigation filter presents a standard deviation of 0.8 degrees.

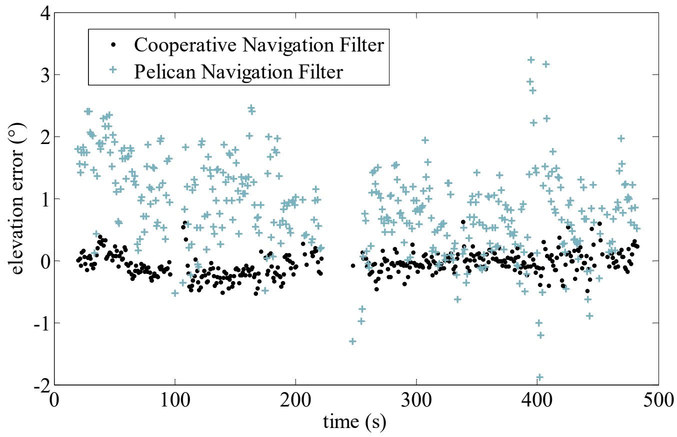

Figure 6.31 Comparison of the pointing accuracy of tightly coupled CDGPS/Vision EKF and Pelican Navigation Filter, in terms of Elevation error.

Table 6.2 Pointing Error Statistics of the tightly coupled CDGPS/Vision EKF

	Azimuth [°]		**Elevation [°]**	
Estimation Method	*Mean*	*Standard Deviation*	*Mean*	*Standard Deviation*
Tightly coupled CDGPS/Vision EKF	0.1	0.08	-0.05	0.18
Pelican Navigation Filter	-24.1	15.6	1	0.8

Chapter 7: High Accuracy Baseline Estimation for Cooperative Spacecraft with differential GNSS

It is worldwide recognized that upcoming space missions and systems will rely on co-flying, cooperating platforms to replace current monolithic systems, and to implement missions otherwise impossible (e.g., those requiring very large sensor apertures) or extremely complex. Indeed, the payload functionality can be distributed among the different elements of the formation. This may lead to a number of advantages, including overall system reliability, flexibility and modularity as well as enhanced responsiveness and decreased vulnerability. The advantage in using a formation flying strategy over a larger monolithic configuration has been widely demonstrated in terms of cost, mission duration and ease to reach mission purpose [1, 2]. In addition formation flying applications enable missions that were not allowed for monolithic satellites, e.g. space interferometry [17], geodesy [19] and magnetosphere investigation [175].

Formation flying is naturally coupled with the use of small space platforms, since the system overall cost is lower, the replacement of a failed satellite is easier and faster, and finally it is possible to gradually upgrade on board technologies by incrementally replacing elements of the formation, which is generally an issue for large space systems. Actually, small satellite-based missions offer the opportunity to fast and flexibly react to technology advancements. However, using more co-flying platforms to realize a given mission objective poses many technology challenges, including the autonomous determination in real-time, on board, of the relative positions of the formation members. This information is relevant to both formation acquisition and maintenance and to scientific objective achievement, which may require a very precise knowledge of the satellites' relative positions. The nominal separation (baseline) in a formation of two satellites for remote sensing applications can range from few hundreds of meters [17, 176] to few hundreds of kilometers [19, 177]. In addition, the inter-satellite separation can be extremely variable during the mission. For scientific needs, up to millimeter-level accuracy in relative position estimation may be required even if the satellites' separation is very large. In Low Earth Orbit (LEO), precise estimation of the relative positioning between two cooperative satellites it typically performed by carrier phase differential GPS-based navigation filters [178], exploiting double differenced information, see section 6.2.3. Paste works demonstrate this approach ensures centimetric or millimetric precision in baseline estimation [20, 179–181]. However, in real time applications both accuracy and robustness of relative GPS-based positioning systems for LEO satellites can be limited by ephemeris errors and rapidly changing ionospheric conditions. The ionosphere affects the propagation of radio electromagnetic waves by introducing a group delay with respect to vacuum conditions. This time delay is related to the total number of electrons encountered by the radio wave on its path, at least to first order [182]. Non-perfect compensation of ionospheric delay causes residual ionospheric errors in GPS observables, which degrade the achievable positioning accuracy.

The ionospheric delay compensation has a fundamental role when dealing with real-time relative positioning. Indeed, these applications requires a precise resolution of the double differenced (DD) integer ambiguities. Integer ambiguity resolution (IAR) could fail when the ionospheric delay is larger than half the carrier baseline [160]. Therefore, ionospheric delays have a fundamental role in precise positioning, especially over long baselines (> 100 km) and a proper model is needed for their estimation. Different approaches can be used for this purpose. The most common ones are referred to as ionospheric-float and ionospheric-free, respectively. In the former case, ionospheric delays are treated as completely unknown parameters to be estimated [183], whereas in the latter the ionospheric delays are cancelled by measurement combinations [184].

Contrary to the ionospheric-free and ionospheric-float approaches, the ionospheric models can be introduced. Among several alternatives, the use of stochastic models, e.g., first-order Gauss-Markov process, is a common solution [180, 185, 186]. However, these approaches give low improvement by themselves, because of the low fidelity of stochastic models. They typically yield results similar to ionospheric-free and ionospheric-float approaches, but with ionospheric delays that are smoother in time. Adding exogenous ionospheric models as pseudo-observations is a common practice in ground-based Real Time Kinematic (RTK) networks when ionospheric-weighted approaches are used [187]. However, their applicability to high-dynamic conditions, such as in LEO formation flying, has not been assessed yet [188]. Finally, using functional models of the ionospheric delay can be a viable solution to improve IAR performance. Several precise models have been developed for ground based receivers [189, 190]. These models assume the ionosphere as a combination of basis function [159, 191]. The correct estimation of the coefficients of the basis function defines the ionosphere intensity distribution and requires a long observation time and a high computational cost. Typically, most coefficients in these functional models are set to a-priori values [182, 192], leaving only a few variables as floating parameters for ionospheric delays estimation. Thus, the effectiveness of these approaches is limited by the accuracy in estimating ionospheric delays with a small number of parameters. Often, these latter are estimated concurrently with the other unknowns to improve their accuracy [20–22, 193, 194]. Nevertheless, due to the low computational cost required in spaceborne applications simpler Ionospheric models are required.

The standard ionosphere model for real-time GPS applications in LEO is that proposed by Lear [22], which uses the Vertical Total Electron Content (*VTEC*) above the receiver and a specific mapping function for performing TEC evaluation along a given ray path. With specific reference to LEO formation flying, it is worth discussing the advantages of ionosphere modeling over the ionospheric-free solution. Specifically, in both cases, IAR can be implemented [195], but different performance can be achieved. With specific reference to the Lear model, results on flight data demonstrated that Lear outperforms ionospheric-free combinations in mild ionospheric conditions, whereas in intense ionospheric errors in Lear model become more significant and better results are obtained by the ionospheric-free approach. However, the latter is still unsatisfactory from IAR perspective (less than 80% correct IAR).

For this reason, this chapter introduces a novel model for ionospheric delays estimation capable of describing the ionosphere with a series of basis function, without compromising the real time requirement. This model, referred to as Linear Thin Shell (LTS) is capable of capturing local horizontal gradients in the electron content. Hence, LTS presents similarities with the approach proposed by [196], and can be interpreted as its generalization to the case of real-time ionospheric delay estimation on-board a

LEO satellite. The Lear and LTS models estimate undifferenced ionospheric delays, but they can be used to compute differential ionospheric delays as a combination of the undifferenced ones. It is expected that LTS model enhances real-time filter capability to estimate ionospheric delays and the number of correctly estimated integer ambiguities, thus improving the baseline (inter-satellite separation) estimate precision.

The main reason for the introduction of a LTS model [197] is creating a more reactive model than the Lear's to be used in DD real-time filtering [20, 194]. Therefore Lear and LTS models are described in section 7.1, whereas the derivation of double differenced and undifferenced ionospheric delays with the LTS model is reported in section 7.2. Integration of the LTS model in a real-time relative positioning filter for baseline estimation [198, 199] with LEO platforms is described in section 7.3. Finally, the performance of the LTS model are assessed in section 7.4, where a comparison with the Lear model is performed using data collected by Gravity Recovery and Climate Experiment mission (GRACE) mission [19]. GRACE mission is based on two satellites flying in formation and separated by more than 200 km.

7.1 IONOSPHERIC MODELS

The ionosphere induced delay, I, of a radio signal with frequency, f, can be modelled at a first order [200] as the integral of the linear electron density, n_e, along the ray path between a GPS satellite, i, and the receiver, r,

$$I_r^i = \frac{40.3\ m^3/s^2}{f^2} TEC_r^i ; TEC_r^i = \int_{\mathbf{x}_r}^{\mathbf{x}^i} n_e(\mathbf{x}) d\mathbf{x} \tag{7.1}$$

where TEC_r^i is the Total Electron Content along the ray path from the satellite to the receiver and $\mathbf{x} = [\phi, l, h]^T$ is the position of a generic point of the ray path in terms of latitude, longitude and altitude above the earth, respectively.

7.1.1.1 Lear Model

The model introduced by Lear [22] is currently the most used one for TEC estimation in real time GNSS-based navigation of LEO satellites [20, 201, 202]. It separates the geometrical effect, depending on the relative position between satellite and receiver, from that generated by electron anisotropy. The former one is included in the mapping function, M, whereas the latter is represented by the Vertical TEC

above the receiver. Specifically, Lear model [22] estimates the total electron content as

$$TEC_r^i = \frac{2.037}{\sin E_r^i + \sqrt{\sin^2 E_r^i + 0.076}} \cdot VTEC_r = M_{Lear}\left(E_r^i\right) \cdot VTEC_r \tag{7.2}$$

where E_r^i is the elevation of i-th satellite, see Figure 7.1. It is worth noting that the coefficients in (7.2) were estimated as a best fit of real LEO GPS flight data [22]. Nonetheless, one can easily verify that Lear model can be derived from a thick shell assumption [203, 204] considering

- the receiver altitude equals the lower bound of the shell,
- the GPS satellite elevation greater than zero
- a uniform electron density within the shell.

Hence, when significant electron density gradients occur, as under intense solar activity, the capability of Lear model to estimate ionospheric delays with sufficient level of accuracy can be degraded notably [20, 194]. The spatial variation of the electron density shall be accounted for in order to improve ionospheric model accuracy. A voxel grid representing the spatial distribution of the electron density is a viable solution to compute the integral in (7.1). According to this idea, and for the sake of reducing the number of parameters to be estimated, models have to be introduced.

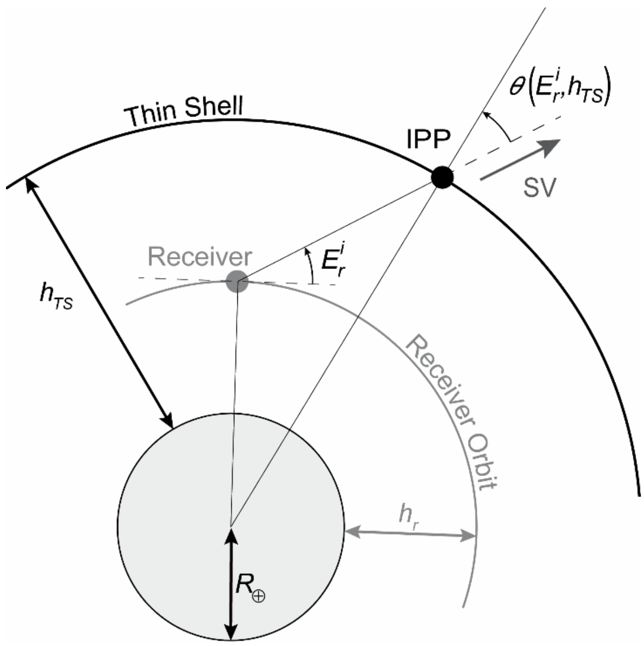

Figure 7.1 Thin Shell model and Ionospheric Pierce Point definition, two-dimensional illustration, for clarity.

Concerning this, the separation between vertical and horizontal variability is a common solution [159, 200]. This is the case of tomographic approaches to electron density reconstruction, e.g., in Multi Instrument Data Analysis System (MIDAS) [205]. Specifically, the vertical variation can be assumed either to fit analytical profiles, i.e. Chapman, Epstein, Exponential [206, 207] or to result as the superposition of Empirical Orthogonal Functions (EOF) [208, 209]. As far as horizontal variation is concerned, a linear combination of basis functions can be used, as performed in [191], in which the relevant coefficients are evaluated as those minimizing differences between model and measurements. Spherical harmonics and polynomials are different common choices for the basis function. In more detail, spherical harmonics are typically used when a global ionospheric map has to be generated, thus requiring the computation of more than 10-15 independent coefficients. On the contrary, polynomial horizontal variations perform better for local areas analysis taking advantage of the reduced number of coefficients to be estimated [191].

7.1.1.2 LTS Model

With the aim of reproducing local variations of electron density by a limited number of independent parameters, a specific model, referred to as Linear Thin Shell (LTS) model, is introduced. It is based on the thin shell assumption or single-layer ionospheric model [159, 204, 210] and considers a bilinear *VTEC* horizontal variation [190, 196, 211]. Indeed, this model allows creating a local map of the ionosphere with only three parameters, thus not significantly increasing the computation load with respect to Lear model. As well known, the thin shell model assumes the ionosphere confined within a layer of altitude h_{TS}, which is the thin shell altitude, see Figure 1. This assumption simplifies the *TEC* estimation since the electron density along the ray-path from the GPS satellite or SV (space vehicle) to the receiver is everywhere zero except at the intersection point between ray-path and shell. This point is called Ionospheric Pierce Point (IPP). It is well known that the IPP definition is singular at poles. Therefore non-ambiguous equation must be used at high latitudes, i.e., greater than 70 degrees [212]. The *TEC* over the ray path can be evaluated as [159, 204]:

$$TEC_r^i = M_{TS}\left(E_r^i, h_{TS}\right) VTEC_{IPP}\left(\phi_{IPP}, l_{IPP}\right) \tag{7.3}$$

where $VTEC_{IPP}$ is the vertical *TEC* above the IPP and M_{TS} is thin shell mapping function that depends on θ, namely the angle between the ray-path and IPP radial direction (Figure 1). The Vertical TEC of IPP is a function of its latitude and longitude, ϕ_{IPP} and l_{IPP}, respectively. The thin shell mapping function is [204]:

$$M_{TS}\left(E_r^i, h_{TS}\right) = \frac{1}{\cos\theta\left(E_r^i, h_{TS}\right)} = \frac{1}{\dfrac{R_\oplus + h_r}{R_\oplus + h_{TS}}\sqrt{\left(\dfrac{R_\oplus + h_{TS}}{R_\oplus + h_r}\right)^2 - \cos^2 E_r^i}} \tag{7.4}$$

where h_r is the receiver altitude and $R_\oplus$ is the spherical Earth radius. It is evident that a value for the thin shell altitude must be selected in equation (7.4), and this value must be higher than the receiver altitude. A common choice for ground-based receivers is setting h_{TS} as the altitude of the F2 peak. There is no specific reason for this choice except that the thin shell is placed at an altitude representative of a significant peak of ionospheric intensity. However, most of LEO satellites are above that altitude, so no representative ionosphere intensity peak is available. This means that the height of the shell can be used as an additional free parameter to be tuned to improve the accuracy of the model [213]. According to this approach, the thin shell height is set in this work as the height for which LTS mapping function fits that of Lear model. Even if no theoretical proofs are provided herein, the experimental results presented in this research clearly indicates that the proposed one is the best choice to minimize LTS errors in the prediction of DD ionospheric delays, so it should be preferred when LTS is used to support IAR. More on this will be provided later when discussing the performance of LTS model. With respect to the selected bilinear model for *VTEC* variations [190, 196, 211] one can write:

$$\begin{gathered} VTEC_{IPP}\left(\phi_{IPP}, \lambda_{IPP}\right) = v_0 + v_1 \Delta\phi_{IPP} + v_2 \Delta l_{IPP} \\ \Delta\phi_{IPP} = \phi_{IPP} - \phi_C;\ \Delta l_{IPP} = l_{IPP} - l_C \end{gathered} \tag{7.5}$$

Hence, *VTEC* depends on the latitude and longitude differences between the IPP and a reference point *C* with same latitude and longitude as the receiver but located on the thin shell (Figure 7.2). It is worth outlining that the LTS model includes the *VTEC* above the receiver through the bias coefficient v_0, as well as the *VTEC* variations as a function of latitude and longitude through the coefficients v_1 and v_2. Figure 7.2 shows the *VTEC* distribution around the point *C* located on the receiver's vertical.

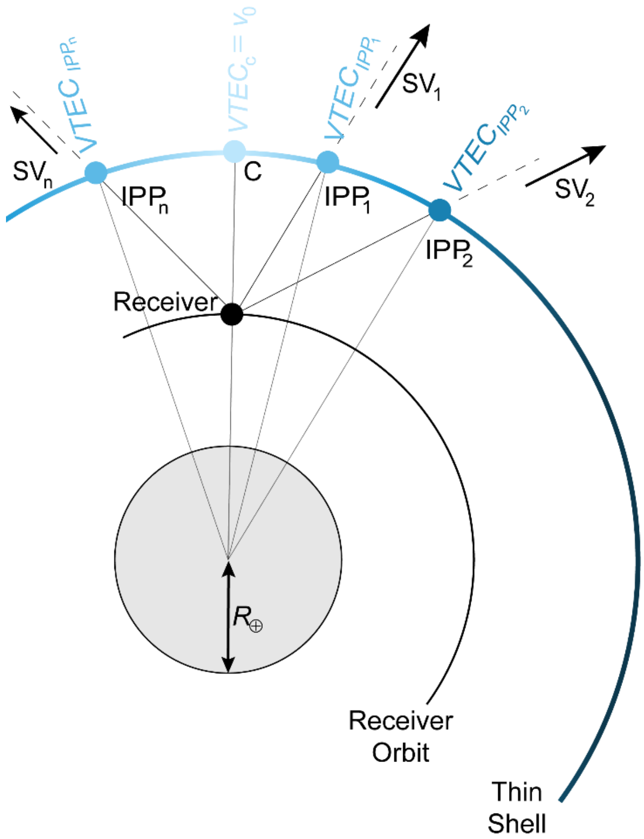

Figure 7.2 *VTEC* variation in LTS model, two-dimensional illustration, for clarity.

Unlike Lear model, a horizontal *VTEC* variation is introduced by the coefficients v_0, v_1, and v_2, since a different *VTEC* value can be provided for any tracked GPS satellite, or more precisely, for the related IPP. Such a horizontal gradient is expected to lead to a more realistic representation of ionosphere behaviour above the receiver. Finally, it is worth noting that, from a theoretical point of view, higher order polynomial terms could be included in equation (7.5), to improve the accuracy of the selected model further, as routinely done in ground-based applications [211]. However, this increases the number of parameters to estimate, and, more important, the results presented in [214] clearly indicate that higher order terms tend to be not estimable for LEO receivers.

7.2 IONOSPHERIC DELAY ESTIMATION

The first attempt in assessing the performance of the LTS model, includes the comparison between the measured delay and the predicted with the proposed model. This section describes how to estimate the measured and predicted delays in the undifferenced (UD) and double-differenced (DD) case. A conceptual scheme of the used procedure is reported in Figure 7.3.

"Measured" delays are derived by means of receiver position knowledge and GPS measurements, which are assumed to include pseudorange (PR) and carrier phase (CP) observables on L1 and L2 frequency, respectively. The UD pseudoranges, denoted as P, and carrier phases, denoted as L, can be modelled as [120, 202]:

$$\left(P_F\right)_r^i = \rho_r^i + CM_r^i + \left(\gamma^{-2}\right)^{F-1} I_r^i + \left(b_F^{Pr}\right)_r + \left(b_F^{Pr}\right)^i + \left(\sigma_F\right)_r \tag{7.6}$$

$$\left(L_F\right)_r^i = \rho_r^i + CM_r^i - \left(\gamma^{-2}\right)^{F-1} I_r^i + \left(b_F^{Cp}\right)_r + \left(b_F^{Cp}\right)^i + \left(\varepsilon_F\right)_r + \lambda_F \left(\psi_F\right)_r^i \tag{7.7}$$

The subscript F is equal to 1 or 2 and indicates the frequency L1 or L2, ρ_r^i is the geometric range between the receiver r and the SV i. The common mode errors, CM_r^i include the GPS satellite clock and ephemeris error, the absolute ionospheric delay I_r^i and ratio of L1 and L2 frequency $\gamma = f_2 / f_1$. The bias term, b, accounts for all the dispersive hardware effects for both receiver and GPS satellite.

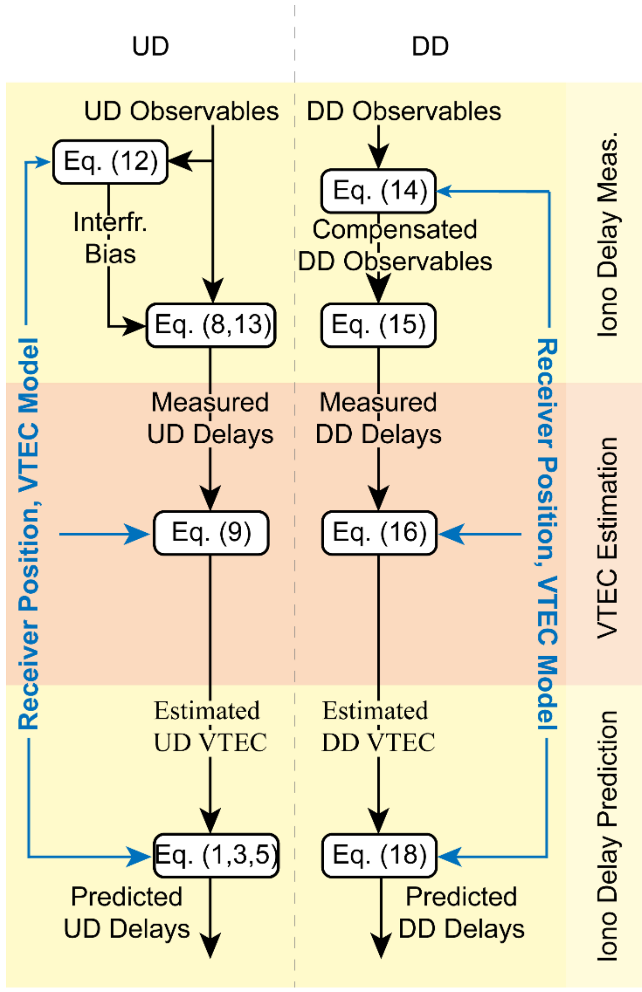

Figure 7.3 Flow chart for computing measured and predicted ionospheric delays.

σ and ε are the measurement thermal noises for PR and CP, respectively. White noise models are assumed for both σ and ε. Finally, $\lambda\left(\psi\right)_r^i$ is the cycle ambiguity term. DD observables [120, 202] can be defined for two receivers and two satellites as equation (6.7) that is reported herein for the sake of completeness:

$$\begin{aligned}\left(P_F\right)_{rq}^{ji} &= \rho_{rq}^{ji} + \left(\gamma^{-2}\right)^{F-1} I_{rq}^{ji} + \left(\sigma_F\right)_{rq}^{ji} \\ \left(L_F\right)_{rq}^{ji} &= \rho_{rq}^{ji} - \left(\gamma^{-2}\right)^{F-1} I_{rq}^{ji} + \left(\varepsilon_F\right)_{rq}^{ji} + \lambda_F\left(n_F\right)_{rq}^{ji}\end{aligned} \tag{7.8}$$

where r and q identify the two receivers and j denotes the reference satellite selected to evaluate the DD observables, namely the pivot satellite. i indicates any other visible satellite, ρ_{rq}^{ji} is the DD geometrical term, $\left(\sigma_F\right)_{rq}^{ji}$ and $\left(\varepsilon_F\right)_{rq}^{ji}$ are the DD PR and CP thermal noises, respectively, and $\left(n_F\right)_{rq}^{ji}$ is the integer ambiguity. Tropospheric error has been cancelled out, because the altitude of the LEO spacecrafts, that ensure GPS signal is propagated only in the ionosphere.

7.2.1 Measured Delays

The measured UD ionospheric delay can be obtained by combining L1 and L2 pseudorange observables in equation (7.6) as follows:

$$\left(\tilde{I}_{Pr}\right)_r^i = \frac{\gamma^2}{\gamma^2-1}\left[\left(P_1\right)_r^i - \left(P_2\right)_r^i - \left(b^{Pr}\right)_r - \left(b^{Pr}\right)^i\right] \tag{7.9}$$

where $\left(b^{Pr}\right)_r = \left(b_1^{Pr}\right)_r - \left(b_2^{Pr}\right)_r$ is the receiver inter-frequency bias and $\left(b^{Pr}\right)^i = \left(b_1^{Pr}\right)^i - \left(b_2^{Pr}\right)^i$ is the i-th satellite's inter-frequency bias, also known as Differential Code Bias (DCB). CODE product of Bernese GPS software [215] is used in this work as reference DCB values. Receiver inter-frequency bias estimation is thus mandatory for estimating $\left(\tilde{I}_{Pr}\right)_r^i$. An estimation technique for receiver inter-frequency bias was proposed in [216] dealing with Lear model. This formulation is herein extended to the LTS model. Specifically, equations (7.1), (7.3) and (7.5) can be rearranged as follows:

$$\begin{bmatrix} \left(I_{Pr}\right)_r^1 \\ \left(I_{Pr}\right)_r^2 \\ \vdots \\ \left(I_{Pr}\right)_r^{n_r} \end{bmatrix} = \frac{40.3}{f_1^2}\mathbf{M}\begin{bmatrix} \left(v_0\right)_r \\ \left(v_1\right)_r \\ \left(v_2\right)_r \end{bmatrix} \tag{7.10}$$

$$\mathbf{M} = \begin{pmatrix} \mathbf{M}_r^1 \\ \mathbf{M}_r^2 \\ \vdots \\ \mathbf{M}_r^{n_r} \end{pmatrix}; \mathbf{M}_r^i = \begin{pmatrix} \left(M_{TS}\right)_r^i \\ \left(M_{TS}\right)_r^i \left(\Delta\phi_{IPP}\right)_r^i \\ \left(M_{TS}\right)_r^i \left(\Delta l_{IPP}\right)_r^i \end{pmatrix}^T \tag{7.11}$$

where n_r is the number of tracked GPS satellites, and the $n_r\times 3$ matrix $\mathbf{M}$ transforms the *VTEC* coefficients into ionospheric delays. Since $\mathbf{M}$ is in general not a square matrix, the solution of equation (7.10) in v_0, v_1 and v_2 can be obtained by applying a Least square (LSQ) method, provided that $n_r \geq 3$. Is worth clarifying the LSQ returns an exact solution only when the number of unknowns is equal to the number of known elements, in the other case only an approximate solution is available, obtained by minimizing the sum of squared residuals.

For the *i*-th satellite we have:

$$\left(I_{Pr}\right)_r^i = \frac{40.3}{f_1^2}\left(M_{TS}\right)_r^i \begin{bmatrix} 1 & \left(\Delta\phi_{IPP}\right)_r^i & \left(\Delta l_{IPP}\right)_r^i \end{bmatrix} \begin{bmatrix} \left(v_0\right)_r \\ \left(v_1\right)_r \\ \left(v_2\right)_r \end{bmatrix} \tag{7.12}$$

and the coefficients of the LTS model are given by the inversion of (7.10), i.e.

$$\begin{bmatrix} \left(v_0\right)_r \\ \left(v_1\right)_r \\ \left(v_2\right)_r \end{bmatrix} = \mathbf{M}^+ \begin{bmatrix} \left(I_{Pr}\right)_r^1 \\ \left(I_{Pr}\right)_r^2 \\ \vdots \\ \left(I_{Pr}\right)_r^{n_r} \end{bmatrix} \tag{7.13}$$

where $\mathbf{M}^+ = \left(\mathbf{M}^T\mathbf{M}\right)^{-1}\mathbf{M}^T$. Then using in (7.13) the ionospheric delays estimated in (7.9) provides the following expression for the receiver inter-frequency biases for each GPS satellite:

$$\left(b^{Pr}\right)_r^i = \frac{\sum_{l=1}^{n_r}\left(\left(G_l\right)_r^i\left[\left(P_1\right)_r^l-\left(P_2\right)_r^l-\left(b^{Pr}\right)^l\right]\right)-\left[\left(P_1\right)_r^i-\left(P_2\right)_r^i-\left(b^{Pr}\right)^i\right]}{\sum_{l=1}^{n^r}\left(\left(G_l\right)_r^i\right)-1} \tag{7.14}$$

where

$$\left(G_l\right)_r^i = \left(M_{TS}\right)_r^i\left(\left(\mathbf{M}^+\right)_{1,l}+\left(\Delta\phi_{IPP}\right)_r^i\left(\mathbf{M}^+\right)_{2,l}+\left(\Delta l_{IPP}\right)_r^i\left(\mathbf{M}^+\right)_{3,l}\right) \tag{7.15}$$

As far as equation (7.14) is concerned, it is important to remark that, owing to different noise realizations, different samples of the same inter-frequency bias are computed in different time instants. The receiver inter-frequency bias is often modelled as a daily constant [216–219]. As a consequence, the statistical distribution of the inter-frequency bias can be evaluated throughout the 24-hour period. As shown in [216], if the same technique is applied to Lear model a Gaussian distribution is obtained, thus allowing one to estimate the daily bias as the mean value of the distribution. On the contrary, the LTS model can be verified to exhibit a non-Gaussian distribution as demonstrated by results given in section 7.4.1. Thus, the mode is used as the representative value for the daily bias.

For the carrier phase observables, the measured UD ionospheric delay is given by [120]:

$$\begin{gathered}\left(\tilde{I}_{Cp}\right)_r^i = -\frac{\gamma^2}{\gamma^2-1}\left[\left(L_1\right)_r^i-\left(L_2\right)_r^i\right]+\Delta B \\ \Delta B = \frac{\gamma^2}{\gamma^2-1}\left(\lambda_1\left(\psi_1\right)_r^i-\lambda_2\left(\psi_2\right)_r^i+\left(b^{Cp}\right)_r+\left(b^{Cp}\right)^i\right)\end{gathered} \tag{7.16}$$

where ΔB includes the cycle ambiguities and receiver and satellite inter-frequency biases. These terms cannot be estimated separately as performed for the pseudorange case, thus (7.16) can be solved estimating ΔB by a complementary filter exploiting both CP and PR observables, as described by [120].

To obtain the DD delays, the DD observables in (7.8) must be compensated for the geometrical term and the integer ambiguities estimated as in [218]. Compensated DD observables, respectively $P_F{}'$ and $L_F{}'$ for PR and CP, can be thus written as follows:

$$\begin{aligned} \left(P_F{}'\right)_{rq}^{ji} &= \left(P_F\right)_{rq}^{ji} - \rho_{rq}^{ji} = \left(\gamma^{-2}\right)^{F-1} I_{rq}^{ji} + \left(\sigma_F\right)_{rq}^{ji} \\ \left(L_F{}'\right)_{rq}^{ji} &= \left(L_F\right)_{rq}^{ji} - \rho_{rq}^{ji} - \lambda_F \left(n_F\right)_{rq}^{ji} = \left(\gamma^{-2}\right)^{F-1} I_{rq}^{ji} + \left(\varepsilon_F\right)_{rq}^{ji} \end{aligned} \tag{7.17}$$

The measured DD delays vector $\tilde{\mathbf{x}} = \begin{bmatrix} \tilde{I}_{rq}^{12} & \cdots & \tilde{I}_{rq}^{1n} \end{bmatrix}^T$ and its covariance matrix are computed applying the Weighted Least Square (WLS) technique to the linear system obtained rearranging equation (7.17) as follows:

$$\begin{gathered} \begin{bmatrix} \mathbf{P}_1 \\ \mathbf{P}_2 \\ \mathbf{L}_1 \\ \mathbf{L}_2 \end{bmatrix} = \begin{pmatrix} \mathbf{I} & \gamma^{-2}\mathbf{I} & -\mathbf{I} & -\gamma^{-2}\mathbf{I} \end{pmatrix} \begin{bmatrix} I_{rq}^{12} \\ \vdots \\ I_{rq}^{1n} \end{bmatrix} \\ \mathbf{P}_f = \begin{bmatrix} \left(P_f{}'\right)_{rq}^{12} & \cdots & \left(P_f{}'\right)_{rq}^{1n} \end{bmatrix}^T ;\ \mathbf{L}_f = \begin{bmatrix} \left(L_f{}'\right)_{rq}^{12} & \cdots & \left(L_f{}'\right)_{rq}^{1n} \end{bmatrix}^T \end{gathered} \tag{7.18}$$

where n is the number of common in view SVs.

7.2.2 Assessment of VTEC Coefficients and Ionospheric Delay estimation

The starting point for the estimation of *VTEC* coefficients is the definition of the point C that identifies the center of the bilinear *VTEC* function of (7.5). In the UD case, the point C is located at the thin shell along the receiver's vertical as shown in Figure 7.2. For the DD case, as illustrated in Figure 7.4, the same point C, located along the vertical direction above one of the receiver r, is used for all the satellites in common view. As a consequence, in DD case, all the latitude and longitude differences are computed with respect to the same point.

Estimation of the *VTEC* coefficients in the UD case exploits a WLS algorithm applied to the system described by (7.10), in which the left-hand side includes the PR measurements, which are assumed to have an identity covariance matrix. The calculated *VTEC* coefficients can be then used to model *VTEC* variations as a function of latitude and longitude differences with respect to the current location of the C point. The same approach can then be applied to derive a different estimate of the *VTEC* coefficients by fitting CP data. Based on these two sets of coefficients, two different UD predicted ionospheric delays can be estimated at any time instant using PR and CP measurements, respectively. The predicted delays are estimated using (7.1), (7.3), and (7.5), for any couple of receiver and GPS satellite. Concerning this, it is very important to point out that, from a theoretical point of view, the measured UD ionospheric delays estimated using PR observables should be the same as those estimated from CP observables, but differences arise, in practice, depending on different noise and bias characteristics of PR and CP data.

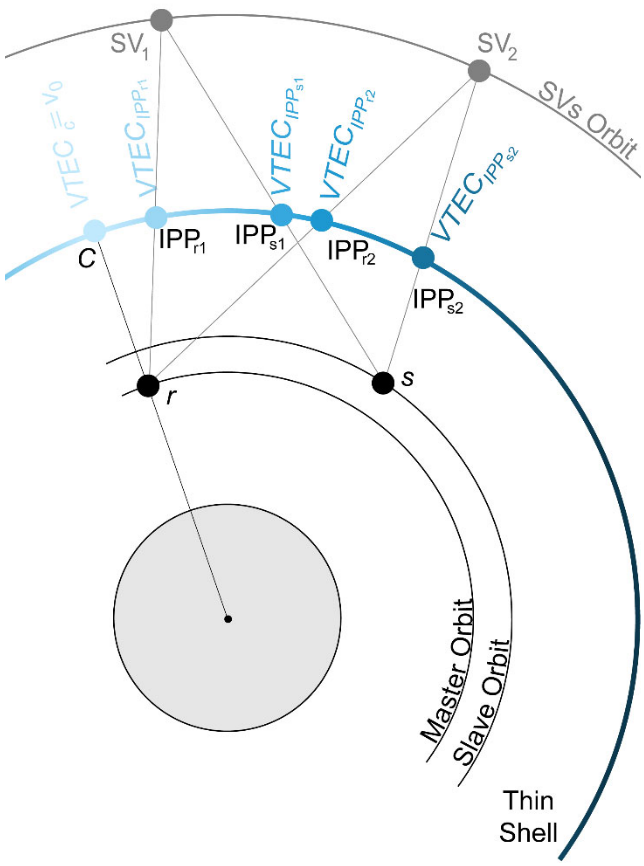

Figure 7.4 DD formation and IPPs definition (two-dimensional, not to scale illustration, for clarity). IPP_{ri} is the IPP along the ray-path between the receiver *r* and SV *i*.

The estimation of DD predicted delays involves computation of the *VTEC* coefficients for the DD case, starting from the measured DD ionospheric delay stacked in the vector $\tilde{\mathbf{x}}$. This is performed by a WLS algorithm applied to the following system:

$$\tilde{\mathbf{x}} = \mathbf{A}\begin{bmatrix} v_0^{DD} \\ v_1^{DD} \\ v_2^{DD} \end{bmatrix} = \begin{bmatrix} \mathbf{A}_{1,1} & \mathbf{A}_{1,2} & \mathbf{A}_{1,3} \\ \vdots & \vdots & \vdots \\ \mathbf{A}_{n-1,1} & \mathbf{A}_{n-1,2} & \mathbf{A}_{n-1,3} \end{bmatrix}\begin{bmatrix} v_0^{DD} \\ v_1^{DD} \\ v_2^{DD} \end{bmatrix} \tag{7.19}$$

where

$$\left(\mathbf{A_a}\right)_{i,1} = \frac{40.3}{f_1^2}\left(\left(M_{TS}\right)_q^i - \left(M_{TS}\right)_r^i - \left(\left(M_{TS}\right)_q^1 - \left(M_{TS}\right)_r^1\right)\right)$$
$$\left(\mathbf{A_a}\right)_{i,2} = \frac{40.3}{f_1^2}\left(\left(M_{TS}\Delta\phi_{IPP}\right)_q^i - \left(M_{TS}\Delta\phi_{IPP}\right)_r^i - \left(\left(M_{TS}\Delta\phi_{IPP}\right)_q^1 - \left(M_{TS}\Delta\phi_{IPP}\right)_r^1\right)\right) \quad (7.20)$$
$$\left(\mathbf{A_a}\right)_{i,3} = \frac{40.3}{f_1^2}\left(\left(M_{TS}\Delta l_{IPP}\right)_q^i - \left(M_{TS}\Delta l_{IPP}\right)_r^i - \left(\left(M_{TS}\Delta l_{IPP}\right)_q^1 - \left(M_{TS}\Delta l_{IPP}\right)_r^1\right)\right)$$

and i ranges from 1 to $n-1$ indicating the couple defined by pivot satellite, j, and the i-th other in view satellite ($i \neq j$). $\mathbf{A_a}$ is a $(n-1)\times 3$ matrix and the WLS algorithm can be applied when $(n-1) \geq 3$. Once the DD *VTEC* coefficients have been estimated, the predicted DD ionospheric delay can be obtained by rearranging (7.1), (7.3) and (7.5), yielding:

$$\begin{aligned}\hat{I}_{rs}^{ji} = \frac{40.3}{f_1^2}\Big(&\left(M_{TS}\right)_q^i\left(\tilde{v}_0^{DD} + \tilde{v}_1^{DD}\left(\Delta\phi_{IPP}\right)_q^i + \tilde{v}_2^{DD}\left(\Delta l_{IPP}\right)_q^i\right)\\ &-\left(M_{TS}\right)_r^i\left(\tilde{v}_0^{DD} + \tilde{v}_1^{DD}\left(\Delta\phi_{IPP}\right)_r^i + \tilde{v}_2^{DD}\left(\Delta l_{IPP}\right)_r^i\right)\\ &-\left(M_{TS}\right)_q^j\left(\tilde{v}_0^{DD} + \tilde{v}_1^{DD}\left(\Delta\phi_{IPP}\right)_q^j + \tilde{v}_2^{DD}\left(\Delta l_{IPP}\right)_q^j\right)\\ &+\left(M_{TS}\right)_r^j\left(\tilde{v}_0^{DD} + \tilde{v}_1^{DD}\left(\Delta\phi_{IPP}\right)_r^j + \tilde{v}_2^{DD}\left(\Delta l_{IPP}\right)_r^j\right)\Big)\end{aligned} \quad (7.21)$$

The estimation of *VTEC* coefficients requires the number of UD, both PR and CP, or DD observations to be at least equal to three. When UD measurements, PR or CP, are used the three *VTEC* coefficients can be estimated almost at any time epoch. Indeed, the number of available measurements that correspond to the number of available satellites, n_r, is usually greater than three. Contrarily, in the DD case the number of observables is the number of SVs in common in view by the two satellites minus one and will always be lower than n_r, thus resulting in a noisier estimate of DD *VTEC* coefficients.

7.3 REAL-TIME RELATIVE POSITIONING OVER LARGE BASELINES USING LTS MODEL

The relative positioning problem over large-baseline has been tackled in previous studies exploiting dual frequency measurements [20, 179–181]. Following this method, the work reported in this chapter uses a two-steps approach to estimate the baseline.

- The first step consists in a Carrier Phase Differential GPS (CDGPS)-based EKF that uses dual frequency Carrier Phase and Pseudo-range Double

Difference (DD) Measurements in order to estimate DD Integer Ambiguities (IA).

- In the second step, the IA are then used to estimate with high precision the baseline with a kinematic filter.

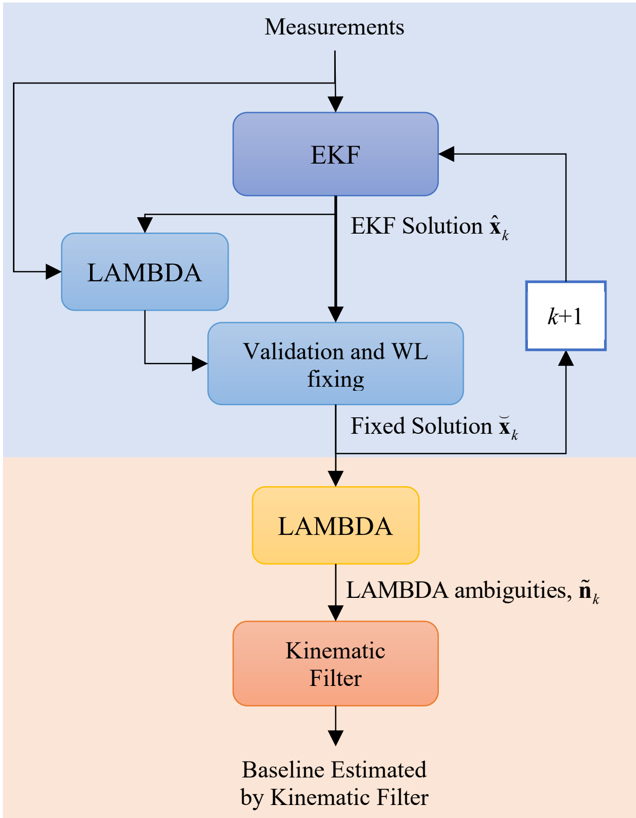

Figure 7.5 Flowchart for relative positioning estimation of two spacecrafts in LEO orbit.

The proposed filter, which flow chart is depicted in Figure 7.5 is inspired to [20]. However, with respect to [20], in the filter presented in this section uses the LTS as ionospheric model, which is capable of capturing local ionosphere gradients, so to improve filters performance in inter ambiguities fixing, thus improving also the relative positioning accuracy.

The filter state vector $\mathbf{x}$ is composed by the 3×1 baseline, $\mathbf{b}$, and its corresponding time derivative, $\dot{\mathbf{b}}$, the three VTEC coefficients, v_0, v_1 and v_2, and the $(n-1)\times 1$ vectors that includes the Wide Lane and L1 integer ambiguities, $\mathbf{n}_w$ and $\mathbf{n}_1$, respectively. n is the number of common in view SVs by the chief and deputy satellite.

$$\mathbf{x} \in \mathbb{R}^{(9+2(q-1))\times 1};\ \mathbf{x} = \begin{pmatrix} \mathbf{b} & \dot{\mathbf{b}} & v_0 & v_1 & v_2 & \mathbf{n}_w & \mathbf{n}_1 \end{pmatrix}^T \tag{7.22}$$

It is worth noting that modeling the horizontal gradients involves the size of the state vector to be increased by one component with respect to the same filter using a Lear's model.

The baseline propagation is provided by a nonlinear Keplerian relative orbital motion model, including the effect of the second zonal harmonic of the gravity field (J_2), the ambiguities are modeled as a random walk process and the VTEC coefficients are modeled as a Gauss Markov process with correlation time τ:

$$\dot{v}_m = -\frac{1}{\tau_m} v_m + W_m \tag{7.23}$$

where m = 1,2,3 and W_m is a white noise (WN) with standard deviation $\sigma_{W,m}$ and zero mean. This white noise is associated to the Gauss-Markov process that models the v_m correlation coefficient.

The filter correction step is performed exploiting DD measurements. The EKF is combined with a Least Square Ambiguity Decorrelation Adjustment (LAMBDA) [162] estimator that extracts integer numbers from the float estimates of $\mathbf{n}_W$ and $\mathbf{n}_1$. A validation technique is then used to validate and fix the Wide Lane integer ambiguities estimated by LAMBDA. The validation technique consist of the same Melbourne-Wubbena (MW) and WL tests described in [20]. Once an ambiguity is validated, it will remain fixed until a cycle slip occurs, or the satellite disappears. The fixed ambiguities are used at the current epoch to correct the real valued EKF solution (yielding the fixed solution) that is fed-back to improve the solution at the following time epochs.

Table 7.1 Overview of models used in the filter

			Baseline	**Non linear keplerian relative orbital motion with J_2**
Models	**EKF**	**Propagation**	*chief satellite positioning*	GPS position fix
			VTEC coeffs	Gauss Markow Process
			ambiguities	Random walk
		Correction	*Ionospheric delays*	LTS model
			Correction Equations	DD measurements equations
	Ambiguities Estimation and Validation	Estimation	LAMBDA algorithm	
		Validation	Melbourne-Wubbena Test	
	Kinematic Filter	Baseline is obtained with a WLS algorithm applied on the Ionofree measurements corrected by the ambiguities estimated by the secondary LAMBDA. Three or more L_{IF} are needed to estimate the baseline		

Moreover, the fixed solution is used in an additional LAMBDA in order to get the L1 integer ambiguities. These ambiguities are then used in the kinematic filter, as in [20], when the number of L1 ambiguities estimated by the additional LAMBDA is greater than three. The kinematic filter uses the WL and L1 ambiguities estimated by a secondary LAMBDA to correct Iono-free mesurements. Kinematic baseline is estimated from corrected Iono-free measurements (L_{IF}) applying a weighted least square (WLS) algorithm. When the kinematic solution is not available, the baseline estimate is provided by the EKF only. A summary of the models used in the filter, which are described in Figure 7.5, is reported in Table 7.1.

7.4 RESULTS

The effectiveness of the proposed LTS model for ionospheric delay estimation is investigated using real-world GPS data of GRACE mission. Specifically, Level 1B (L1B) GPS data, available from ftp://podaac.jpl.nasa.gov/allData/grace/L1B and sampled at a 0.1 Hz refresh rate, have been processed. A mask angle is applied to L1B GPS data to discard measurements from SVs with an elevation lower than 15 degrees. GRACE mission consists of two satellites, namely GRACE A and GRACE B, flying in an almost polar orbit, about 450 kilometers above the earth, with a nominal separation of about 220 kilometers (Tapley et al. 2004). GRACE Navigation data (GNV) are also used, providing the absolute location of GRACE satellites with centimeter-scale precision. The current section compares the performance of LTS model in predicting atmospheric delays in 7.4.1. Hence, the results of the filter described in section 7.3 and used for baseline estimation are reported in section 7.4.2.

7.4.1 Performance of LTS model

Data selected to assess the performance of the proposed ionospheric model refers to nine days of October 12-20, 2011. This period has been selected as an example of significant solar activity [194]. Measured and predicted ionospheric delays are also computed for Lear model using the approach presented in [218].

With specific reference to the selection of the thin shell height, and as discussed above, the thin shell height is selected as that for which the thin shell mapping function fits the Lear one. Concerning this, [204] verified that selecting a thin shell altitude equal to 550 km for a receiver altitude of 450 km, i.e. 100 km above the receiver altitude, yields a mapping function that fits the Lear one for SV elevation higher than

10 deg. The result is herein generalized. Specifically, according to Figure 7.6, for a receiver altitude ranging from 200 to 750 km the thin shell mapping function fits Lear one if the altitude of the layer is selected 100 km above the receiver, i.e. $\Delta h = h_{TS} - h_r = 100\ km$. Based on the selected thin shell height, Figure 7.7-Figure 7.9 illustrate the RMS (Root Mean Square error) of the residuals, i.e., measured minus predicted ionospheric delays, for the Lear and LTS models over the first stack of processed GRACE data. Percentage values show a performance improvement of the LTS model with respect to Lear model. The LTS model outperforms the Lear one over the entire period for both UD and DD. The improvement with respect to Lear model ranges from 40% to 50% for UD delays and from 20% to 30% for DD delays.

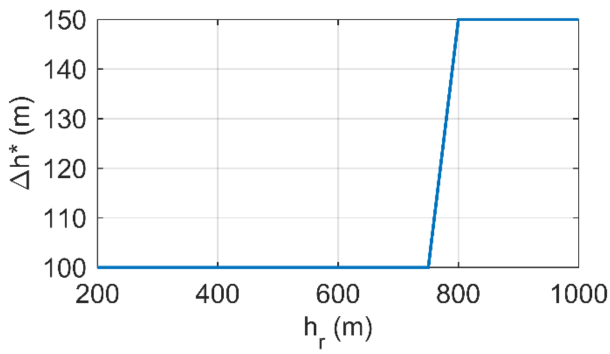

Figure 7.6 Altitude of the thin shell to fit the Lear's mapping function with respect to the altitude of the receiver. Δh^* is the difference of receiver and shell altitude for which the thin shell mapping function matches the Lear's one.

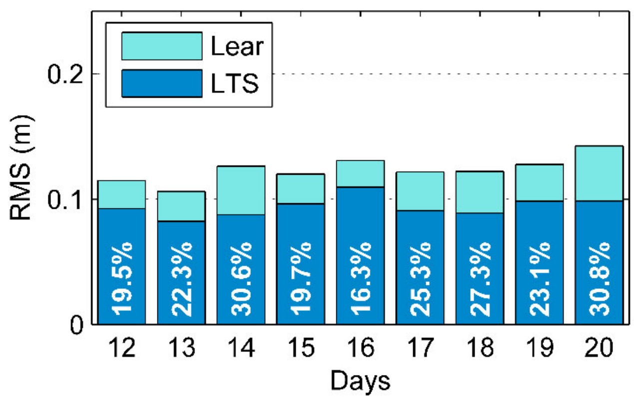

Figure 7.7 Daily RMS of DD ionospheric delays from October 12 - 20, 2011.

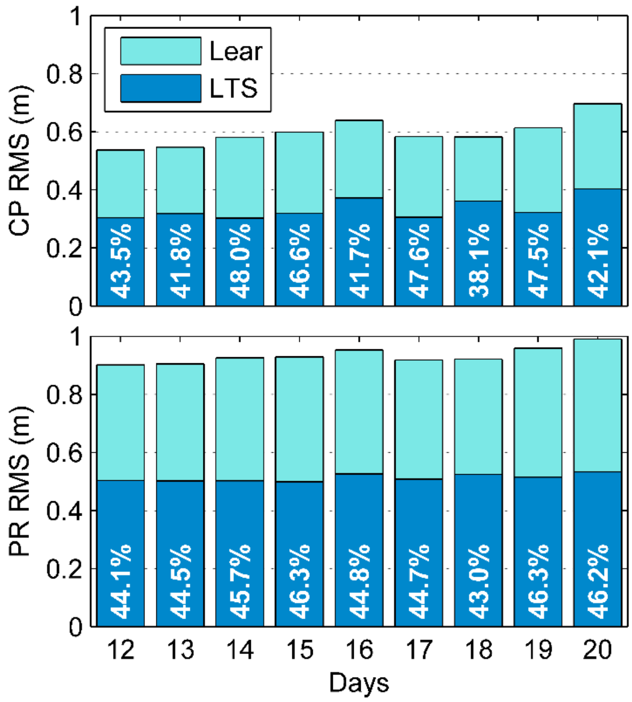

Figure 7.8 Daily RMS of UD ionospheric delay residuals for GRACE A, from October 12 - 20, 2011.

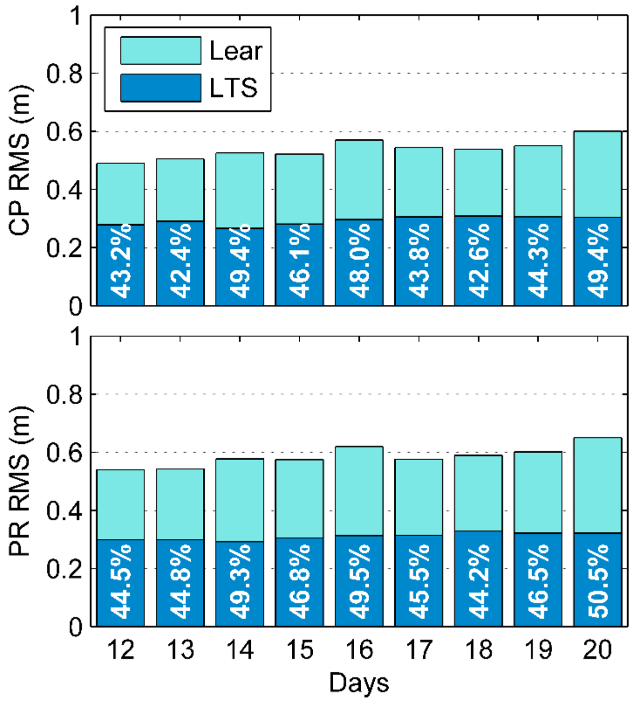

Figure 7.9 Daily RMS of UD ionospheric delay residuals for GRACE B, from October 12 - 20, 2011.

The role of shell height is analyzed in Figure 7.10 and Figure 7.11, where RMS variations of the residuals as a function of altitude differences between the receiver and thin shell are presented for both DD and UD cases. Specifically, the RMS variation, ΔRMS, is normalized with respect to its minimum, i.e. $\Delta RMS = \left(RMS - RMS_{\min}\right)/RMS_{\min}$. The presented results cover a larger time span of GRACE data, i.e., from 2005 to 2011, characterized by altitudes of the receivers ranging from 470 to 450 km. Even if variations of RMS are limited to a few percentage points, it is clear that in the DD case (Figure 7.10), the minimum RMS occurs for Δh = 100 km. This means that the best performance of LTS with respect to the estimation DD ionospheric delays is obtained selecting this shell altitude for which the mapping function fits the Lear one.

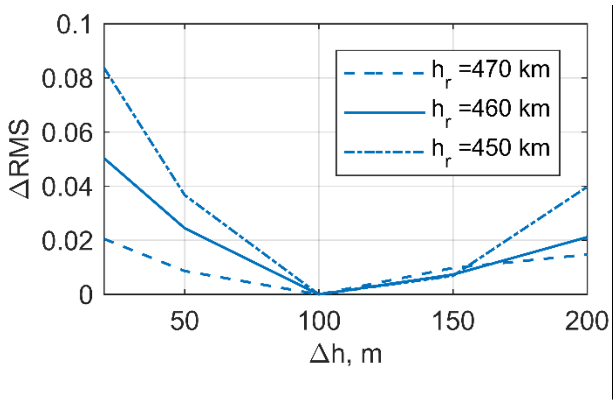

Figure 7.10 RMS variation as a function of Δh and h_r for DD delays.

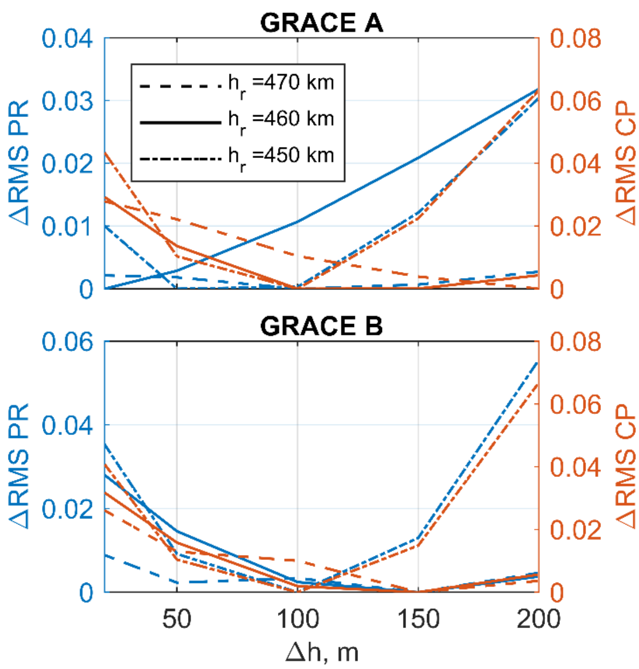

Figure 7.11 RMS variation as a function of Δh and h_r for UD delays.

Concerning model performance in different ionospheric conditions, a comparison between the LTS and Lear models is shown in Figure 7.12 as a function of the daily Solar Spot Number (SSN) for the DD measurements, for UD case results are similar. Indeed, it is well known that the SSN is directly related to the level of ionosphere activity. From the figure, it is possible to conclude that for low SSN values the two models attain similar performance. The LTS model, instead, exhibits better performance with increasing SSN, thanks to the capability to reproduce horizontal *VTEC* gradients, which are expected to be much more significant for intense ionospheric activity. The values of daily SSN, reported in Figure 7.12, refer to a very long time span, from 2005 to 2011, capturing both minima and maxima of solar activity. This means that the RMS values of Figure 7.12 represent the performance of LTS and Lear models over data set representative of almost all possible ionospheric conditions. The plot indeed includes daily RMS from the lowest ionosphere intensity condition, i.e., days from 2009, to the highest achievable intensity, i.e., 2011. In this regard, it is worth noting that even if the maximum of the solar activity is located in 2014, the corresponding SSN is comparable to the values reached in October 2011.

7.4.1.1 Daily Results

A single day within the considered period has been selected to highlight peculiarities of the LTS model. Results shown in this section refers to October 14, 2011. Specifically, Figure 7.13 and Figure 7.14 show the correlation indices between estimated and measured ionospheric delays using GRACE-B data: UD pseudorange and DD, respectively, for the LTS and Lear models. Corresponding RMS values are indicated in the plots, as well.

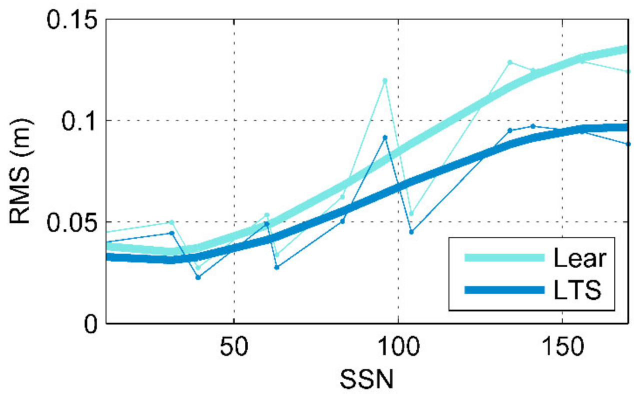

Figure 7.12 Daily RMS of DD ionospheric delay residuals vs SSN. Dots represent daily values whereas bold lines represent data regression.

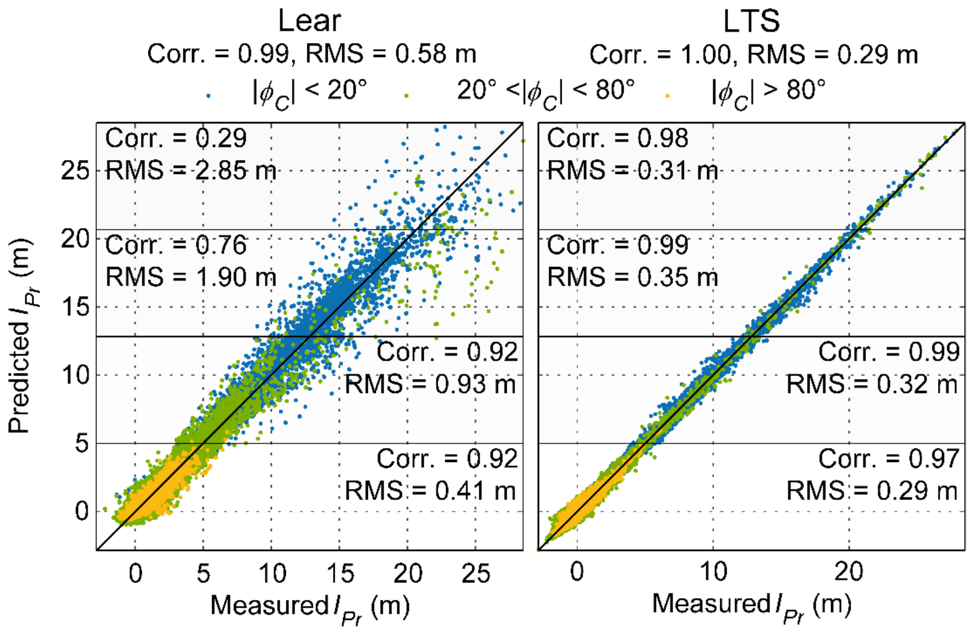

Figure 7.13 PR UD ionospheric delay correlation plot for GRACE-B.

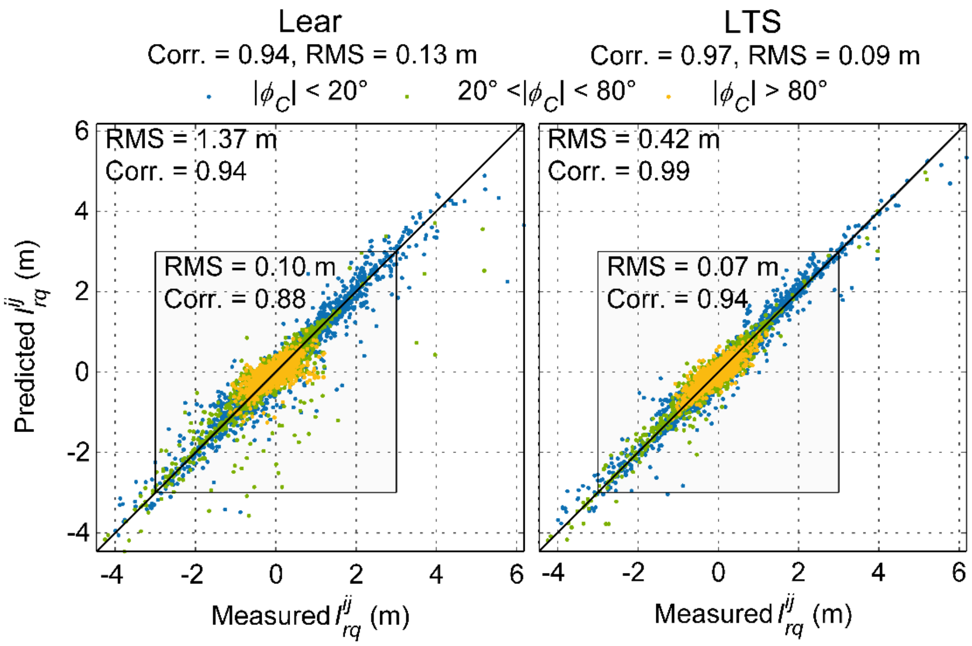

Figure 7.14 DD ionospheric delays correlation plot.

Focusing on the PR UD case, see Figure 7.13, it is possible to see that the LTS model exhibits a more uniform performance over the investigated ionospheric delay range, both in terms of correlation coefficient and RMS values. More importantly, for the LTS model the RMS is much lower than for the Lear model, being half if computed over the entire ionospheric delay range and up to one third within specific intervals. Figure 7.13 and Figure 7.14 highlight that when the central point of *VTEC* distribution is around the equator, represented by blue dots, the ionospheric delays are greater than at poles, i.e., yellow dots. In addition, Figure 7.13 underlines that the Lear model error in estimating ionospheric delays increases with delay values. This behaviour is not observed in the LTS case, where a higher correlation between measured and predicted delays is achieved over the entire ionospheric delays range.

It is worth noting that even if the LTS model suffers from longitude gradient ambiguities near the poles, this does not affect the model performance that is uniform with latitude. This uniformity is the main achievement of the LTS model over the Lear one. As far as the DD delays are concerned, the RMS improvement, even if smaller than in the UD case, is still significant, being up to 30% for DD ionospheric delays shorter than 3 m and up to 50% for DD delays longer than 3 m. It is worth noting that less than 10 cm of RMS is achieved for DD delays shorter than 3 m, which represent more than 99% of the samples in Figure 7.14.

In addition to daily correlation plots, it is useful to show the inter-frequency bias distribution. In this regard, Figure 7.15 shows GRACE-B inter-frequency bias histogram for all the GPS satellites in view over the 24-hour period. As discussed above, the inter-frequency bias estimated with the LTS model has a non-Gaussian distribution; hence, the mode of the distribution, i.e., the vertical line, can be adopted as an estimate of the daily value.

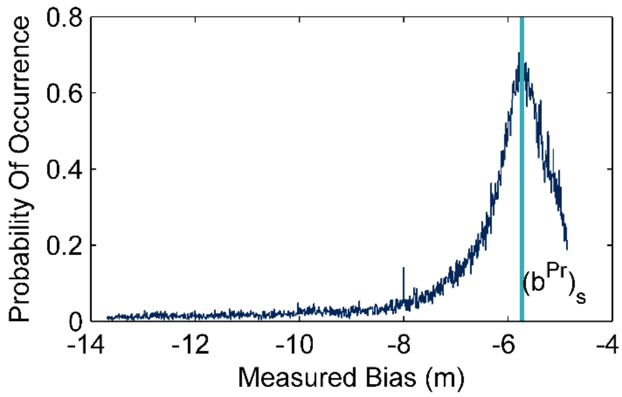

Figure 7.15 Estimated receiver inter-frequency bias for GRACE-B.

Figure 7.16 (a-c) and Figure 7.17 (a-c) allow understanding the effect of the various coefficients of the bilinear *VTEC* model on the LTS performance for the UD and DD case, respectively, in terms of correlation index and RMS values. Concerning this, it is important to recall that v_1 and v_2 represent latitude and longitude coefficients, respectively, so, for instance, setting $v_1 = 0$ represents the case of un-modeled *VTEC* latitude variations around the point *C* that is equivalent to use the thin shell model. In the same figures, the full bilinear *VTEC* model results are reported for reader convenience in panels (d). With reference to Figure 7.16, it is evident that latitude gradients are more important than longitude ones. Specifically, similar performance is achieved when a single coefficient is used, see Figure 7.16.a representing no horizontal gradients of *VTEC*. When longitude-only gradients are taken into account, see Figure 7.16.b. On the contrary, performance is improved notably in Figure 7.16.c when latitude-only gradients are considered with 20% RMS reduction with respect to the case of no horizontal gradients. Similar conclusions can be drawn from the DD case in Figure 7.17. However, in both cases, the best performance is achieved when the complete bilinear model is used, see Figure 7.16.d and Figure 7.17.d.

Based on Figure 7.16 and Figure 7.17 additional considerations can be observed on the LTS and Lear models. Indeed, although the two models are theoretically different, the Lear model is derived from the thick shell assumption whereas the LTS model relies on the thin shell assumption when both models use the same number of coefficients a similar performance is achieved. In the UD case, this can be observed comparing Figure 7.16.d with Figure 7.16.a, obtained setting to zero the latitude and longitude coefficients of the bilinear model. In this case, both models adopt only one parameter, since the Lear model involves the estimation of the *VTEC* only, assumed uniform in the shell. This result is confirmed by the analysis of the DD case. When differential ionospheric delays have to be represented, two different *VTEC*s are used by the Lear model [20, 21, 218], one for each receiver.

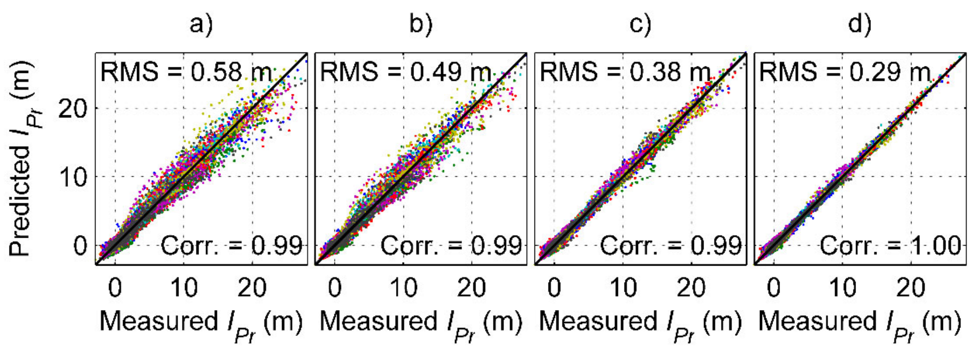

Figure 7.16 PR UD ionospheric delay correlation plot for GRACE-B with reduced forms of the *VTEC* model: a) $v_0 \neq 0, v_1 = v_2 = 0$; b) $v_0 \neq v_2 \neq 0, v_1 = 0$; c) $v_0 \neq v_1 \neq 0, v_2 = 0$; d) $v_0 \neq v_1 \neq v_2 \neq 0$.

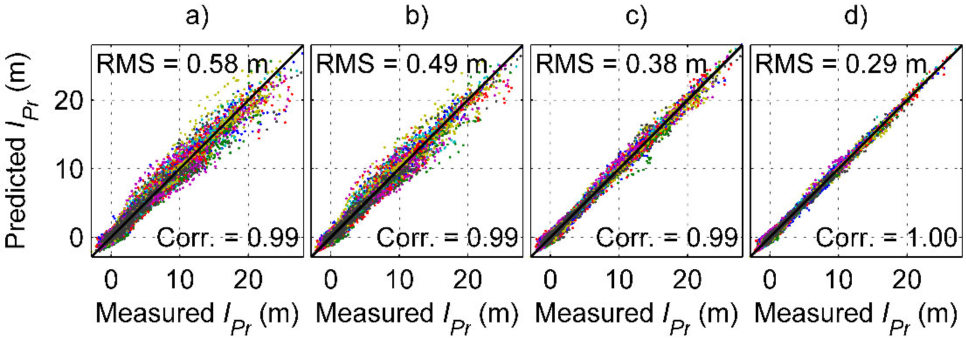

Figure 7.17 DD ionospheric delays correlation plot with reduced forms of the *VTEC* model: a) $v_0 \neq 0, v_1 = v_2 = 0$; b) $v_0 \neq v_2 \neq 0, v_1 = 0$; c) $v_0 \neq v_1 \neq 0, v_2 = 0$; d) $v_0 \neq v_1 \neq v_2 \neq 0$.

Thus, results in Figure 7.17.d are similar, although slightly worse, to the ones in Figure 7.17.c, obtained with a LTS model based only on two coefficients. In conclusion, the results suggest that the cost to pay to improve the ionospheric delay estimation accuracy with the LTS model is the estimation of an additional coefficient with respect to the Lear model.

7.4.2 Filter Results

Filter performance have been evaluated considering both low and severe ionosphere activity conditions. The day selected to show filter performances in low ionospheric condition is January 14th, 2009.

The filter is able to estimate the integer ambiguities under low ionosphere with a percentage of success (P_s) higher than 90%, both for L1 and WL ambiguities, as shown in Figure 7.18. The ambiguity estimated by the second LAMBDA step are compared with the measured ambiguities (estimated from GNV and GPS L1B data) [20, 218]. If the estimated ambiguities are fixed and correct, i.e. equal to the measured one, they succeed the test. The wrong ambiguities concur to define the failure rate (P_f). Ambiguities that are not fixed or do not have the reference counterpart are included in the unknown set. Note that both L1 and WL P_s are required to be greater than 80% to make the EKF estimate reliable [178].

The Kinematic filter exploits the integer ambiguities to improve the EKF's baseline precision and thus requires a higher percentage of success for a reliable solution. The high success rate resulting from the application to GRACE flight data (WL P_s = 95.7%, L1 P_s = 91.2%) allows the EKF to estimate the baseline with high precision, achieving a max baseline norm error $\Delta|\mathbf{b}|$ = 38.1 cm and an RMS of 4.2 cm.

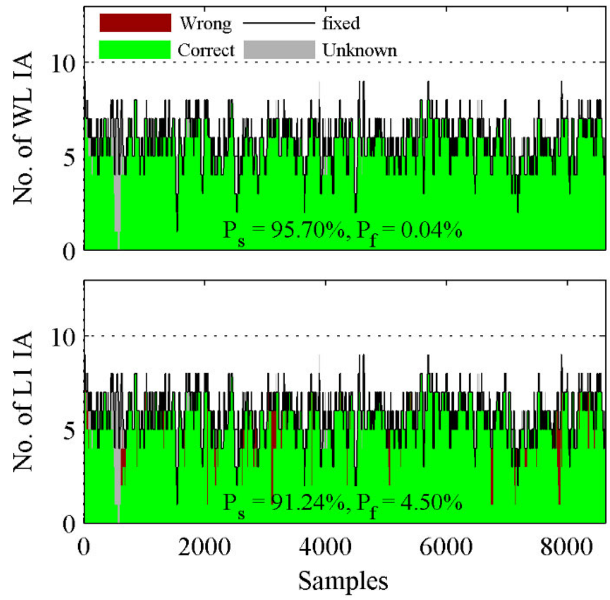

Figure 7.18 L1 and WL daily ambiguities tests for January 14th, 2009

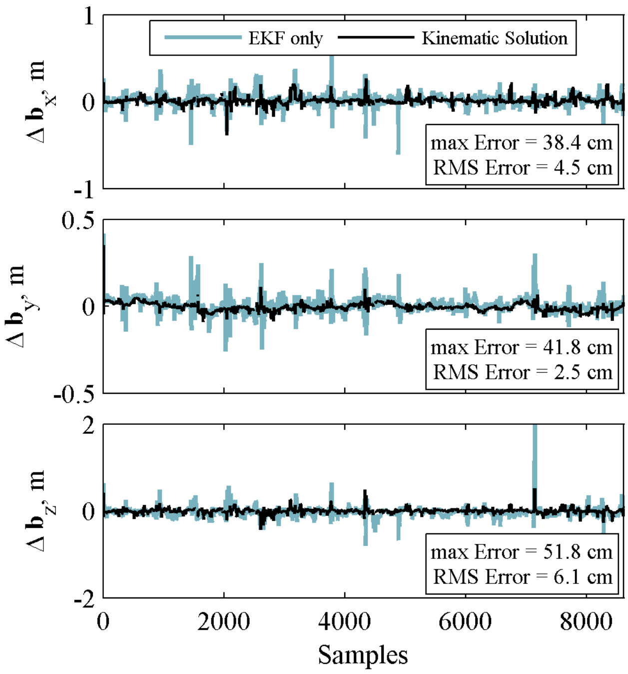

Figure 7.19 ECEF components of the Baseline's Error for January 14th, 2009

Figure 7.19 depicts the baseline's error in the three components of the Earth Centered Earth Fixed (ECEF) frame. Both EKF and Kinematic solutions are shown. The errors are estimated with reference to GNV data. Maximum and RMS errors are estimated using the EKF results only when the kinematic solution is not available. The effectiveness of the kinematic filter is quite evident: the maximum error in the radial component is 51.8 cm, even though the EKF maximum error is about two meters (see Figure 7.19).

Figure 7.20 shows the Ionospheric delays correlation plot, obtained comparing the DD delays estimated by the filter with the measured ones, i.e. estimated from GPS and GNV L1B data as described in [218]. The figure highlights the 90th and 99th percentile samples, to point out that most of the data show very high degree of correlation. The maximum error in Ionospheric delay estimated by the filter is 62.6 cm with 5.4 cm of RMS error.

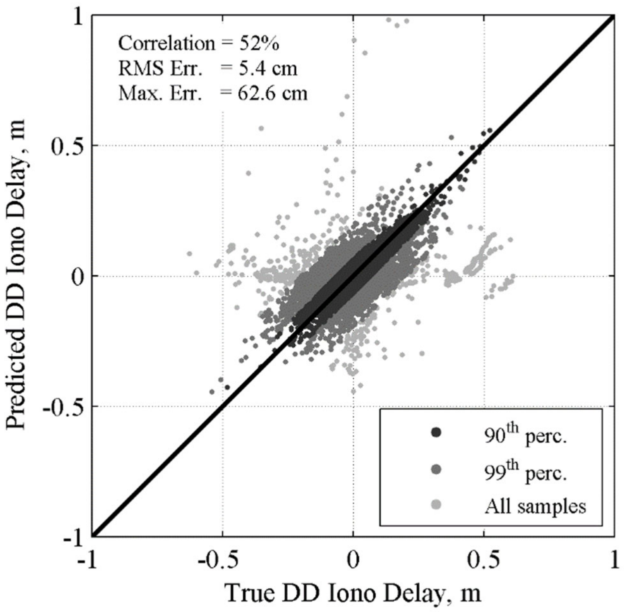

Figure 7.20 Correlation plot of ionospheric delays predicted by the filter for January 14th, 2009.

To investigate the effect of increasing ionosphere activity level, daily results for January 14th, 2009 are compared with those for October 22nd, 2011, that was characterized by a very high ionospheric intensity [194]. Results are shown in Table 7.2. It can be observed that the filter performance degrades in presence of intense ionosphere activity. Overall, performance is degraded by a factor ranging from 4 to 6.

The performance degradation is strictly related to the reduction of the percentage of success in L1 ambiguity fixing. Indeed, only 58.4% of L1 ambiguity are correctly fixed, in spite of the high percentage of WL ambiguities. This spoils the EKF estimation and the Kinematic correction effectiveness.

Table 7.2 Comparison of filter's results in Low and High ionospheric conditions

Parameters	***Low Ionosphere Intensity January 14th 2009***	***High Ionospheric Intensity October 22nd 2011***
max $\Delta\mathbf{b}_x$, *cm*	38.4	196.2
$\Delta\mathbf{b}_x$ RMS, *cm*	4.5	26.4
max $\Delta\mathbf{b}_y$, *cm*	41.8	176.4
$\Delta\mathbf{b}_y$ RMS, *cm*	2.5	12.7
max $\Delta\mathbf{b}_z$, *cm*	51.8	297.2
$\Delta\mathbf{b}_z$ RMS, *cm*	6.1	37.2
max $\Delta\|\mathbf{b}\|$, *cm*	38.1	194.4
$\Delta\|\mathbf{b}\|$ RMS, *cm*	4.2	26.8
WL P_s	95.70%	88.92%
WL P_f	0.04%	1.14%
L1 P_s	91.24%	58.35%
L1 P_f	4.50%	31.72%

However, notwithstanding the performance degradation in intense ionosphere conditions, the adopted filter allows improving positioning performance if compared to the same filtering approach using an isotropic model, i.e. Lear model, to predict ionospheric delays, as in [20]. A preliminary comparison is illustrated in Figure 7.21. The gain in the baseline modulus and maximum error is higher than 50% with respect to the isotropic model. Concerning ambiguity fixing, using the LTS model helps improving the L1 percentage of success much more that the WL one.

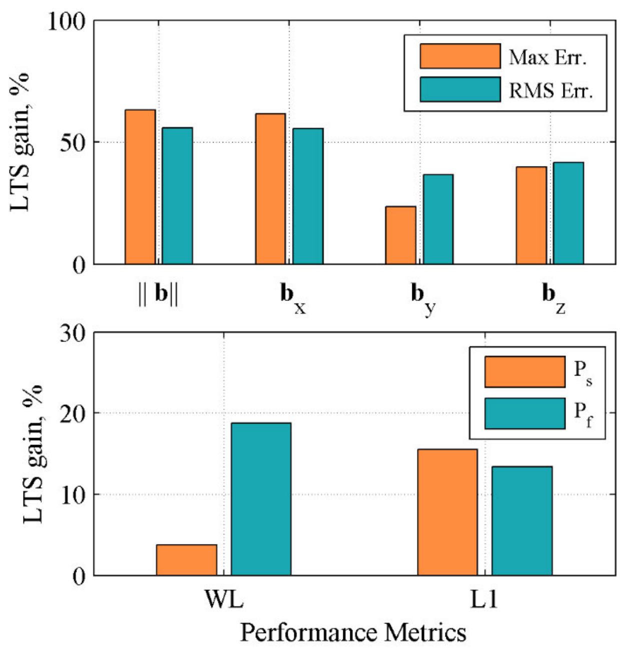

Figure 7.21 Performance improvement of LTS with respect to Lear model for October 22nd, 2011.

This result confirms that the observability of WL ambiguities is not affected by ionosphere conditions and modelling, whereas the accuracy of the adopted ionospheric model can improve both success and fail rate of L1 ambiguities, notably.

Figure 7.22 and Figure 7.23 depict the Ionospheric delays predicted by the filter in intense Ionospheric condition in the case the Lear's and LTS models are used, respectively. These delays are compared with the measured by correlation plots. Modelling the Ionospheric horizontal gradients yields an effective improvement in the filter's Ionospheric delays prediction, characterized by an increase of correlation coefficient and a reduction of the RMS error. The maximum error in Ionospheric delays estimation remains still large also with the LTS model, since the high ionospheric intensity affects the ionospheric delays prediction. A more precise estimation of Ionospheric delays reduces the error in Integer ambiguity estimation, improving the fixing success rate in particular for L1 ambiguities, see Table 7.2. The cost to pay for an accurate modelling of the atmosphere in the filter, resulting in better filter performance is only to add a component to the state vector, which has a very slight impact on the computational burden, suggesting that the scheme with LTS can be used in real time, too.

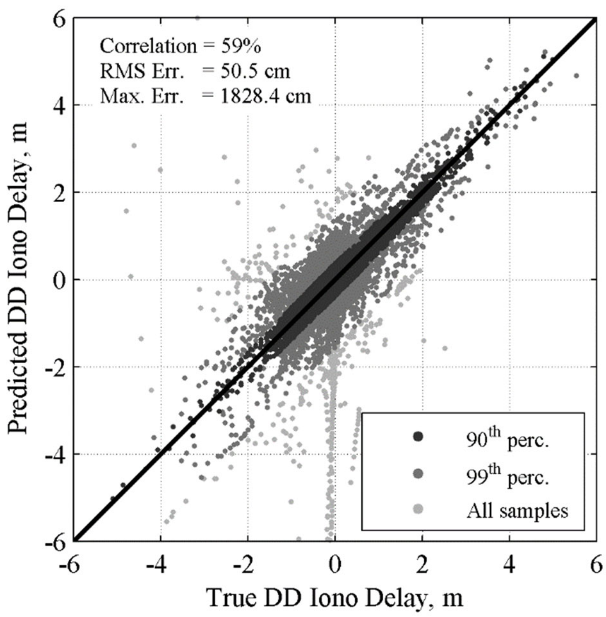

Figure 7.22 Correlation plot of ionospheric delay predicted by the filter for October 22nd, 2011 using Lear's model.

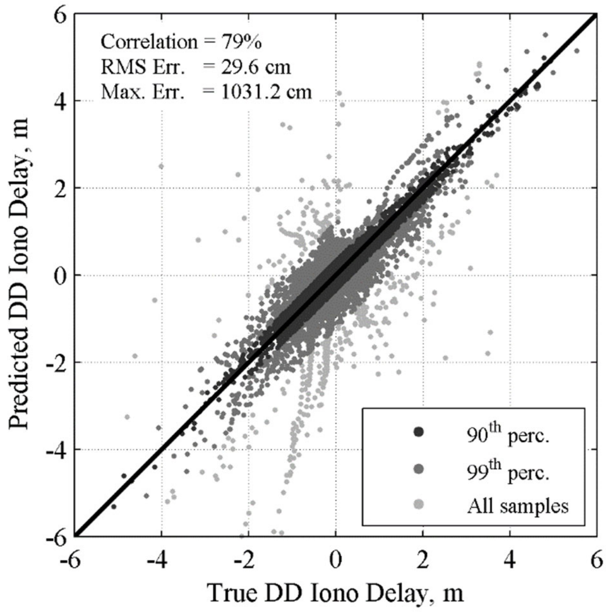

Figure 7.23 Correlation plot of ionospheric delay predicted by the filter for October 22nd, 2011 using LTS model.

Chapter 8: Conclusions

This thesis discussed navigation techniques for distributed cooperative spacecraft and UAV. Cooperation among UAV was used to overcome the limitation of the single vehicle configuration and improve navigation performance both under nominal and non-nominal GNSS coverage. To this aim planning and guidance technique were developed for a UAV formation to guarantee satisfactory navigation performance in GNSS challenging scenarios. As far as, the spacecraft are concerned an improved technique for estimating ionosphere delay has been developed to enhance the performance in baseline estimation between the platform using double difference carrier phase GNSS measurements.

Navigation in GNSS challenging scenario, has been ensured by supporting the flight of the vehicle in the challenging area, deemed son, with one or more cooperative vehicle, i.e. father(s). Fathers, always under nominal GNSS coverage, share their absolute position that is known with very high accuracy. Due to the dependence of the cooperative navigation performance to the position of the father, this thesis introduced the geDOP concept to predict son positioning accuracy. Generalized DOP does not take only geometrical aspects into account, but also includes performance parameters relevant to father navigation and relative sensing. Both numerical and experimental analyses confirmed the potential of the concept: for a given set of aiding measurements, optimizing father placement makes positioning observable and can significantly improve the achieved accuracy. As expected, optimal formation geometries in the case of cooperative range or angular aiding are complementary. In general, the three-dimensional mission scenario and the consequent geometry of available GNSS pseudoranges have a strong impact on generalized DOP dependencies. Thus, a coarse knowledge of the mission scenario is important to optimize formation flight to the aim of cooperative navigation.

Based on the geDOP concept, this thesis introduced a planning technique for a tandem cooperative formation. The trajectory of a single father has been designed to improve the navigation performance of the son. The path of the son is based on the mission it has to accomplish, whereas the father trajectory is responsible for maximizing the accuracy in son positioning estimation. Two strategy have been proposed for offline and online implementation. The online trajectory planning allows the planned trajectory for the father to adapt to the son motion, and is complemented with a guidance strategy that prevents from loss of line of sight between cooperating UAVs. Trajectory planning is solved by means of a PSO algorithm that can solve optimization problems with non-convex, non-quadratic cost function. Due to the heuristic nature of the PSO, planning output changes run-by-run. Nevertheless, the constrained optimization problem always allows the relative geometry to fulfil cooperation requirements. Results demonstrate that cooperative navigation performance in GNSS challenging environments strictly depends on the father's trajectory. Therefore, having a cooperative aiding vehicle is not sufficient to improve the son positioning accuracy; a proper path for the aiding vehicle must be designed.

A technique for routing multiple UAVs in a 3D environment with heterogenous GNSS coverage was presented in this thesis to insert the tandem planning in a more complex scenario. In absence of navigation issues, the proposed path planning approach aims at maximizing the efficiency in task assignment by distributing the targets among the UAVs. Whereas, in challenging areas, planning allows exploiting cooperative navigation between son and father UAVs. Thus, the multi-UAV fleet is naturally conceived at planning level as a reconfigurable distributed system. The complexity of the problem is tackled by a multi-step strategy. The simplified version of the proposed algorithm provides the same results of MILP, with a lower computational burden. The technique provides effective planning solutions taking full advantage from the number of available UAVs, while the computational time is reasonably small even for relatively large number of targets to be covered.

Cooperation among UAV has been also used under nominal GNSS coverage as a mean to improve attitude precision, and make it compliant with fine pointing accuracy requirements, by extending the concept of multi-antenna GNSS attitude estimation to a distributed aircraft scenario. To this aim the attitude of one chief is improved by using the measurements of one or more deputies. Flight test results demonstrates the used techniques allow achieving a heading uncertainty that can approach 0.1°. Despite the requirement of multi-antenna GNSS attitude estimation to use at least two deputies, the tight integration of the measurements in the EKF allows to obtain improvements in attitude angles also in the case only one cooperative platform is available. In addition, the measurement independence on magnetometer and inertial flight history makes the measurement reliable along the whole flight, being it insensitive to the error accumulation phenomena and independent on inertial sensor biases.

This thesis introduces a functional model for ionospheric delay compensation in real-time absolute and relative positioning applications of LEO, that accounts for the effect of ionosphere spatial variation. The effectiveness of the proposed model has been verified using real flight data from GRACE mission. Specifically, undifferenced (UD) and double-differenced (DD) ionospheric delays have been estimated with the proposed model in high solar activity condition, to stress model verification. In the UD case, the results show that the proposed model outperforms the classic model for ionosphere estimation, i.e. Lear model. The results put into evidence the much higher performance uniformity of the bilinear model over the investigated ionospheric delay range. More important, the RMS is much lower than for the Lear model, reducing up to 70% over specific ionospheric delay ranges. These results are confirmed in the DD case, even if to a lower extent. The novel ionospheric delay model has been tested in a filter for baseline estimation. The filter sequentially uses EKF and Kinematic filtering. The filter exhibits good performances in low ionospheric intensity condition, yielding a percentage of success for both L1 and WL ambiguities higher than 90%. In severe ionosphere conditions, in spite of a filter performance reduction (only 58% of L1 ambiguities fixed by the filter are correct) the positioning accuracy is better than the one achievable exploiting Lear model.

Bibliography

[1] Krieger, G., and Moreira, A., "Spaceborne bi- and multistatic SAR: potential and challenges," *IEE Proceedings Radar Sonar and Navigation*, 2006, pp. 184–198

[2] D'Errico, M., and Fasano, G., "Design of interferometric and bistatic mission phases of COSMO/SkyMed constellation," *Acta Astronautica*, vol. 62, Jan. 2008, pp. 97–111

[3] Valavanis, K. P., and Vachtsevanos, G. J., *Handbook of unmanned aerial vehicles*, 2015

[4] Brooks, M., "Welcome to the personal drone revolution," *New Scientist*, vol. 216, 2012, pp. 42–45

[5] Mokhtarzadeh, H., and Gebre-Egziabher, D., "Performance of networked dead reckoning navigation system," *IEEE Transactions on Aerospace and Electronic Systems*, vol. 52, 2016, pp. 2539–2553

[6] Rutkowski, A. J., Barnes, J. E., and Smith, A. T., "Path planning for optimal cooperative navigation," *Proceedings of the IEEE/ION Position, Location and Navigation Symposium, PLANS 2016*, 2016, pp. 359–365

[7] Vetrella, A. R., Fasano, G., and Accardo, D., "Cooperative navigation in GPS-challenging environments exploiting position broadcast and vision-based tracking," *2016 International Conference on Unmanned Aircraft Systems, ICUAS 2016*, 2016, pp. 447–456

[8] Cledat, E., and Cucci, D. A., "Mapping GNSS restricted environment with a drone tandem and indirect position control," *ISPRS*, 2017

[9] Sivaneri, V. O., and Gross, J. N., "UGV-to-UAV cooperative ranging for robust navigation in GNSS-challenged environments," *Aerospace Science and Technology*, vol. 71, 2017, pp. 245–255

[10] Eling, C., Klingbeil, L., and Kuhlmann, H., "Real-Time Single-Frequency GPS/MEMS-IMU Attitude Determination of Lightweight UAVs," *Sensors*, vol. 15, 2015, pp. 26212–26235

[11] Chowdhary, G., Johnson, E. N., Magree, D., Wu, A., and Shein, A., "GPS-denied Indoor and Outdoor Monocular Vision Aided Navigation and Control of Unmanned Aircraft," *Journal of Field Robotics*, vol. 30, 2013, pp. 415–438

[12] Vetrella, A., Fasano, G., Accardo, D., and Moccia, A., "Differential GNSS and Vision-Based Tracking to Improve Navigation Performance in Cooperative Multi-UAV Systems," *Sensors*, vol. 16, Dec. 2016, p. 2164

[13] De Vivo, F., Battipede, M., and Gili, P., "Nonvisible satellite estimation algorithm for improved uav navigation in mountainous regions," *IEEE Aerospace and Electronic Systems Magazine*, vol. 33, 2018, pp. 4–19

[14] Zimmermann, F., Eling, C., Klingbeil, L., and Kuhlmann, H., "Precise Positioning of UAVs - Dealing with Challenging Rtk-Gps Measurement Conditions During Automated UAV Flights," *ISPRS Annals of the Photogrammetry, Remote Sensing and Spatial Information Sciences*, 2017, pp. 95–102

[15] Vetrella, A. R., Fasano, G., and Accardo, D., "Attitude estimation for cooperating UAVs based on tight integration of GNSS and vision measurements," *Aerospace Science and Technology*, vol. 84, 2019, pp. 966–979

[16] Lu, G., and Cannon, M. E., "Attitude determination using a multi-antenna GPS system for hydrographic applications," *Marine Geodesy*, vol. 17, Oct. 1994, pp. 237–250

[17] Krieger, G., Moreira, A., Fiedler, H., Hajnsek, I., Werner, M., Younis, M., and Zink, M., "TanDEM-X: A satellite formation for high-resolution SAR interferometry," *IEEE Transactions on Geoscience and Remote Sensing*, vol. 45, 2007, pp. 3317–3340

[18] Fridlund, C. V. M., and Capaccioni, F., "Infrared space interferometry — the DARWIN mission," *Advances in Space Research*, vol. 30, 2002, pp. 2135–2145

[19] Tapley, B. D., Bettadpur, S., Watkins, M., and Reigber, C., "The gravity recovery and climate experiment: Mission overview and early results," *Geophysical Research Letters*, URL http://dx.doi.org/10.1029/2004GL019920: paper no. L09607, 2004

[20] Tancredi, U., Renga, A., and Grassi, M., "Real-Time Relative Positioning of Spacecraft over Long Baselines," *Journal of Guidance, Control, and Dynamics*, vol. 37, 2014, pp. 47–58

[21] Leung, S., and Montenbruck, O., "Real-time navigation of formation-flying spacecraft using global-positioning-system measurements," *Journal of Guidance, Control, and Dynamics*, vol. 28, 2005, pp. 226–235

[22] Lear, W. M., *GPS Navigation for low Earth Orbiting Vehicles*, 1988

[23] Mozaffari, M., Saad, W., Bennis, M., Nam, Y., and Debbah, M., "A Tutorial on UAVs for Wireless Networks: Applications, Challenges, and Open Problems," *IEEE Communications Surveys & Tutorials*, 2019, p. 1

[24] Allen, A., "Drone market worth $127bn," *Supply Management* Available: https://www.cips.org/en/supply-management/news/2018/may/drone-market-worth-127bn/

[25] Silvagni, M., Tonoli, A., Zenerino, E., and Chiaberge, M., "Multipurpose UAV for search and rescue operations in mountain avalanche events," *Geomatics, Natural Hazards and Risk*, vol. 8, Jan. 2017, pp. 18–33

[26] Schumacher, C., and Shima, T., "Single-Task Tours," *UAV Cooperative Decision and Control*, Society for Industrial and Applied Mathematics, 2009, pp. 37–51

[27] Atkinson, M., "Results Analysis of Using Free Market Auctions to Distribute Control of UAVs," *AIAA 3rd "Unmanned Unlimited" Technical Conference, Workshop and Exhibit*, American Institute of Aeronautics and Astronautics, 2004

[28] Menouar, H., Guvenc, I., Akkaya, K., Uluagac, A. S., Kadri, A., and Tuncer, A., "UAV-Enabled Intelligent Transportation Systems for the Smart City: Applications and Challenges," *IEEE Communications Magazine*, vol. 55, 2017, pp. 22–28

[29] Popović, M., Vidal-Calleja, T., Hitz, G., Sa, I., Siegwart, R., and Nieto, J., "Multiresolution mapping and informative path planning for UAV-based terrain monitoring," *2017 IEEE/RSJ International Conference on Intelligent Robots and Systems (IROS)*, 2017, pp. 1382–1388

[30] Wheeler, M., Schrick, B., Whitacre, W., Campbell, M., Rysdyk, R., and Wise, R., "Cooperative Tracking of Moving Targets by a Team of Autonomous UAVs," *2006 ieee/aiaa 25TH Digital Avionics Systems Conference*, 2006, pp. 1–9

[31] Casbeer, D. W., Kingston, D. B., Beard, R. W., and McLain, T. W., "Cooperative forest fire surveillance using a team of small unmanned air vehicles," *International Journal of Systems Science*, vol. 37, May 2006, pp. 351–360

[32] Chao, H., Baumann, M., Jensen, A., Chen, Y., Cao, Y., Ren, W., and McKee, M., "Band-reconfigurable Multi-UAV-based Cooperative Remote Sensing for Real-time Water Management and Distributed Irrigation Control," *IFAC Proceedings Volumes*, vol. 41, 2008, pp. 11744–11749

[33] Bircher, A., Alexis, K., Burri, M., Oettershagen, P., Omari, S., Mantel, T., and Siegwart, R., "Structural inspection path planning via iterative viewpoint resampling with application to aerial robotics," *2015 IEEE International Conference on Robotics and Automation (ICRA)*, 2015, pp. 6423–6430

[34] Balampanis, F., Maza, I., and Ollero, A., "Area decomposition, partition and coverage with multiple remotely piloted aircraft systems operating in coastal regions," *2016 International Conference on Unmanned Aircraft Systems (ICUAS)*, 2016, pp. 275–283

[35] Quaritsch, M., Kruggl, K., Wischounig-Strucl, D., Bhattacharya, S., Shah, M., and Rinner, B., "Networked UAVs as aerial sensor network for disaster management applications," *e & i Elektrotechnik und Informationstechnik*, vol. 127, 2010, pp. 56–63

[36] Toth, P., and Vigo, D., *The Vehicle Routing Problem*, Society for Industrial and Applied Mathematics, 2002

[37] Michael, N., Fink, J., and Kumar, V., "Cooperative manipulation and transportation with aerial robots," *Autonomous Robots*, vol. 30, 2011, pp. 73–86

[38] Kim, S., Silson, P., Tsourdos, A., and Shanmugavel, M., "Dubins Path Planning of Multiple Unmanned Airborne Vehicles for Communication Relay," *Proceedings of the Institution of Mechanical Engineers, Part G: Journal of Aerospace Engineering*, vol. 225, Jan. 2011, pp. 12–25

[39] Scherer, J., Yahyanejad, S., Hayat, S., Yanmaz, E., Andre, T., Khan, A., Vukadinovic, V., Bettstetter, C., Hellwagner, H., and Rinner, B., "An Autonomous Multi-UAV System for Search and Rescue," *Proceedings of the First Workshop on Micro Aerial Vehicle Networks, Systems, and Applications for Civilian Use*, New York, NY, USA: ACM, 2015, pp. 33–38

[40] Flint, M., Polycarpou, M., and Fernandez-Gaucherand, E., "Cooperative control for multiple autonomous UAV's searching for targets," *Proceedings of the 41st IEEE Conference on Decision and Control, 2002.*, 2002, pp. 2823–2828 vol.3

[41] Hu, J., Xie, L., and Xu, J., "Vision-based multi-agent cooperative target search," *2012 12th International Conference on Control Automation Robotics & Vision (ICARCV)*, 2012, pp. 895–900

[42] Tian, Y., Yi-Yin, L. Ka., Ok, K., Tran, L., Allen, D., Nicholas, A. J., Roy, P. S., and How, J. P., "Search and Rescue under the Forest Canopy using Multiple UAS," *International Symposium on Experimental Robotics (ISER)*, 2018

[43] Calderón, R., Navas-Cortés, J. A., Lucena, C., and Zarco-Tejada, P. J., "High-resolution airborne hyperspectral and thermal imagery for early detection of Verticillium wilt of olive using fluorescence, temperature and narrow-band spectral indices," *Remote Sensing of Environment*, vol. 139, 2013, pp. 231–245

[44] Maza, I., Caballero, F., Capitán, J., Martínez-de-Dios, J. R., and Ollero, A., "Experimental Results in Multi-UAV Coordination for Disaster Management and Civil Security Applications," *Journal of Intelligent & Robotic Systems*, vol. 61, 2011, pp. 563–585

[45] Gu, G., Chandler, P. R., Schumacher, C. J., Sparks, A., and Pachter, M., "Optimal Cooperative Sensing using a Team of UAVs," *IEEE Transactions on Aerospace and Electronic Systems*, vol. 42, 2006, pp. 1446–1458

[46] Bethke, B., Valenti, M., and How, J., "Cooperative Vision Based Estimation and Tracking Using Multiple UAVs BT - Advances in Cooperative Control and Optimization," P.M. Pardalos, R. Murphey, D. Grundel, and M.J. Hirsch, eds., Berlin, Heidelberg: Springer Berlin Heidelberg, 2007, pp. 179–189

[47] Sinha, A., Kirubarajan, T., and Bar-Shalom, Y., "Autonomous Ground Target Tracking by Multiple Cooperative UAVs," *2005 IEEE Aerospace Conference*, 2005, pp. 1–9

[48] Furukawa, T., Bourgault, F., Lavis, B., and Durrant-Whyte, H. F., "Recursive Bayesian search-and-tracking using coordinated uavs for lost targets," *Proceedings 2006 IEEE International Conference on Robotics and Automation, 2006. ICRA 2006.*, 2006, pp. 2521–2526

[49] Sinha, A., Kirubarajan, T., and Bar-Shalom, Y., "Optimal cooperative placement of UAVs for ground target tracking with Doppler radar," *SPIE 5429, Signal Processing, Sensor Fusion, and Target Recognition XIII, 95*, 2004, pp. 95–104

[50] Hirsch, M., and Schroeder, D., "Dynamic Decentralized Cooperative Control of Multiple Autonomous Vehicles with Multiple Tasks for Urban Operations," *AIAA Guidance, Navigation, and Control Conference*, American Institute of Aeronautics and Astronautics, 2012

[51] Frew, E. W., "Information-theoretic Integration of Sensing and Communication for Active Robot Networks," *Proceedings of the 1st International Conference on Robot Communication and Coordination*, Piscataway, NJ, USA: IEEE Press, 2007, pp. 18:1--18:8

[52] Viguria, A., Maza, I., and Ollero, A., "Distributed Service-Based Cooperation in Aerial/Ground Robot Teams Applied to Fire Detection and Extinguishing Missions," *Advanced Robotics*, vol. 24, Jan. 2010, pp. 1–23

[53] Shakhatreh, H., Sawalmeh, A. H., Al-Fuqaha, A., Dou, Z., Almaita, E., Khalil, I., Othman, N. S., Khreishah, A., and Guizani, M., "Unmanned Aerial Vehicles (UAVs): A Survey on Civil Applications and Key Research Challenges," *IEEE Access*, vol. 7, 2019, pp. 48572–48634

[54] Maza, I., and Ollero, A., "Multiple UAV cooperative searching operation using polygon area decomposition and efficient coverage algorithms," *Distributed Autonomous Robotic Systems 6*, R. Alami, R. Chatila, and H. Asama, eds., Tokyo: Springer Japan, 2007, pp. 221–230

[55] Franchi, A., Freda, L., Oriolo, G., and Vendittelli, M., "A Decentralized Strategy for Cooperative Robot Exploration," *Proceedings of the 1st International Conference on Robot Communication and Coordination*, Piscataway, NJ, USA: IEEE Press, 2007, pp. 7:1--7:8

[56] Dias, M. B., Zinck, M., Zlot, R., and Stentz, A., "Robust multirobot coordination in dynamic environments," *IEEE International Conference on Robotics and Automation (ICRA), 2004.*, 2004, pp. 3435-3442 Vol.4

[57] Wei, Y., Blake, M. B., and Madey, G. R., "An Operation-Time Simulation Framework for UAV Swarm Configuration and Mission Planning," *Procedia Computer Science*, vol. 18, 2013, pp. 1949–1958

[58] Cekmez, U., Ozsiginan, M., and Sahingoz, O. K., "Multi colony ant optimization for UAV path

planning with obstacle avoidance," *2016 International Conference on Unmanned Aircraft Systems, ICUAS 2016*, 2016, pp. 47–52

[59] Oh, H., Kim, S., Tsourdos, A., and White, B. A., "Coordinated road-network search route planning by a team of UAVs," *International Journal of Systems Science*, vol. 45, 2014, pp. 825–840

[60] Bellingham, J., Tillerson, M., Richards, A., and How, J. P., "Multi-Task Allocation and Path Planning for Cooperating UAVs," *Cooperative Control: Models, Applications and Algorithms*, S. Butenko, R. Murphey, and P.M. Pardalos, eds., Boston, MA: Springer US, 2003, pp. 23–41

[61] Ruiz, R., Maroto, C., and Alcaraz, J., "A decision support system for a real vehicle routing problem," *European Journal of Operational Research*, vol. 153, 2004, pp. 593–606

[62] Kothari, M., Postlethwaite, I., and Gu, D., "Multi-UAV path planning in obstacle rich environments using Rapidly-exploring Random Trees," *Proceedings of the 48h IEEE Conference on Decision and Control (CDC) held jointly with 2009 28th Chinese Control Conference*, 2009, pp. 3069–3074

[63] Perez-Carabaza, S., Bermudez-Ortega, J., Besada-Portas, E., Lopez-Orozco, J. A., and de la Cruz, J. M., "A multi-UAV Minimum Time Search Planner Based on ACOR," *Proceedings of the Genetic and Evolutionary Computation Conference*, New York, NY, USA: ACM, 2017, pp. 35–42

[64] Bertuccelli, L. F., and How, J. P., "Active Exploration in Robust Unmanned Vehicle Task Assignment," *Journal of Aerospace Computing, Information, and Communication*, vol. 8, 2011, pp. 250–268

[65] Moon, S., Oh, E., and Shim, D. H., "An Integral Framework of Task Assignment and Path Planning for Multiple Unmanned Aerial Vehicles in Dynamic Environments," *Journal of Intelligent & Robotic Systems*, vol. 70, 2013, pp. 303–313

[66] Ousingsawat, J., and Campbell, M. E., "On-line estimation and path planning for multiple vehicles in an uncertain environment," *International Journal of Robust and Nonlinear Control*, vol. 14, Apr. 2004, pp. 741–766

[67] Pan, F., Hu, X., Eberhart, R., and Chen, Y., "A new UAV assignment model based on PSO," *2008 IEEE Swarm Intelligence Symposium*, 2008, pp. 1–7

[68] Omidshafiei, S., Agha-mohammadi, A. a., Amato, C., and How, J. P., "Decentralized control of Partially Observable Markov Decision Processes using belief space macro-actions," *2015 IEEE International Conference on Robotics and Automation (ICRA)*, 2015, pp. 5962–5969

[69] Premack, R., "UPS just beat out Amazon, FedEx, and Uber to make America's first revenue-generating drone delivery," *Business Insider* Available: https://www.businessinsider.com/ups-first-revenue-generating-drone-delivery-with-matternet-2019-3?IR=T

[70] Zaveri, M., "Wing, Owned by Google's Parent Company, Gets First Approval for Drone Deliveries in U.S.," *The New York Times* Available: https://www.nytimes.com/2019/04/23/technology/drone-deliveries-google-wing.html

[71] Kosuge, K., Oosumi, T., Satou, M., Chiba, K., and Takeo, K., "Transportation of a single object by two decentralized-controlled nonholonomic mobile robots," *Proceedings. 1998 IEEE International Conference on Robotics and Automation (Cat. No.98CH36146)*, 1998, pp. 2989–2994 vol.4

[72] Sugar, T. G., and Kumar, V., "Control of cooperating mobile manipulators," *IEEE Transactions on Robotics and Automation*, vol. 18, 2002, pp. 94–103

[73] Tagliabue, A., Kamel, M., Verling, S., Siegwart, R., and Nieto, J., "Collaborative transportation using MAVs via passive force control," *2017 IEEE International Conference on Robotics and Automation (ICRA)*, 2017, pp. 5766–5773

[74] Mozaffari, M., Saad, W., Bennis, M., and Debbah, M., "Optimal transport theory for power-efficient deployment of unmanned aerial vehicles," *2016 IEEE International Conference on Communications (ICC)*, 2016, pp. 1–6

[75] Mozaffari, M., Saad, W., Bennis, M., and Debbah, M., "Efficient Deployment of Multiple Unmanned Aerial Vehicles for Optimal Wireless Coverage," *IEEE Communications Letters*, vol. 20, 2016, pp. 1647–1650

[76] Kalantari, E., Yanikomeroglu, H., and Yongacoglu, A., "On the Number and 3D Placement of Drone Base Stations in Wireless Cellular Networks," *2016 IEEE 84th Vehicular Technology Conference (VTC-Fall)*, 2016, pp. 1–6

[77] De Palma, D., Indiveri, G., and Parlangeli, G., “Multi-vehicle relative localization based on single range measurements,” *IFAC-PapersOnLine*, vol. 48, 2015, pp. 17–22

[78] Seco, F., Jiménez, A. R., and Zheng, X., “RFID-based centralized cooperative localization in indoor environments,” *2016 International Conference on Indoor Positioning and Indoor Navigation (IPIN)*, 2016, pp. 1–7

[79] Wymeersch, H., Lien, J., and Win, M. Z., “Cooperative Localization in Wireless Networks,” *Proceedings of the IEEE*, vol. 97, 2009, pp. 427–450

[80] de Haag, M. U., and Huschbeck, S., “sUAS Swarm Navigation using Inertial, Range Radios and Partial GNSS,” *2019 IEEE/AIAA 38th Digital Avionics Systems Conference (DASC)*, 2019, pp. 1–10

[81] Lu, J., Gao, C., Zhao, G., and Liu, S., “Decentralized State Estimation for Networked Navigation Systems with Communication Delay and Packet Loss: The Receding Horizon Case,” *IFAC-PapersOnLine*, vol. 48, 2015, pp. 1094–1099

[82] Bailey, T., Bryson, M., Mu, H., Vial, J., McCalman, L., and Durrant-Whyte, H., “Decentralised cooperative localisation for heterogeneous teams of mobile robots,” *2011 IEEE International Conference on Robotics and Automation*, 2011, pp. 2859–2865

[83] Nerurkar, E. D., and Roumeliotis, S. I., “Asynchronous Multi-Centralized Cooperative Localization,” *2010 IEEE/RSJ International Conference on Intelligent Robots and Systems*, 2010, pp. 4352–4359

[84] Rigatos, G. G., “Distributed filtering over sensor networks for autonomous navigation of UAVs,” *Intelligent Service Robotics*, vol. 5, 2012, pp. 179–198

[85] Salil, G., Allison, K., Vassilis, G., Guenther, R., Charles, T., Dorota-Grejner, B., and Bharat, L., “Cooperative Localization of Unmanned Aerial Vehicles Using GNSS, MEMS Inertial, and UWB Sensors,” *Journal of Surveying Engineering*, vol. 143, Nov. 2017, p. 4017007

[86] Dinh, V., and Kia, S. S., “A server-client based distributed processing for an Unscented Kalman filter for cooperative localization,” *2015 IEEE International Conference on Multisensor Fusion and Integration for Intelligent Systems (MFI)*, 2015, pp. 43–48

[87] Suh, J., You, S., Choi, S., and Oh, S., “Vision-Based Coordinated Localization for Mobile Sensor Networks,” *IEEE Transactions on Automation Science and Engineering*, vol. 13, 2016, pp. 611–620

[88] Rushan, S. M., Mehrandezh, M., and Paranjape, R., “Localization of a Team of Heterogeneous Robots for a Distributed Sensing Task,” *2006 Canadian Conference on Electrical and Computer Engineering*, 2006, pp. 1522–1525

[89] Kurazume, R., and Hirose, S., “An Experimental Study of a Cooperative Positioning System,” *Autonomous Robots*, vol. 8, 2000, pp. 43–52

[90] Miller, I., Schimpf, B., Campbell, M., and Leyssens, J., “Tightly-coupled GPS / INS system design for autonomous urban navigation,” *2008 IEEE/ION Position, Location and Navigation Symposium*, 2008, pp. 1297–1310

[91] Zhu, N., Marais, J., Bétaille, D., and Berbineau, M., “GNSS Position Integrity in Urban Environments: A Review of Literature,” *IEEE Transactions on Intelligent Transportation Systems*, vol. 19, 2018, pp. 2762–2778

[92] Wang, L., Groves, P. D., and Ziebart, M. K., “Multi-Constellation GNSS Performance Evaluation for Urban Canyons Using Large Virtual Reality City Models,” *Journal of Navigation*, vol. 65, 2012, pp. 459–476

[93] Watanabe, Y., Veillard, A., and Chanel, C., “Navigation and Guidance Strategy Planning for UAV Urban Operation,” *AIAA Infotech @ Aerospace*, American Institute of Aeronautics and Astronautics, 2016

[94] Sundar, K., Misra, S., Rathinam, S., and Sharma, R., “Routing unmanned vehicles in GPS-denied environments,” *2017 International Conference on Unmanned Aircraft Systems (ICUAS)*, 2017, pp. 62–71

[95] Obst, M., Bauer, S., Reisdorf, P., and Wanielik, G., “Multipath detection with 3D digital maps for robust multi-constellation GNSS/INS vehicle localization in urban areas,” *2012 IEEE Intelligent Vehicles Symposium*, 2012, pp. 184–190

[96] Chiang, K.-W., Duong, T. T., and Liao, J.-K., “The Performance Analysis of a Real-Time Integrated INS/GPS Vehicle Navigation System with Abnormal GPS Measurement

Elimination," *Sensors* , vol. 13, 2013

[97] Ko, H., Kim, B., and Kong, S., "GNSS Multipath-Resistant Cooperative Navigation in Urban Vehicular Networks," *IEEE Transactions on Vehicular Technology*, vol. 64, 2015, pp. 5450–5463

[98] Godha, S., and Cannon, M. E., "GPS/MEMS INS integrated system for navigation in urban areas," *GPS Solutions*, vol. 11, 2007, pp. 193–203

[99] Weiss, S., Scaramuzza, D., and Siegwart, R., "Monocular-SLAM–based navigation for autonomous micro helicopters in GPS-denied environments," *Journal of Field Robotics*, vol. 28, Nov. 2011, pp. 854–874

[100] Celik, K., Chung, S.-J., and Somani, A., "MVCSLAM: Mono-Vision Corner SLAM for Autonomous Micro-Helicopters in GPS Denied Environments," *AIAA Guidance, Navigation and Control Conference and Exhibit*, American Institute of Aeronautics and Astronautics, 2008

[101] Bachrach, A., Winter, A. de, He, R., Hemann, G., Prentice, S., and Roy, N., "RANGE - robust autonomous navigation in GPS-denied environments," *2010 IEEE International Conference on Robotics and Automation*, 2010, pp. 1096–1097

[102] Madison, R., Andrews, G., Debitetto, P. A., Rasmussen, S., and Bottkol, M., *Vision-Aided Navigation for Small UAVs in GPS-Challenged Environments*, 2007

[103] Ahrens, S., Levine, D., Andrews, G., and How, J. P., "Vision-based guidance and control of a hovering vehicle in unknown, GPS-denied environments," *2009 IEEE International Conference on Robotics and Automation*, 2009, pp. 2643–2648

[104] Bayer, J., and Faigl, J., "Localization Fusion for Aerial Vehicles in Partially GNSS Denied Environments BT - Modelling and Simulation for Autonomous Systems," J. Mazal, ed., Cham: Springer International Publishing, 2019, pp. 251–262

[105] Lie, A., Mokhtarzadeh, H., Freeman, P., Larson, J., Layh, T., Hu, B., Taylor, B., Gerbe-Egziabher, D., Seiler, P., and Balas, G., "An Airborne Experimental Test Platform, from theory to flight," *Inside GNSS*, 2014, pp. 40–47

[106] Pesyna Jr., K. M., Kassas, Z. M., Bhatti, J. A., and Humphreys, T. E., "Tightly-coupled opportunistic navigation for deep urban and indoor positioning," *24th International Technical Meeting of the Satellite Division of the Institute of Navigation 2011, ION GNSS 2011*, 2011, pp. 3605–3616

[107] Kapoor, R., Ramasamy, S., Gardi, A., Bieber, C., Silverberg, L., and Sabatini, R., "A Novel 3D Multilateration Sensor Using Distributed Ultrasonic Beacons for Indoor Navigation," *Sensors* , vol. 16, 2016

[108] Rabiee, R., Zhong, X., Yan, Y., and Tay, W. P., "LaIF: A Lane-Level Self-Positioning Scheme for Vehicles in GNSS-Denied Environments," *IEEE Transactions on Intelligent Transportation Systems*, vol. 20, 2019, pp. 2944–2961

[109] Kanaki, S., Hashimoto, M., Yoden, Y., and Takahashi, K., "Laser-based cooperative tracking of vehicles and people by multiple mobile robots in GNSS-denied environments," *2017 IEEE International Conference on Advanced Intelligent Mechatronics (AIM)*, 2017, pp. 1228–1233

[110] Hening, S., Ippolito, C. A., Krishnakumar, K. S., Stepanyan, V., and Teodorescu, M., "3D LiDAR SLAM Integration with GPS/INS for UAVs in Urban GPS-Degraded Environments," *AIAA Information Systems-AIAA Infotech @ Aerospace*, American Institute of Aeronautics and Astronautics, 2017

[111] Hemann, G., Singh, S., and Kaess, M., "Long-range GPS-denied aerial inertial navigation with LIDAR localization," *2016 IEEE/RSJ International Conference on Intelligent Robots and Systems (IROS)*, 2016, pp. 1659–1666

[112] Mostafa, M., Zahran, S., Moussa, A., El-Sheimy, N., and Sesay, A., "Radar and Visual Odometry Integrated System Aided Navigation for UAVS in GNSS Denied Environment," *Sensors* , vol. 18, 2018

[113] Zahran, S., Moussa, A., and El-Sheimy, N., "Enhanced UAV navigation in GNSS denied environment using repeated dynamics pattern recognition," *2018 IEEE/ION Position, Location and Navigation Symposium (PLANS)*, 2018, pp. 1135–1142

[114] Zhu, Z., Roumeliotis, S., Hesch, J., Park, H., and Venable, D., "Architecture for asymmetric collaborative navigation," *IEEE PLANS*, 2012, pp. 777–782

[115] Indelman, V., Gurfil, P., Rivlin, E., and Rotstein, H., "Real-Time Vision-Aided Localization

and Navigation Based on Three-View Geometry," *IEEE Transactions on Aerospace and Electronic Systems*, vol. 48, 2012, pp. 2239–2259

[116] Merino, L., Wiklund, J., Caballero, F., Moe, A., Dios, J. R. M. De, Forssen, P.-., Nordberg, K., and Ollero, A., "Vision-based multi-UAV position estimation," *IEEE Robotics & Automation Magazine*, vol. 13, 2006, pp. 53–62

[117] Sivaneri, V. O., and Gross, J. N., "Flight-testing of a cooperative UGV-to-UAV strategy for improved positioning in challenging GNSS environments," *Aerospace Science and Technology*, vol. 82–83, 2018, pp. 575–582

[118] Sharma, R., and Taylor, C., "Cooperative navigation of MAVs In GPS denied areas," *2008 IEEE International Conference on Multisensor Fusion and Integration for Intelligent Systems*, 2008, pp. 481–486

[119] Sharma, R., and Taylor, C., "Vision Based Distributed Cooperative Navigation for MAVs in GPS denied areas," *AIAA Infotech@Aerospace Conference*, American Institute of Aeronautics and Astronautics, 2009

[120] Farrell, J., *Aided Navigation: GPS with High Rate Sensors*, New York, NY, USA: McGraw-Hill, Inc., 2008

[121] Causa, F., Vetrella, A. R., Fasano, G., and Accardo, D., "Multi-UAV Formation Geometries for Cooperative Navigation in GNSS-challenging Environments," *IEEE/ION PLANS*, 2018, pp. 775–785

[122] Causa, F., Fasano, G., and Grassi, M., "Enabling Autonomous Flight in GNSS-challenging Environments: Cooperative Navigation and generalized Dilution of Precision," *Submitted to TAES*

[123] Groves, P. D., *Principles of GNSS, Inertial, and Multisensor Integrated Navigation Systems*, Noordwood, MA, USA: Artech House, 2008

[124] IGS RINEX, "RINEX – the Receiver Independent EXchange format, Version 3.03" Available: ftp://igs.org/pub/data/format/rinex303.pdf

[125] Montenbruck, O., Steigenberger, P., Prange, L., Deng, Z., Zhao, Q., Perosanz, F., Romero, I., Noll, C., Stürze, A., Weber, G., Schmid, R., MacLeod, K., and Schaer, S., "The Multi-GNSS Experiment (MGEX) of the International GNSS Service (IGS) – Achievements, prospects and challenges," *Advances in Space Research*, vol. 59, 2017, pp. 1671–1697

[126] Caporali, A., and Nicolini, L., "Interoperability of the GNSS's for Positioning and Timing BT - New Advanced GNSS and 3D Spatial Techniques," R. Cefalo, J.B. Zieliński, and M. Barbarella, eds., Cham: Springer International Publishing, 2018, pp. 73–85

[127] Causa, F., Popović, M., Fasano, G., Grassi, M., Nieto, J., and Siegwart, R., "Navigation aware planning for tandem UAV missions in GNSS challenging Environments," *2019 AIAA Guidance, Navigation, and Control Conference*, 2019

[128] Honeywell, "HG1120 MEMS Inertial Measurement Unit" Available: https://aerospace.honeywell.com/en/~/media/aerospace/files/brochures/n61-1524-000-004-hg1120-mems-inertial-measurement-unit-bro.pdf

[129] Kam, H. R., Lee, S.-H., Park, T., and Kim, C.-H., "RViz: A Toolkit for Real Domain Data Visualization," *Telecommun. Syst.*, vol. 60, 2015, pp. 337–345

[130] Ublox, "u-blox 8 / u-blox M8 Receiver Description - Manual" Available: https://www.u-blox.com/sites/default/files/products/documents/u-blox8-M8_ReceiverDescrProtSpec_%28UBX-13003221%29_Public.pdf

[131] Takasu, T., and Yasuda, A., "Development of the low-cost RTK-GPS receiver with an open source program package RTKLIB," *International Symposium on GPS/GNSS*, Jan. 2009

[132] Chattopadhyay, P., Jha, D. K., Sarkar, S., and Ray, A., "Path planning in GPS-denied environments: A collective intelligence approach," *2015 American Control Conference (ACC)*, 2015, pp. 3082–3087

[133] Singh, S., and Sujit, P. B., "Landmarks based path planning for UAVs in GPS-denied areas∗∗This work is partially funded by FCT grant SFRH/BPD/103962/2014.," *IFAC-PapersOnLine*, vol. 49, 2016, pp. 396–400

[134] Bopardikar, S. D., Englot, B., and Speranzon, A., "Multi-objective path planning in GPS denied environments under localization constraints," *2014 American Control Conference*, 2014, pp. 1872–1879

[135] Rathinam, S., and Sharma, R., "A multiple vehicle path covering problem with localization constraints: Formulation and algorithms," *2015 American Control Conference (ACC)*, 2015, pp. 3746–3751

[136] Richter, C., Bry, A., and Roy, N., "Polynomial Trajectory Planning for Aggressive Quadrotor Flight in Dense Indoor Environments," *Robotics Research: The 16th International Symposium ISRR*, M. Inaba and P. Corke, eds., Cham: Springer International Publishing, 2016, pp. 649–666

[137] Burri, M., Oleynikova, H., Achtelik, M. W., and Siegwart, R., "Real-time visual-inertial mapping, re-localization and planning onboard MAVs in unknown environments," *2015 IEEE/RSJ International Conference on Intelligent Robots and Systems (IROS)*, 2015, pp. 1872–1878

[138] Kennedy, J., and Eberhart, R., "Particle swarm optimization," *Neural Networks, 1995. Proceedings., IEEE International Conference on*, 1995, pp. 1942–1948 vol.4

[139] Furrer, F., Burri, M., Achtelik, M., and Siegwart, R., "RotorS—A Modular Gazebo MAV Simulator Framework BT - Robot Operating System (ROS): The Complete Reference (Volume 1)," A. Koubaa, ed., Cham: Springer International Publishing, 2016, pp. 595–625

[140] Causa, F., Fasano, G., and Grassi, M., "Improving Autonomy in GNSS-Challenging Environments by Multi-UAV Cooperation," *2019 IEEE/AIAA 38th Digital Avionics Systems Conference (DASC)*, 2019, pp. 1–10

[141] Mayne, D. Q., Rawlings, J. B., Rao, C. V, and Scokaert, P. O. M., "Constrained model predictive control: Stability and optimality," *Automatica*, vol. 36, 2000, pp. 789–814

[142] Breivik, M., and Fossen, T. I., "Guidance-based path following for autonomous underwater vehicles," *Proceedings of OCEANS 2005 MTS/IEEE*, 2005, pp. 2807-2814 Vol. 3

[143] Prentice, S., and Roy, N., "The Belief Roadmap: Efficient Planning in Belief Space by Factoring the Covariance," *The International Journal of Robotics Research*, vol. 28, Jul. 2009, pp. 1448–1465

[144] Avellar, S. G., Pereira, A. G., Pimenta, C. L., and Iscold, P., "Multi-UAV Routing for Area Coverage and Remote Sensing with Minimum Time," *Sensors* , vol. 15, 2015

[145] Maddula, T., Minai, A. A., and Polycarpou, M. M., "Multi-Target Assignment and Path Planning for Groups of UAVs," *Recent Developments in Cooperative Control and Optimization*, S. Butenko, R. Murphey, and P.M. Pardalos, eds., Boston, MA: Springer US, 2004, pp. 261–272

[146] Oh, H., Kim, S., Suk, J., and Tsourdos, A., "Coordinated Trajectory Planning for Efficient Communication Relay Using Multiple UAVs," *IFAC Proceedings Volumes*, vol. 46, 2013, pp. 119–124

[147] Opromolla, R., Fasano, G., and Accardo, D., "A Vision-Based Approach to UAV Detection and Tracking in Cooperative Applications," *Sensors* , vol. 18, 2018

[148] Eling, C., Wieland, M., Hess, C., Klingbeil, L., and Kuhlmann, H., "Development and Evaluation of UAV based mapping system for remote sensing and surveying application," *Int. Arch. Photogramm. Remote Sens. Spatial Inf. Sci.*, vol. XL-1/W4, Aug. 2015, pp. 233–239

[149] Jozkow, G., Toth, C., and Grejner-Brzezinska, D., "UAS topographic mapping with velodine LiDAR sensor," *ISPRS Ann. Photogramm. Remote Sens. Spatial Inf. Sci.*, vol. III–1, Jun. 2016, pp. 201–208

[150] Rehak, M., and Skaloud, J., "Applicability of new approaches of sensor orientation to micro aerial vehicles," *XXIII ISPRS Congress, Prague, Czech Republic*, vol. III–3, 2016, pp. 441–447

[151] "Swift Navigation Piksi GNSS modules" Available: https://www.swiftnav.com/piksi-gnss-modules

[152] Rehak, M., and Skaloud, J., "Performance Assessment of Integrated Sensor orientation with a low-cost GNSS receiver," *International Conference on Unmanned Aerial Vehicles in Geomatics, Bonn, Germany*, ISPRS Annals of the Photogrammetry, Remote Sensing and Spatial Information Sciences, 2017, pp. 1–6

[153] Parkins, A., "Increasing GNSS RTK Availability with a New Single-Epoch Batch Partial Ambiguity Resolution Algorithm," *GPS Solutions*, vol. 15, 2011, pp. 391–402

[154] Hu, G., Abbey, D. A., Castleden, N., Featherstone, W. E., Earls, C., Ovstedal, O., and Weihing, D., "An Approach for Instantaneous Ambiguity Resolution for Medium- to Long-Range

Multiple Reference Station Networks," *GPS Solutions*, vol. 9, 2005, pp. 1–11

[155] Stoecker, C., Nex, F., Koeva, M., and Gerke, M., "Quality assessment of combined IMU/GNSS data for direct georeferencing in the context of UAV-based mapping," *International Conference on Unmanned Aerial Vehicles in Geomatics, Bonn, Germany*, ISPRS Annals of the Photogrammetry, Remote Sensing and Spatial Information Sciences, 2017, pp. 1–7

[156] Vetrella, A. R., Fasano, G., and Accardo, D., "Satellite and Vision-aided Sensor Fusion for Cooperative Navigation of Unmanned Aircraft Swarms," *Journal of Aerospace and Information Systems*, vol. 14, 2017, pp. 327–344

[157] Vetrella, A. R., Causa, F., Renga, A., Fasano, G., Accardo, D., and Grassi, M., "Flight demonstration of multi-UAV CDGPS and vision-based sensing for high accuracy attitude estimation," *2017 International Conference on Unmanned Aircraft Systems (ICUAS)*, IEEE, 2017, pp. 237–246

[158] Vetrella, A. R., Causa, F., Renga, A., Fasano, G., Accardo, D., and Grassi, M., "Multi-UAV Carrier Phase Differential GPS and Vision-based Sensing for High Accuracy Attitude Estimation," *Journal of Intelligent and Robotic Systems: Theory and Applications*, 2018

[159] Mannucci, A. J., Iijima, B. A., Lindqwister, U. J., Pi, X., Sparks, L., Wilson, B. D., and Mannucci, T., "GPS and Ionosphere," *The Review of Radio Science 1996-1999*, W. Ross Stone, ed., New York: Oxford Univeristy Press, 1999, pp. 625–665

[160] Liu, J., Cannon, M. E., Alves, P., Petovello, M. G., Lachapelle, G., MacGougan, G., and deGroot, L., "A performance comparison of single and dual frequency GPS ambiguity resolution strategies," *GPS Solutions*, vol. 7, 2003, pp. 87–100

[161] Renga, A., Fasano, G., Accardo, D., Grassi, M., Tancredi, U., Rufino, G., and Simonetti, A., "Navigation facility for high accuracy offline trajectory and attitude estimation in airborne applications," *International Journal of Navigation and Observation*, vol. 2013, 2013

[162] Teunissen, P. J. G., "The least-squares ambiguity decorrelation adjustment: a method for fast GPS integer ambiguity estimation," *Journal of Geodesy*, vol. 70, 1995, pp. 65–82

[163] Verhagen, S., "The GNSS integer ambiguities: estimation and validation," *Journal of Geodesy*, 2005

[164] Melbourne, W. G., "The Case for Ranging in GPS-based Geodetic Systems," *1st International Symposium on Precise Positioning with the Global Positioning System, Rockville, MD, USA, 15–19 April*, 1985, pp. 373–386

[165] Wübbena, G., "Software Developments for Geodetic Positioning with GPS using TI-4100 Code and Carrier Measurements," *1st International Symposium on Precise Positioning with the Global Positioning System, Rockville, MD, USA, 15–19 April*, 1985, pp. 403–412

[166] Verhagen, S., "Integer ambiguity validation: an open problem?," *GPS Solutions*, vol. 8, 2004, pp. 36–43

[167] Verhagen, S., and Bofeng, L., "LAMBDA software package, Matlab Implementation, Version 3.0," 2012

[168] Wang, J., and Feng, Y., "Reliability of partial ambiguity fixing with multiple GNSS constellations," *Journal of Geodesy*, vol. 87, 2013, pp. 1–14

[169] Li, P., and Zhang, X., "Precise Point Positioning with Partial Ambiguity Fixing," *Sensors*, vol. 15, 2015, pp. 13627–13643

[170] Vetrella, A. R., Fasano, G., and Accardo, D., "Cooperative attitude estimation for UAV Swarms based on tight integration of GNSS and vision measurements," *Submitted to IEEE Transactions on Robotics*

[171] Shuster, M. D., and Oh, S. D., "Three-axis attitude determination from vector observations," *Journal of Guidance, Control, and Dynamics*, vol. 4, Jan. 1981, pp. 70–77

[172] Shuster, M. D., "The quest for better attitudes," *The Journal of the Astronautical Sciences*, vol. 54, 2006, pp. 657–683

[173] Vetrella, A. R., Causa, F., Renga, A., Fasano, G., Accardo, D., and Grassi, M., "Multi-UAV Carrier Phase Differential GPS and Vision-based Sensing for High Accuracy Attitude Estimation," *Journal of Intelligent & Robotic Systems*, vol. 93, 2019, pp. 245–260

[174] Cheng, Y., and Shuster, M. D., "QUEST and The Anti-QUEST : Good and Evil Attitude Estimation," *Journal of the Astronautical Sciences*, vol. 53, 2005, pp. 337–351

[175] Guzman, J. J., and Edery, A., "Mission design for the MMS tetrahedron formation," *2004 IEEE*

Aerospace Conference Proceedings (IEEE Cat. No.04TH8720), Vol 1, 2004, pp. 533–540

[176] Gill, E., and Runge, H., "Tight formation flying for an along-track SAR interferometer," *Acta Astronautica*, vol. 55, Aug. 2004, pp. 473–485

[177] Renga, A., Moccia, A., D'Errico, M., Dellepiane, S., Angiati, E., Vernazza, G., Lombardo, P., Colone, F., Sedehi, M., Cristallini, D., Pignataro, S., Rioli, Q., Milillo, G., Bruno, C., Giorgio, F. Di, and Labriola, M., "From the expected scientific applications to the functional specifications, products and performance of the SABRINA missions," *2008 IEEE Radar Conference*, 2008, pp. 1–6

[178] Kroes, R., "Precise Relative Positioning of Formation Flying Spacecraft using GPS," *Publications on Geodesy 61*, 2006, p. 184

[179] Wolfe, J. D., Seyer, J. L., Soonsik, H., Jae Lee, Y., and Lee, E., "Estimation of Relative Satellite Position Using Transformed Differential Carrier-Phase GPS Measurements," *Journal of Guidance, Control, and Dynamics*, vol. 30, 2007, pp. 1217–1227

[180] Kroes, R., Montenbruck, O., Bertiger, W., and Visser, P., "Precise GRACE baseline determination using GPS," *GPS Solutions*, vol. 9, 2005, pp. 21–31

[181] Wu, S.-C., and Bar-Sever, Y. E., "Real-Time Sub-cm Differential Orbit Determination of Two Low-Earth Orbiters with GPS Bias Fixing," *19th International Technical Meeting of the Satellite Division of the Institute od Navigation (ION GNSS)*, 2006, pp. 2515–2522

[182] Klobuchar, J. A., "Ionospheric effects on GPS," *Global Positioning System: Theory and Applications, Volume I*, B.W. Parkinson and J.J. Spilker, eds., Washington, District of Columbia: American Institute of Aeronautics and Astronautics Inc., 1996, pp. 485–515

[183] Teunissen, P. J. G., "The geometry-free GPS ambiguity search space with a weighted ionosphere," *Journal of Geodesy*, vol. 71, 1997, pp. 370–383

[184] Dennis, O., "Ionosphere-Free Phase Combinations for Modernized GPS," *Journal of Surveying Engineering*, vol. 129, Nov. 2003, pp. 165–173

[185] Skone, S., and Cannon, M. E., "Auroral Zone Ionospheric Considerations for WADGPS," *Navigation*, vol. 45, Jun. 1998, pp. 117–127

[186] Mohiuddin, S., and Psiaki, M. L., "Carrier-Phase Differential Global Positioning System Navigation Filter for High-Altitude Spacecraft," *Journal of Guidance, Control, and Dynamics*, vol. 31, Jul. 2008, pp. 801–814

[187] Odijk, D., and Teunissen, P. J. G., "Improving the speed of CORS Network RTK ambiguity resolution," *IEEE/ION Position, Location and Navigation Symposium*, 2010, pp. 79–84

[188] Verhagen, S., Odijk, D., Teunissen, P. J. G., and Huisman, L., "Performance improvement with low-cost multi-GNSS receivers," *Programme and Abstract Book - 5th ESA Workshop on Satellite Navigation Technologies and European Workshop on GNSS Signals and Signal Processing, NAVITEC 2010*, 2010

[189] Komjathi, A., *Global Ionospheric Total Electron Content Mapping Using the Global Positioning System*, New Brunswick, Canada: 1997

[190] Banville, S., Zhang, W., Ghoddousi-Fard, R., and Langley, R. B., "Ionospheric Monitoring Using 'Integer-Levelled' Observations," *Proc. ION GNSS 2012*, 2012

[191] Jin, R., Jin, S., and Feng, G., "M_DCB: Matlab code for estimating GNSS satellite and receiver differential code biases," *GPS Solutions*, vol. 16, 2012, pp. 541–548

[192] Nava, B., Coïsson, P., and Radicella, S. M., "A new version of the NeQuick ionosphere electron density model," *Journal of Atmospheric and Solar-Terrestrial Physics*, vol. 70, 2008, pp. 1856–1862

[193] Ebinuma, T., Bishop, R. H., and Lightsey, E. G., "Integrated Hardware Investigations of Precision Spacecraft Rendezvous Using the Global Positioning System," *Journal of Guidance, Control, and Dynamics*, vol. 26, May 2003, pp. 425–433

[194] Tancredi, U., Allende-Alba, G., Renga, A., Montenbruck, O., and Grassi, M., "Relative positioning of spacecraft in intense ionospheric conditions by GPS," *Aerospace Science and Technology*, vol. 43, 2015, pp. 191–198

[195] Tancredi, U., Renga, A., and Grassi, M., "Novel closed-loop approaches for precise relative navigation of widely separated GPS receivers in LEO," *Acta Astronautica*, vol. 93, 2014, pp. 243–251

[196] Komjathy, A., and Langley, R. B., "An Assessment of Predicted and Measured Ionospheric

Total Electron Content Using a Regional GPS Network," *Proc. ION NTM 1996, Santa Monica, California USA, January 22-23: 615-624*, 1996

[197] Renga, A., Causa, F., Tancredi, U., and Grassi, M., "Accurate ionospheric delay model for real-time GPS-based positioning of LEO satellites using horizontal VTEC gradient estimation," *GPS Solutions*, vol. 22, 2018

[198] Causa, F., Renga, A., and Grassi, M., "Ionosphere-gradient based filtering approach for precise relative navigation in LEO," *4th IEEE International Workshop on Metrology for AeroSpace, MetroAeroSpace 2017 - Proceedings*, 2017, pp. 56–61

[199] Causa, F., Renga, A., and Grassi, M., "Robust filter setting in GPS-based relative positioning of small-satellite LEO formations," *Advances in Space Research*, vol. 62, 2018, pp. 3369–3382

[200] Klobuchar, J. A., "Ionospheric Time-Delay Algorithm for Single-Frequency GPS Users," *IEEE Transactions on Aerospace and Electronic Systems*, vol. AES-23, 1987, pp. 325–331

[201] Montenbruck, O., "Kinematic GPS positioning of LEO satellites using ionosphere-free single frequency measurements," *Aerospace Science and Technology*, vol. 7, 2003, pp. 396–405

[202] Montenbruck, O., and D'Amico, S., "GPS Based Relative Navigation," *Distributed Space Missions for Earth System Monitoring*, M. D'Errico, ed., New York, NY: Springer New York, 2013, pp. 185–223

[203] Spilker, J. J., "GPS Navigation Data," *Global Positioning System: Theory and Applications, Volume I*, B.W. Parkinson and J.J. Spliker, eds., Washington, District of Columbia: American Institute of Aeronautics and Astronautics Inc., 1996, pp. 230–257

[204] Tancredi, U., Renga, A., and Grassi, M., "Geometric total electron content models for topside ionospheric sounding," *EESMS 2014 - 2014 IEEE Workshop on Environmental, Energy and Structural Monitoring Systems, Proceedings*, 2014, pp. 163–168

[205] Allain, D. J., and Mitchell, C. N., "Ionospheric delay corrections for single-frequency GPS receivers over Europe using tomographic mapping," *GPS Solutions*, vol. 13, 2009, pp. 141–151

[206] Rawer, K., "Synthesis of ionospheric electron density profiles with Epstein functions," *Advances in Space Research*, vol. 8, 1988, pp. 191–199

[207] Verhulst, T., and Stankov, S. M., "Ionospheric specification with analytical profilers: Evidences of non-Chapman electron density distribution in the upper ionosphere," *Advances in Space Research*, vol. 55, 2015, pp. 2058–2069

[208] Howe, B. M., Runciman, K., and Secan, J. A., "Tomography of the ionosphere: Four-dimensional simulations," *Radio Science*, vol. 33, 1998, pp. 109–128

[209] Zhang, W., Langley, R. B., Komjathi, A., and Banville, S., "Eliminating Potential Errors Caused by the Thin Shell Assumption: An Extended 3D UNB Ionospheric Modelling Technique," *26th International Technical Meeting of The Satellite Division of the Institute of Navigation (ION GNSS+ 2013)*, Nashville, TN: 2013, pp. 2447–2462

[210] Huang, Z., and Yuan, H., "Analysis and improvement of ionospheric thin shell model used in {SBAS} for China region," *Advances in Space Research*, vol. 51, 2013, pp. 2035–2042

[211] Shi, C., Gu, S., Lou, Y., and Ge, M., "An improved approach to model ionospheric delays for single-frequency Precise Point Positioning," *Advances in Space Research*, vol. 49, 2012, pp. 1698–1708

[212] Allien, A., Taillandier, C., Capo, C., Priselow, K., Legenne, J., Marechal, J., and Jeannot, M., *User guide For EGNOS application developers*, 2011

[213] Zhong, J., Lei, J., Dou, X., and Yue, X., "Assessment of vertical TEC mapping functions for space-based GNSS observations," *GPS Solutions*, vol. 20, 2016, pp. 353–362

[214] Mitch, R. H., Psiaki, M. L., and Tong, D. M., "Local ionosphere model estimation from dual-frequency global navigation satellite system observables," *Radio Science*, vol. 48, 2013, pp. 671–684

[215] Dach, R., Schaer, S., Arnold, D., Prange, L., Susnik, A., Villiger, A., and Jäggi, A., "CODE final product series for the IGS," 2016

[216] van Barneveld, P. W. L., Montenbruck, O., and Visser, P. N., "Differential ionospheric effects in GPS based navigation," *3rd international symposium on formation flying, Mission and Technology*, K. Fletcher, ed., ESA/ESTEC, Noordwijk, The Netherlands: Vol. SP-654, 2007, pp. 1–8

[217] Sardón, E., and Zarraoa, N., "Estimation of total electron content using GPS data: How stable

are the differential satellite and receiver instrumental biases?," *Radio Science*, vol. 32, 1997, p. 1899

[218] Tancredi, U., Renga, A., and Grassi, M., "Ionospheric path delay models for spaceborne GPS receivers flying in formation with large baselines," *Advances in Space Research*, vol. 48, 2011, pp. 507–520

[219] Zhong, J., Lei, J., Yue, X., and Dou, X., "Determination of Differential Code Bias of GNSS Receiver Onboard Low Earth Orbit Satellite," *IEEE Transactions on Geoscience and Remote Sensing*, vol. 54, 2016, pp. 4896–4905